NASA/CR-2000-210308

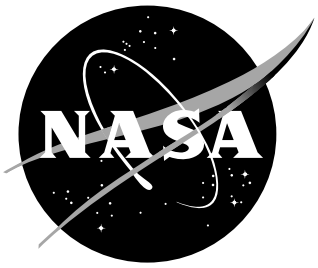

Finite Element Analysis of a Composite Semi-Span Test Article With and Without Discrete Damage

Andrew E. Lovejoy
Analytical Services and Materials, Inc., Hampton, Virginia

August 2000

The NASA STI Program Office ... in Profile

Since its founding, NASA has been dedicated to the advancement of aeronautics and space science. The NASA Scientific and Technical Information (STI) Program Office plays a key part in helping NASA maintain this important role.

The NASA STI Program Office is operated by Langley Research Center, the lead center for NASA's scientific and technical information. The NASA STI Program Office provides access to the NASA STI Database, the largest collection of aeronautical and space science STI in the world. The Program Office is also NASA's institutional mechanism for disseminating the results of its research and development activities. These results are published by NASA in the NASA STI Report Series, which includes the following report types:

- TECHNICAL PUBLICATION. Reports of completed research or a major significant phase of research that present the results of NASA programs and include extensive data or theoretical analysis. Includes compilations of significant scientific and technical data and information deemed to be of continuing reference value. NASA counterpart of peer-reviewed formal professional papers, but having less stringent limitations on manuscript length and extent of graphic presentations.

- TECHNICAL MEMORANDUM. Scientific and technical findings that are preliminary or of specialized interest, e.g., quick release reports, working papers, and bibliographies that contain minimal annotation. Does not contain extensive analysis.

- CONTRACTOR REPORT. Scientific and technical findings by NASA-sponsored contractors and grantees.

- CONFERENCE PUBLICATION. Collected papers from scientific and technical conferences, symposia, seminars, or other meetings sponsored or co-sponsored by NASA.

- SPECIAL PUBLICATION. Scientific, technical, or historical information from NASA programs, projects, and missions, often concerned with subjects having substantial public interest.

- TECHNICAL TRANSLATION. English-language translations of foreign scientific and technical material pertinent to NASA's mission.

Specialized services that complement the STI Program Office's diverse offerings include creating custom thesauri, building customized databases, organizing and publishing research results ... even providing videos.

For more information about the NASA STI Program Office, see the following:

- Access the NASA STI Program Home Page at ***http://www.sti.nasa.gov***

- E-mail your question via the Internet to help@sti.nasa.gov

- Fax your question to the NASA STI Help Desk at (301) 621-0134

- Phone the NASA STI Help Desk at (301) 621-0390

- Write to:
  NASA STI Help Desk
  NASA Center for AeroSpace Information
  7121 Standard Drive
  Hanover, MD 21076-1320

NASA/CR-2000-210308

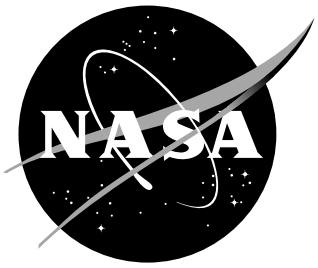

Finite Element Analysis of a Composite Semi-Span Test Article With and Without Discrete Damage

Andrew E. Lovejoy
Analytical Services and Materials, Inc., Hampton, Virginia

National Aeronautics and
Space Administration

Langley Research Center
Hampton, Virginia 23681-2199

Prepared for Langley Research Center
under Contract NAS1-96014

August 2000

The use of trademarks or names of manufacturers in the report is for accurate reporting and does not constitute an official endorsement, either expressed or implied, of such products or manufacturers by the National Aeronautics and Space Administration.

Available from:

NASA Center for AeroSpace Information (CASI)
7121 Standard Drive
Hanover, MD 21076-1320
(301) 621-0390

National Technical Information Service (NTIS)
5285 Port Royal Road
Springfield, VA 22161-2171
(703) 605-6000

Abstract

AS&M, Inc. performed finite element analysis, with and without discrete damage, of a composite semi-span test article that represents the Boeing 220-passenger transport aircraft composite semi-span test article. A NASTRAN bulk data file and drawings of the test mount fixtures and semi-span components were utilized to generate the baseline finite element model. In this model, the stringer blades are represented by shell elements, and the stringer flanges are combined with the skin. Numerous modeling modifications and discrete source damage scenarios were applied to the test article model throughout the course of the study. This report details the analysis method and results obtained from the composite semi-span study. Analyses were carried out for three load cases: Braked Roll, 1.0G Down-Bending and 2.5G Up-Bending. These analyses included linear and nonlinear static response, as well as linear and nonlinear buckling response. Results are presented in the form of stress and strain plots, factors of safety for failed elements, buckling loads and modes, deflection prediction tables and plots, and strain gage prediction tables and plots. The collected results are presented within this report for comparison to test results.

Table of Contents

1. Introduction

AS&M, Inc. was contracted by NASA Langley Research Center to perform a number of analyses on the Boeing 220-passenger transport aircraft composite semi-span test article. The government provided a NASTRAN finite element model and the drawings necessary for creation of a STAGS finite element model. Loading and damage conditions were also specified, and detailed analyses were conducted when required. This report details the methods and results from work completed by AS&M on the composite semi-span test article.

A NASTRAN finite element model of the Boeing composite semi-span test article, dated January 24, 1996, was provided to AS&M. In this finite element model, stringers, rib stiffeners and intercostals were modeled as offset beams, while the skin was modeled with plate elements. The NASTRAN bulk data file was imported into a PATRAN database for modification, and several STAGS models were developed from the new database for use in the various analyses conducted. Material properties used in the newly developed models were also obtained from the NASTRAN bulk data file and from additional provided documentation. Finite element models were developed both with and without discrete damage. Details of the finite element models, modeling techniques and discrete source damage are discussed in Sections 3 and 4 of this report.

The STAGS finite element analysis program was used to analyze the newly developed models under three load conditions. These load cases, namely Braked Roll, 1.0G Down-Bending and 2.5G Up-Bending are described in Section 2 of this report titled Load Case Definitions. Linear and nonlinear analyses were carried out for these three load cases to determine the static and buckling response of the composite semi-span. Results are presented in the form of stress and strain plots, factors of safety for failed elements, buckling loads and modes, deflection prediction tables and plots, and strain gage prediction tables and plots.

2. Load Case Definitions

2.1 Description

AS&M investigated the composite semi-span response under three load cases. Experimental loads are applied to the test article by means of load cell actuators which are numbered and located as shown in Figure 2.1. Actuator Design Ultimate Loads (DUL) values for the three cases are given in Table 2.1. The three load cases are as follows: load case 1 is 1.0G Down-Bending, load case 2 is 2.5G Up-Bending and load case 3 is Braked Roll. Loads are introduced into the finite element model as point loads at the appropriate nodes. Figures 2.2-2.4 show the three load cases as applied to the loads model (defined in Section 3.3.1). Although during the experiment the direction of the applied load can vary depending upon the deflection of the test article, and therefore affect the orientation of the load, load directions are fixed during the initial analyses since the change of orientation is expected to be minimal. All applied loads in the initial analyses act parallel to the global z-axis, with the exception of the actuator 7a load in Braked Roll. This actuator 7a load is decomposed to 110100 lbs. in the global y-direction and 150750 lbs. in the global z-direction. Follower loads at actuator 7a were later deemed necessary as described in Section 11. For all nonlinear runs except those discussed in Section 11, the load factors given in Table 2.2 are used at the corresponding load steps. Table 2.3 shows the load factors and load steps used during the follower load analysis of Section 11.

2.2 Tables

Table 2.1: Actuator Design Ultimate Load (DUL) Values.

Actuator	Load Case 1 (1G Down-Bending) (lbs.)	Load Case 2 (2.5G Up-Bending) (lbs.)	Load Case 3 (Braked Roll) (lbs.)
1	-9000	40500	-1500
2	-45000	99750	-3000
3	-33000	-3000	-1500
4	12000	21000	-3000
5	-9000	15000	-12000
6	17250	-45000	-17250
7a	N/A	N/A	186675
7b	-4500	45000	N/A
8	-14250	6000	15000

Table 2.2: Load Steps and Load Factors (times DUL) Used in the Nonlinear STAGS Analyses.

Load Step	Undamaged Load Factor	Damaged Load Factor
1	0.20	0.200
2	0.40	0.250
3	0.60	0.300
4	0.70	0.350
5	0.80	0.375
6	0.90	0.400
7	0.95	0.425
8	1.00	0.450
9	1.05	0.475
10	1.10	0.500

Table 2.3: Load Steps and Load Factors (times DUL) Used in the Nonlinear Follower Load STAGS Analyses.

Load Step	Load Factor
1	0.20
2	0.30
3	0.40
4	0.4667
5	0.50
6	0.60
7	0.6667
8	1.00

2.3 Figures

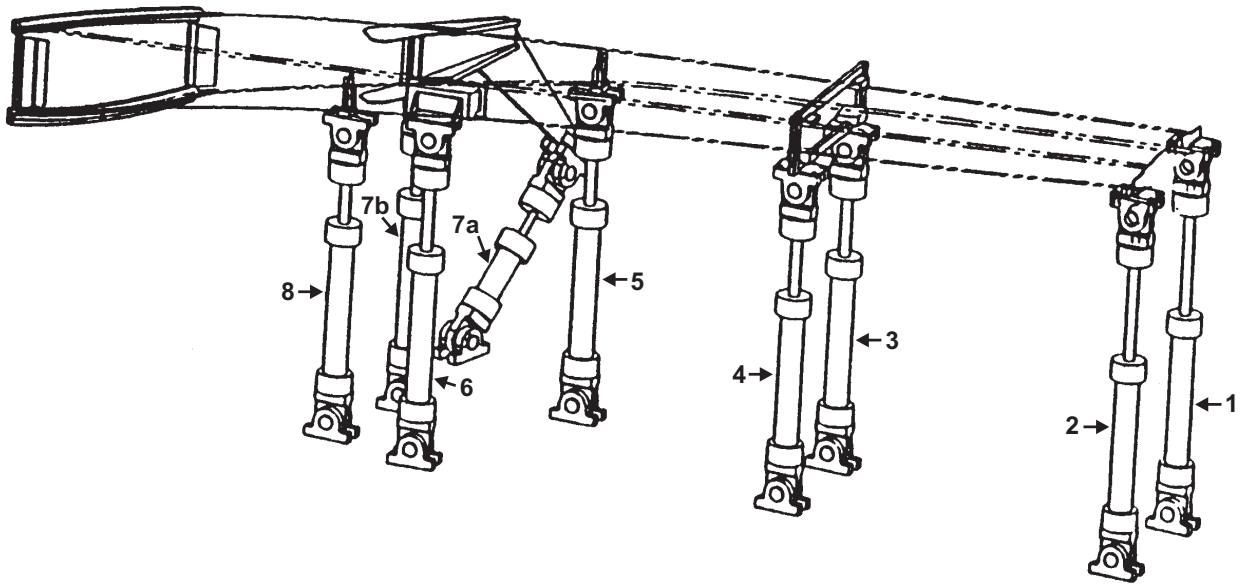

Figure 2.1: Load Cell Actuator Numbers and Locations (Modified from CRAD-9503-TR-1417).

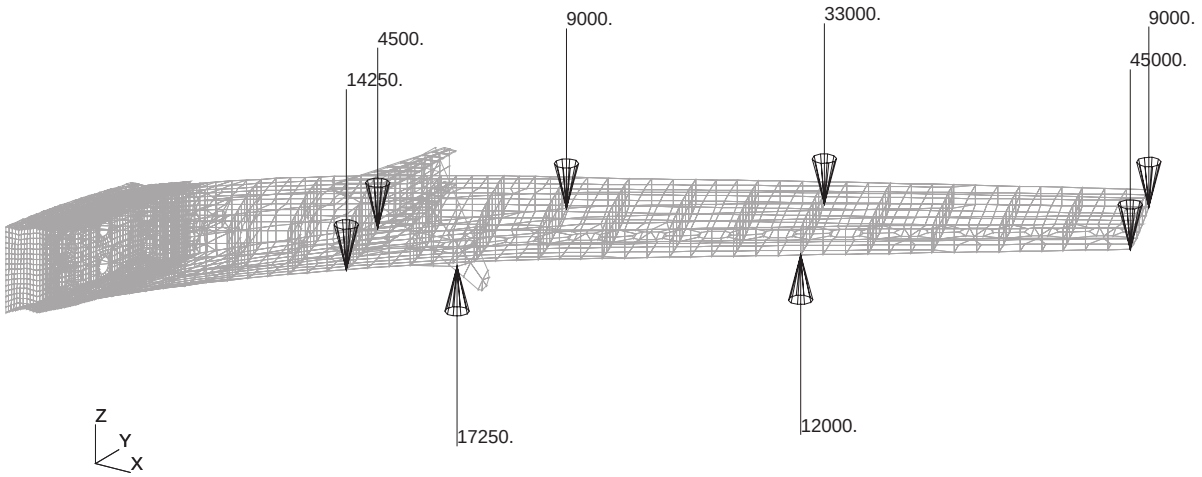

Figure 2.2: Loads Model with Load Case 1, 1.0G Down-Bending, Loads (lbs.) Shown.

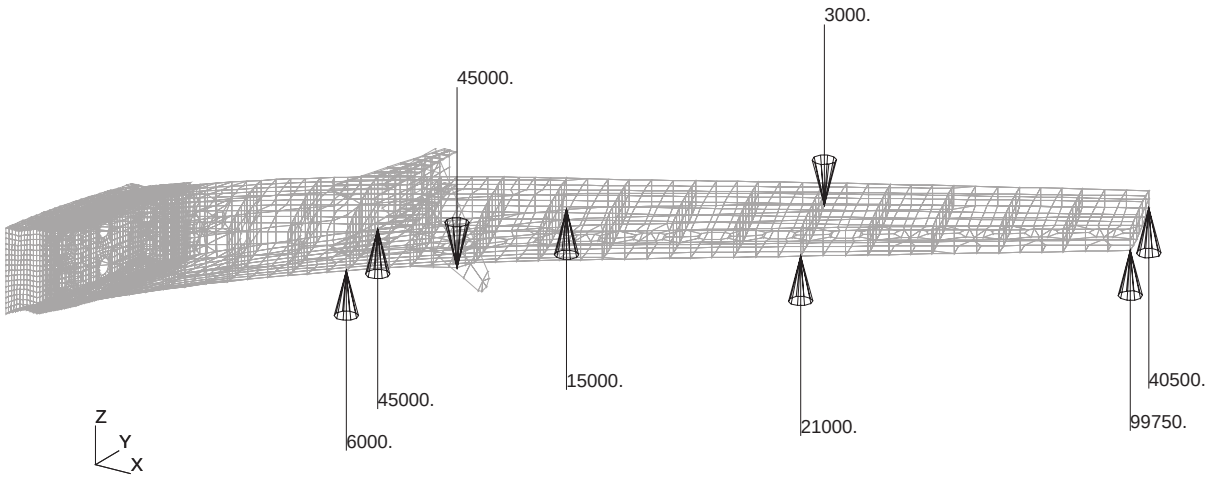

Figure 2.3: Loads Model with Load Case 2, 2.5G Up-Bending, Loads (lbs.) Shown.

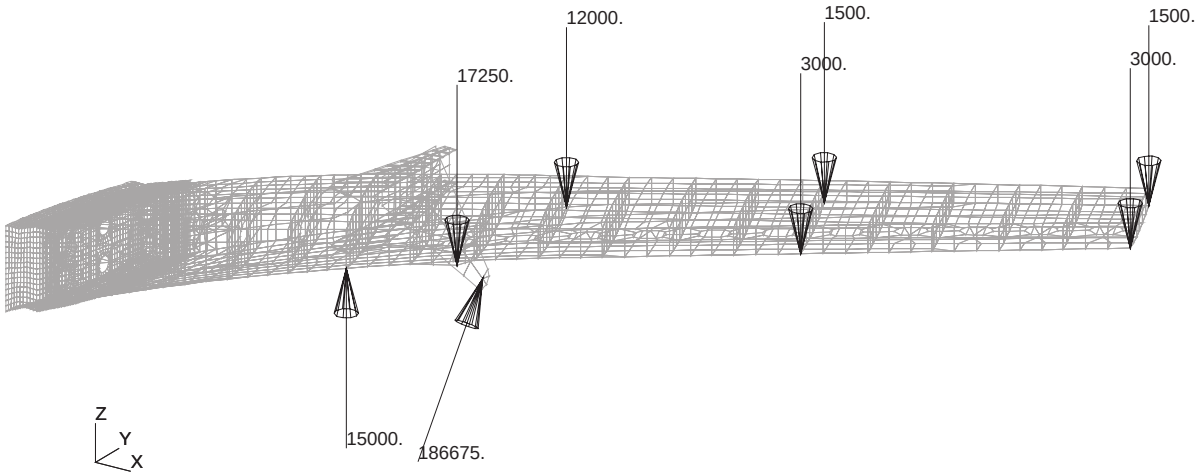

Figure 2.4: Loads Model with Load Case 3, Braked Roll, Loads (lbs.) Shown.

3. Models and Modeling Technique

3.1 Method

Model data was provided to AS&M, Inc. in the form of a NASTRAN bulk data file, a limited number of drawings and other documentation. Models were generated for the current study by importing the NASTRAN bulk data file into a PATRAN database, then making the required modifications. These models were then analyzed with the STAGS finite element analysis software using 210 beam elements, 310 triangular shell elements and 410 quadrilateral shell elements. Beam section properties were taken directly from the NASTRAN bulk data file when possible, or calculated from geometric specifications. Composite material equivalent properties are provided for "stacks" of 10 plies, and components are defined by specifying the number of stacks. Differences in shell element thicknesses were accounted for by using appropriate offsets where necessary. Upper and lower cover skin elements having a thickness of 5 stacks serve as a baseline and are specified to have no element offset. All other skin (and subsequent skin/flange) elements are given an offset that guarantees that the outer surface is continuous and smooth. Similarly, the test mount fixtures are modeled with offsets such that the interior surface is continuous and smooth, with the thickness of 1.3 inches and more having zero offset.

3.2 Model Development/Evolution

Six new finite element models were developed in this study and have been termed the loads model, refined model, detailed model, strain gage model, tapered-height model and loadarm model. The loads model was developed first in order to study the response of the root mount fixture. The refined model was then developed to study the response of the composite semi-span itself. Buckling response problems discovered using the refined model, as discussed in Section 7.2.1, required a modifications which lead to the detailed model. Next, strain gage predictions were made using the strain gage model, which has refinements to the detailed model at the strain gage locations. A tapered-height model was then developed to account for design changes that occured in the stringer geometry of the upper cover stringer runouts. Lastly, a loadarm model was developed to study the effect of the braked-roll loading on the loadarm deflections under follower loads. Variations of these models, with the exception of the loads and loadarm models, were also studied with discrete damage introduced as required.

3.3 Model Descriptions

The composite semi-span test article consists of upper and lower covers, fore and aft spars, ribs, stringers, stiffeners and intercostals that connect the ribs to the covers and spars. Figures 3.1 and 3.2 show the upper and lower cover planforms, respectively, with the rib and stringer numbering schemes indicated. Table 3.1 summarizes the stringer termination locations that can be seen in the figures. The ribs and fore and aft spars connect the upper and lower covers. Attachment of the semi-span to the wall is accomplished with a set of test mount fixtures. Appropriate models for the semi-span and test mount fixtures are developed focussing on the area(s) of interest. Descriptions of the basic models are provided in the following sections.

3.3.1 Loads Model

As previously mentioned, the loads model was developed to analyze the root mount fixture. The geometry for the root mount fixture was generated from information provided in the form of drawings and from the NASTRAN finite element model. The root mount fixture consists of four (4) upper and four (4) lower mount plates, as well as side shear plates. A single drawing of one each for the upper and

lower mounting plates was provided. The reference surfaces were generated based upon the thickness of the plates and the required offset, with thicknesses of 1.3 inches and more represented by their mid-planes with zero offset. These surfaces were discretized and the resulting shell finite element mesh is shown in Figure 3.3, with free edges shown in Figure 3.4. Meshing of the mount plates is highly depended upon the location of the bolts that attach the mount plates to the semi-span. Bolts can not be located over stringers, and therefore were spaced between the stringer locations. Four rows of bolts attach the upper and lower plates to the semi-span covers, and three rows attach the shear plates to the semi-span spars. Figure 3.5 shows the locations of the attachment bolts, which were modeled as beam elements with high stiffness.

Side shear plates attach the upper and lower fore and aft mount plates. These shear plates are attached to the upper and lower mount plates between the wall and wing root, but are not attached the upper and lower mount plates outboard of the root rib. Separation of the shear plates and upper and lower mount plates is due to cutouts that are present to permit the semi-span overhangs (not present in the loads model) to extend fore and aft of the shear plates. Bolts then attach the free portion of the shear plates to the semi-span spars. The upper and lower plates are numbered from the leading edge to the trailing edge, with plate 1 located at the leading edge and plate 4 located at the trailing edge for both upper and lower, as seen in Figure 3.6. At these plate separations, the shear flow at the wall must be zero. To ensure this condition, the nodes located at the junctions of the plate separations and the wall have been left free, that is, no boundary conditions are imposed at those nodes during the finite element analysis. This is also done to eliminate the stress singularities that occur at corners having one clamped and one free edge. Additionally, the root mount plates have been designed such that no moments are to be generated at the wall. Therefore, all other root mount plate nodes located at the wall have only their translational degrees of freedom restrained. The completed loads model consisted of 9346 nodes and is shown in Figure 3.7.

3.3.2 Refined Model

A refined model was produced to study the response of the composite semi-span test article. In the refined model, the stringer and spar-cap beam approximations used in the NASTRAN model were replaced with appropriate shell elements. Corrections to the rib thicknesses were also made in accordance with the values shown in Table 3.2. Door covers that were absent on the provided NASTRAN model were added to the ribs. Lastly, various stiffener and cutout sizes and locations on the ribs were corrected where the NASTRAN model did not match with the current semi-span design. Rib stiffener and intercostal offset beam approximations were retained from the loads model.

Stringer flanges were incorporated with the cover skins through the introduction of skin/flange elements. Additional shell properties, with offsets, were created for the combined skin/flange. The stringer blades were introduced with additional shell elements, with new shell properties created for the stringer blades having zero offsets. NASA provided the stringer flange and blade definitions, and although the stringers were created by folding out the flanges from the blade stacks, the provided flange thicknesses are slightly smaller than what is expected from direct stack calculations. These smaller flange thicknesses were added to the skin thickness to create the skin/flange property sets. Blade thicknesses are equal to the expected thicknesses given by the number of stacks.

Rib property sets were modified to reflect the new thicknesses provided. The rib 2 doors were included in the refined model using equivalent shell properties that were determined from the door stacking sequence. Although the flexibility of the bolted door should be accounted for through

reductions in the door equivalent shell properties, such reductions were not included in this model. Equivalent beam properties for the rib 2 doors were also calculated and added to the refined model.

Detailed information provided by NASA regarding the spar/skin attachment indicates that interleaving of the spar and skin exists. Part of this attachment region includes a 4.25 inch overhang that has 6 stacks everywhere. The flange portion interior to the spars is blended with the skin so that there are 6 stacks minimum in this flange region. The flange area takes on the skin value when the skin is greater than six stacks (i.e., a 5 stack skin bay has 1 stack added to make a flange area with 6 stacks, while a 7 stack skin bay area has a flange area of 7 stacks). Essentially, this means that a flange of 6 stacks is added when the skin thickness is 5 or less stacks, and when the skin thickness is 6 or more stacks there is no separate flange. Appropriate property sets and elements were added to account for the fore and aft overhangs and spar-cap flanges.

Several areas of the basic mesh were refined to capture localized effects. Four rows of elements were created in the overhang to increase the chance of finding any overhang buckling response. The area around the stringer 1 runout on the upper cover was also refined due to a buckling problem that was found in this area (see Section 7.2.1.1). This mesh refinement included the stringer blade, stringer flange, the surrounding skin bays between ribs 4 and 5 and between ribs 5 and 6, and the forward overhang. Additional property sets were also created to define the stringer blade stack drop-off regions present for the upper cover stringer terminations. Lastly, the overhang was reduced to 1.65 inches to eliminate the myriad of overhang buckling modes found during the study of the skin bay buckling. Figure 3.8 shows the complete refined model finite element mesh that has 16937 nodes.

3.3.3 Detailed Model

The detailed model was created due to the buckling problems that were encountered during the refined model analysis. A modification was made to the refined model, where 1 stack of upper cover material was added to the upper cover skin bay bounded by rib 4, the forward spar, rib 5, and stringer #2. This modification was made by adjusting the element property set assignments, yielding the detailed model which is the base model for subsequent analysis and model development. The only additional change was to create a model with a reduced overhang length, 4.0 inches, based upon the buckling response (see Section 7.2.2.3). This modification was accomplished by adjusting the exterior row of elements of the overhangs to meet the new overhang length. The detailed model has the same number of nodes as the refined model shown in Figure 3.8, and the same mesh with the exception of the exterior rows of elements on the overhangs.

3.3.4 Strain Gage Model

The strain gage model was developed from the detailed model by modifying the regions surrounding the strain gages. These regions were refined to include only reasonably shaped quadrilateral elements in the general vicinity of the strain gages. Transition of these regions with the remainder of the model was performed using combinations of triangular elements and trapezoidal quadrilateral elements. Strain gage regions were successively refined during a convergence study, described in Section 9.1. The model yielding the converged results, consisting of 29586 nodes, is the strain gage model. Figures 3.9 and 3.10 provide views showing the upper cover and lower cover strain gage refinements, respectively.

3.3.5 Tapered-Height Model

A design change in the upper cover stringers #2 and #10 was included in the tapered-height model, where these stringer terminations are modified to now have a height taper. The initial design as modeled in the refined model includes a thickness taper which is achieved by ply drops every 3 inches while the stringer height remains constant. However, an 8 degree angle height taper is now incorporated into the stringers #2 and #10 runouts. For these 2.5 inch tall stringers, this taper angle produces a tapered region that is approximately 17.788 inches in length. Modifications were made to the base model, which was taken as the converged strain gage model of Section 3.3.4. As much as possible, the mesh remains unchanged for the modified taper geometry with the following exceptions. For stringer #2, the base model has larger elements at the actual termination since this region was of little interest in the strain gage and damage predictions. Therefore, it was necessary to slightly refine the mesh at the end of the tapered runout to accurately capture the load transfer from the stringer to the skin. Modifications to stringer #10 include additional splits in elements away from the termination, and blending of element rows into the new tapered edge via triangular elements. 30749 nodes comprise the tapered-height model. Close-ups of the upper cover stringer #2 and stringer #10 mesh refinements can be seen in Figures 3.11 and 3.12, respectively. The associated cover mesh refinements are shown in Figures 3.13 and 3.14.

3.3.6 Loadarm Model

A loadarm model was necessary to incorporate the changes in the loadarm region that is required for the braked roll loading condition. From drawings provided by NASA, and from a NASA provided NASTRAN input file called flat.bdf, the loadarm region that includes the loadarm plate, loadarm I-beam and upper and lower cover doublers was modified. The loadarm plate is the portion of the loadarm assembly that attaches the load actuator to the loadarm I-beam via two "super-bolts". Doublers are bolted to the I-beam section flanges and to the upper and lower covers, tying the I-beam flanges to the covers. The I-beam is also connected to the aft spar via angle plates that are bolted to the span and the I-beam web. Figure 3.15 shows the finite element mesh for the loadarm assembly with the individual components being labled. Numerous changes were made to the tapered-height model to create the loadarm model.

First, since the loads outboard of rib 7 are low for the braked roll case, and the response in the outboard region was not of primary concern, the mesh outboard of rib 7 was made more coarse by eliminating all refinements associated with strain gages and discrete damage. Additionally, several of the refinements inboard of rib 7 were eliminated or modified to match the current geometry changes.

Second, the loadarm plate geometry was generated and the finite element mesh created. This includes a beam element to represent the load actuator, as well as beams to represent the actuator connection fitting that attaches the end of the actuator to the loadarm plate. The beam representing the load actuator is given an area of zero to provide no axial stiffness, while it has large moments of inertia to prevent actuator bending and torsion. Actuator connection beams were provided with large area and moments of inertia to represent the highly rigid connection fitting. In the model, the load actuator beam has a node that is coincident with the node attached to the actuator connection beams. These nodes are then translationally tied together through Lagrange constraints defined on the STAGS G3 and G4 records, which enforce compatibility of the translational degrees of freedom for the two nodes. The actuator load is then applied to the node attached to the load actuator beam so that this load becomes a follower load with respect to the load actuator and not the loadarm plate. Finally, the anchor node for the load actuator beam was fixed in all three translations, and was also fixed in rotation about the y-axis to eliminate rigid

body rotations. Figure 3.16 shows the loadarm plate, radial super-bolt connection beams, load cell connection fixture beams and load actuator beam.

Third, the planforms of the upper and lower doubler plates were corrected to represent the current design, and new doubler plate surfaces were generated. These surfaces were then subdivided according to thickness changes in the doublers and the bolt locations. This was done to ensure that meshing of the surfaces provided nodes at or near the bolt locations so that when nodes were positioned at the correct bolt locations, distortion of the finite element mesh was minimized. Similar steps were applied to the semi-span covers for generating the mesh and bolt locations. Meshes for the upper and lower doubler plates are shown in Figure 3.17.

Fourth, the I-beam was matched to the doubler plates and the aft spar. Meshing of the I-beam flanges was linked to the bolt locations of the doublers and the web location, while meshing of the web was linked to the location of the super-bolts and spar elements. The angles connecting the I-beam web to the aft spar were ignored in this model, therefore, the I-beam web elements were directly connected to the aft spar elements.

Lastly, the super-bolts were modeled as beams that were connected to the loadarm plate by stiff beams. The radial beams were located so that they were centered about the expected line of action of the forces acting on the loadarm plate, and extend through an arc of approximately 150 degrees. The radial super-bolt connection beams are clearly seen in Figure 3.16.

The finite element mesh for the entire loadarm model is shown in Figure 3.18. The loadarm model has a total of 24370 nodes.

3.4 Tables

Table 3.1: Stringer Termination Locations.

Stringer Number	Upper Cover Termination Rib*	Lower Cover Termination Rib*
1	4	4
2	9	10
3	15	15
4	FL	FL
5	FL	FL
6	FL	2
7	FL	FL
8	FL	FL
9	15	15
10	9	8

*FL Indicates the Stringer Runs the Full Length of the Semi-Span

Table 3.2: Rib Thicknesses From the Old NASTRAN Database and the New Updated Information.

Rib	Old Thickness	New Thickness
1	0.154	0.330
2	0.154	0.176
3	0.110	0.143
4	0.110	0.198
5	0.110	0.264
6	0.220	0.440
7	0.143	0.143
8	0.143	0.143
9	0.143	0.143
10	0.143	0.143
11	0.143	0.143
12	0.143	0.143
13	0.143	0.143
14	0.143	0.143
15	0.143	0.143
16	0.143	0.143
17	0.143	0.143
18	0.440	0.750

3.5 Figures

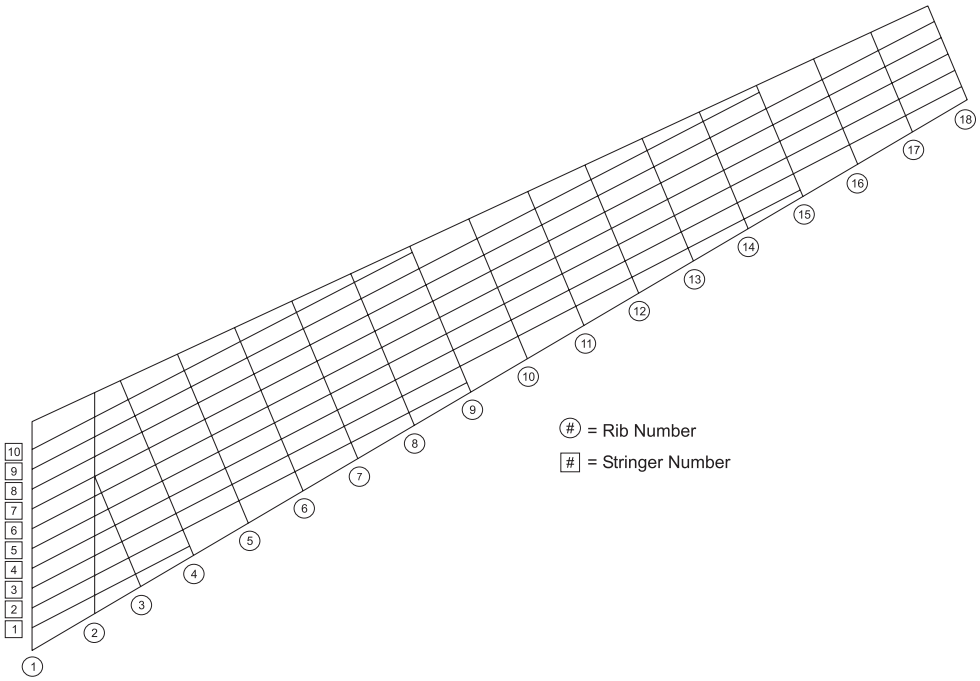

Figure 3.1: Plan View Sketch of Upper Cover Showing Rib and Stringer Numbering. Note: Rib 1 is the Root Rib and Stringer 1 is the Foremost Stringer.

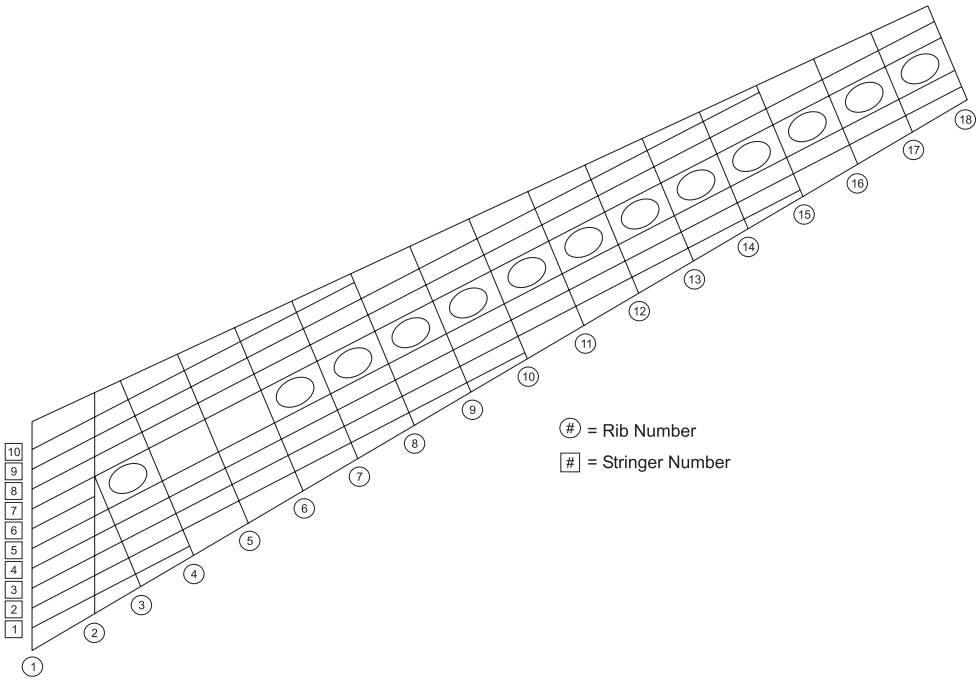

Figure 3.2: Plan View Sketch of Lower Cover Showing Rib and Stringer Numbering and Cutout Locations. Note: Rib 1 is the Root Rib and Stringer 1 is the Foremost Stringer.

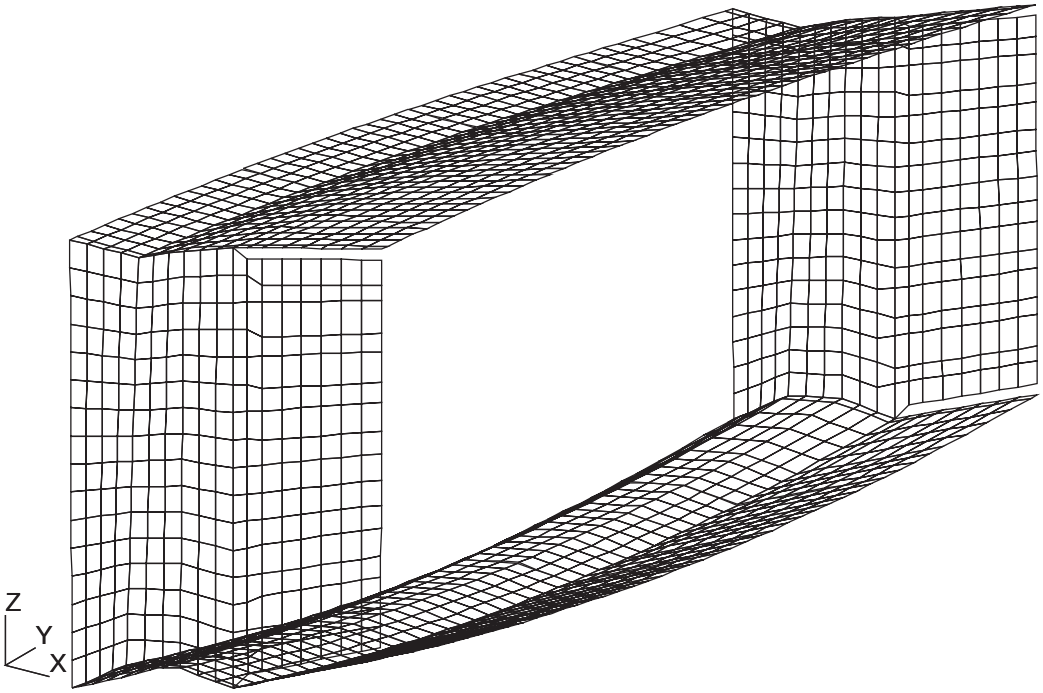

Figure 3.3: Finite Element Discretization of the Root Mount Plates.

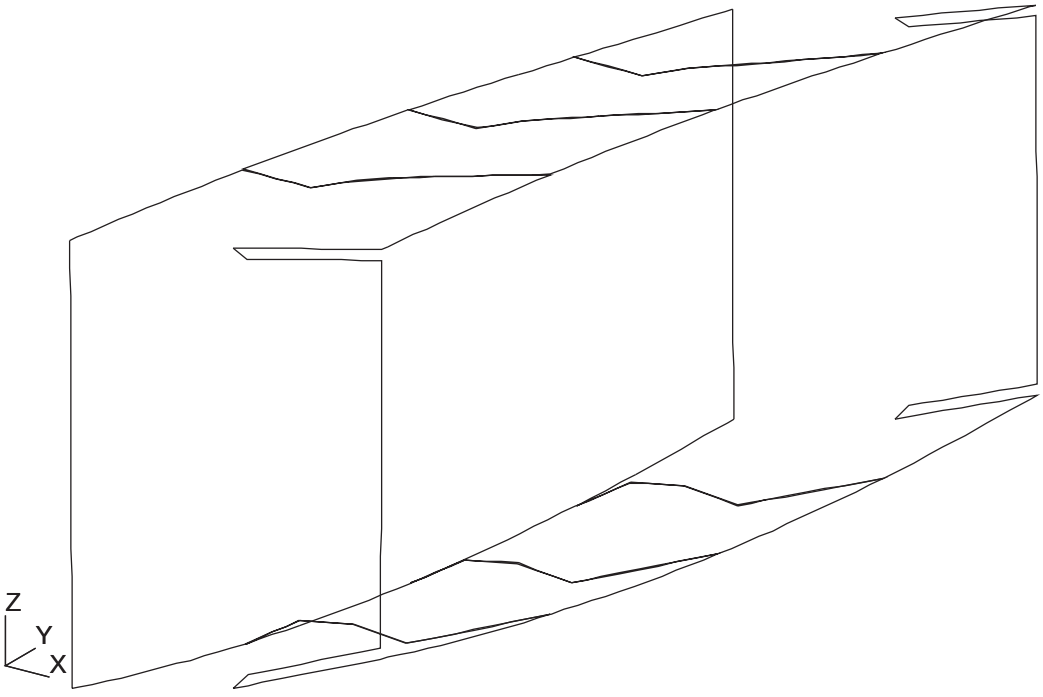

Figure 3.4: Root Mount Plate Free Edges Clearly Showing Top and Bottom Plate Separations.

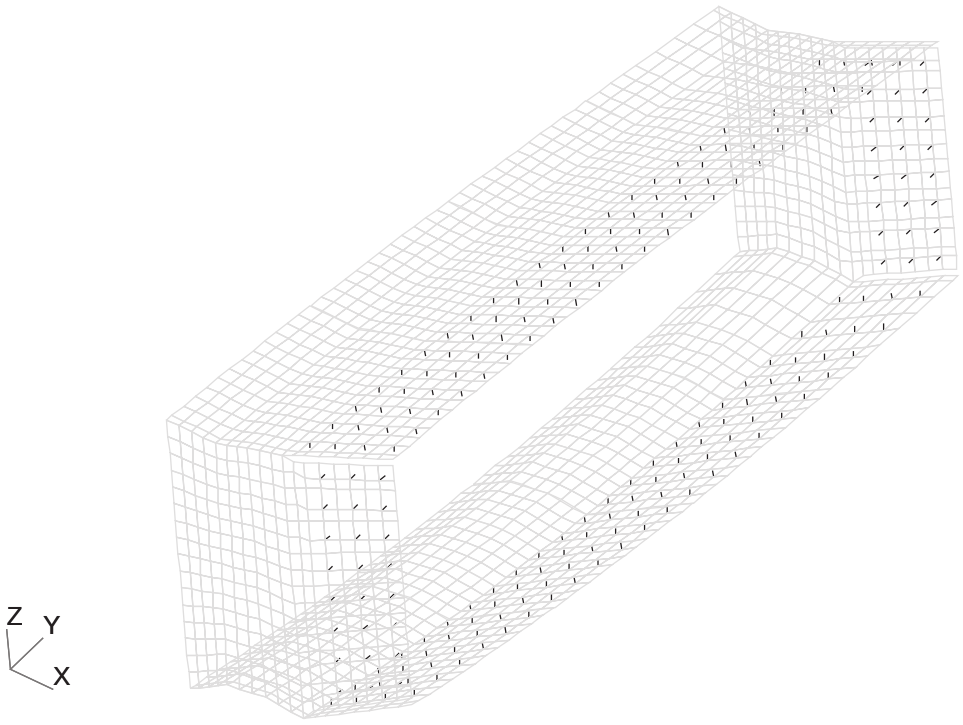

Figure 3.5: Bolt Finite Element Locations (black lines) for Attaching the Root Mount Plates (grey lines) to the Composite Semi-Span.

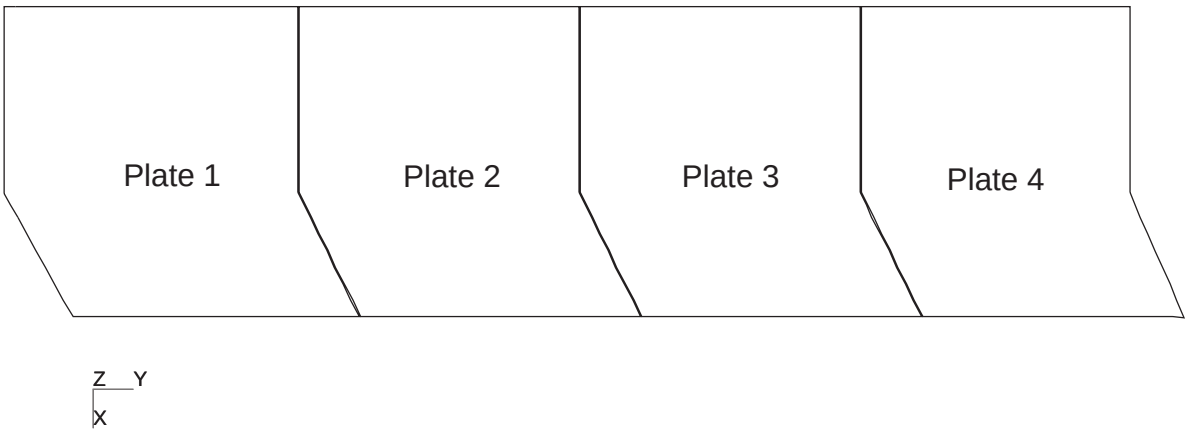

Figure 3.6: Plan View of Top and Bottom Root Mount Plate Number Scheme.

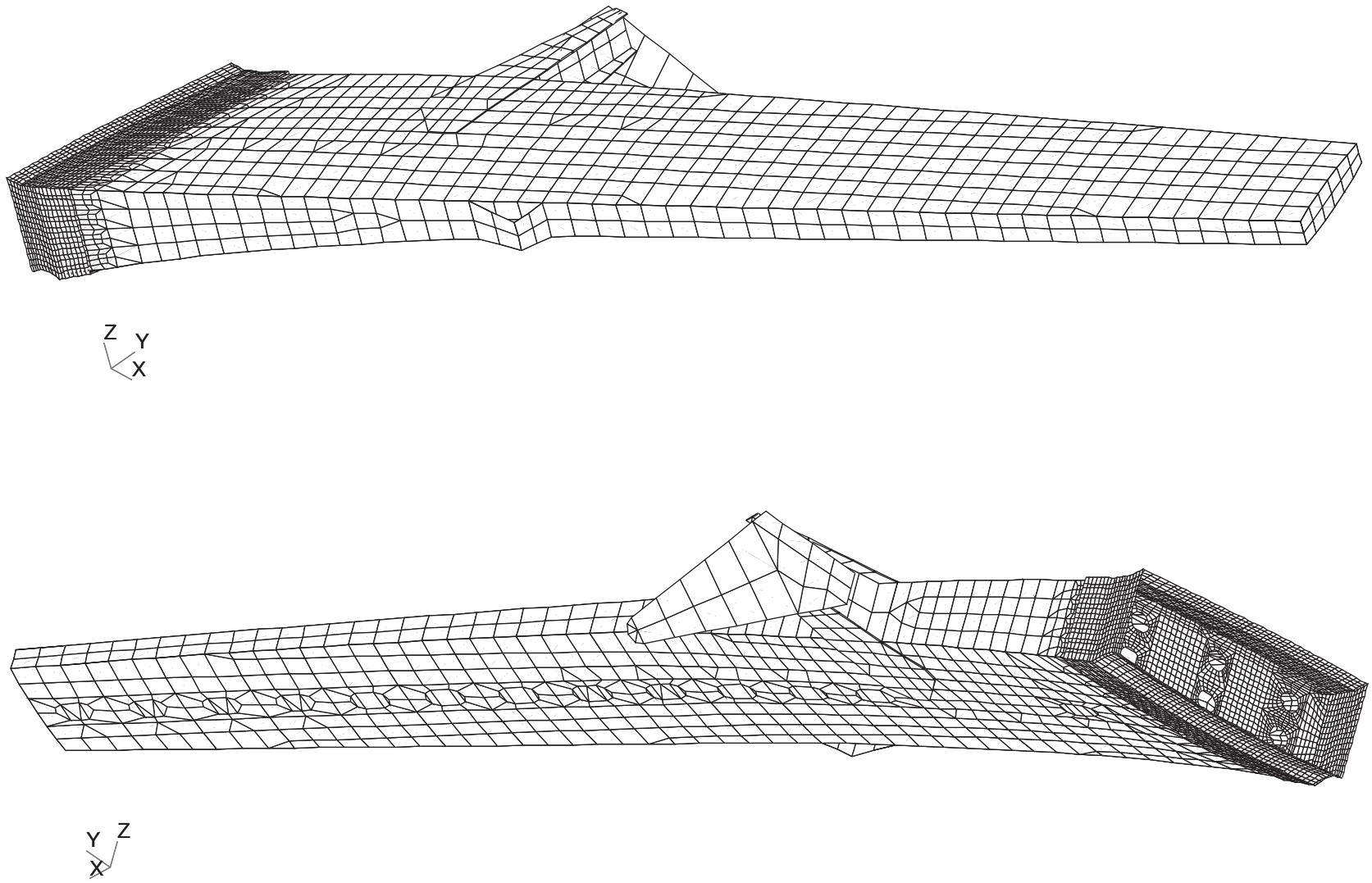

Figure 3.7: Loads Model Finite Element Mesh.

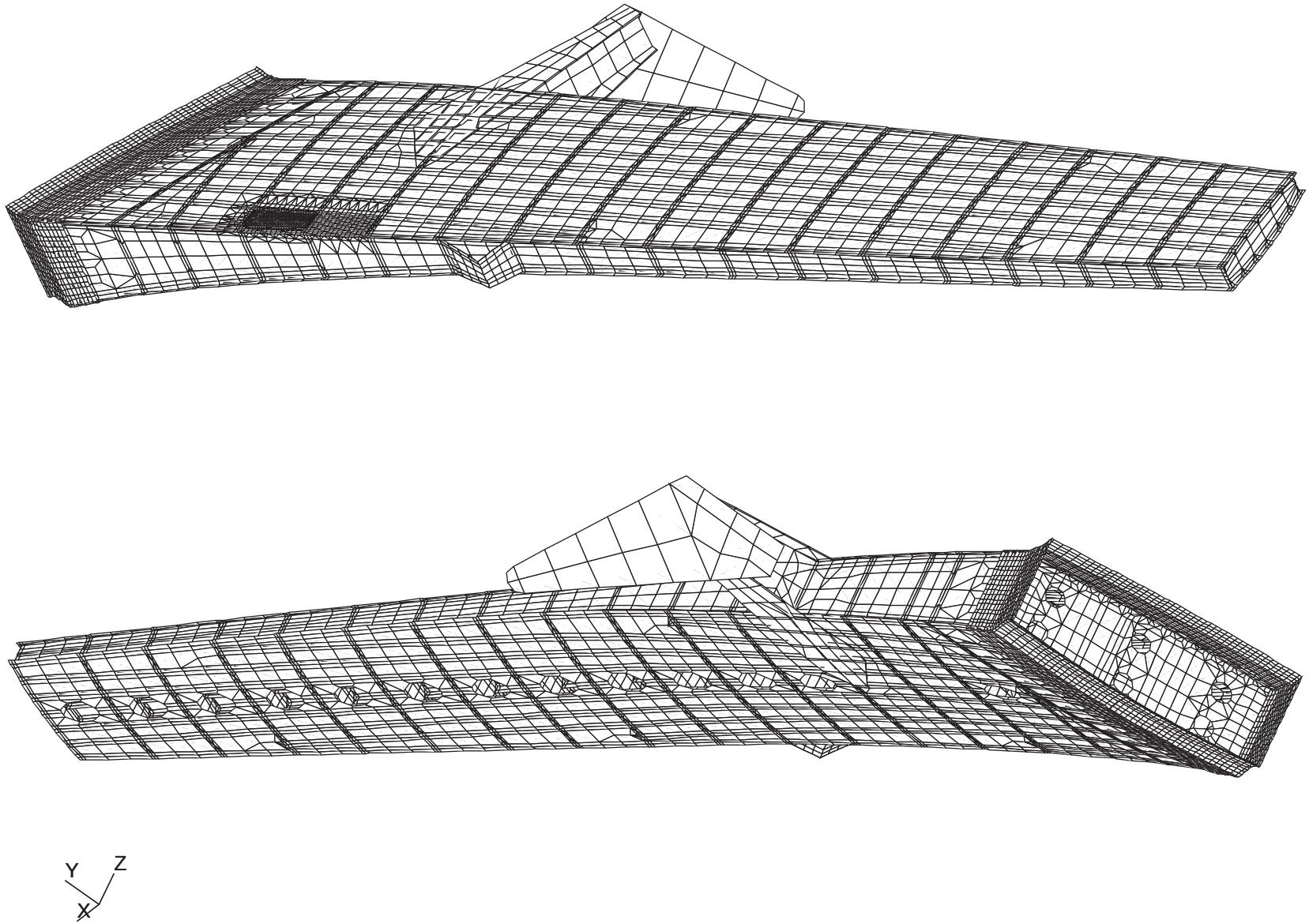

Figure 3.8: Refined Model Finite Element Mesh, Overhangs Reduced to 1.65 Inches for Skin Bay Buckling Analysis.

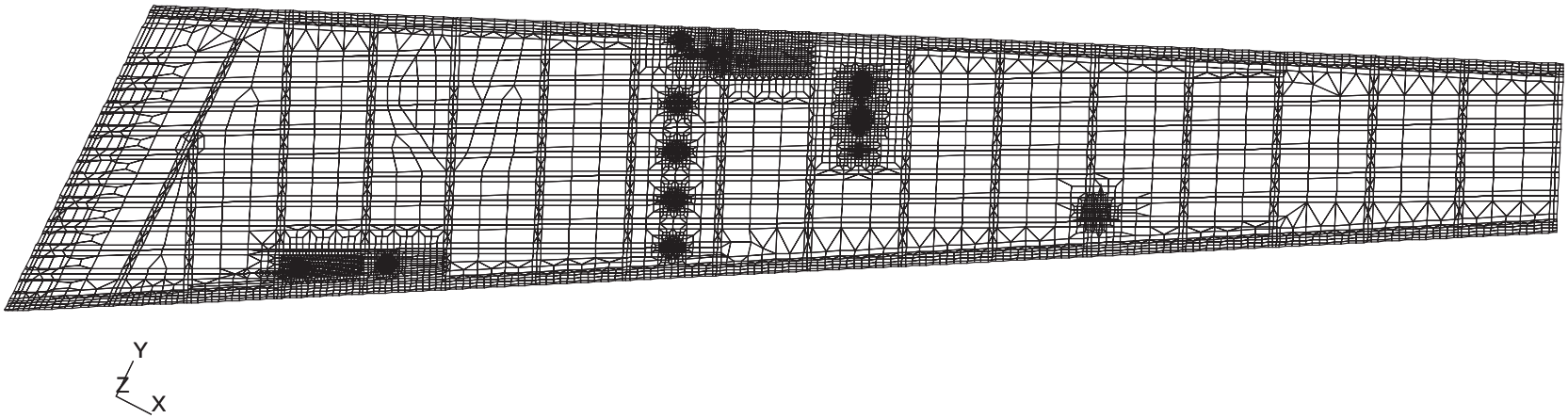

Figure 3.9: Upper Cover Mesh Refinement for Strain Gage Model.

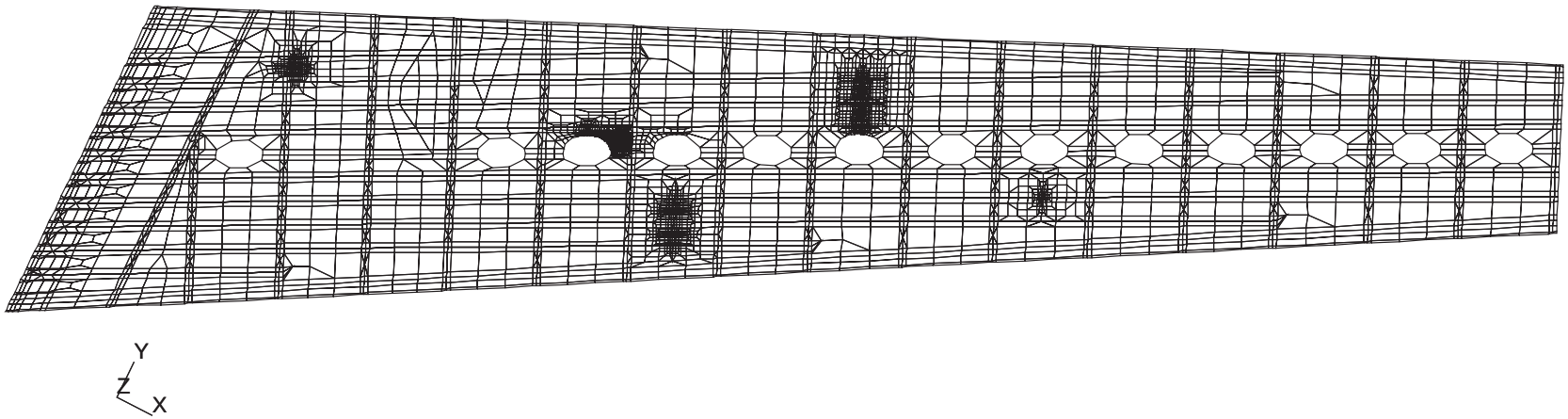

Figure 3.10: Lower Cover Mesh Refinement for Strain Gage Model.

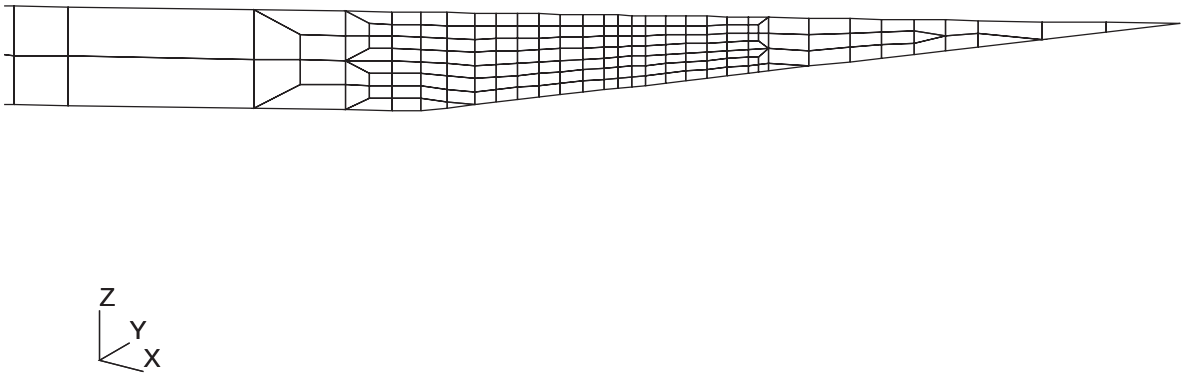

Figure 3.11: Tapered Height Model Stringer #2 Finite Element Mesh.

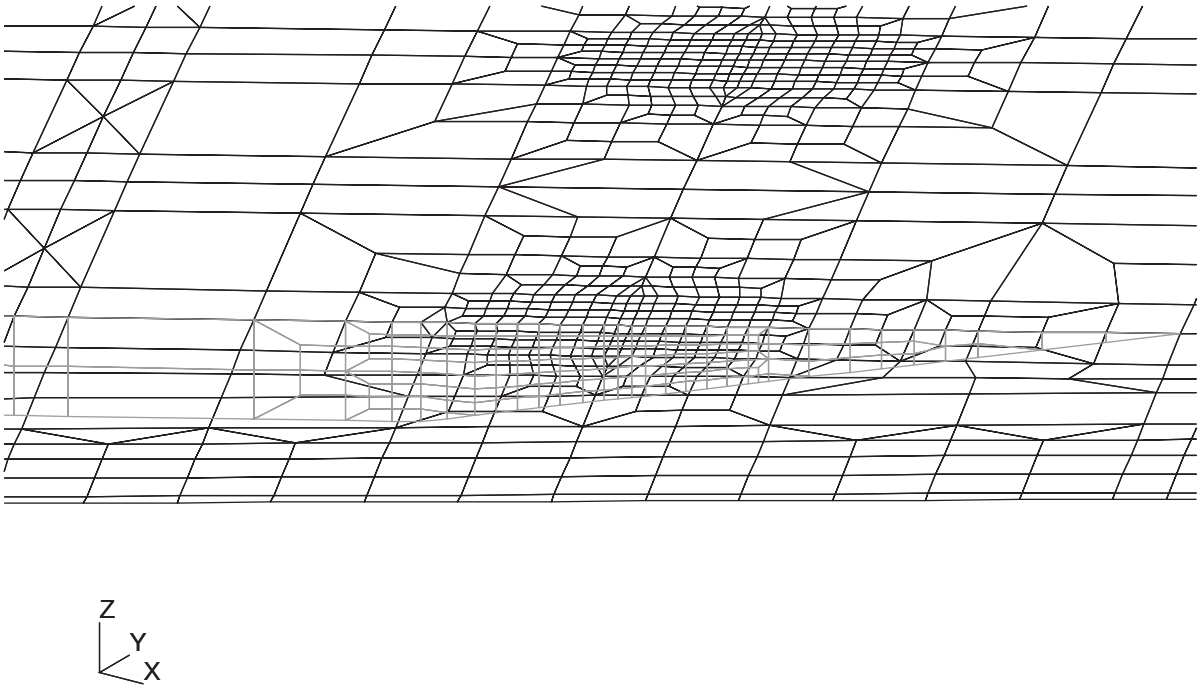

Figure 3.12: Tapered Height Model Stringer #2 Skin Finite Element Mesh (Stringer Web Shown in Grey).

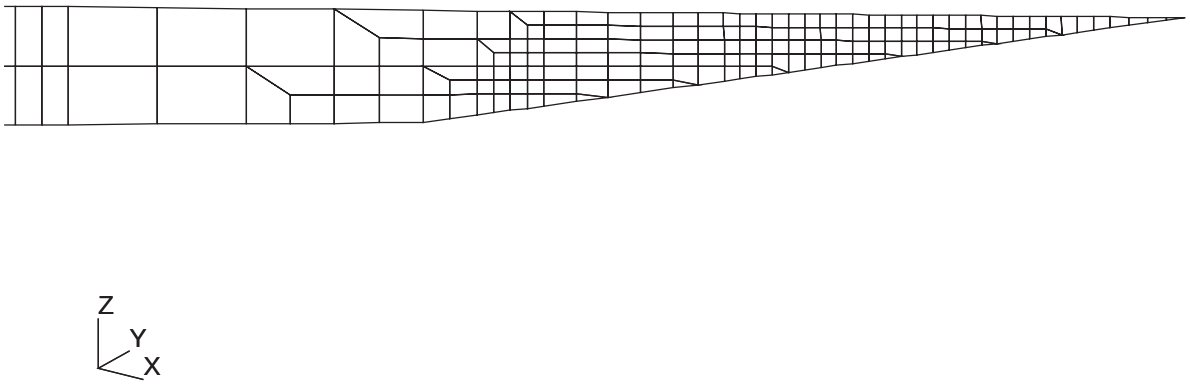

Figure 3.13: Tapered Height Model Stringer #10 Finite Element Mesh.

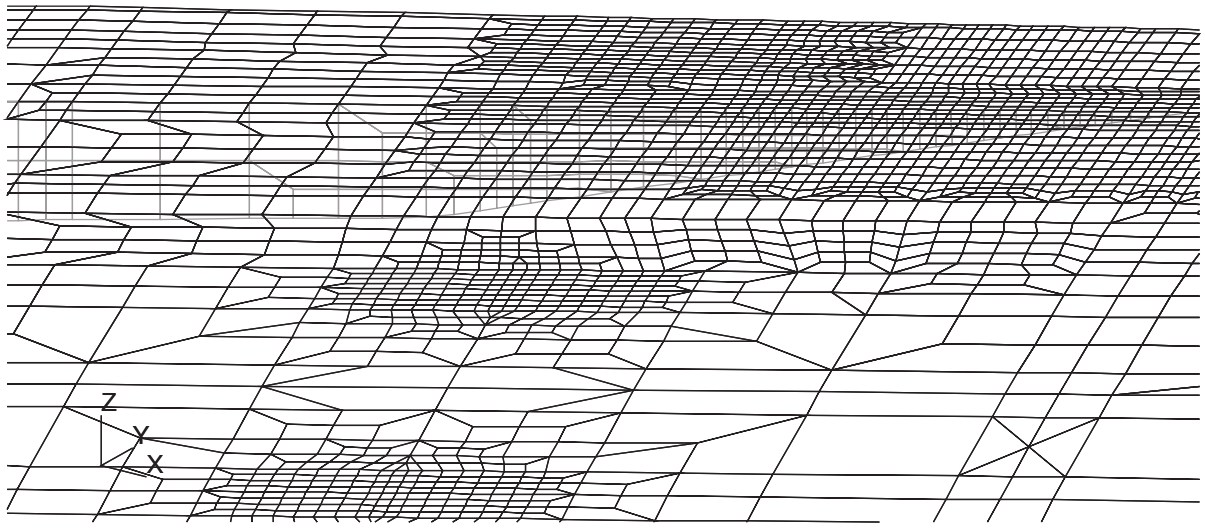

Figure 3.14: Tapered Height Model Stringer #10 Skin Finite Element Mesh (Stringer Web Shown in Grey).

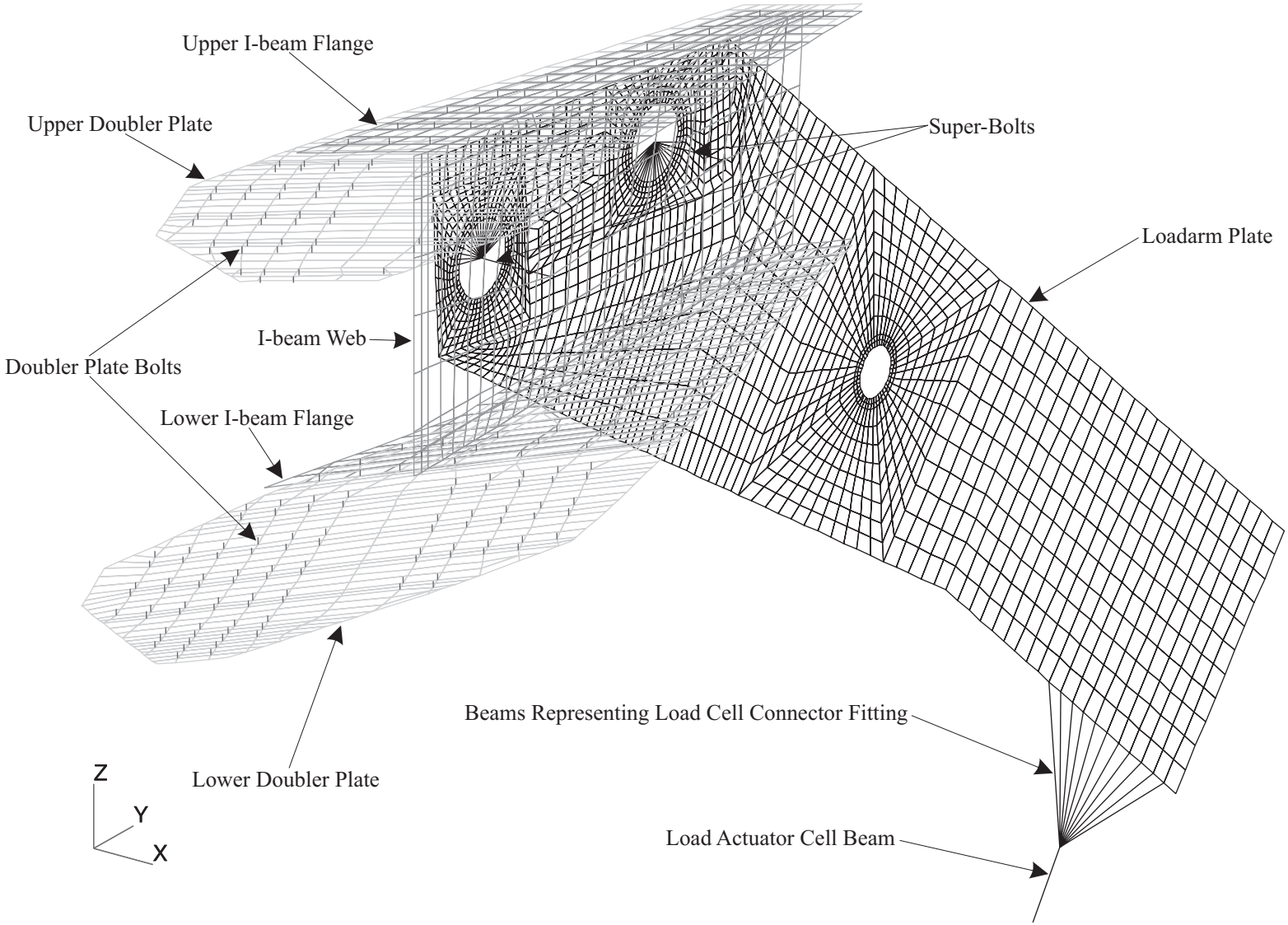

Figure 3.15: Loadarm Assembly Finite Element Mesh with Loadarm Components Identified.

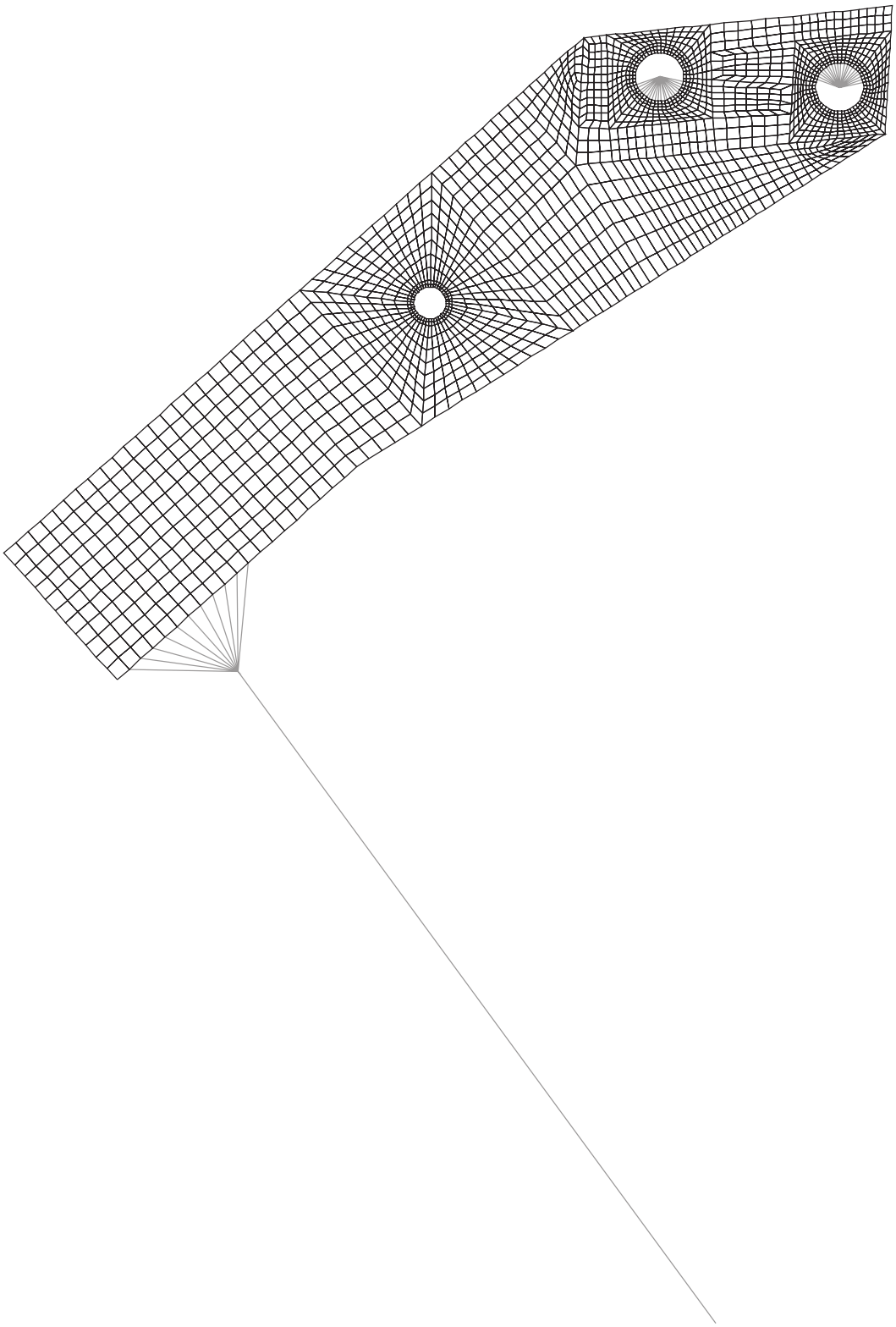

Figure 3.16: Finite Element Mesh of the Loadarm Plate, Super-bolt Radial Beams, Beams Representing the Load Cell Connection Fitting and the Load Actuator Beam.

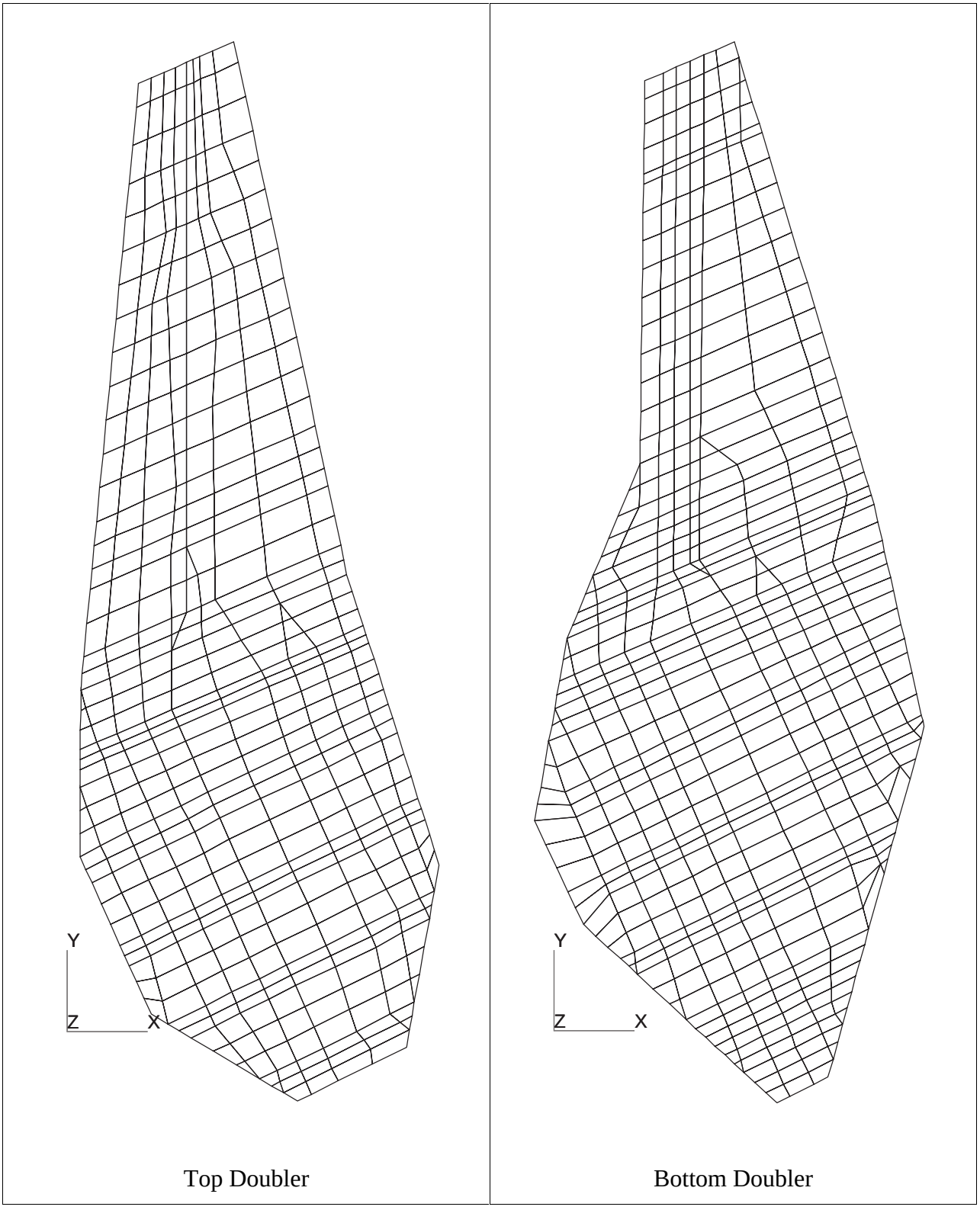

Figure 3.17: Top and Bottom Doubler Plate Finite Element Meshes.

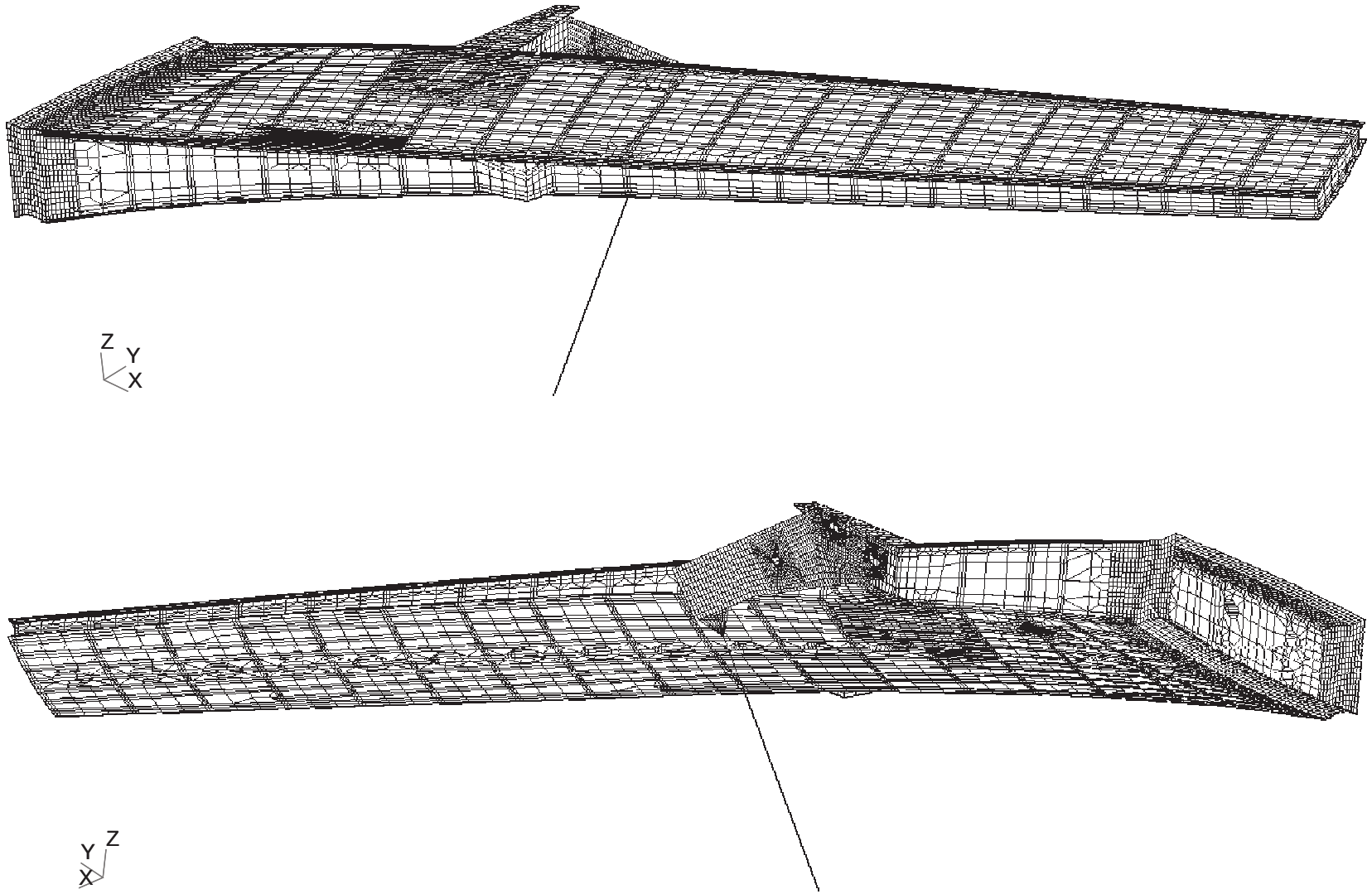

Figure 3.18: Loadarm Model Finite Element Mesh.

4. Discrete Damage Definitions

4.1 Upper Cover Sawcut

The first discrete damage scenario is a 7.0 inch long by 0.19 inch wide sawcut with 0.19 inch diameter semi-circular ends. This sawcut is introduced into the upper cover skin and stringers. It is centered between ribs 10 and 11, and is centered across stringer 8, where both the cover and the stringer blade are completely cut through the thickness. Figure 4.1 shows a close-up view of the finite element mesh in the upper cover sawcut region. The same region is shown in Figure 4.2 where only the element free edges are displayed, clearly showing the crack edge and the stringer blade edges. Addition of the upper cover sawcut increases the size of the detailed model from 16937 nodes to 20016 nodes.

4.2 Lower Cover Sawcut

The second discrete damage scenario is also a 7.0 inch long by 0.19 inch wide sawcut with 0.19 inch diameter semi-circular ends. However, this sawcut is introduced into the lower cover skin and stringers. As with the upper cover sawcut, this lower cover sawcut is centered between ribs 10 and 11, and is centered across stringer 8, where both the cover and the stringer blade are completely cut through the thickness. Figure 4.3 shows a close-up view of the finite element mesh in the lower cover sawcut region. The same region is shown in Figure 4.4 where only the element free edges are displayed, clearly showing the crack edge, stringer blade edges and cutout edges. The detailed model size increases from the 16937 nodes to 20148 nodes with the addition of the lower cover sawcut.

4.3 Figures

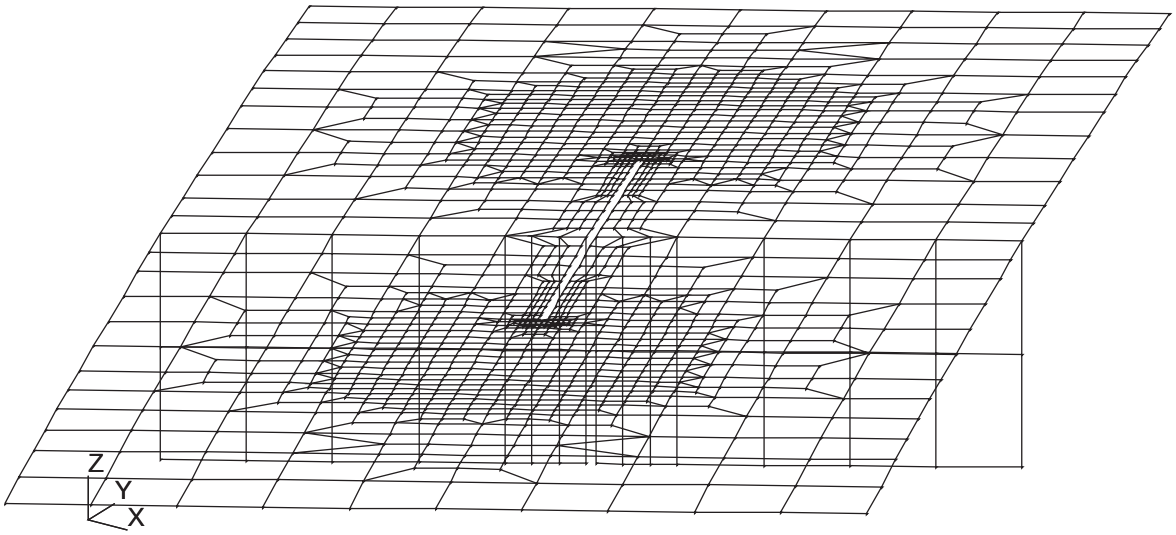

Figure 4.1: Upper Cover Sawcut Finite Elment Mesh Showing Sawcut Region Located Between Ribs 10 and 11 and Cutting Stringer #9.

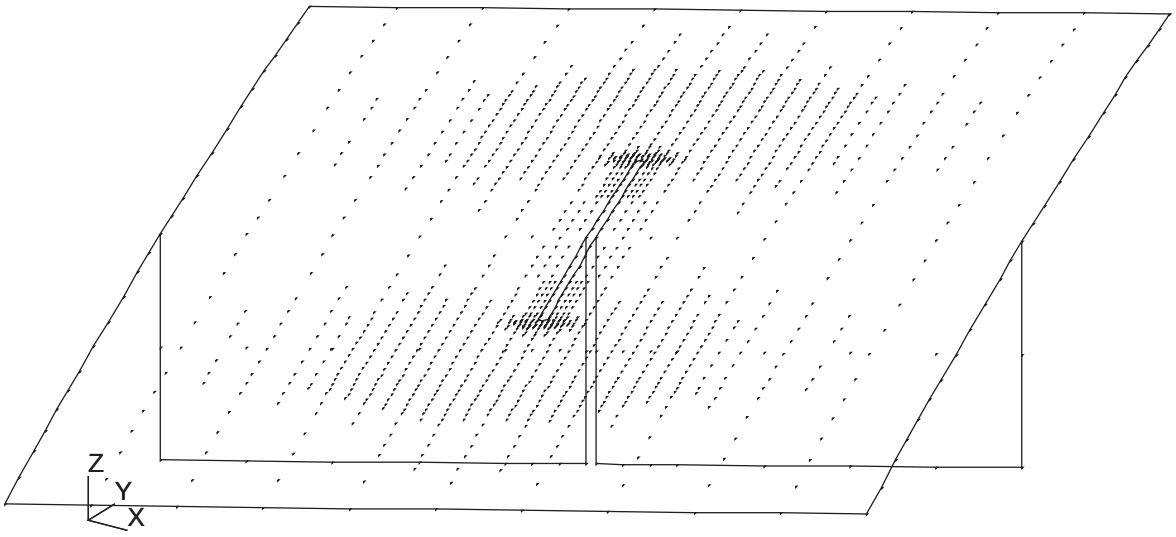

Figure 4.2: Upper Cover Sawcut Free Edges Showing Sawcut Region Located Between Ribs 10 and 11 and Cutting Stringer #9.

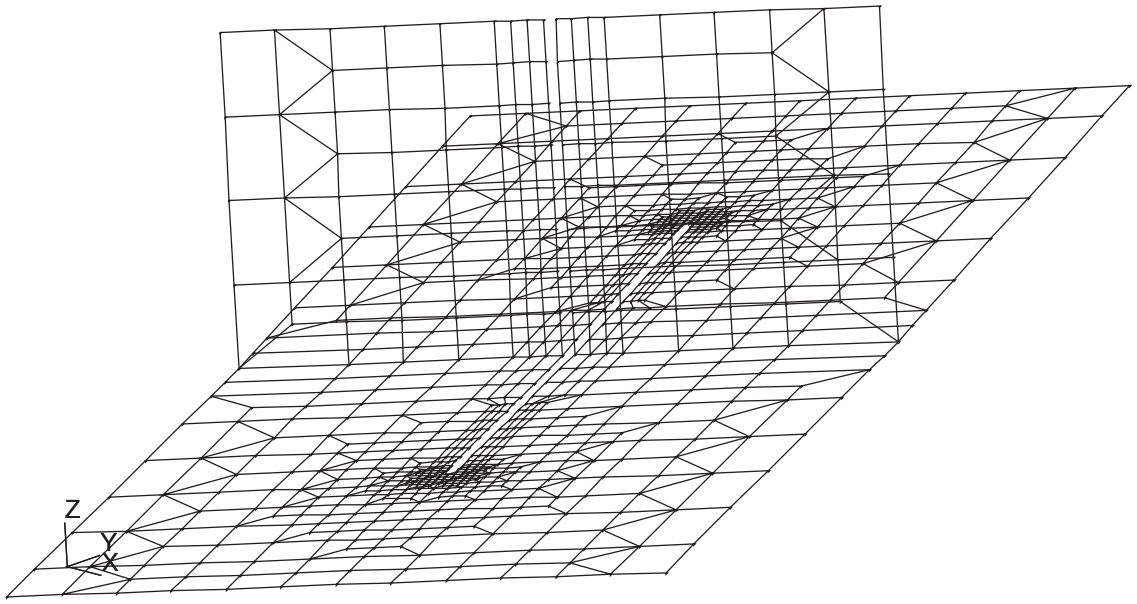

Figure 4.3: Lower Cover Sawcut Finite Elment Mesh Showing Sawcut Region Located Between Ribs 10 and 11 and Cutting Stringer #9.

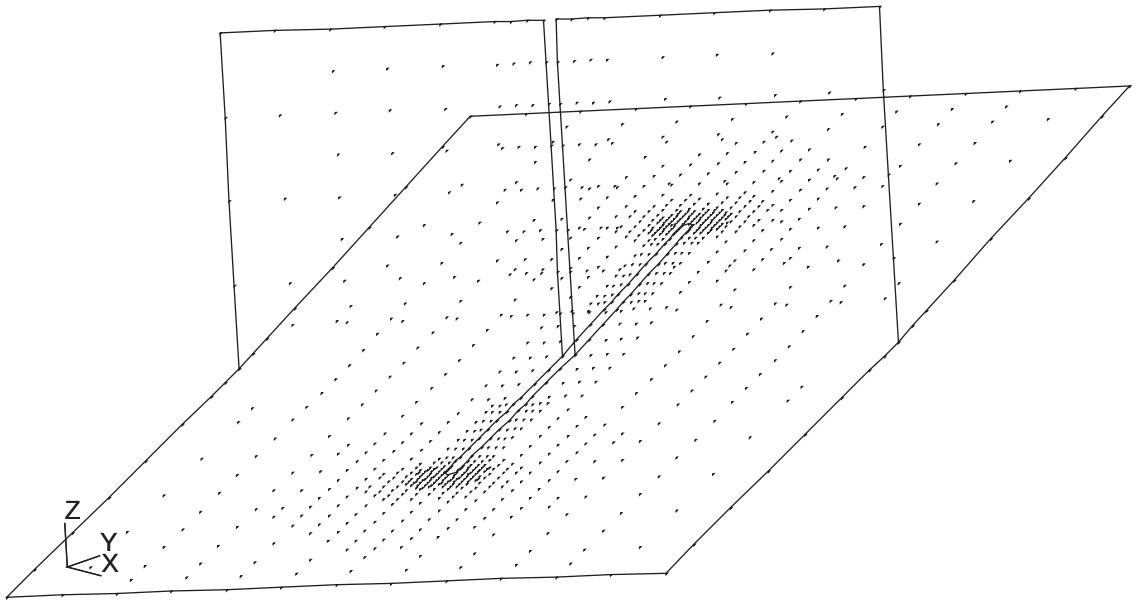

Figure 4.4: Lower Cover Sawcut Free Edges Showing Sawcut Region Located Between Ribs 10 and 11 and Cutting Stringer #9.

5. Effects of Geometric Nonlinearity

5.1 Discussion

Both linear and nonlinear analyses were carried out on the detailed model and the tapered-height model to investigate the effects of geometrically nonlinear effects. Load/deflection curves for the detailed model are plotted for several nodes up to DUL, and are shown in Figures 5.1-5.8. Mild nonlinearity, i.e., small deviation from linear response, is seen for several of these nodes. Table 5.1 shows the percent deviation of the nonlinear response at DUL compared to linear extrapolation for the nodes referenced in Figures 5.1-5.8. The linear extrapolations shown in the figures and referenced in Table 5.1 are based upon the response at a load factor of 0.2, which is extrapolated to the 1.0 load factor representing DUL. The nodes discussed exhibit the most nonlinear response of all nodes observed in the model. As seen in Figure 5.9, an exaggerated deflection plot for the upper cover from rib 2 to rib 10, the overhangs exhibit mildly nonlinear deflections.

Similarly, examination of the strains in the vicinity of the upper cover stringer #10 runout also indicates mildly nonlinear response. A close-up of the strain values for this region are shown in Figures 5.10 and 5.11, showing the bottom surface spanwise strain in the tapered-height model for both the linear and nonlinear analyses, respectively. Maximum strain values for the linear analysis occur at the stringer ply drop-off locations, and are approximately 5350 με, as seen in Figure 5.10. Examination of Figure 5.11 yields maximum strain values in the same location as those found in the linear analysis, except that the value is now approximately 5650 με. Therefore, the nonlinear strain value is about 6% higher than the linear strain value. Again, this is a demonstration that the semi-span response is mildly nonlinear.

Lastly, comparison of linear and nonlinear buckling results for several models indicates that there is very little difference between the linear and nonlinear calculated buckling load factors. Therefore, it is concluded that the composite semi-span as modeled is globally linear, but that it has mild geometrically nonlinear response in localized regions. Since several of the localized regions that exhibit geometrically nonlinear response are located in the areas of interest, e.g., stringer runouts, nonlinear analyses were performed in order to obtain the required static response results. Nonlinear results for the undamaged semi-span are investigated for strain and failure up to a load factor of 1.0 DUL, and up to a load factor of 0.475 DUL for the damaged semi-span scenarios. The load factor of 0.475 represents approximately 0.7 of design limit load (DLL), which is the maximum loading that must be sustained by the damaged semi-span. However, linear buckling analyses were conducted to determine the buckling response of the composite semi-span.

5.2 Tables

Table 5.1: Percent Deviation of Nonlinear Deflection Response Compared to Linear Extrapolation for Nodes Exhibiting the Most Nonlinear Response.

Node Number	Percent Increase of Nonlinear Z-Displacement Over Linear Extrapolation	Percent Increase of Nonlinear Total Displacement Over Linear Extrapolation
13535	9.354096175	8.832149608
13539	8.474841147	8.185774491
13927	8.461228681	8.078875567
12860	6.593586811	6.57750966
13925	6.419955191	6.548540561
12859	6.260524762	6.266008117
12861	5.813244147	5.912328762
13542	5.396165271	5.802627797

5.3 Figures

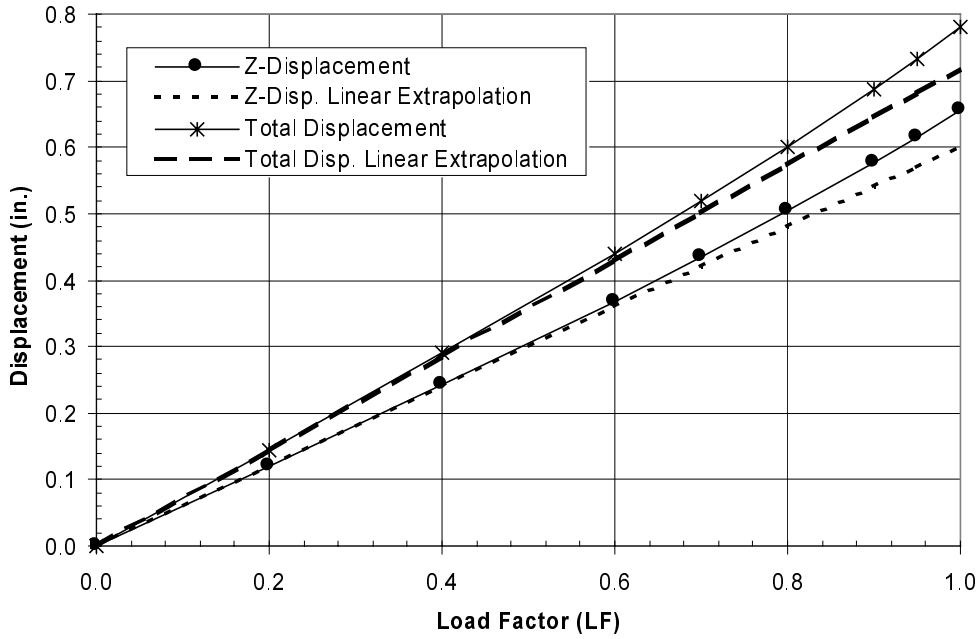

Figure 5.1: Node 13535 Comparison of Nodal Nonlinear Z- and Total Displacements with Linear Extrapolations Based Upon Displacements at LF = 0.2.

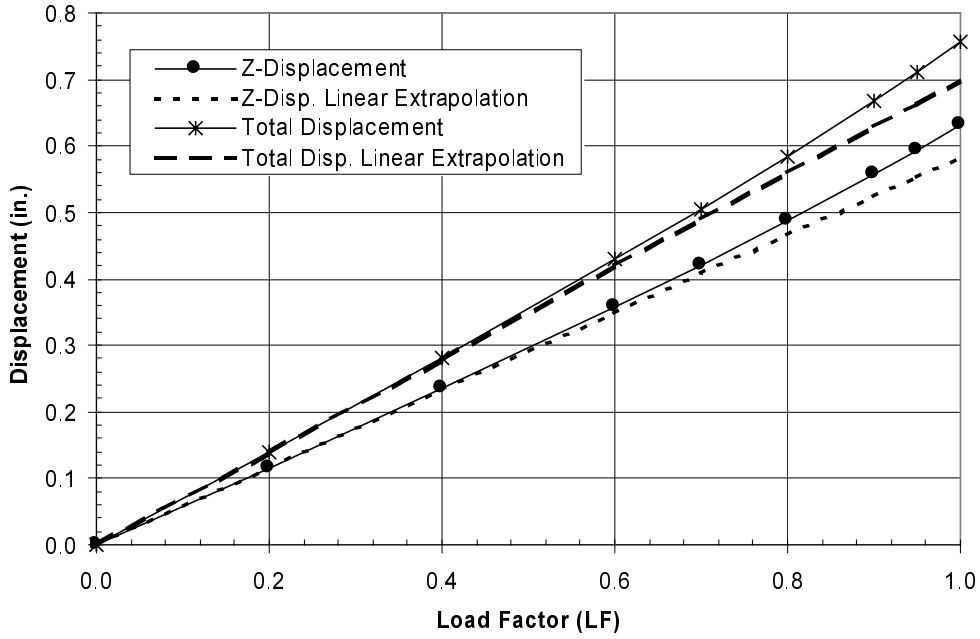

Figure 5.2: Node 13539 Comparison of Nodal Nonlinear Z- and Total Displacements with Linear Extrapolations Based Upon Displacements at LF = 0.2.

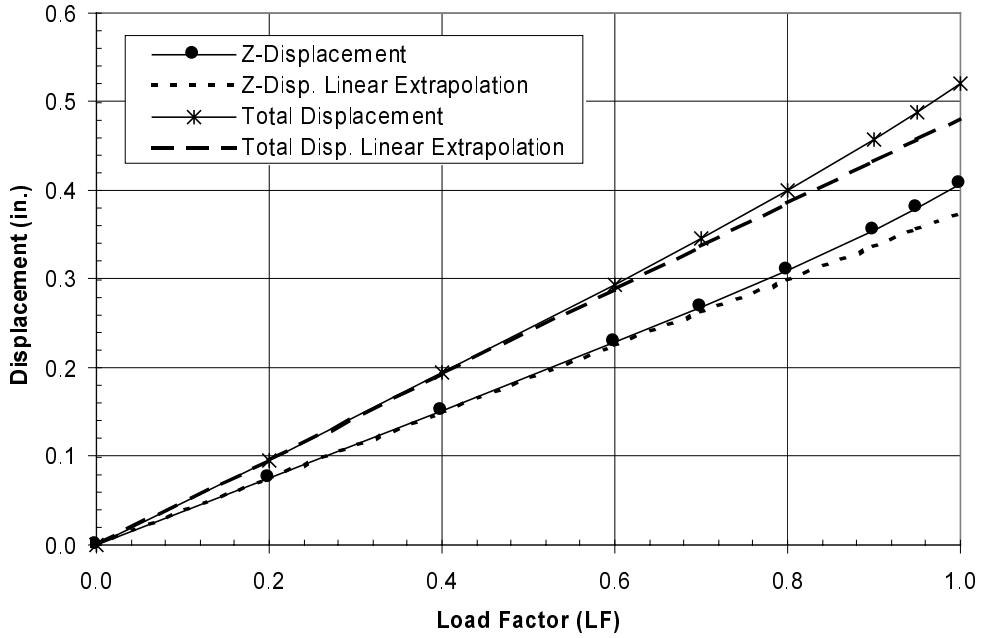

Figure 5.3: Node 13927 Comparison of Nodal Nonlinear Z- and Total Displacements with Linear Extrapolations Based Upon Displacements at LF = 0.2.

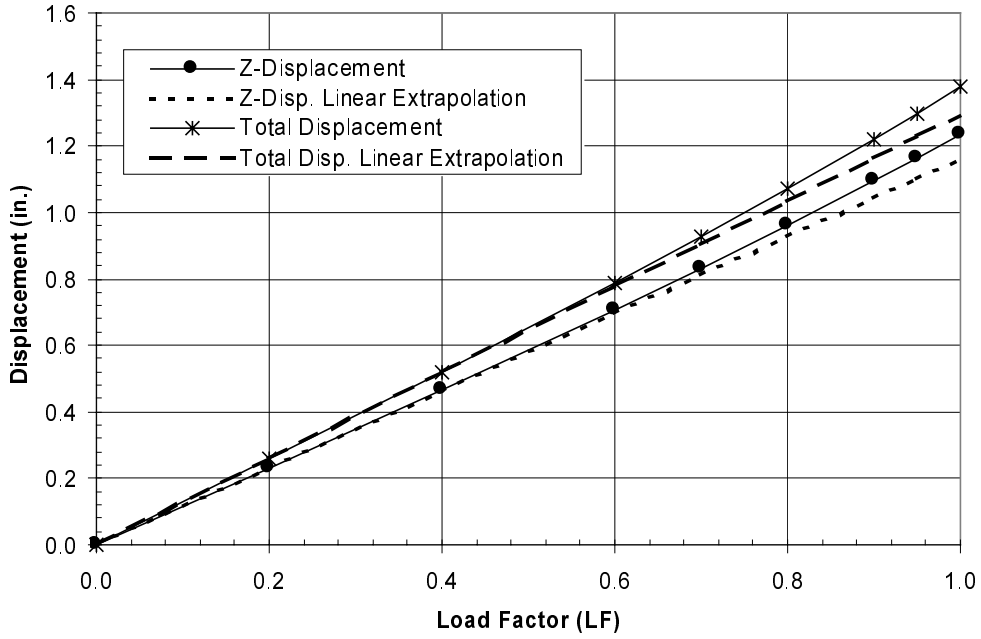

Figure 5.4: Node 12860 Comparison of Nodal Nonlinear Z- and Total Displacements with Linear Extrapolations Based Upon Displacements at LF = 0.2.

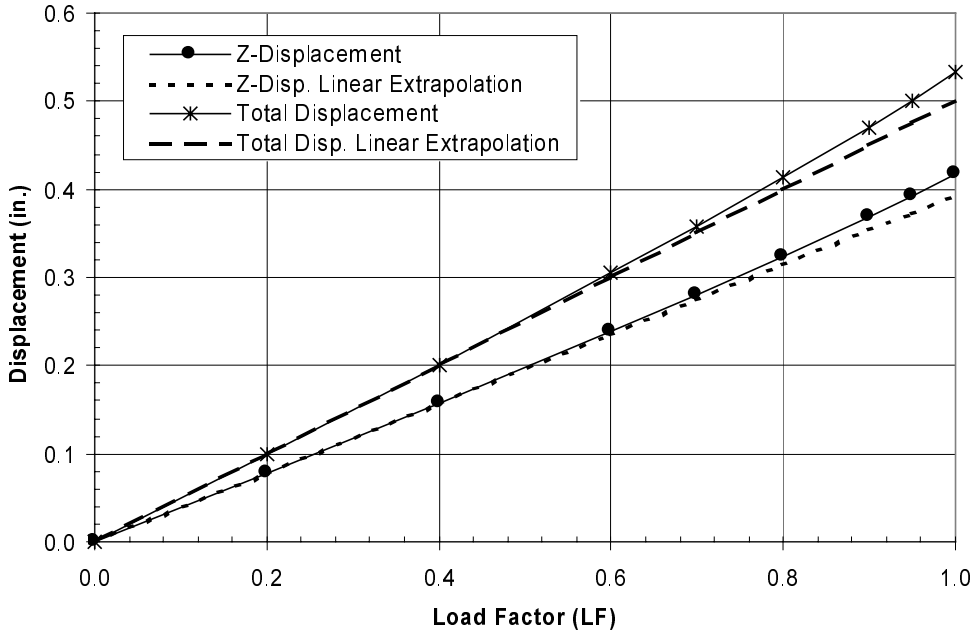

Figure 5.5: Node 13925 Comparison of Nodal Nonlinear Z- and Total Displacements with Linear Extrapolations Based Upon Displacements at LF = 0.2.

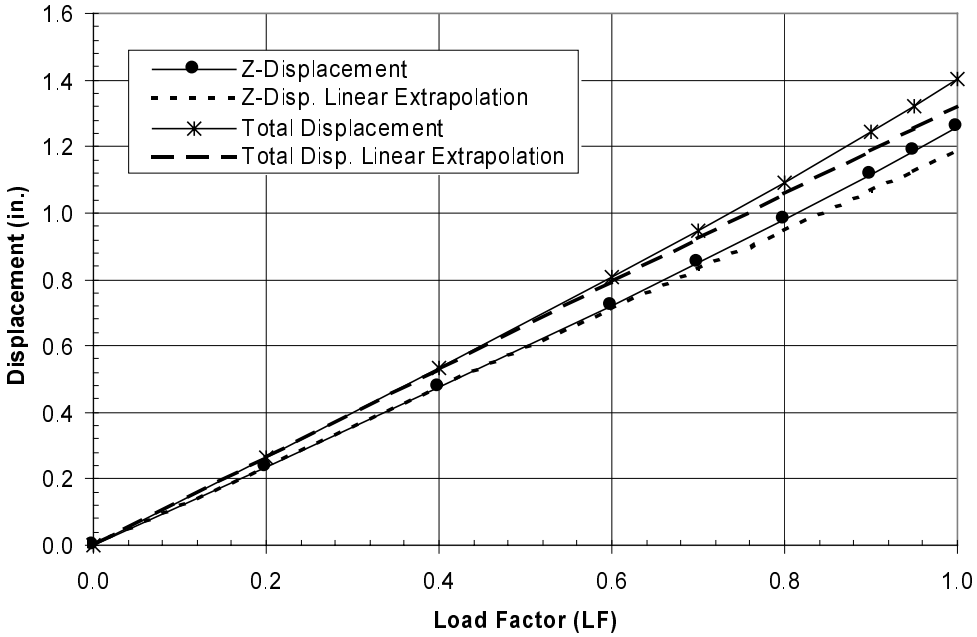

Figure 5.6: Node 12859 Comparison of Nodal Nonlinear Z- and Total Displacements with Linear Extrapolations Based Upon Displacements at LF = 0.2.

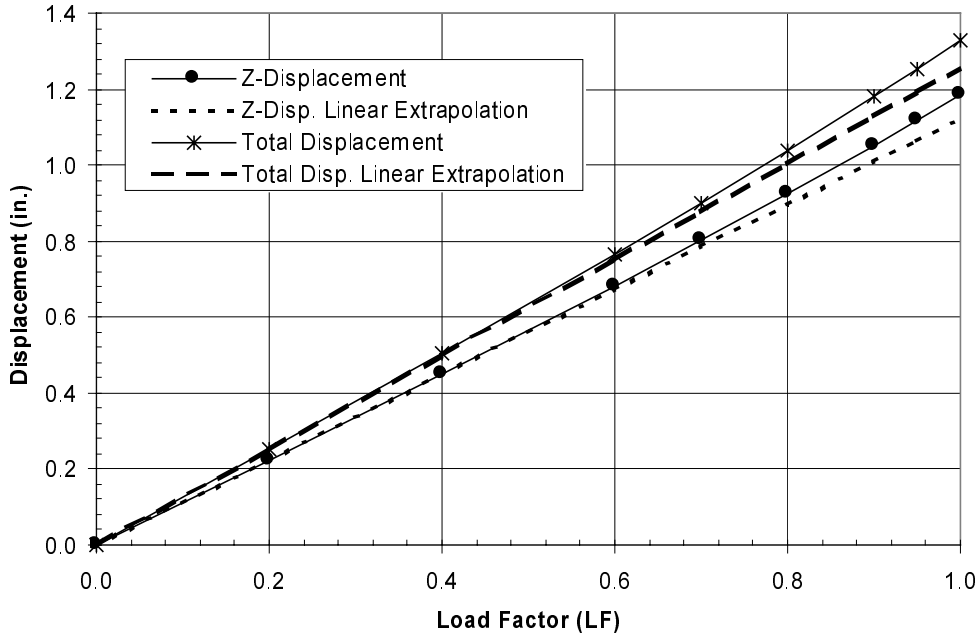

Figure 5.7: Node 12861 Comparison of Nodal Nonlinear Z- and Total Displacements with Linear Extrapolations Based Upon Displacements at LF = 0.2.

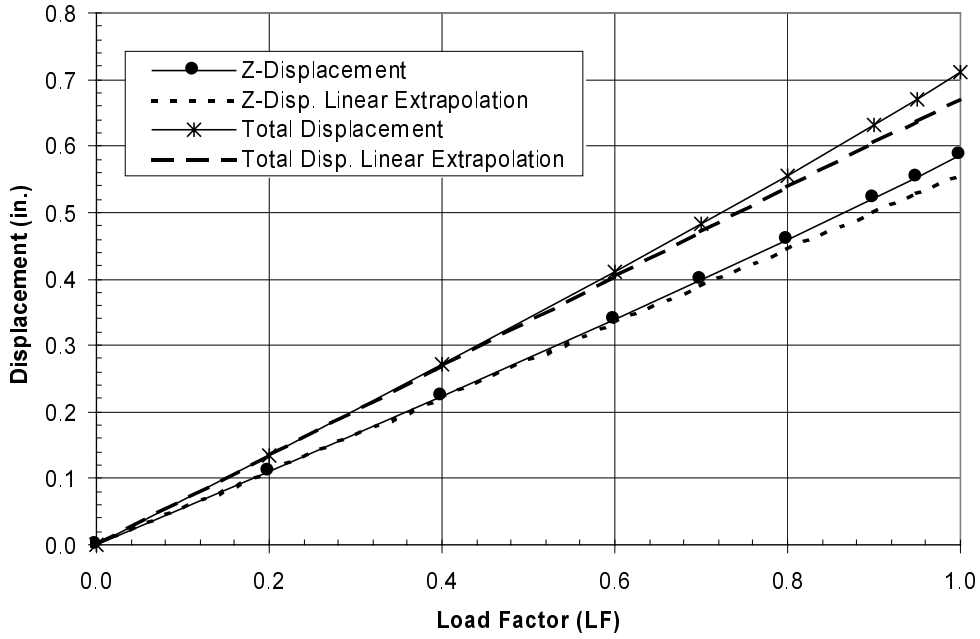

Figure 5.8: Node 13542 Comparison of Nodal Nonlinear Z- and Total Displacements with Linear Extrapolations Based Upon Displacements at LF = 0.2.

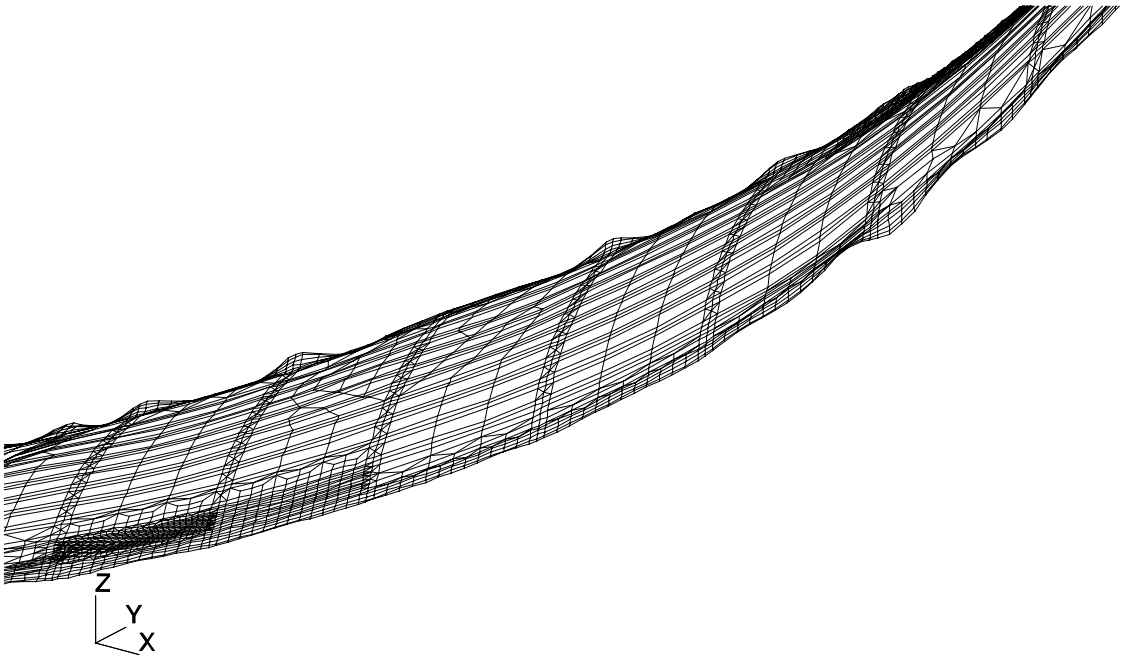

Figure 5.9: Close-Up of the Upper Cover Nonlinear Deflection for 2.5G Up-Bending Showing Overhang Response (Scaled by a Factor of 10).

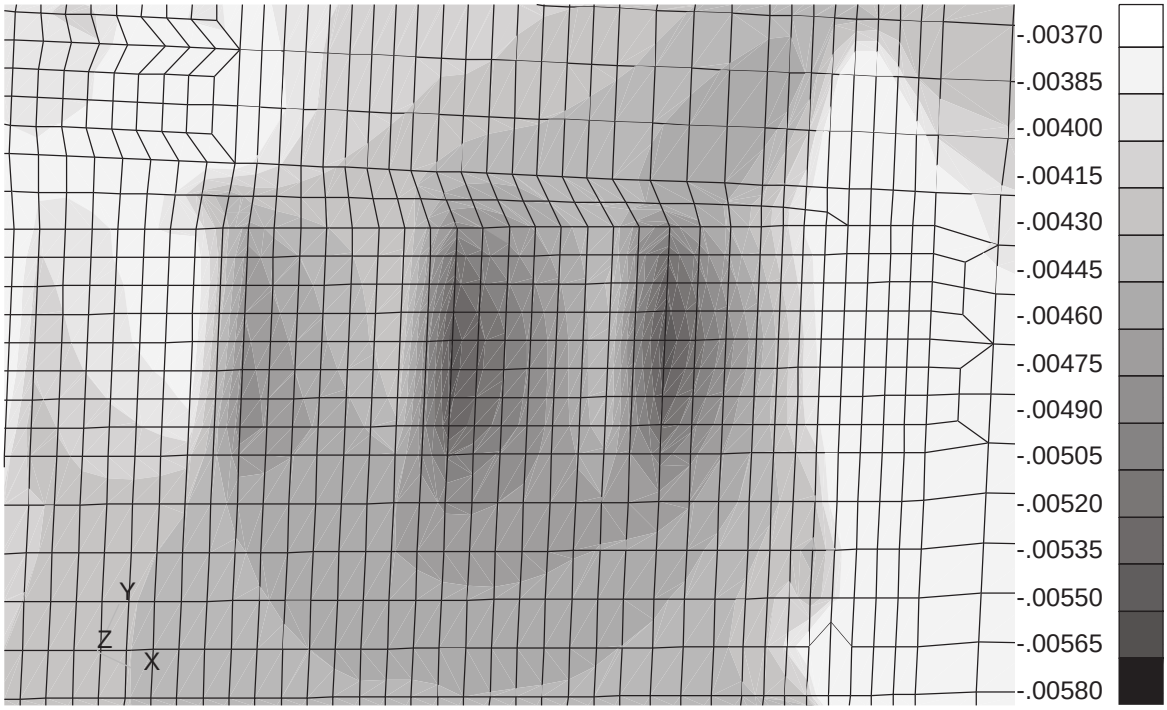

Figure 5.10: Linear Analysis Spanwise Strain for the Upper Cover Bottom Surface at the Tapered-Height Stringer #10 Termination.

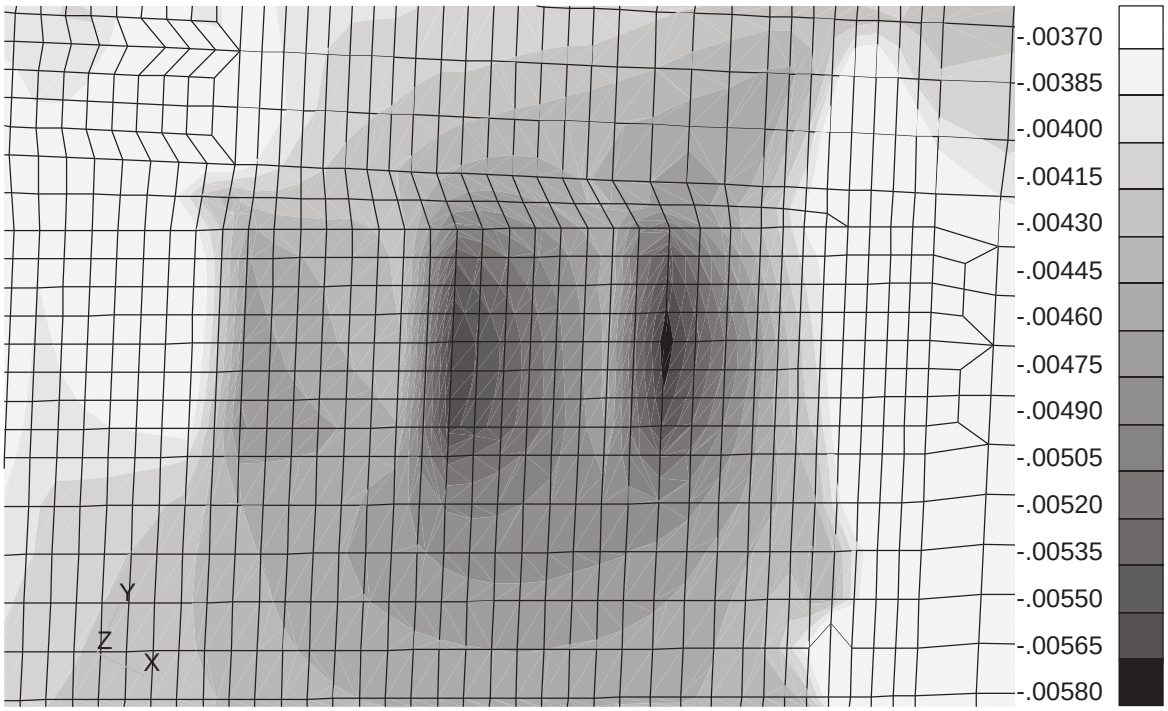

Figure 5.11: Nonlinear Analysis Spanwise Strain for the Upper Cover Bottom Surface at the Tapered-Height Stringer #10 Termination.

6. Root Mount Plate Analysis

Utilizing the loads model, linear STAGS runs were conducted for the three load cases to investigate the forces and stresses associated with the root mount plates of the composite semi-span test article. Results of interest include the reaction forces at the wall, the root plate stress resultants along the wall, and the stresses in the plates. The reaction forces and stress resultants are provided for use in determining the bolt arrangement and sizing performed by NASA Langley. Stresses in the root mount plates are studied in order to determine whether failure will occur under the three specified load conditions.

6.1 Failure Requirements

The root mount upper and lower plates are fabricated from 6 inch thick 7075-T651 aluminum stock. Military handbook MIL-HDBK-5G, dated 1 November 1994, provides a set of allowable stresses for plates up to 4 inches thick. Therefore, linear extrapolation was used to estimate the allowable stresses for the 6 inch thick plate stock. From the graph and linear extrapolation shown in Figure 6.1, the following allowables are obtained: tension ultimate = 52 ksi, tension yield = 40.5 ksi, compression yield = 33.5 ksi and shear ultimate = 32 ksi. Data points were plotted at the lower limit of the stock thickness ranges, e.g., for 3.5 to 4.0 inch thick stock the value was plotted at 3.5 inches. Boeing assumes no extrapolation and assumes the strength properties of the 6.0 inch thick plate are the same as the 3.5 inch thick plate.

The fore and aft shear mount plates are fabricated from much thinner 7075-T651 aluminum stock, and allowables can be found directly from the table given in MIL-HDBK-5G. For the 0.5 inch plate stock, the handbook provides the following values: tension ultimate = 77 ksi, tension yield = 70 ksi, compression yield = 68 ksi and shear ultimate = 44 ksi.

Failure was investigated using the effective stress, or von Mises stress, σ_{eff}. This stress was compared to the ultimate stresses as per the maximum distortion energy criteria. Note that ultimate stresses are used instead of the yield stresses. This is because the limit load forces have been multiplied by a factor of safety equal to 1.5 to get the ultimate load forces that are used in the finite element analysis, and which have been given in Table 2.1.

6.2 Results

6.2.1 Reaction Forces

Reaction forces obtained at the wall are of translational type only due to the boundary conditions described in Section 3.3.1. Figures 6.2-6.25 show force plots for the top plates and bottom plates along the y-direction, and for the fore and aft shear plates along the z-direction. Both forces and node location are in the global coordinate system, where the wall is parallel to the yz-plane. There are no reaction moments at the interface between the root mount plates and the wall.

For all load cases and plates, the force F_X plots represent reasonable results as seen in the figures. However, both the F_Y and F_Z forces behave poorly near the plate separations and the shear plate connection corners. This can especially be seen in the F_Z force for the top and bottom plates for all three load cases. A mesh refinement in these separation regions should better determine the forces along the

wall at these points. However, away from these corners the forces shown in the figures are reasonable and no further analysis was carried out since the results obtained were deemed sufficient.

6.2.2 Root Plate Stress Resultants

Forces along the wall have been plotted as stress resultants in order to get the running load for the plate edges located along the wall. Stress resultants for the semi-span root mount plates were generated, and the results for the first three rows of finite elements plotted. The three stress resultants, N_x, N_y and N_{xy} are plotted for each of the three load cases for the upper, lower, fore and aft root mount plates as shown in Figures 6.26-6.37. Large gradients tend to occur at the free corners of the upper and lower plates, again suggesting that refinement of the mesh may be necessary in these areas to accurately capture the response.

6.2.3 Root Plate Stresses

Stress results are presented in the form of plots showing the stress contours for the upper and lower fibers of the plates. Upper and lower fiber designations refer to the extreme fibers of the plates relative to the reference surface, and are indicated by the reference surface material axes. The material axes are located such that the positive z-axis is parallel to the surface normal as determined by the geometry. All surfaces used to generate the root mount plate finite elements have normals which point outward from the root mount plates. That is, the lower fibers are on the inside of the root mount plates toward the test article, and the upper fibers are on the outside of the root mount plates away from the test article.

The von Mises stress is given in Figures 6.38-6.40 for the top root mount plates and in Figures 6.41-6.43 for the bottom root mount plates. Since the stresses in the fore and aft root mount shear plates are lower than the top and bottom plates, and since the ultimate stress value for these shear plates is higher, results for these shear plates are omitted for brevity. It can be seen from the figures that load case 2, the 2.5G up-bending load condition, generates the highest stresses in all of the mount plates, and load case 3, the braked roll condition, generates the lowest stresses in the root mount plates. Thus, the 2.5G load condition results for the top and bottom mount plates are studied in order to predict if failure will occur.

The highest value of stress in the root mount plates occurs in the bottom plates on the lower surface, where σ_{eff} =69.87 ksi. This calculated value is 34.2% higher than the allowable ultimate tensile stress, and thus a possibility of failure for the root mount plates exists. Additionally, it can be seen that this high stress level occurs at the location where the plate bends in both the vertical and horizontal directions. That is, the highest stresses occur near the wing root rib where the plate has a change in sweep angle, particularly on plate 3. It can also be seen that upper plate number 3 and lower plate number 2 obtain stress levels that also suggest a possibility of failure. Therefore, under the 2.5G up-bending loading condition, three root mount plates demonstrate stress levels that indicate possible failure.

It appears from the linear finite element analysis for the root mount plates and the composite semi-span that several of the root mount plates indicate a possibility of failure under load case 2. The highest stress occurs in the obtuse angles on the aft edges of the plates, and dissipates forward and spanwise from this point. This location of the highest stress is expected since the corner has a stress concentration due to the change in sweep.

6.3 Figures

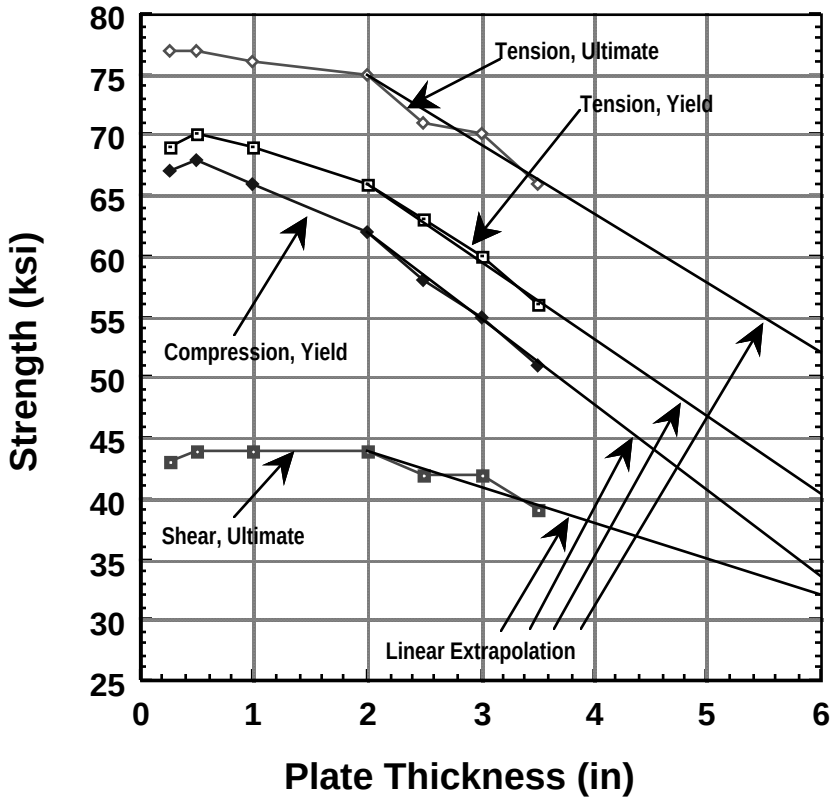

Figure 6.1: 7075-T651 Aluminum Alloy Plate Mechanical Properties from MIL-HDBK-5G, Dated 1 November 1994, and Linear Extrapolation Curves.

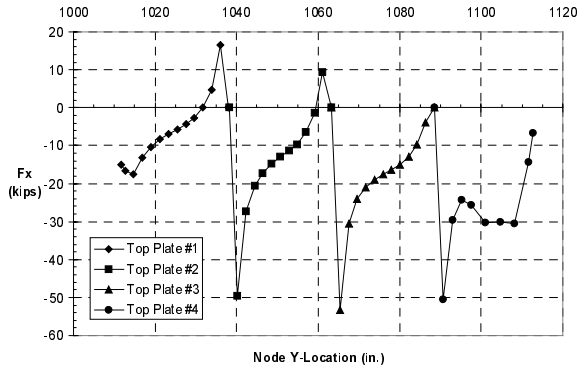

Figure 6.2: Top Root Mount Plate Wall Force, F_x (kips), as a Function of Node Y-Location for the 1.0G Down-Bending Load Case.

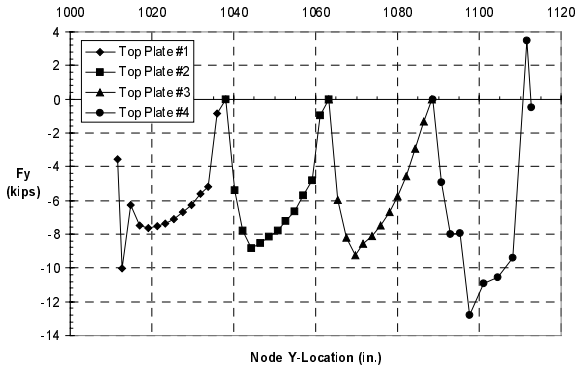

Figure 6.3: Top Root Mount Plate Wall Force, F_y (kips), as a Function of Node Y-Location for the 1.0G Down-Bending Load Case.

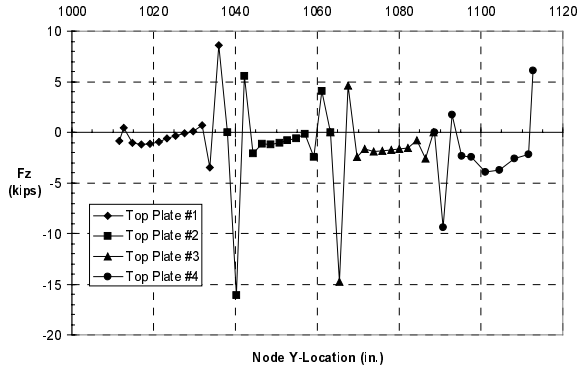

Figure 6.4: Top Root Mount Plate Wall Force, F_z (kips), as a Function of Node Y-Location for the 1.0G Down-Bending Load Case.

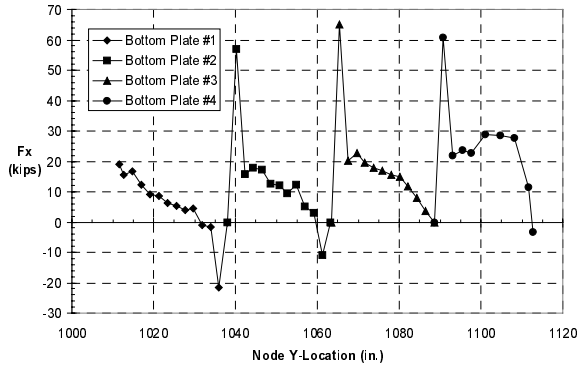

Figure 6.5: Bottom Root Mount Plate Wall Force, F_x (kips), as a Function of Node Y-Location for the 1.0G Down-Bending Load Case.

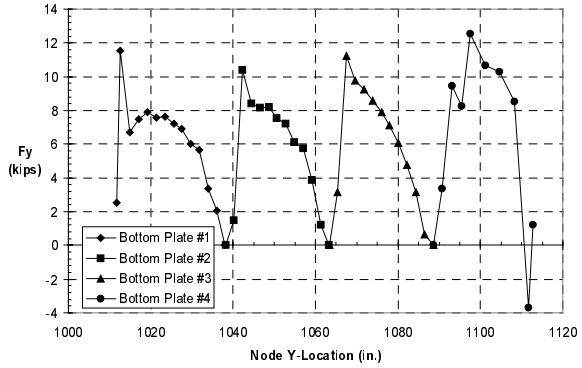

Figure 6.6: Bottom Root Mount Plate Wall Force, F_y (kips), as a Function of Node Y-Location for the 1.0G Down-Bending Load Case.

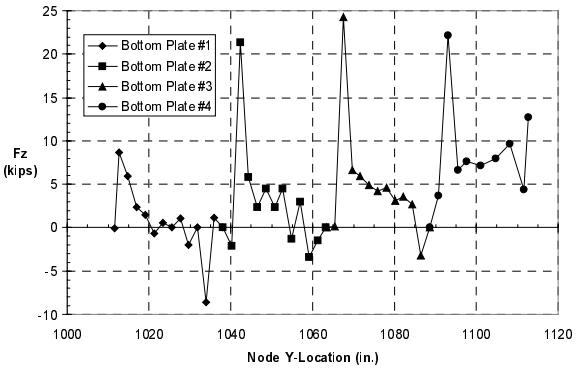

Figure 6.7: Bottom Root Mount Plate Wall Force, F_z (kips), as a Function of Node Y-Location for the 1.0G Down-Bending Load Case.

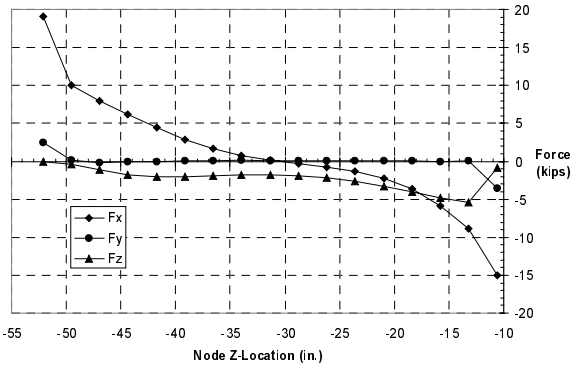

Figure 6.8: Fore Root Mount Shear Plate Wall Force (kips) as a Function of Node Y-Location for the 1.0G Down-Bending Load Case.

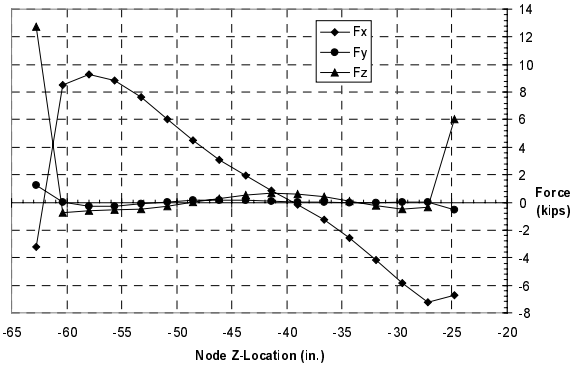

Figure 6.9: Aft Root Mount Shear Plate Wall Force (kips) as a Function of Node Y-Location for the 1.0G Down-Bending Load Case.

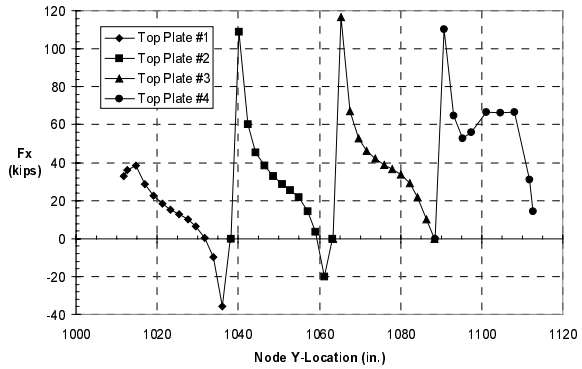

Figure 6.10: Top Root Mount Plate Wall Force, F_x (kips), as a Function of Node Y-Location for the 2.5G Up-Bending Load Case.

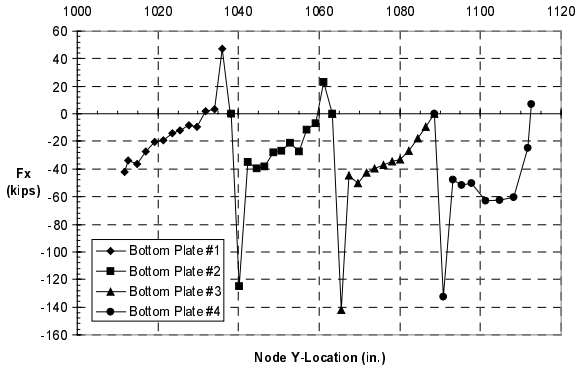

Figure 6.13: Bottom Root Mount Plate Wall Force, F_x (kips), as a Function of Node Y-Location for the 2.5G Up-Bending Load Case.

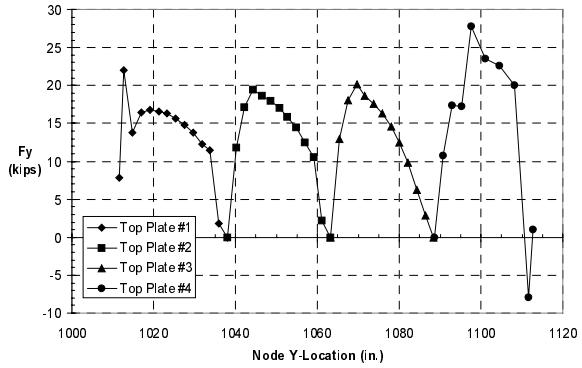

Figure 6.11: Top Root Mount Plate Wall Force, F_y (kips), as a Function of Node Y-Location for the 2.5G Up-Bending Load Case.

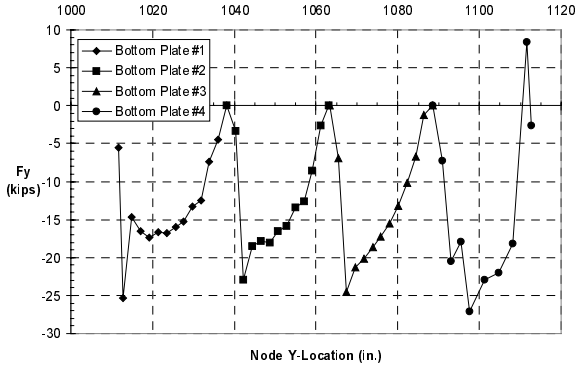

Figure 6.14: Bottom Root Mount Plate Wall Force, F_y (kips), as a Function of Node Y-Location for the 2.5G Up-Bending Load Case.

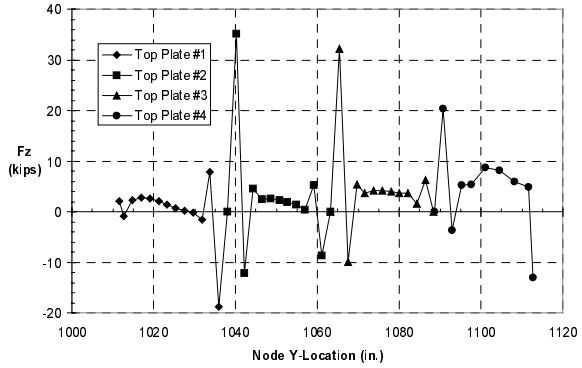

Figure 6.12: Top Root Mount Plate Wall Force, F_z (kips), as a Function of Node Y-Location for the 2.5G Up-Bending Load Case.

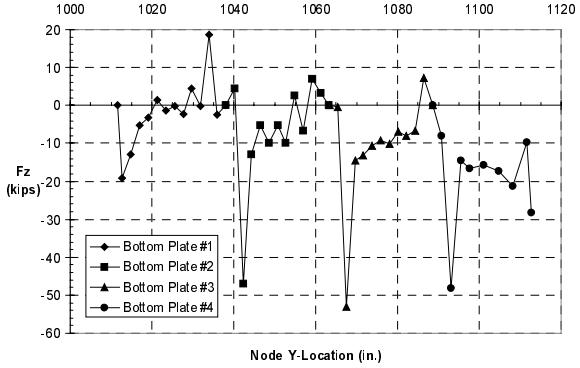

Figure 6.15: Bottom Root Mount Plate Wall Force, F_z (kips), as a Function of Node Y-Location for the 2.5G Up-Bending Load Case.

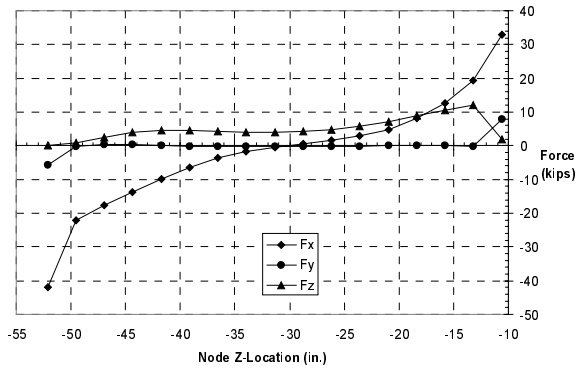

Figure 6.16: Fore Root Mount Shear Plate Wall Force (kips) as a Function of Node Y-Location for the 2.5G Up-Bending Load Case.

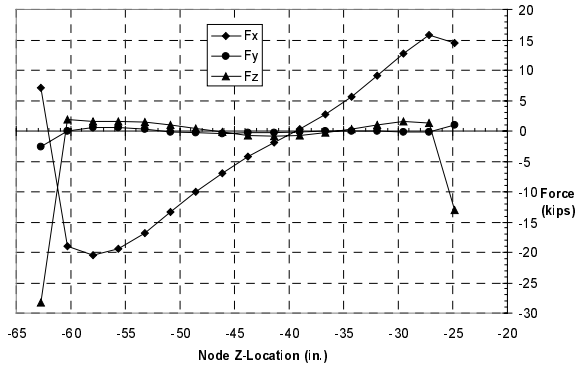

Figure 6.17: Aft Root Mount Shear Plate Wall Force (kips) as a Function of Node Y-Location for the 2.5G Up-Bending Load Case.

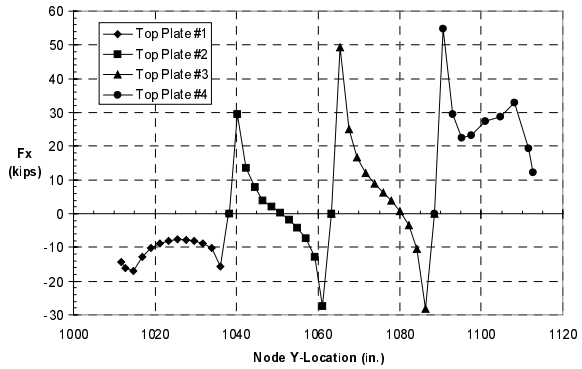

Figure 6.18: Top Root Mount Plate Wall Force, F_x (kips), as a Function of Node Y-Location for the Braked-Roll Load Case.

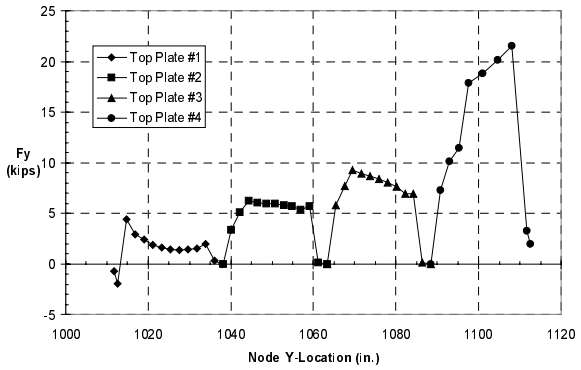

Figure 6.19: Top Root Mount Plate Wall Force, F_y (kips), as a Function of Node Y-Location for the Braked-Roll Load Case.

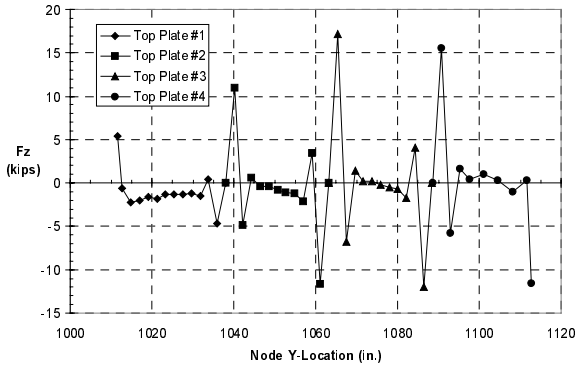

Figure 6.20: Top Root Mount Plate Wall Force, F_z (kips), as a Function of Node Y-Location for the Braked-Roll Load Case.

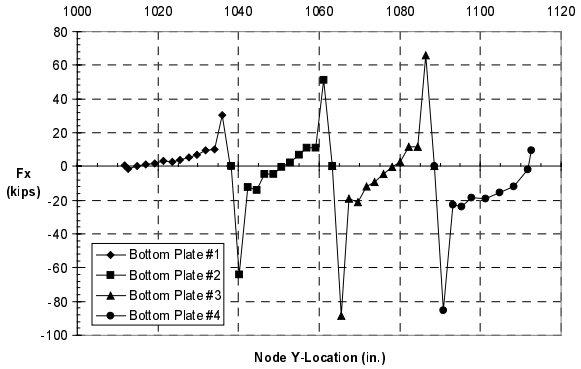

Figure 6.21: Bottom Root Mount Plate Wall Force, F_x (kips), as a Function of Node Y-Location for the Braked-Roll Load Case.

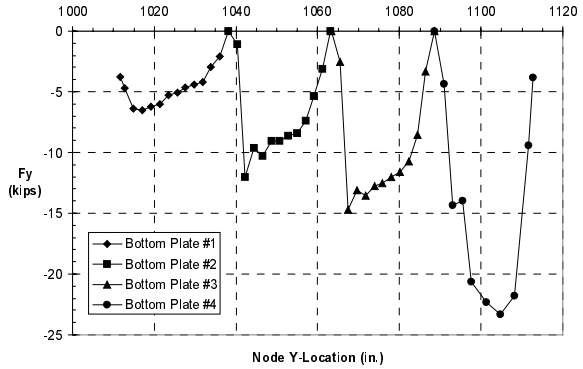

Figure 6.22: Bottom Root Mount Plate Wall Force, F_y (kips), as a Function of Node Y-Location for the Braked-Roll Load Case.

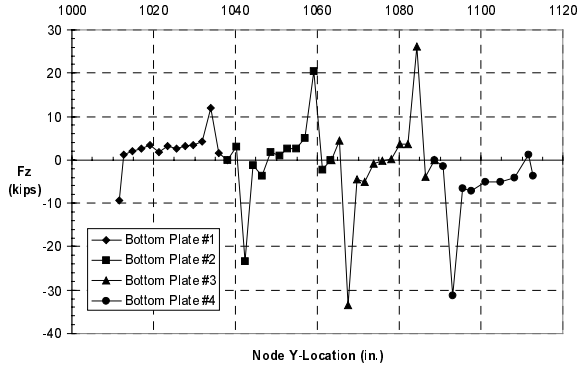

Figure 6.23: Bottom Root Mount Plate Wall Force, F_z (kips), as a Function of Node Y-Location for the Braked-Roll Load Case.

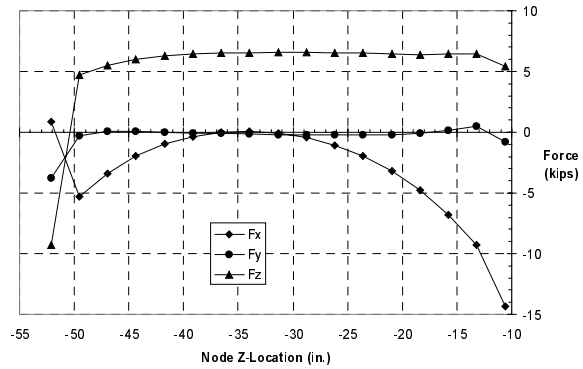

Figure 6.24: Fore Root Mount Shear Plate Wall Force (kips) as a Function of Node Y-Location for the Braked-Roll Load Case.

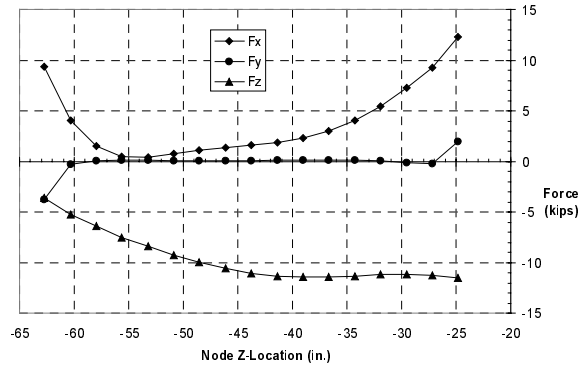

Figure 6.25: Aft Root Mount Shear Plate Wall Force (kips) as a Function of Node Y-Location for the Braked-Roll Load Case.

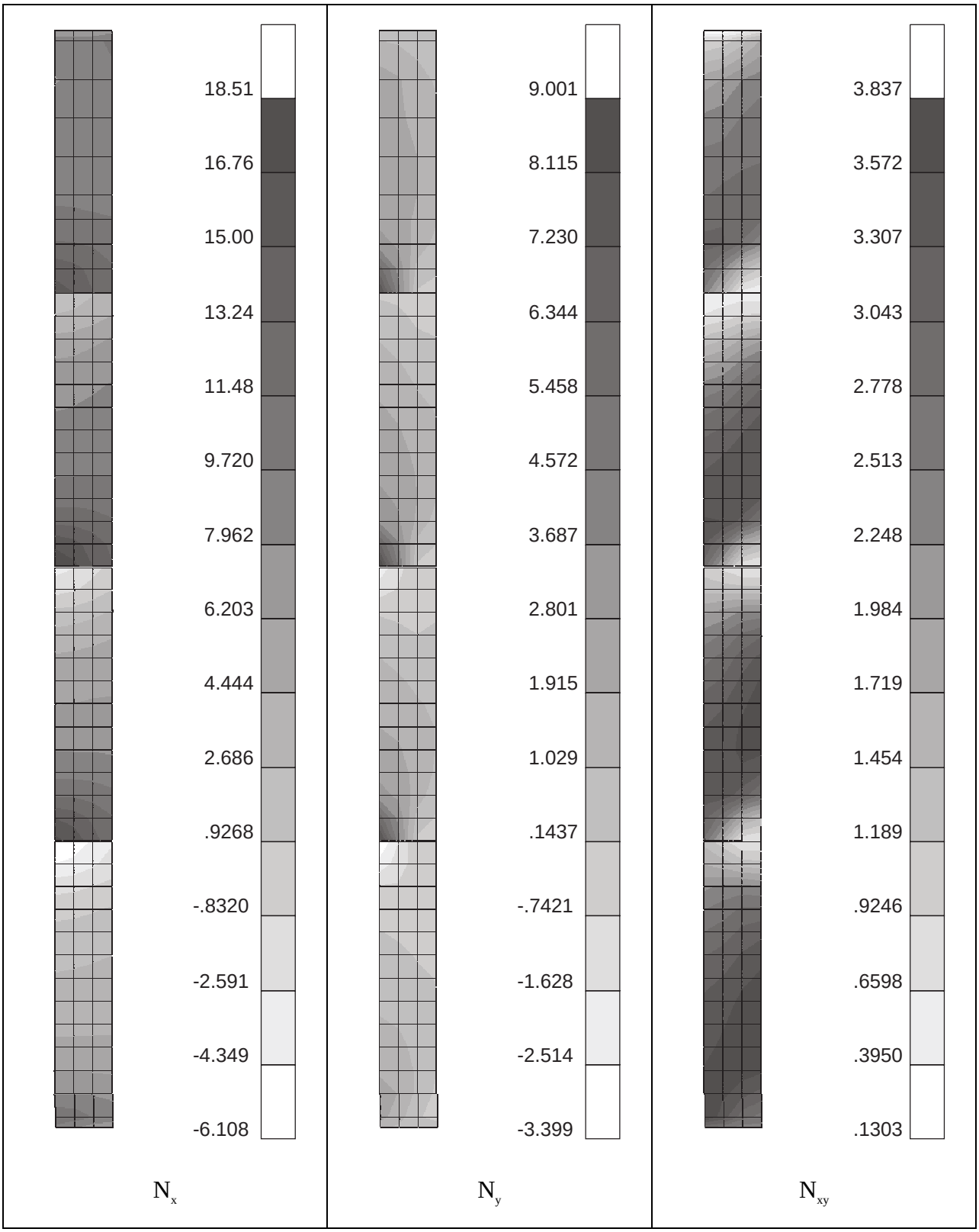

Figure 6.26: Plan View of Top Root Mount Plate Stress Resultants (kips/in.) Near the Wall for Load Case 1. Note: Wall is on the Left Side of the Plots.

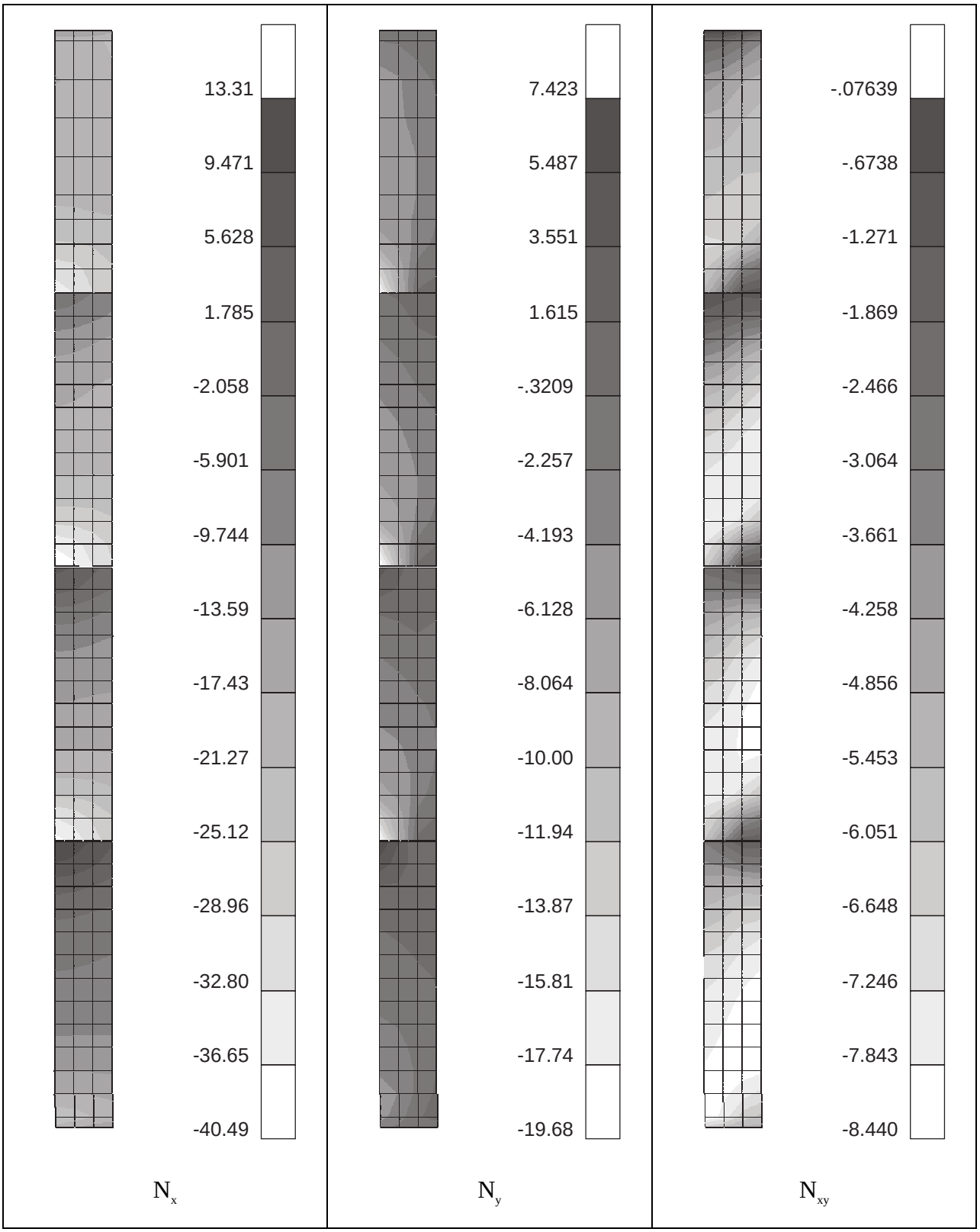

Figure 6.27: Plan View of the Top Root Mount Plate Stress Resultants (kips/in.) Near the Wall for Load Case 2. Note: Wall is on the Left Side of the Plots.

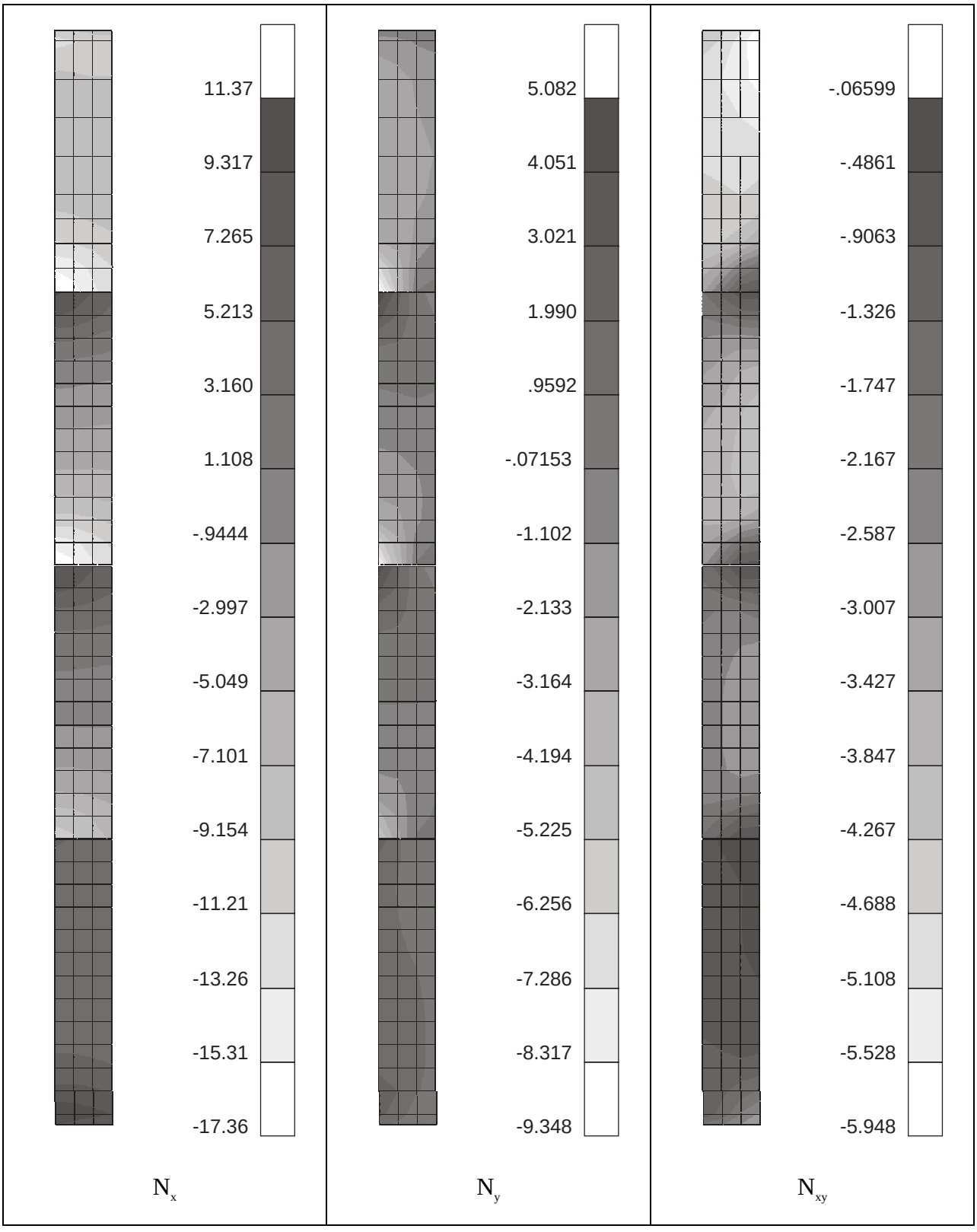

Figure 6.28: Plan View of the Top Root Mount Plate Stress Resultants (kips/in.) Near the Wall for Load Case 3. Note: Wall is on the Left Side of the Plots.

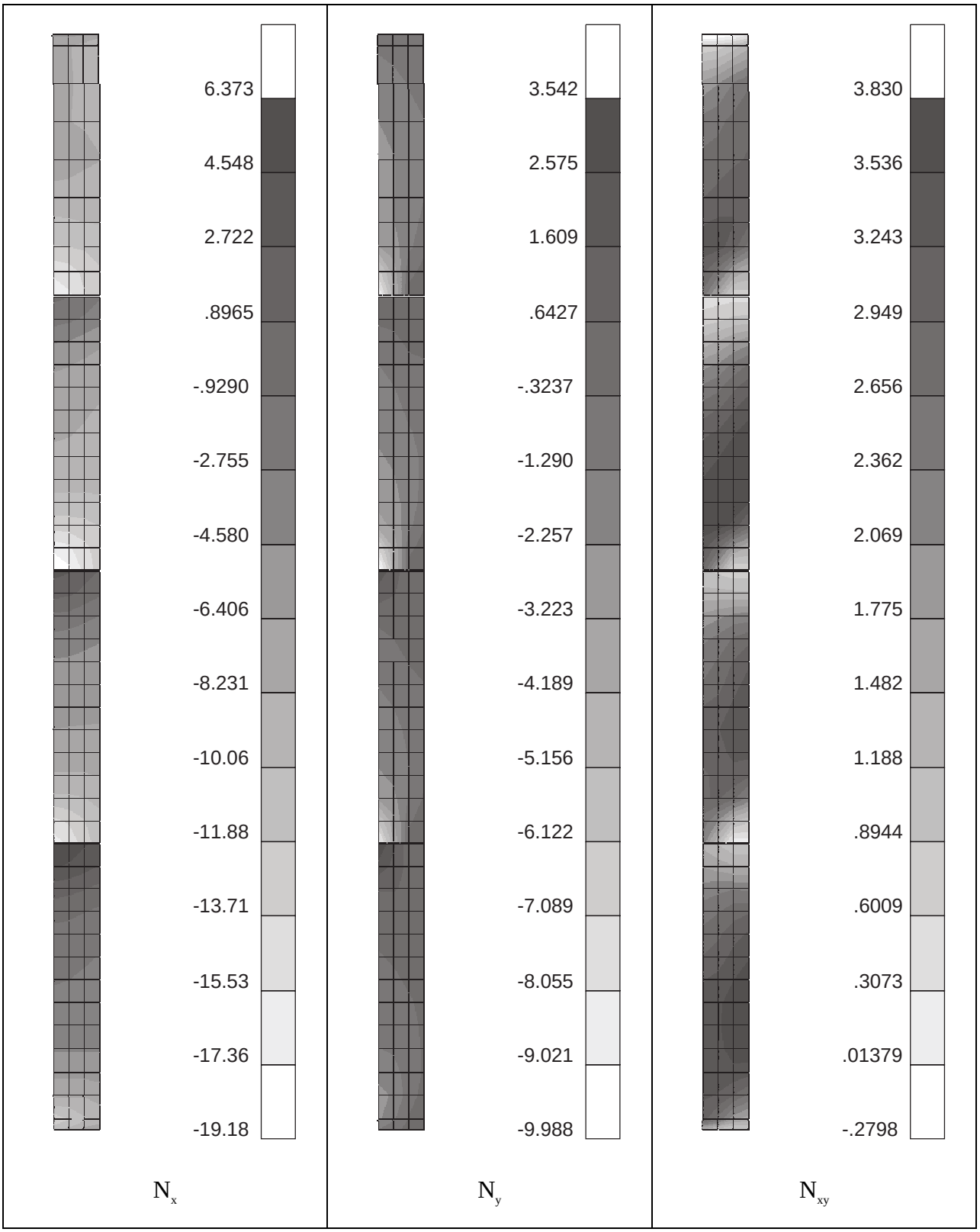

Figure 6.29: Plan View of the Bottom Root Mount Plate Stress Resultants (kips/in.) Near the Wall for Load Case 1. Note: Wall is on the Left Side of the Plots.

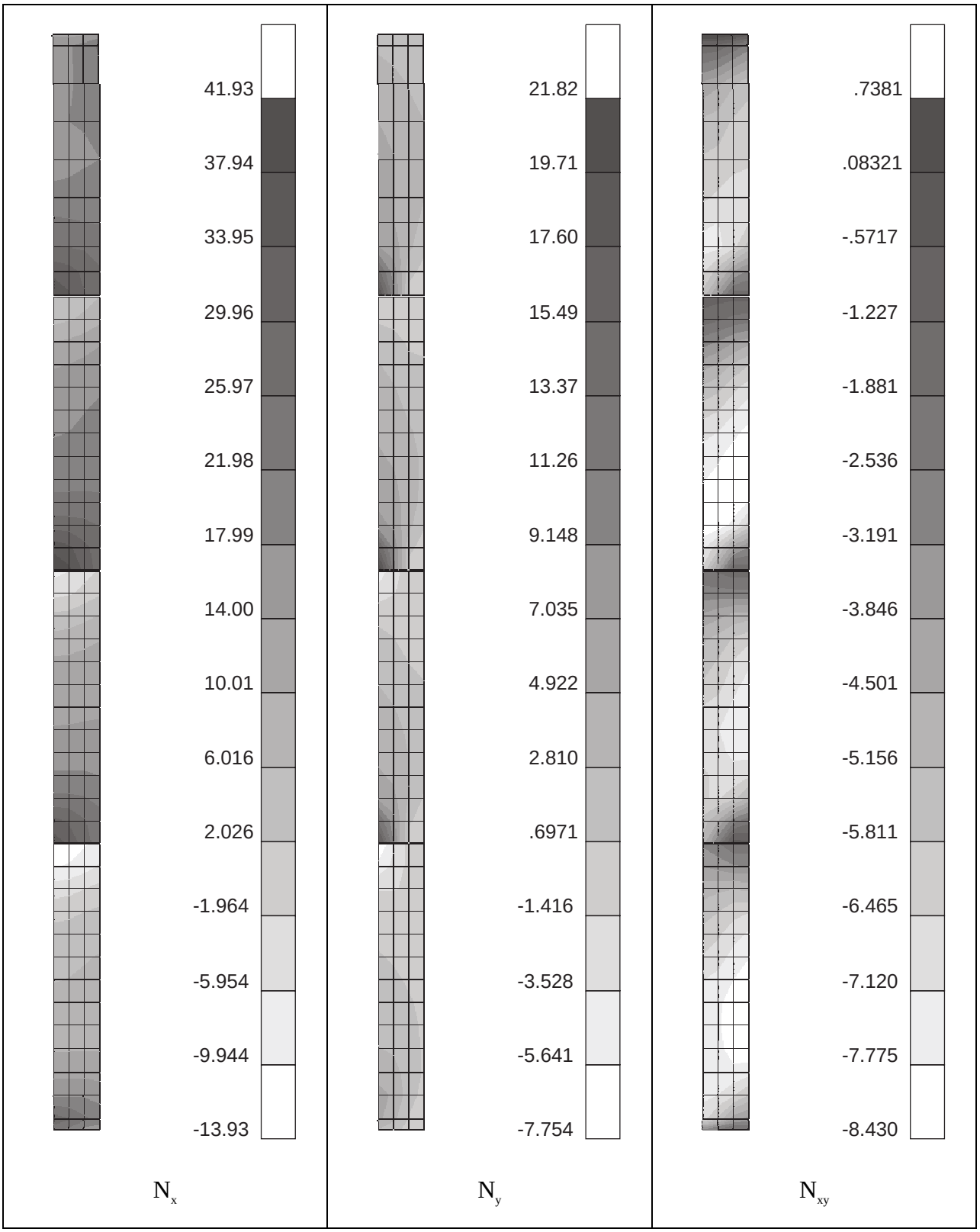

Figure 6.30: Plan View of the Bottom Root Mount Plate Stress Resultants (kips/in.) Near the Wall for Load Case 2. Note: Wall is on the Left Side of the Plots.

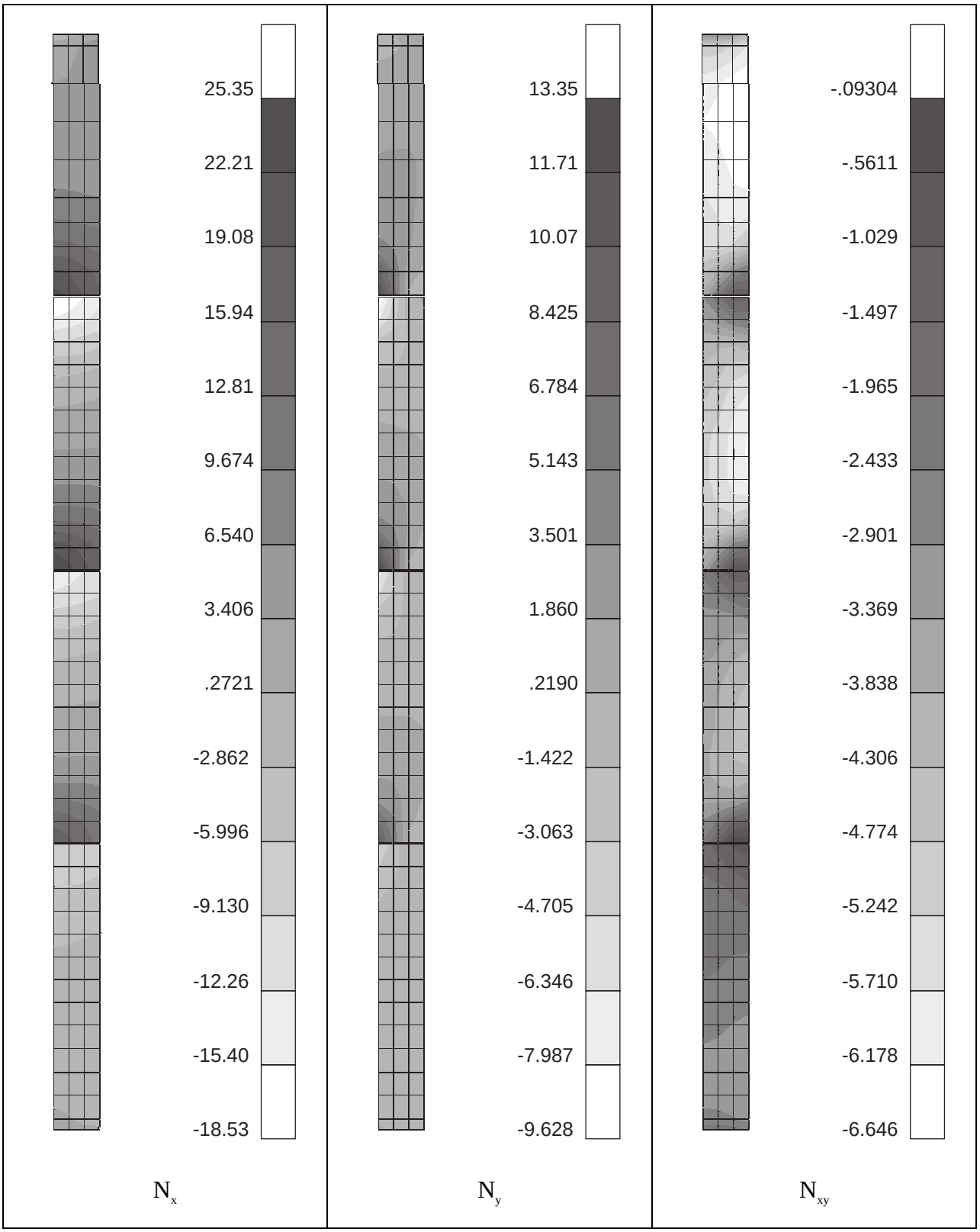

Figure 6.31: Plan View of the Bottom Root Mount Plate Stress Resultants (kips/in.) Near the Wall for Load Case 3. Note: Wall is on the Left Side of the Plots.

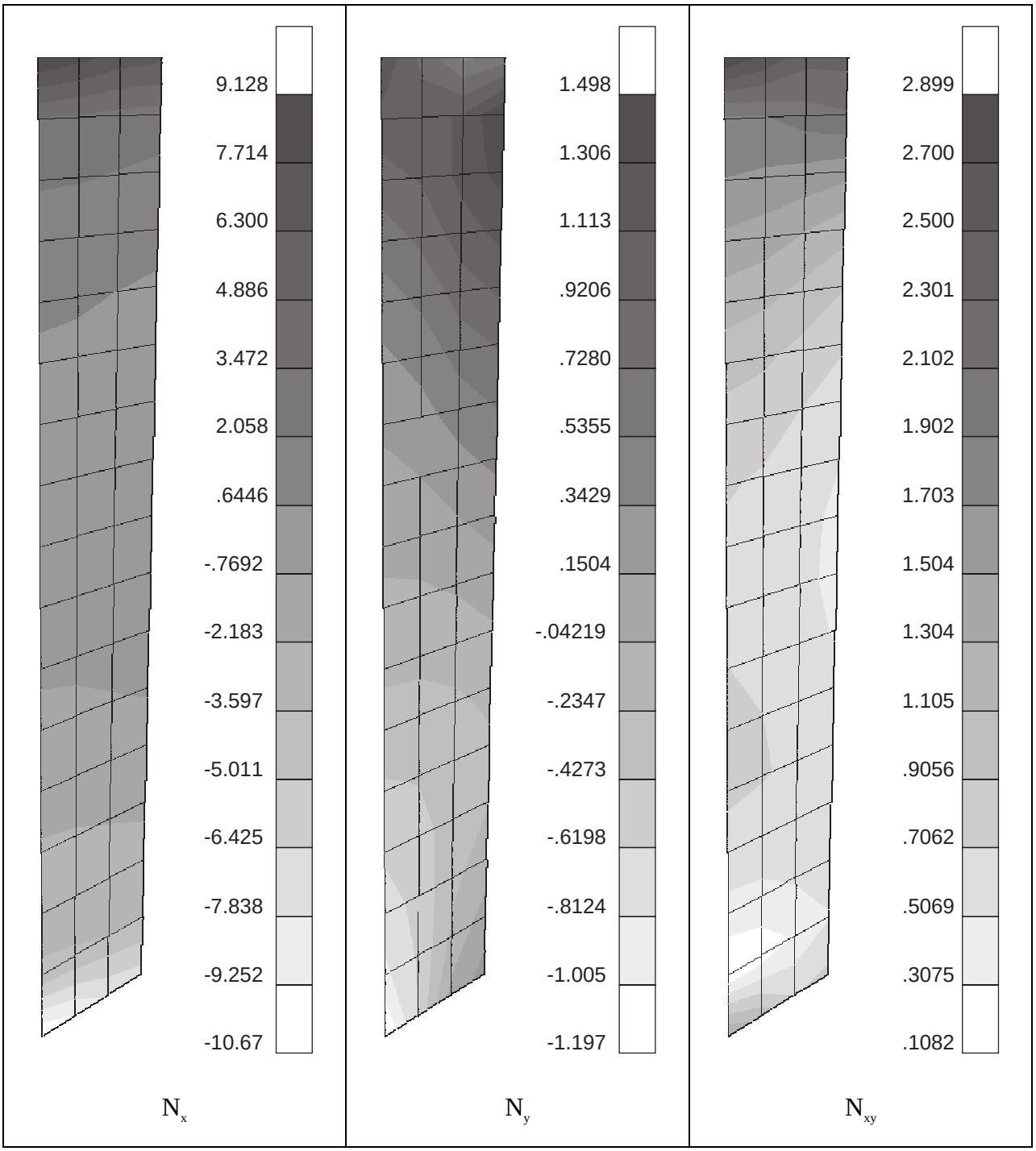

Figure 6.32: View Looking Aft for the Forward Root Mount Plate Stress Resultants (kips/in.) Near the Wall for Load Case 1. Note: Wall is on the Left Side of the Plots.

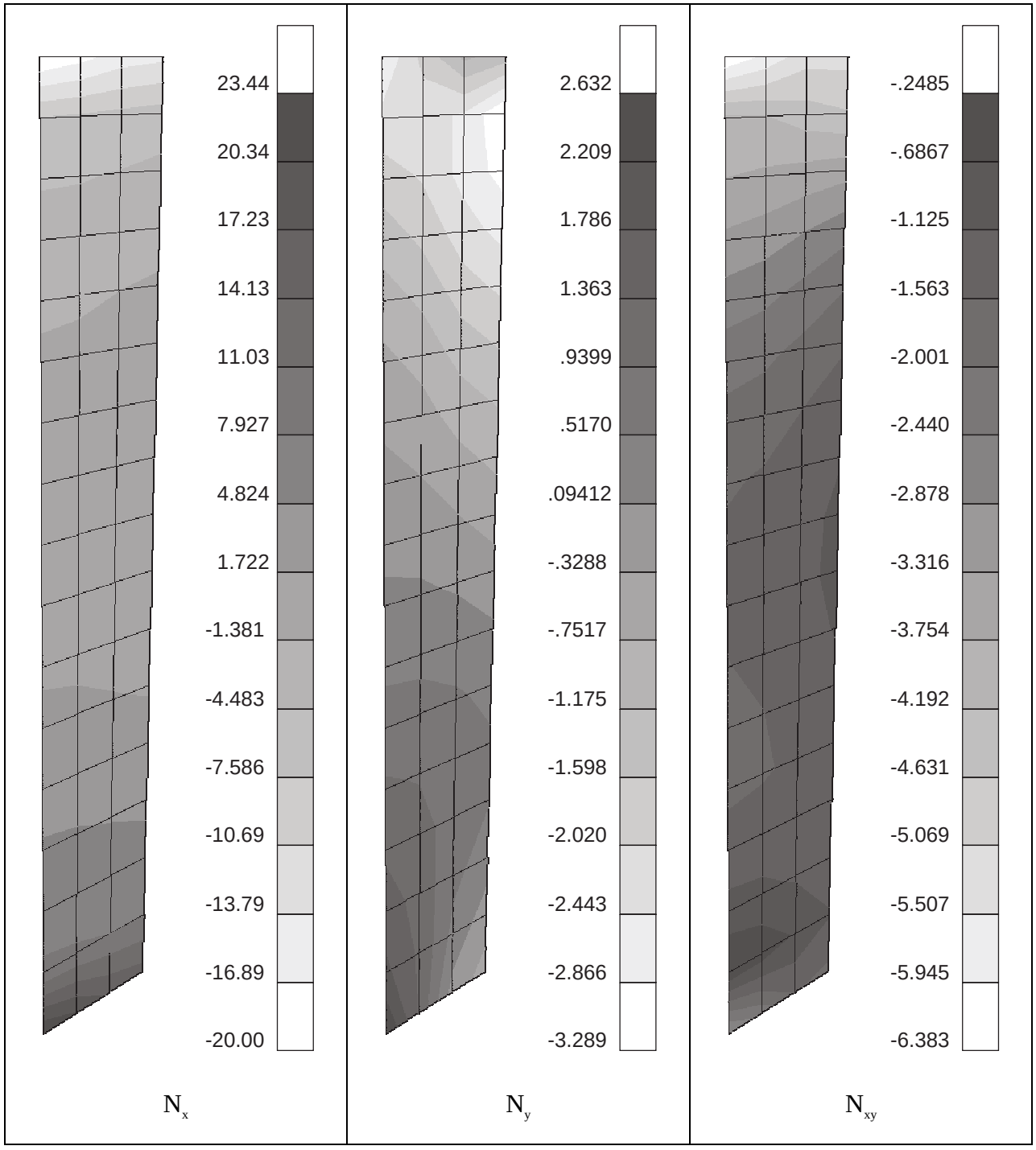

Figure 6.33: View Looking Aft for the Forward Root Mount Plate Stress Resultants (kips/in.) Near the Wall for Load Case 2, View Looking Aft. Note: Wall is on the Left Side of the Plots.

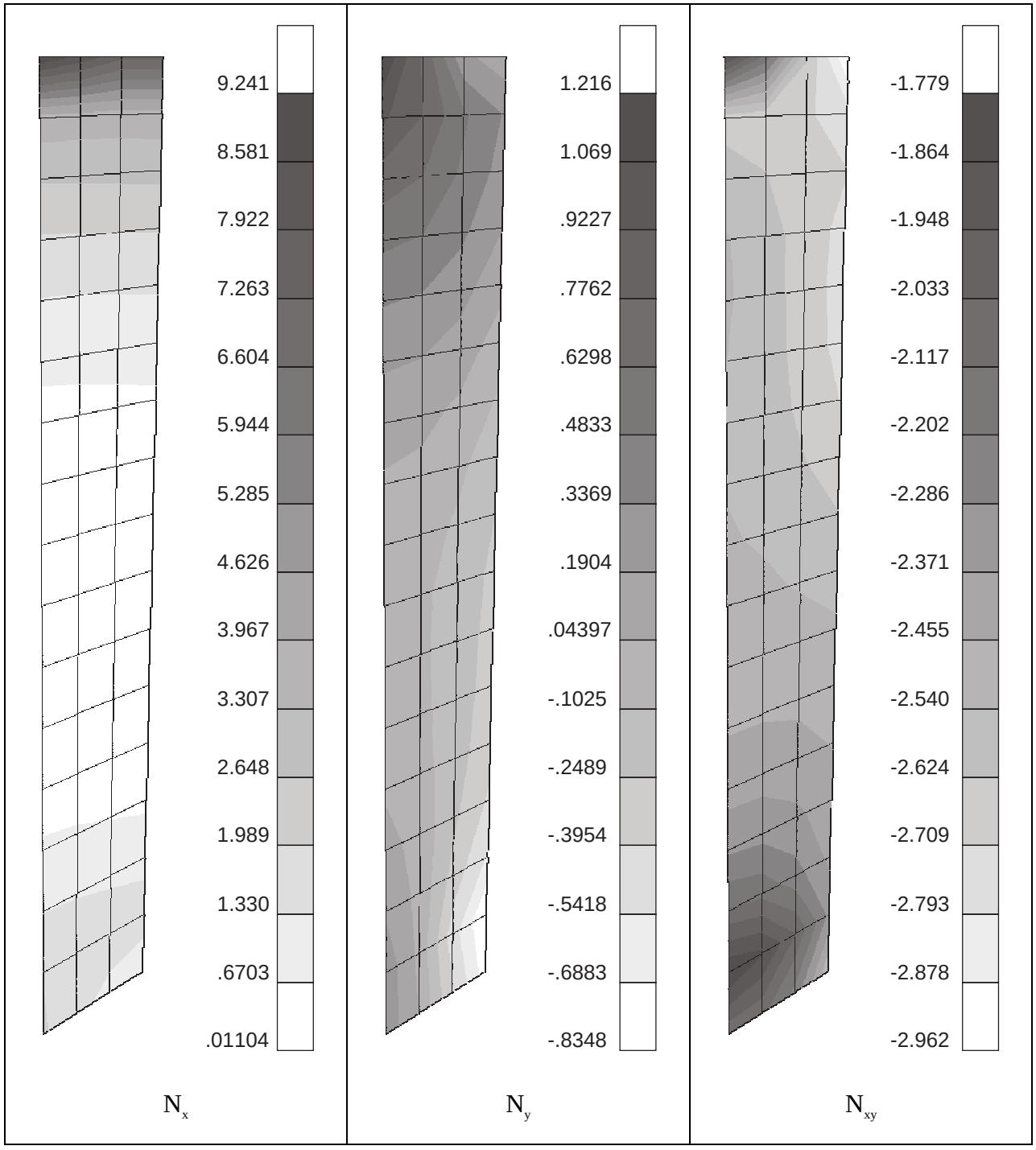

Figure 6.34: View Looking Aft for the Fore Root Mount Plate Stress Resultants (kips/in.) Near the Wall for Load Case 3. Note: Wall is on the Left Side of the Plots.

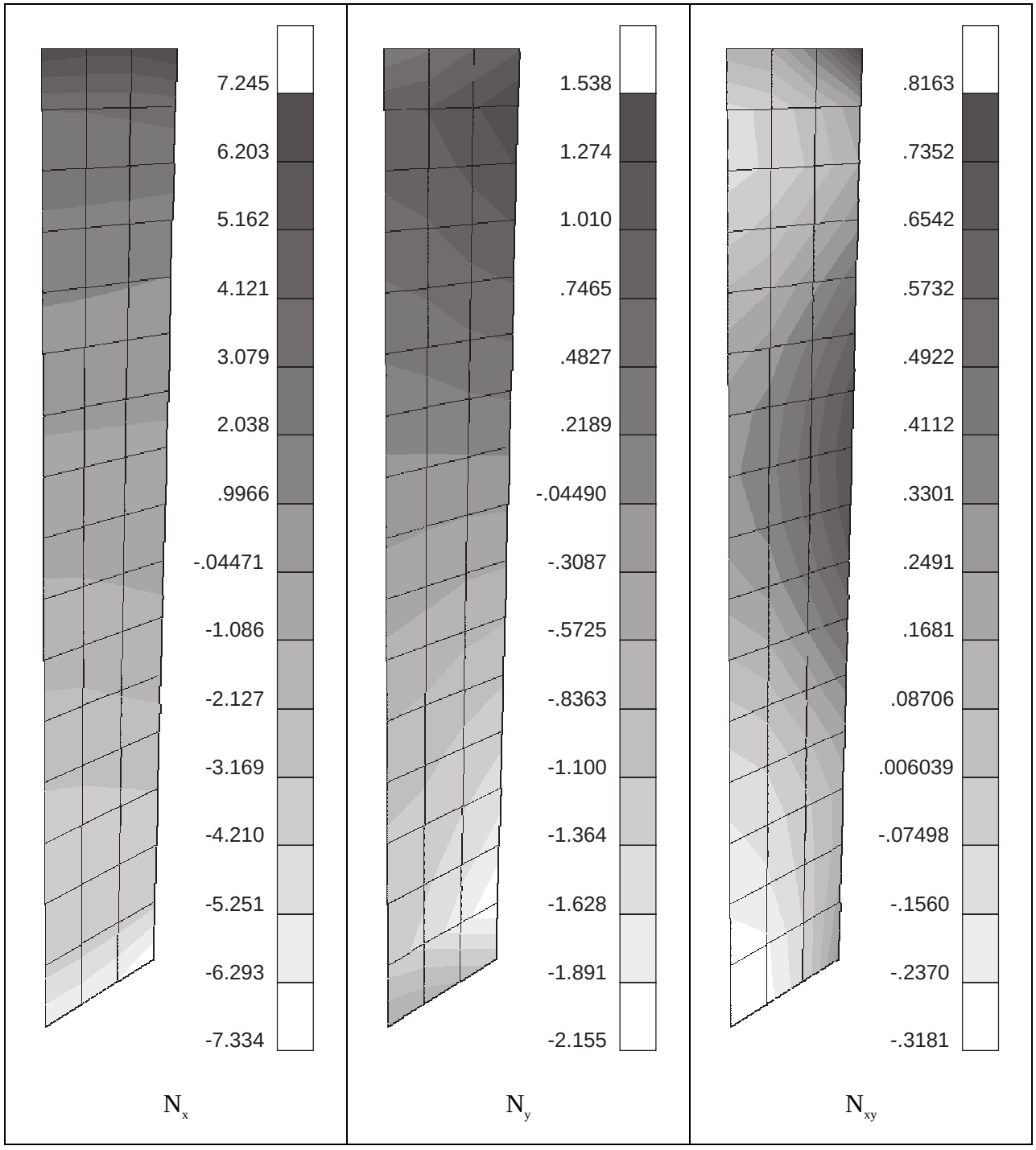

Figure 6.35: View Looking Aft for the Aft Root Mount Plate Stress Resultants (kips/in.) Near the Wall for Load Case 1. Note: Wall is on the Left Side of the Plots.

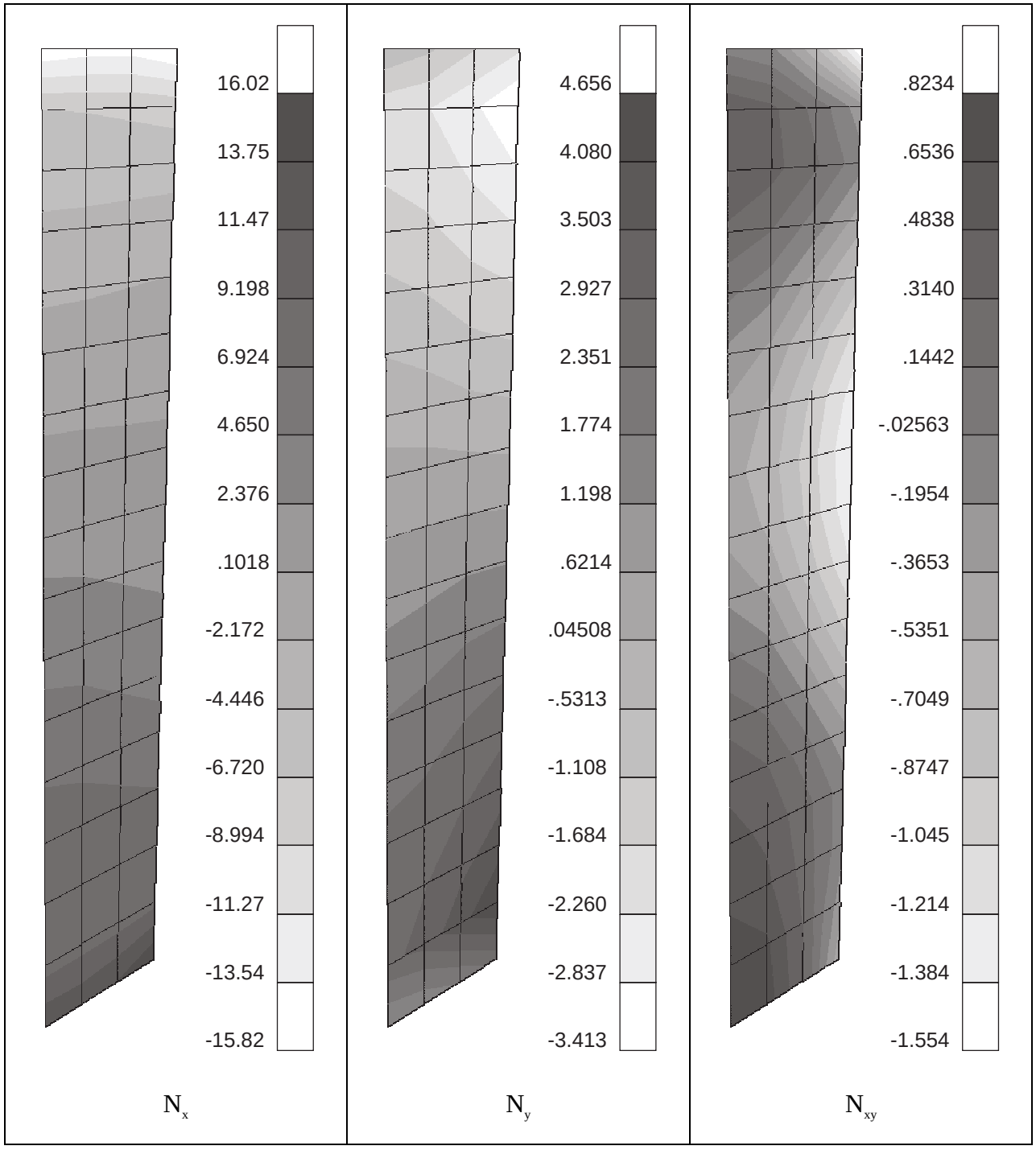

Figure 6.36: View Looking Aft for the Aft Root Mount Plate Stress Resultants (kips/in.) Near the Wall for Load Case 2. Note: Wall is on the Left Side of the Plots.

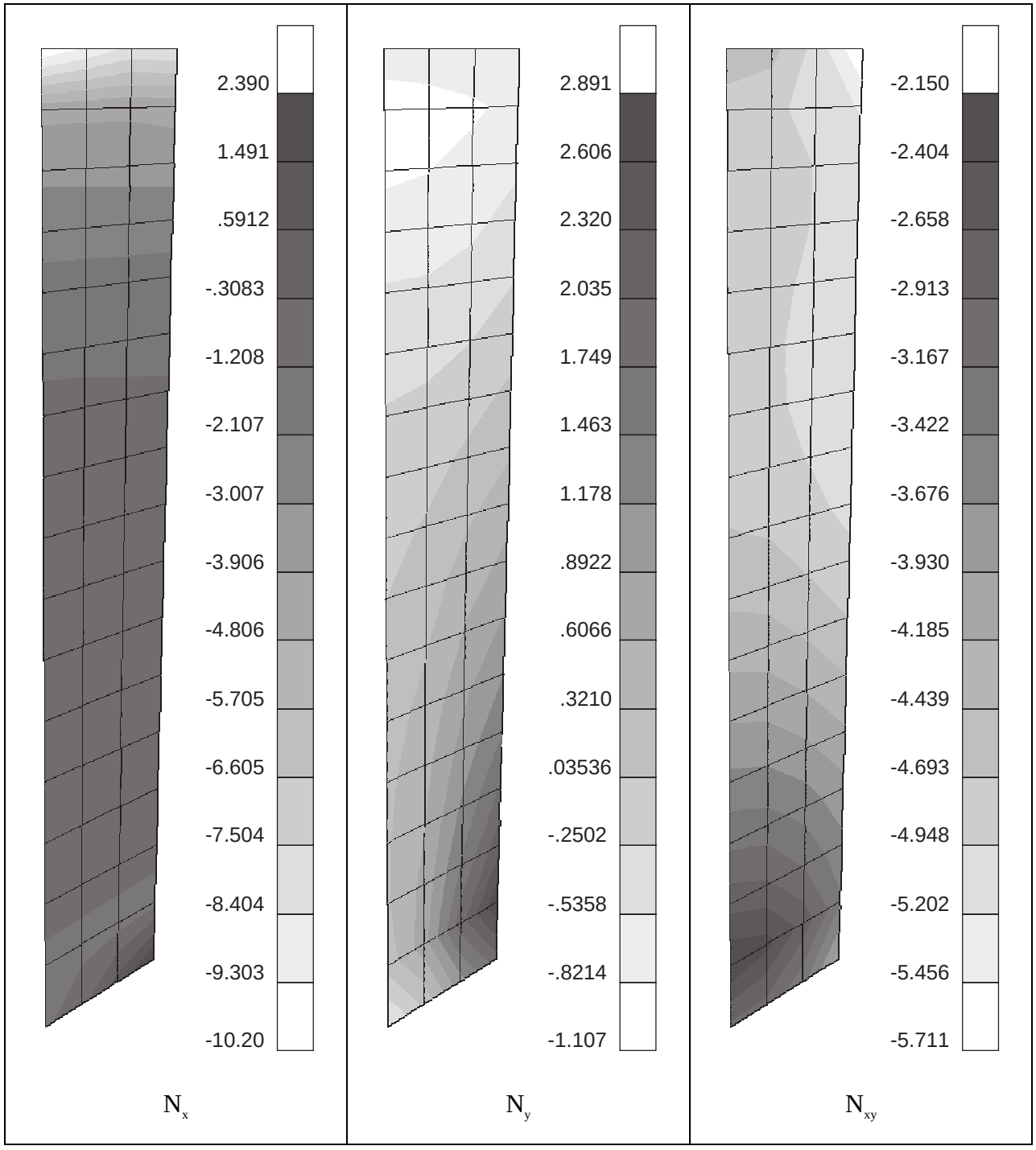

Figure 6.37: View Looking Aft for the Aft Root Mount Plate Stress Resultants (kips/in.) Near the Wall for Load Case 3. Note: Wall is on the Left Side of the Plots.

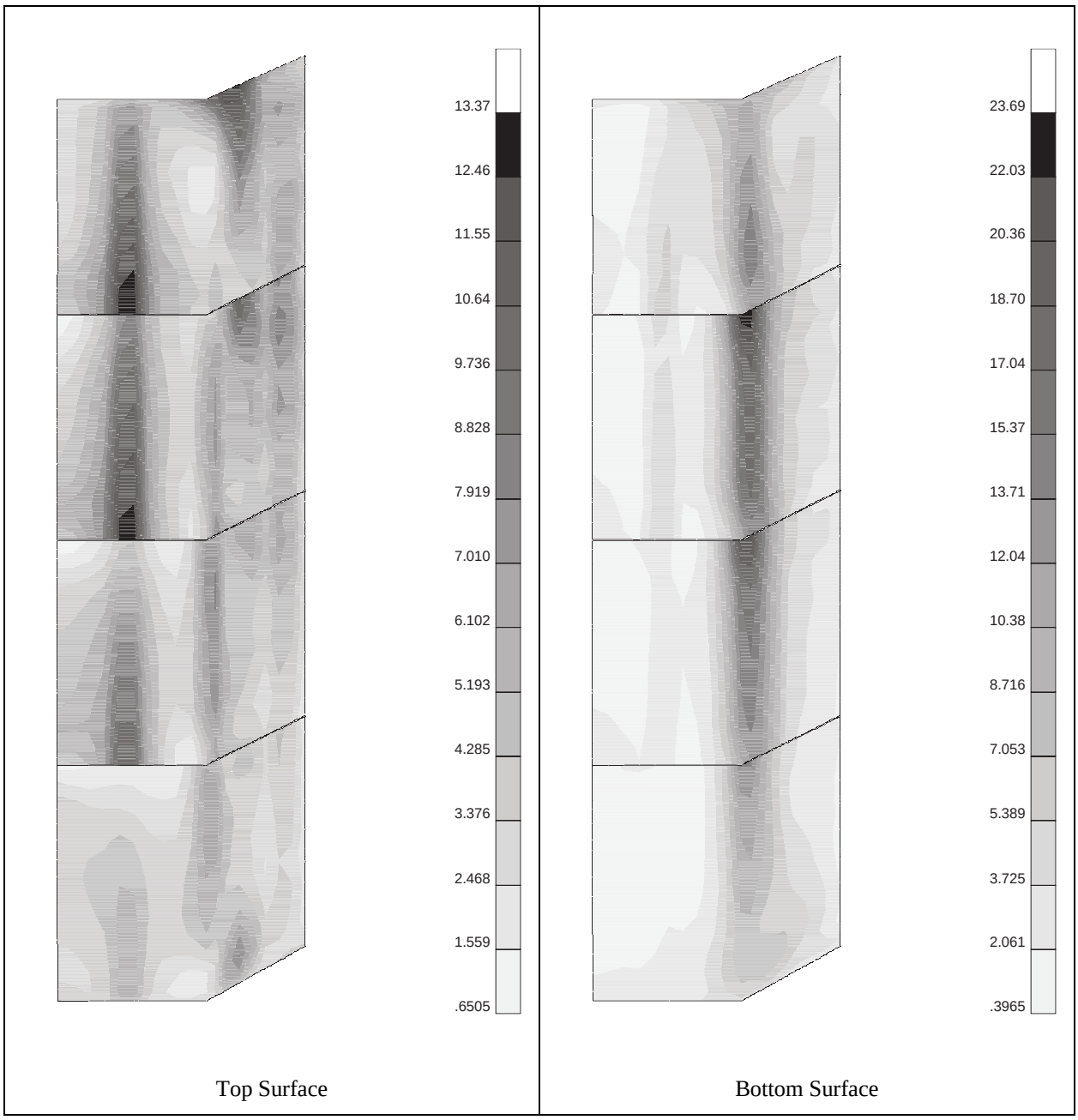

Figure 6.38: Top Root Mount Plate von Mises Stress (ksi), σ_{eff}, for Load Case 1.

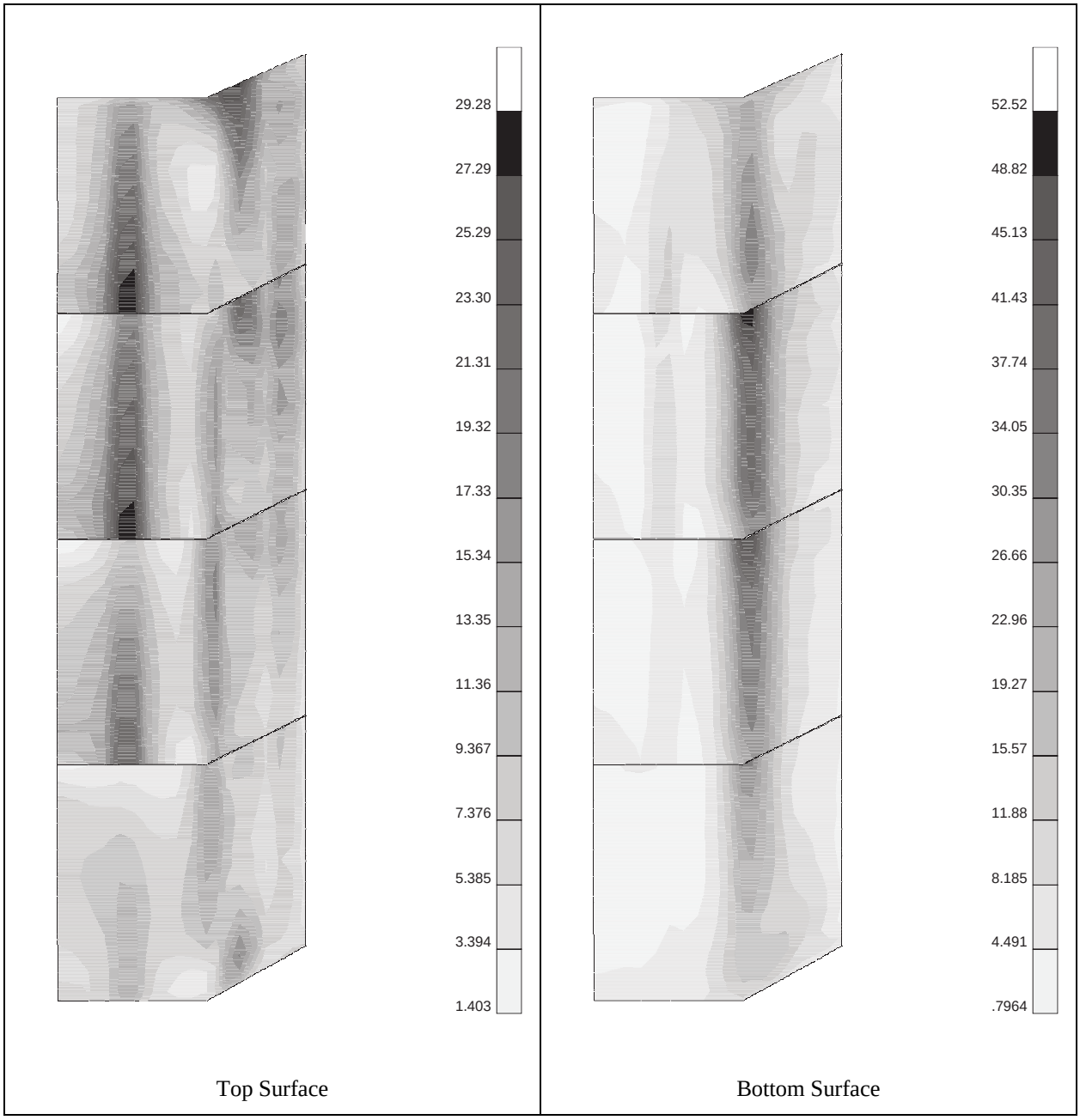

Figure 6.39: Top Root Mount Plate von Mises Stress (ksi), σ_{eff}, for Load Case2.

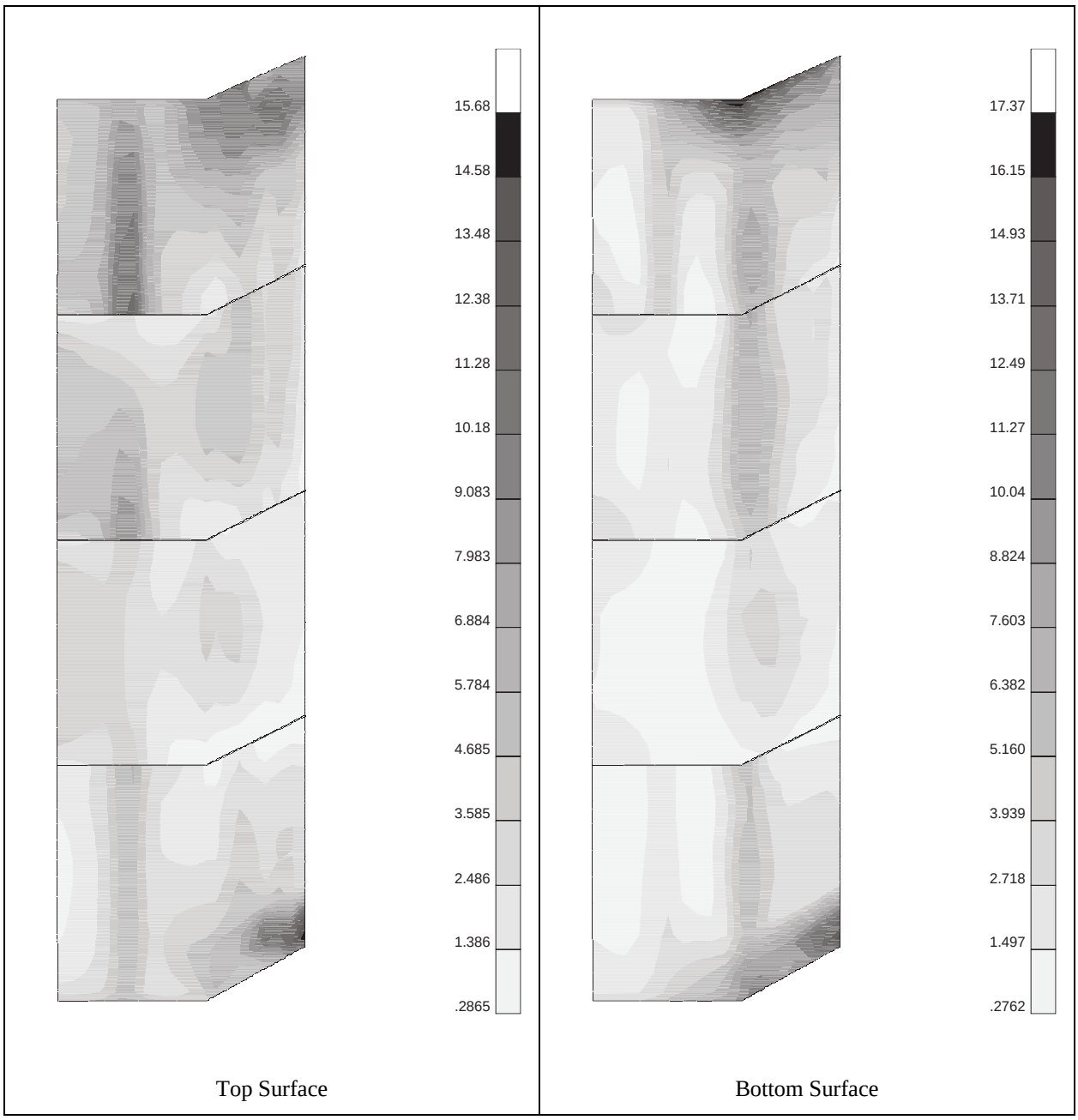

Figure 6.40: Top Root Mount Plate von Mises Stress (ksi), σ_{eff}, for Load Case 3.

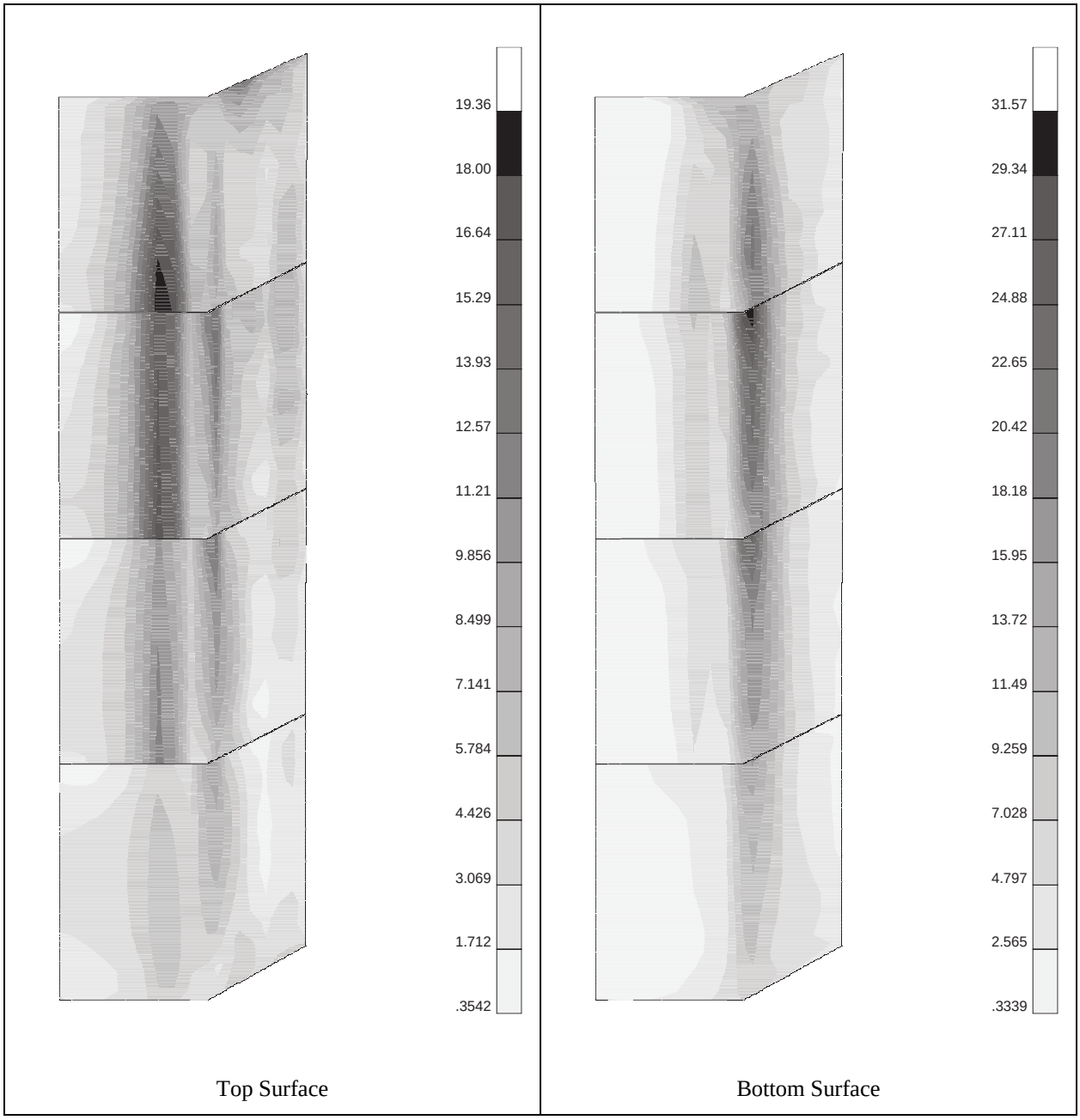

Figure 6.41: Bottom Root Mount Plate von Mises Stress (ksi), σ_{eff}, for Load Case 1.

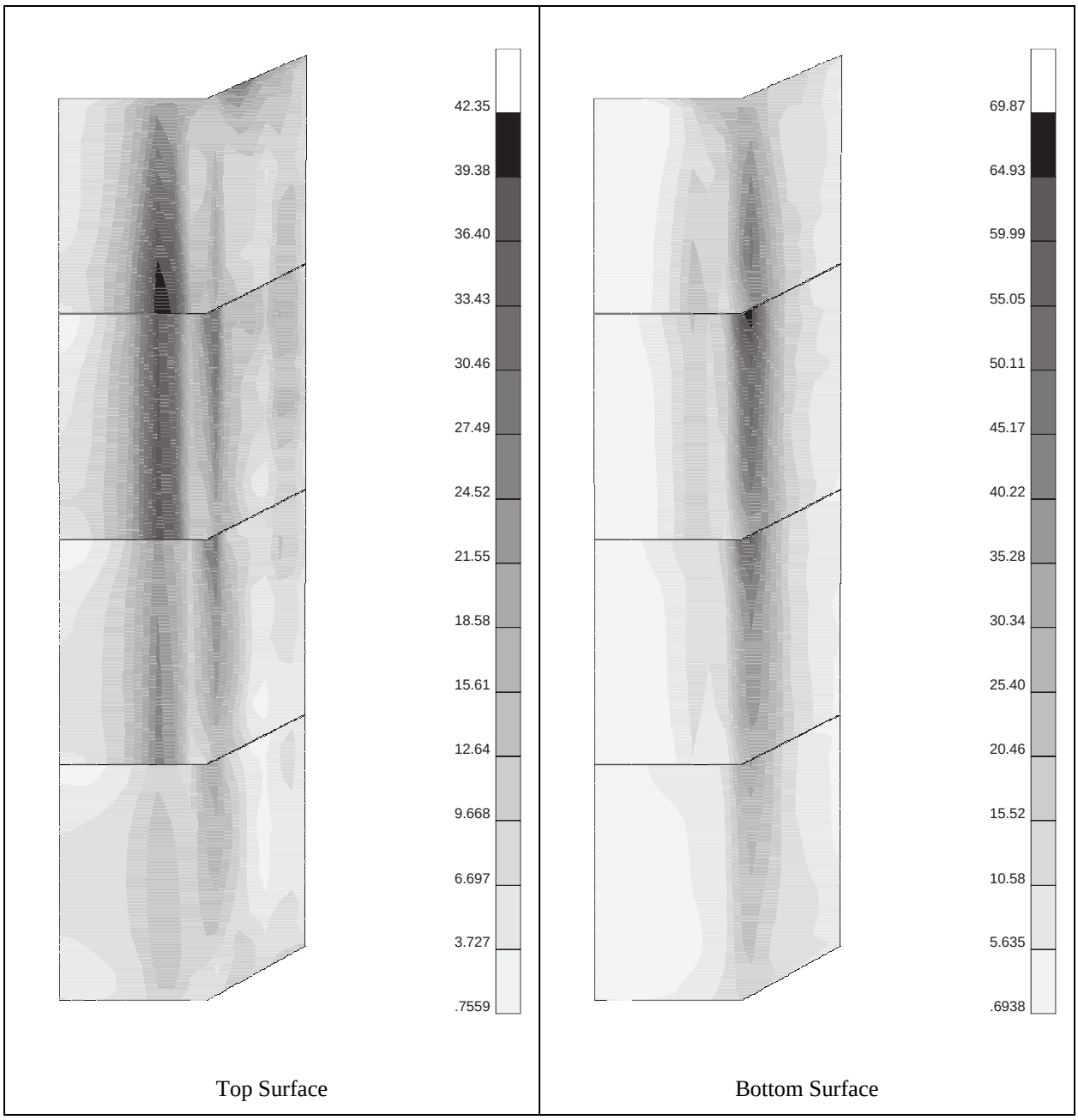

Figure 6.42: Bottom Root Mount Plate von Mises Stress (ksi), σ_{eff}, for Load Case 2.

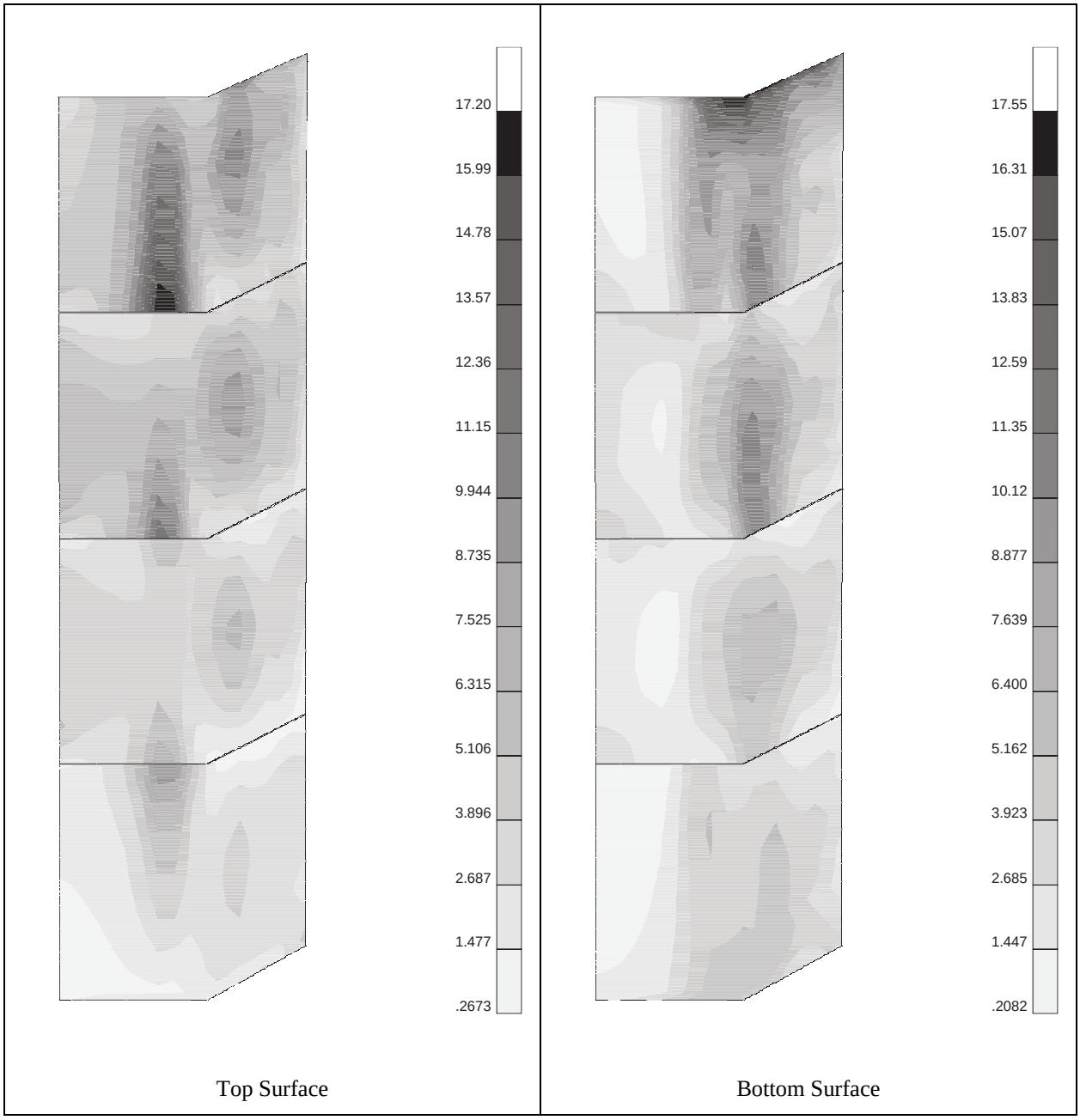

Figure 6.43: Bottom Root Mount Plate von Mises Stress (ksi), σ_{eff}, for Load Case 3.

7. Semi-Span Buckling Analysis

7.1 Buckling Requirements

The buckling design requirement for the composite semi-span is that the fundamental buckling load factor must be greater than 1.1 DUL. In order to ensure that the requirement was satisfied, linear buckling analyses were carried out on several of the models. Results for these analyses are presented in the following sections.

7.2 Results

7.2.1 Refined Model

7.2.1.1 Undamaged

Linear buckling analysis with the refined model showed that many buckling load factors associated with overhang buckling did not satisfy the buckling design requirement, particularly for the 2.5G up-bending. However, the most important instance of low buckling load factors was associated with upper cover skin bay buckling for the 2.5G up-bending load case. Figure 7.1 shows the mesh refinement necessary in the area of the upper skin bay buckling location to accurately capture the mode shapes and load factors. Mode shapes for the two violating load factors, 1.0025 and 1.0835, are shown in Figures 7.2 and 7.3, respectively. Only the upper cover is plotted in these two figures. It is seen that these modes primarily encompass the upper cover skin bay that is bounded by the forward spar, stringer #2, rib 4 and rib 5. The skin thickness for this particular bay was provided as 5 stacks.

Because this model did not satisfy the buckling design requirement, no further analyses were carried out on this model. Instead, a recommendation was made by AS&M, and subsequently adopted, in which an extra stack was added to this upper cover skin bay. To demonstrate the effectiveness of this skin thickness correction, the detailed model was developed and analyzed.

7.2.2 Detailed Model

7.2.2.1 Undamaged

Linear buckling analyses were carried out on the detailed model in order to determine the critical buckling load factors for the three load cases and demonstrate the effectiveness of the upper cover skin thickness correction proposed by AS&M. Results for the undamaged detailed model are presented in Tables 7.1-7.3. It is seen from the tables that the semi-span passes the 1.1 DUL buckling requirement for the 1.0G down-bending and braked roll load cases. However, for load case 2, 2.5G up-bending, two buckling modes occur for load factors less than the required 1.1 DUL. These modes are along the overhang at the trailing edge of the upper cover and are 1.0834 and 1.0901. As discussed in Section 7.2.2.3, a small reduction of the overhangs increases the buckling load factors above the required value.

Figures 7.4 and 7.5 show the mode shapes that are associated with the first two skin bay buckling load factors for the detailed model, which are 1.3433 and 1.4333, respectively. Therefore, it is seen that the recommendation by AS&M of increasing the skin thickness by 1 stack at the stringer #1 runout between ribs 4 and 5, from 5 stacks to 6 stacks, corrects the skin bay buckling problem.

7.2.2.2 With Discrete Damage

The buckling analysis discussed in the following two subsections for the damaged wing is discussed in accordance with the undamaged buckling requirement. However, the wing with discrete damage is required be able to sustain only 70% of DLL. Therefore, buckling load factors above DUL do not represent a problem for the damaged wing, and the results presented in these subsections should be viewed accordingly.

7.2.2.2.1 Upper Cover Sawcut

The linear buckling load factors for the detailed model having the upper cover sawcut discrete damage described in Section 4.1 are shown in Tables 7.4-7.6. As with the undamaged detailed model, it is seen that the semi-span passes the 1.1 DUL buckling requirement for the 1.0G down-bending and braked roll load cases. However, there are now three buckling load factors below the design requirement for the 2.5G up-bending load case. Again, these modes are present in the overhangs and can be corrected by decreasing the length of the overhangs.

7.2.2.2.2 Lower Cover Sawcut

The linear buckling load factors for the detailed model having the lower cover sawcut discrete damage described in Section 4.2 are shown in Tables 7.7-7.9. As with the undamaged and upper sawcut damaged detailed models, the composite semi-span with the lower cover sawcut satisfied the buckling design requirement for the 1.0G down-bending and braked roll load cases. Although, there is only one buckling load factor for the 2.5G up-bending which does not satisfy the 1.1 DUL requirement. It is also seen that a second buckling load factor is nearly equal to the buckling requirement. Again, note that these buckling modes occur in the overhangs.

7.2.2.3 Elimination of Overhang Buckling

Although the composite semi-span wing box on a real aircraft would not have unsupported overhangs, the test article that is being investigated does have unsupported overhangs. Since it is desirable to have the buckling load factors of the overhangs also satisfy the buckling design requirement, an adjustment to the overhang length was required. It may seem logical to simply cut off a significant portion of the overhang to correct this buckling problem. However, investigation of the strains yielded the fact that the overhang is carrying significant load. Therefore, cutting off the overhang introduces more load in the upper cover skins, resulting in many areas of failure that do not occur with the full 4.25 inch overhang.

An investigation into the effect of overhang length on the fundamental buckling load factor was carried out in order to determine the minimum overhang reduction that would satisfy the buckling requirement. Using the 2.5G up-bending load case, analyses for overhangs of 3.65 and 4.25 inches were carried out and compared. The 3.5 inch overhang has a fundamental buckling load factor of 1.4170, and the 4.25 inch overhang has a fundamental buckling load factor of 1.0834. Performing a linear interpolation between the 3.65 inch and 4.25 inch overhang lengths provides a fundamental buckling load factor of 1.1 at an overhang length of approximately 4.2 inches. Thus, a conservative and practical overhang length was determined to be 4.0 inches. The buckling load factors for the modified detailed model with 4.0 inch overhangs under the 2.5G up-bending load case are given in Table 7.10. Examination of Tables 7.2 and 7.10 indicate that modifying the overhang length from 4.25 to 4.0 inches changes the locations of the buckling modes and their load factor values. The fundamental buckling mode for the 4.25 inch overhang is located in the aft overhang, and the fundamental buckling mode for the 4.0 inch overhang is located in the fore overhang. The fundamental buckling load factor associated

with the fore overhang buckling mode for the 4.0 inch overhang is seen to be 1.2088. Thus, overhang length reduction to 4.0 inches satisfies the buckling design requirement for all three load cases. Therefore, as mentioned in Section 3.3.3, the 4.0 inch overhang was adopted for use as the basis for subsequent models.

7.2.3 Tapered-Height Model

Examination of the buckling results for the detailed model indicate that there are no buckling load factors below or near the allowable value of 1.1 DUL for load cases 1 and 3. Additionally, only load case 2 exhibits buckling modes for the damaged model in the vicinity of the model changes, namely the tapered upper cover stringer runouts added in order to create the tapered-height model. Therefore, only results for load case 2, the 2.5G up-bending load case, are of interest and are presented for the undamaged and discrete damaged tapered height model.

7.2.3.1 Undamaged

Linear buckling analysis of the undamaged tapered-height model was performed and the results are presented in Table 7.11 for the 2.5G up-bending load case. A seen in previous such analyses, overhang buckling dominates. It is also seen that the fundamental buckling load factor has dropped from 1.2088 in the detailed model to 1.1518 in this tapered-height model. This load factor still satisfies the buckling design requirement, and no other adverse buckling effects are observed as a result of introducing the tapered stringer blade height for the stringer #2 and stringer #10 runouts.

7.2.3.2 With Discrete Damage

As with sections 7.2.2.2.1 and 7.2.2.2.2, the results in the following two subsections should be viewed with the understanding that the damaged wing is required to carry only 70% of DLL.

7.2.3.2.1 Upper Cover Sawcut

Linear buckling analysis of the discrete damaged tapered-height model with the upper cover sawcut described in Section 4.1 was performed and the results are presented in Table 7.12 for the 2.5G up-bending load case. It is seen that the fundamental buckling load factor has dropped slightly from 1.1518 in the undamaged tapered-height model to 1.1466 in this tapered-height model with the upper cover sawcut. Although this fundamental buckling load factor still satisfies the buckling design requirement, an additional response was observed as a result of introducing the upper cover sawcut to the tapered-height model. Specifically, the second buckling mode, which now occurs on the aft portion of the upper cover, now includes the skin bay with the stringer #10 runout and the next outboard skin bay. Figure 7.6 shows this buckling mode. Presence of the skin bays in this buckling mode indicates that nonlinear effects may be important in this region as a result of the upper cover sawcut being added.

The 1.0G down-bending and braked roll load cases were not investigated for this damage scenario since this discrete damage is expected to have little effect on the semi-span buckling response for these two load cases.

7.2.3.2.2 Lower Cover Sawcut

Linear buckling analysis of the discrete damaged tapered-height model with the lower cover sawcut described in Section 4.1 was performed and the results are presented in Table 7.13 for the 2.5G up-bending load case. It is seen that the fundamental buckling load factor has dropped slightly from 1.1518

in the undamaged tapered-height model to 1.1414 in this tapered-height model with the lower cover sawcut. This fundamental buckling load factor still satisfies the buckling design requirement and no additional adverse response was observed as a result of introducing the lower cover sawcut to the tapered-height model.

The 1.0G down-bending and braked roll load cases were not investigated for this damage scenario since this discrete damage is expected to have little effect on the semi-span buckling response for these two load cases.

7.3 Tables

Table 7.1: Buckling Load Factors and Mode Locations for Load Case 1, Undamaged Detailed Model.

Mode	LF	Location
1	1.5304	lower cover, aft overhang between ribs 7-11
2	1.6254	lower cover, aft overhang between ribs 2-6
3	1.6875	lower cover, aft overhang between ribs 6-11
4	1.8224	lower cover, aft overhang between ribs 6-12
5	1.8389	lower cover, aft overhang between ribs 2-6

Table 7.2: Buckling Load Factors and Mode Locations for Load Case 2, Undamaged Detailed Model.

Mode	LF	Location
1	1.0834	upper cover, aft overhang between ribs 7-11
2	1.0901	upper cover, fore overhang between ribs 7-11
3	1.1189	upper cover, aft overhang between ribs 6-12
4	1.1362	upper cover, fore overhang between ribs 7-12
5	1.1422	upper cover, aft overhang between ribs 6-12

Table 7.3: Buckling Load Factors and Mode Locations for Load Case 3, Undamaged Detailed Model.

Mode	LF	Location
1	1.8207	rib 4, upper fore portion of cutout
2	1.9285	aft spar between ribs 1 and 2
3	1.9324	rib 4, lower aft portion of cutout
4	1.9352	rib 5, lower aft portion of cutout
5	2.1942	aft spar between ribs 4 and 5

Table 7.4: Buckling Load Factors and Mode Locations for Load Case 1, Detailed Model with Upper Cover Sawcut Discrete Damage.

Mode	LF	Location
1	1.5484	lower cover, aft overhang between ribs 6-10
2	1.6382	lower cover, aft overhang between ribs 2-6
3	1.7111	lower cover, aft overhang between ribs 6-11
4	1.8555	lower cover, aft overhang between ribs 1-6
5	1.8707	lower cover, aft overhang between ribs 6-11

Table 7.5: Buckling Load Factors and Mode Locations for Load Case 2, Detailed Model with Upper Cover Sawcut Discrete Damage.

Mode	LF	Location
1	1.0670	upper cover, aft overhang between ribs 7-11
2	1.0810	upper cover, fore overhang between ribs 7-11
3	1.0892	upper cover, aft overhang between ribs 7-12
4	1.1223	upper cover, aft overhang between ribs 6-12
5	1.1302	upper cover, fore overhang between ribs 7-12

Table 7.6: Buckling Load Factors and Mode Locations for Load Case 3, Detailed Model with Upper Cover Sawcut Discrete Damage.

Mode	LF	Location
1	1.8233	rib 4, upper fore portion of cutout
2	1.8379	aft spar between ribs 1 and 2
3	1.9361	rib 4, lower aft portion of cutout
4	1.9516	rib 5, lower aft portion of cutout
5	2.1298	aft spar between ribs 4 and 5

Table 7.7: Buckling Load Factors and Mode Locations for Load Case 1, Detailed Model with Lower Cover Sawcut Discrete Damage.

Mode	LF	Location
1	1.5196	lower cover, aft overhang between ribs 6-10
2	1.6384	lower cover, aft overhang between ribs 2-6
3	1.6752	lower cover, aft overhang between ribs 6-11
4	1.8111	lower cover, aft overhang between ribs 6-11
5	1.8557	lower cover, aft overhang between ribs 1-6

Table 7.8: Buckling Load Factors and Mode Locations for Load Case 2, Detailed Model with Lower Cover Sawcut Discrete Damage.

Mode	LF	Location
1	1.0753	upper cover, fore overhang between ribs 8-11
2	1.1006	upper cover, aft overhang between ribs 7-11
3	1.1193	upper cover, fore overhang between ribs 7-12
4	1.1349	upper cover, aft overhang between ribs 6-11
5	1.1565	upper cover, fore overhang ribs 6-12 and aft overhang ribs 1-12

Table 7.9: Buckling Load Factors and Mode Locations for Load Case 3, Model with Lower Cover Sawcut Discrete Damage.

Mode	LF	Location
1	1.4178	load arm angle down component
2	1.4975	aft spar between ribs 4 and 5
3	1.5291	aft spar between ribs 1 and 2
4	1.5751	rib 2 center portion fore of rib 3 attachment
5	1.5837	aft spar between ribs 4 and 5

Table 7.10: Buckling Load Factors and Mode Locations for Load Case 2, Undamaged Detailed Model with Overhangs Reduced to 4 Inches.

Mode	LF	Location
1	1.2088	upper cover, fore overhang between ribs 7-11
2	1.2532	upper cover, aft overhang between ribs 7-11
3	1.2629	upper cover, fore overhang between ribs 6-12
4	1.2723	upper cover, aft overhang between ribs 7-12
5	1.2818	upper cover, aft overhang between ribs 6-12

Table 7.11: Buckling Load Factors and Mode Locations for Load Case 2, Undamaged Tapered-Height Model.

Mode	LF	Location
1	1.1518	upper cover, fore overhang between ribs 7-11
2	1.2236	upper cover, fore overhang between ribs 7-12
3	1.2248	upper cover, aft overhang between ribs 7-11
4	1.2511	upper cover, aft overhang between ribs 6-11
5	1.2557	upper cover, fore overhang between ribs 7-12

Table 7.12: Buckling Load Factors and Mode Locations for Load Case 2, Upper Cover Sawcut Discrete Damaged Tapered-Height Model.

Mode	LF	Location
1	1.1466	upper cover, fore overhang between ribs 7-11
2	1.2101	upper cover, aft overhang between ribs 7-12 + first skin bays between ribs 8 and 10
3	1.2192	upper cover, fore overhang between ribs 7-12
4	1.2292	upper cover, aft overhang between ribs 7-12 + first skin bays between ribs 8 and 10
5	1.2531	upper cover, fore overhang between ribs 7-12

Table 7.13: Buckling Load Factors and Mode Locations for Load Case 2, Lower Cover Sawcut Discrete Damaged Tapered-Height Model.

Mode	LF	Location
1	1.1415	upper cover, fore overhang between ribs 7-11
2	1.2109	upper cover, fore overhang between ribs 7-12
3	1.2417	upper cover, fore overhang between ribs 7-12
4	1.2427	upper cover, aft overhang between ribs 7-11
5	1.2744	upper cover, aft overhang between ribs 7-11 + first skin bays between ribs 8 and 10

7.4 Figures

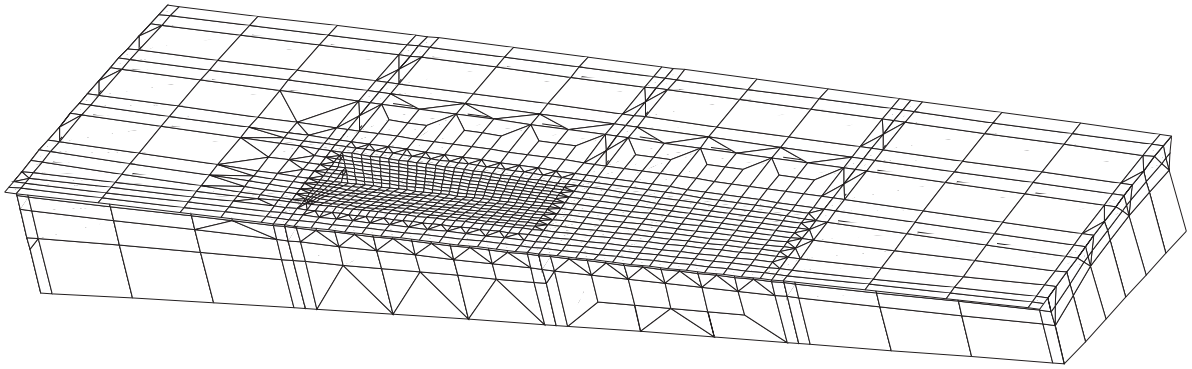

Figure 7.1: Refined Model Upper Cover Skin Buckling Mesh, Located at Stringer 1 Runout Between Ribs 4 and 5.

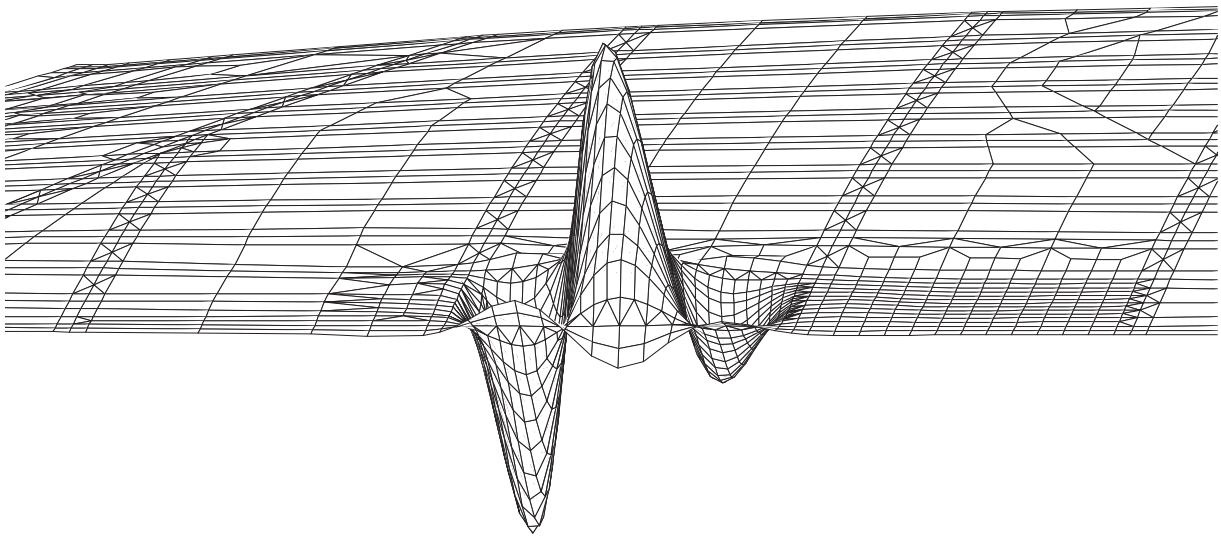

Figure 7.2: Refined Model Upper Cover Skin Buckling Mode #1, Load Factor LF=1.0025, Load Case 2. Located at Stringer 1 Runout Between Ribs 4 and 5, Skin Thickness 5 Stacks.

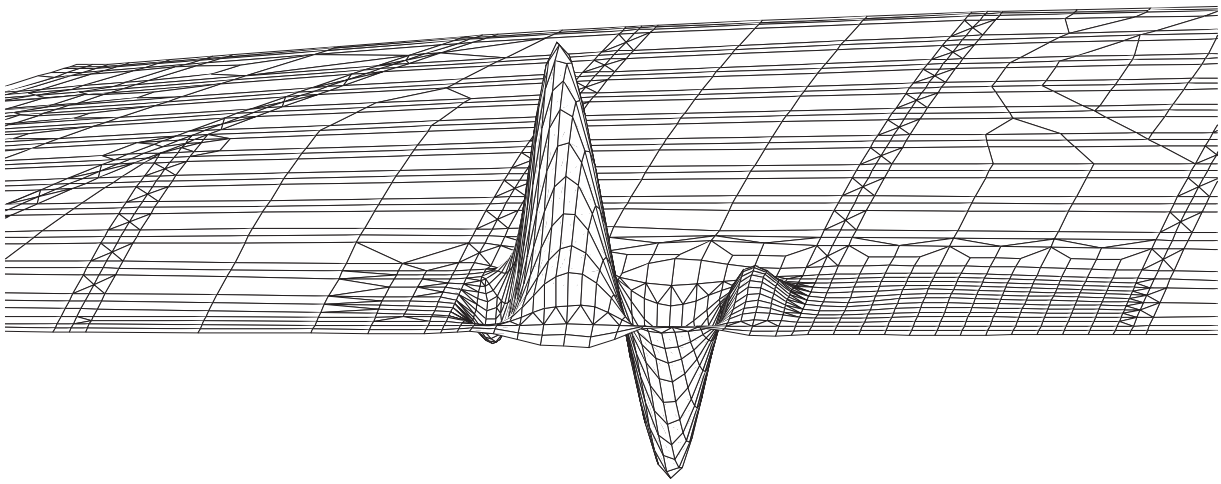

Figure 7.3: Refined Model Upper Cover Skin Buckling Mode #2, Load Factor LF=1.0835, Load Case 2. Located at Stringer 1 Runout Between Ribs 4 and 5, Skin Thickness 5 Stacks.

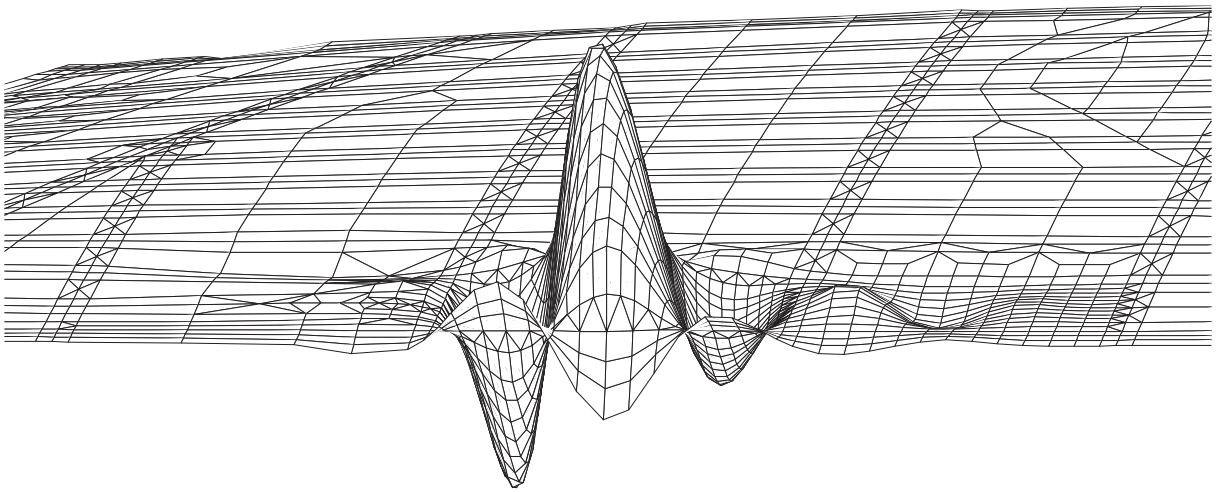

Figure 7.4: First Detailed Model Upper Cover Skin Bay Buckling Mode, Load Factor LF=1.3433, Load Case 2. Located at Stringer 1 Runout Between Ribs 4 and 5, Skin Thickness 6 Stacks as Recommended by AS&M.

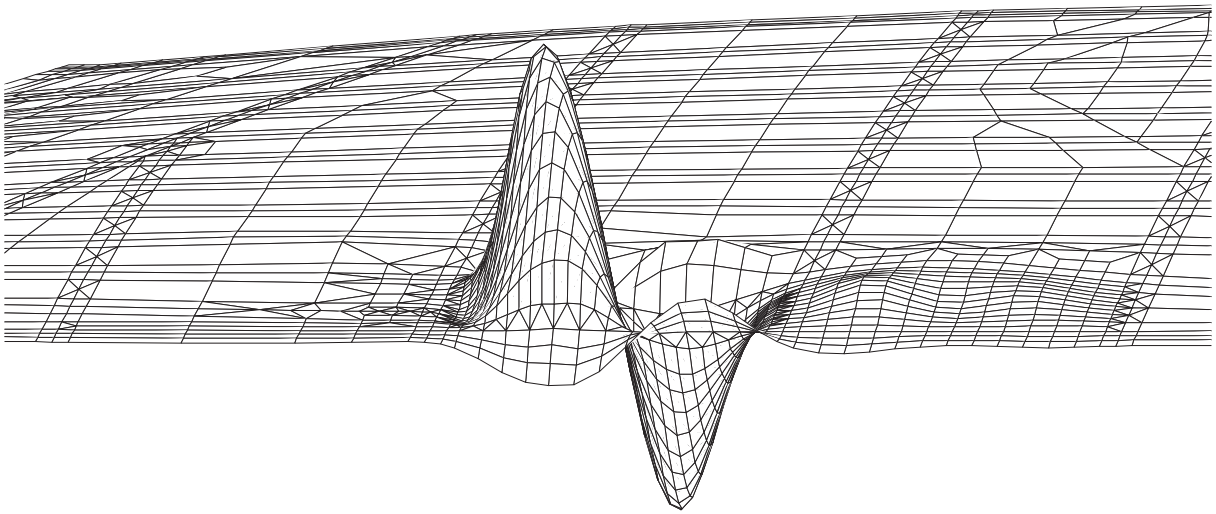

Figure 7.5: Second Detailed Model Upper Cover Skin Bay Buckling Mode, Load Factor LF=1.4333, Load Case 2. Located at Stringer 1 Runout Between Ribs 4 and 5, Skin Thickness 6 Stacks as Recommended by AS&M.

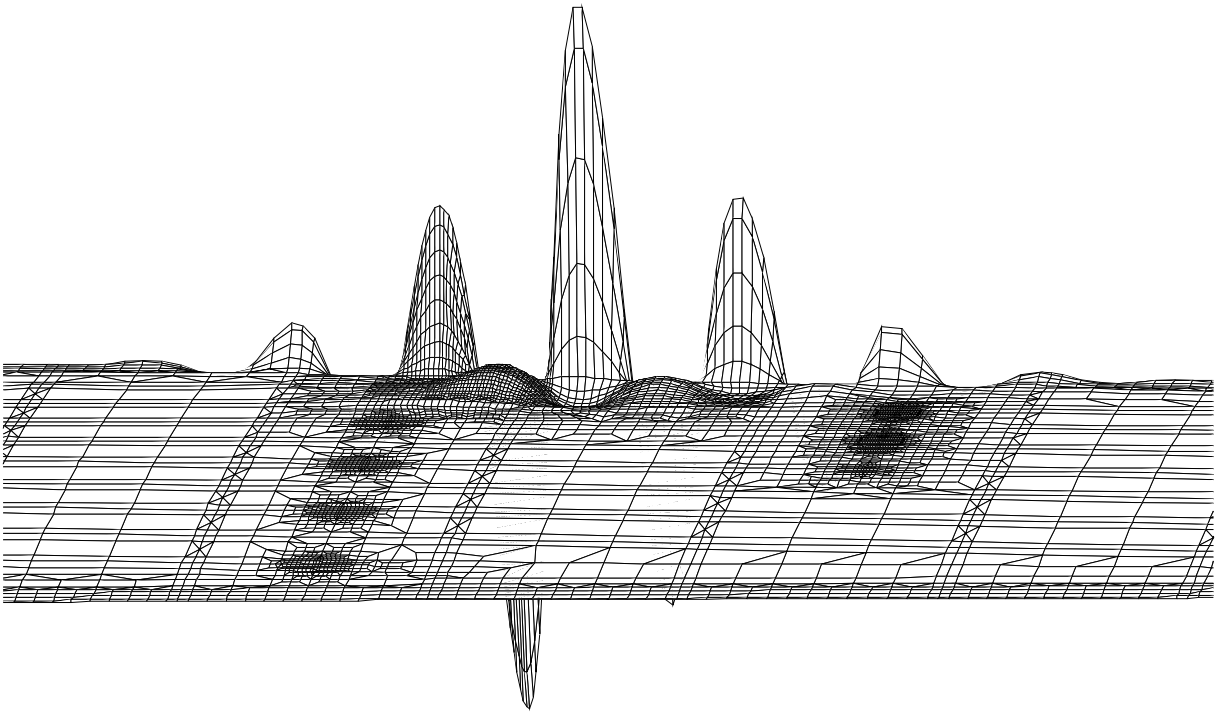

Figure 7.6: Second Buckling Mode for Tapered-Height Model with Upper Cover Sawcut, Load Factor LF=1.2101, Load Case 2. Located on Aft Overhang Between Ribs 7 to 11 and the First Skin Bays Between Ribs 8 and 10.

8. Semi-Span Strain Prediction/Failure Analysis

Strain prediction and failure analysis of the composite semi-span was carried out using both linear and nonlinear analysis. Models with and without discrete damage, as described in Sections 3 and 4, were investigated. Contour plots of strain values are used to present the response of the semi-span for the three load conditions. Failed elements and their associated factors of safety are provided in tables, and plots are given to show the locations of the failed elements within the semi-span. Allowable values of strain for undamaged and damaged material were provided to AS&M through NASA Langley.

8.1 Failure Requirements

Within the context of this report, failure of the semi-span is defined as the calculated strain value exceeding the provided allowable strain value, despite the fact that such a situation does not necessarily indicate that structural failure will occur. As such, the term failure as used in this report simply indicates that the allowable strain value is exceeded at the specified location. These allowable strain values are given for material that will not be damaged and for material that might be damaged, and will be referred to as the undamaged and damaged allowables, respectively. Calculated strain values are compared directly to the allowable strain values since the DUL conditions are applied in the finite element models used in this study. The calculated strain values are given in the component's material coordinate system for comparison to the allowables. Undamaged strain allowables are given in Table 8.1 and damaged strain allowables are given in Table 8.2 for the upper skin, lower skin and spars. Rib strain allowables are different in that they are provided in terms of principal strains. The undamaged and damaged values for the rib material are given in Table 8.3. Table 8.4 gives the tension and compression moduli for the composite semi-span, and Table 8.5 gives the ultimate stress failure values which were used to calculate the strain allowables shown in Table 8.1. Allowable strain values shown in Tables 8.2 and 8.3 were provided directly.

A FORTRAN program was written that takes the PATRAN neutral file for the models and creates a session file with PCL commands. This session file is then run in PATRAN, creating groups for each property set which contains elements. Therefore, each group can be displayed, and the strains for each group plotted. However, in PATRAN, the default using the BASIC results option is to extrapolate strain values to the nodes and then average the nodal values. These averaged nodal values are used to make the fringe plots. Unfortunately, this method has a tendency to "wash out" the large values of strain for some elements if they are surrounded by elements with low strain, especially if the averaging domain is chosen improperly. Individual element strain values can be plotted with PATRAN, but this requires the ADVANCED option in the results menu which has a tendency to cause PATRAN to crash when using STAGS results. Although the crashing problem was corrected in later versions, the attempt to use PATRAN for determining the maximum and minimum values of strains in each property set was abandoned.

In order to accurately study the failure of the elements, a new FORTRAN program was written which compares the element centroidal strain to the allowable for the property set to which the element belongs. This program wrote the values to files representing the top surface, bottom surface and mid-plane strains. When an element is determined to fail, the element number and strain results are written to the appropriate file for the top, bottom and mid-plane surface failures. The maximum and minimum values of strain for each property set are also determined and recorded. Only mid-plane failure of the elements is investigated in this study since the provided allowable strain values are associated with the mid-plane. However, STAGS strain results are obtained at the centroid for the reference, top and bottom surfaces of the shell elements. Since many elements have offsets, the reference surface is not necessarily the mid-

plane of an element. As a result, although the reference surface is continuous, element mid-plane surfaces are not continuous which can lead to significant jumps in mid-plane strain across thickness boundaries. Therefore, the FORTRAN code processes the STAGS data and calculates mid-plane strain values for use in the failure analysis without regard to mid-plane strain continuity across thickness change boundaries. This code then uses the strain allowables, which are provided to the code via association with the element property set identification numbers, to determine failure. Lists of failed elements for each property set are saved to files for easy identification.

Since the failure analysis is carried out for mid-plane strain values only, when significant bending occurs, the failure analysis can be in error. Therefore, an additional feature was added to the FORTRAN code to calculate the significance of bending in the elements. This was accomplished by taking the top-surface strain and subtracting the mid-plane strain, dividing by the top-surface strain, and representing the result as a percent value. Mathematically this is represented by:

$$percent\ bending = \frac{\varepsilon_{xx_{top}} - \varepsilon_{xx_{mid}}}{\varepsilon_{xx_{top}}} \times 100\%$$

Positive and negative values indicate the direction of the bending. However, it is the magnitude of the percent bending value that is of importance since larger absolute values represent higher bending effects. Therefore, elements for which the percent bending absolute value is greater than 20% had the mid-plane and top-surface strains provided to NASA for use in a failure analysis where bending effects are considered.

8.2 Results

Nonlinear analyses were completed for several models for each of the three load cases, and strain values calculated. As mentioned earlier, the strain values are calculated in the material coordinate system of the part under consideration. For the models studied, only the 2.5G up-bending load case produced significant strain values. Significant refers to those strain values that are close to the design allowables. Strain values for the 1.0G down-bending and braked roll load cases are much lower than the design allowables. Therefore, the results for these load cases are not discussed and are omitted for brevity. Additionally, the only components of interest are the upper and lower covers and the stringers. The material coordinate systems for these three components are set up so that the x-axis is oriented along the length of the stringer.

Two models are examined in this results section, namely the detailed model and the tapered-height model. The detailed model is presented as the baseline model for the composite semi-span strain and failure discussion. The tapered-height model is then presented to show the effects of tapering the upper cover stringer height on the strain and failure predictions.

8.2.1 Detailed Model

8.2.1.1 Undamaged, Strain

Strain plots for the composite semi-span were made using PATRAN. Strains were plotted for the top and bottom surfaces of the elements since these are the results returned from the STAGS analysis. Mid-plane strain plots were not made since the mid-plane strain values were calculated from the STAGS output in a custom program, and could not be plotted directly in PATRAN with the output provided from

STAGS. As discussed in the subsequent failure section, strain levels within the main body of the semi-span satisfied the strain requirements for the three loading conditions. Therefore, overall strain plots are of little interest except for providing some insight into the areas of highest strain. However, load case 2 strain results for the upper and lower covers are shown in Figures 8.1 and 8.2 as being representative of the obtained results since these provided the highest strain values. Lastly, Figure 8.3 shows a close-up of the top surface strains for the upper cover in the vicinity of the stringer #10 runout. It is seen from this plot that the overhang exhibits the nonlinear behavior discussed in Section 5.1, leading to the overhang element failures discussed in the following section.

8.2.1.2 Undamaged, Failure

Failure analysis of the undamaged composite semi-span using undamaged allowables indicates that there are no regions within the main body of the semi-span that exhibit strain failures. The main body is defined as all elements interior to the spars, which includes everything except the overhangs. However, using the definition of failure provided earlier, numerous upper cover overhang elements were seen to exhibit failure for load case 2. Details of the failed overhang elements are not reported since the overhang response was, in general, not the focus of the current investigation, but a brief discussion follows.

Failure of the overhang elements can be attributed to the nonlinear behavior of the overhang, which causes significant bending in local regions of the upper cover overhang. Figure 8.4 shows the elements in the vicinity of the stringer #10 runout that exhibited greater than 20% bending as defined in Section 8.1. Several elements in the overhang are seen to exhibit this excessive bending, as are many elements at the stringer termination. As stated earlier, elements exhibiting excessive bending require additional failure analysis since the mid-plane strain evaluation is insufficient. Also seen in the figure are trapezoidal elements that are scattered across the region, but these elements do not accurately represent the large bending effects. Tests were performed where the trapezoidal elements were removed and a regular (nearly rectangular) mesh was generated. Results from the regular mesh did not exhibit the large bending effects in the areas where the trapezoidal elements were removed. Therefore, it was concluded that the strain results of the trapezoidal elements in STAGS are questionable, so trapezoidal elements were avoided near regions of interest and were only used for mesh transition in regions where their results can effectively be ignored.

8.2.1.3 With Discrete Damage, Strain

Analysis of the detailed model with discrete damage was performed using the undamaged allowables for load factors up to 0.475 of DUL. This value is slightly above 70% of DLL, which is the design load factor for these damage scenarios. Load case 1 and 3 strain values are significantly below the allowables for both damage scenarios and no further discussion is included. Results for load case 2 are discussed in the following two sections.

8.2.1.3.1 Upper Cover Sawcut

Strains throughout the main body of the composite semi-span are within the allowable values. The only exception to this is at the crack tips. Figure 8.5 shows the spanwise top surface strains in the vicinity of the sawcut, with Figure 8.6 showing a close-up of the forward most crack tip region strains. As expected, the crack tip acts as a stress concentration where the strains exceed the allowable strains for a distance of approximately 0.3 inches from the crack tip.

8.2.1.3.2 Lower Cover Sawcut

Similar to the upper sawcut model, the lower sawcut model exhibits strains throughout the main body of the composite semi-span within the allowable values. Figure 8.7 shows the spanwise top surface strains in the vicinity of the sawcut, with Figure 8.8 showing a close-up of the forward most crack tip region strains. As expected, the crack tip acts as a stress concentration where the strains exceed the allowable strains for a distance of approximately 0.2 inches from the crack tip.

8.2.1.4 With Discrete Damage, Failure

As with the strain results, only load case 2 results are discussed in the following two sections on failure of the composite semi-span with discrete damage, and failure is based upon the undamaged allowables. This failure discussion only focuses on the prediction of failure for elements based on the original model configuration, with failed elements continuing to contribute to the strength of the structure. That is, no progressive failure analysis or crack propagation analysis was carried out on the composite semi-span. Results from those two types of analysis could yield response significantly different from the analysis carried out and reported herein. Therefore, the presented results should be viewed accordingly.

8.2.1.4.1 Upper Cover Sawcut

Only elements in the vicinity of the crack tip exhibited failure under 2.5G up-bending for load factors up to 0.475 of DUL. Failure initiated in the triangular elements located at the crack tip at a load factor of 0.2. Successive element failures were observed as the load factor gradually increased to the 0.475 maximum. Figures 8.9-8.12 show the failed elements for each load factor at which any elements first exhibit failure. The skin thickness at both crack tips is the same, and since the strains given in Figure 8.5 are fairly symmetric, so are the failed regions shown in the figures. Lastly, factors of safety and margins of safety associated with the failed elements are provided in Table 8.6 for a load factor of 0.475. Also provided in the table are the strain allowable and the calculated strain value for each element.

8.2.1.4.2 Lower Cover Sawcut

The lower cover sawcut model response was similar to the upper cover sawcut model response. Failure initiated at the crack tip at a load factor of 0.2 and successive element failures occurred as the load factor increased to 0.475. Figures 8.13-8.15 show the failed elements in the lower sawcut model for each load factor at which any elements first exhibit failure. Contrary to the upper sawcut model, the lower sawcut model has different skin thicknesses at the two crack tips. However, the allowable is the same everywhere for the lower skin, so since the strains in Figure 8.7 are nearly symmetric about the crack tips, the failure pattern is also nearly symmetric as seen in the figures. Table 8.7 gives the factor of safety, margin of safety, strain allowable and calculated strain for each failed element at a load factor of 0.475.

8.2.2 Tapered-Height Model

8.2.2.1 Undamaged, Strain

Analysis of the composite semi-span was carried out using the tapered-height model described in Section 3.3.4, and strains are similar to those of the detailed model with the exception of the stringer runout areas. A close-up of the upper cover strains in the vicinity of the stringer #10 runout was shown in Figure 5.11 in conjunction with the nonlinearity discussion. No further strain results are presented.

8.2.2.2 Undamaged, Failure

The 2.5G up-bending load case was used in the tapered-height failure analysis since it has been shown to be the critical load case. As discussed in Section 8.2.1.2, failure analysis at 1.0 DUL for the detailed model indicates that no main body elements fail. On the other hand, the tapered-height model indicates that three main body regions exhibit element failure when the damaged allowables are used.

Since the tapered-height model was derived from the strain gage model, numerous regions in the tapered-height model are highly refined when compared to the detailed model. One of these regions is the aft portion of the lower cover cutout located between ribs 7 and 8. As a result, the tapered-height model indicates that the stress concentration that occurs at the cutout edge initiates element strain failure at a load factor of 0.9. Figures 8.16-8.18 show the failed elements around the cutout for load factors of 0.9, 0.95 and 1.0, respectively. Factors of safety and margins of safety for the failed elements at DUL, based on the damaged allowables, are given in Table 8.8, with element numbers shown in Figure 8.19.

Additional failures initiate in the stringer #2 and #10 blades at 0.8 DUL load factor. Figure 8.20 shows the ply drop-off locations in the region of the stringer #10 runout. Failed elements for stringer #10 are then presented in Figures 8.21-8.24 for load factors of 0.8, 0.9, 0.95 and 1.0 DUL, respectively. A study of these failed elements indicates that the failures initially occur at the ply drop-offs, where the thicker region dumps the load into the reduced thickness region. All failed elements occur in the 2-, 4- and 6-ply regions, which have damaged allowables of 4132, 4132 and 4158 microstrain, respectively. Similarly, element failures occur in stringer #2 in the 4- and 6-ply thickness areas. Ply drop-offs for stringer #2 are shown in Figure 8.25, and stringer #2 failed elements are shown for load factors of 0.8, 0.9, 0.95 and 1.0, respectively, in Figures 8.26-8.29. Factors of safety and margins of safety are not provided for the stringer #2 and #10 blades for the results based on the damaged allowables.

Therefore, it is concluded that the height taper for stringers #2 and #10 at the runouts causes significant failures when damaged allowables are utilized. However, since the test article is not to be impacted on the stringer blades, failure analysis based on undamaged allowables can be considered for the stringer #2 and #10 blades. Comparison using undamaged allowables indicates that no stringer blade elements fail. Thus, as long as no damage is introduced to the stringer blades, the tapered height runouts of stringers #2 and #10 should perform safely during the composite semi-span testing. However, element failures found while using the damaged allowable for elements located along the aft edge of the lower cover cutout between ribs 7 and 8 indicate that this area can not have impact damage introduced. However, as with the stringer blades, the lower cover elements in this cutout region do not exhibit failure when utilizing the undamaged allowables. Finally, refinement around the edges of the remaining lower cover cutouts may reveal similar behavior, but such an investigation was not conducted for presentation within this report.

8.2.2.3 With Discrete Damage, Strain

Strain results for the tapered height model with discrete damage are similar to those of the detailed model with discrete damage discussed in Section 8.2.1.3 and its subsections. Therefore, no further results are presented in this section.

8.2.2.4 With Discrete Damage, Failure

Failure results for the tapered height model with discrete damage are similar to those of the detailed model with discrete damage discussed in Section 8.2.1.4 and its subsections. Therefore, no further results are presented in this section.

8.3 Tables

Table 8.1: Undamaged Allowables for Composite Semi-Span.

Component	ε_{xx} **tension** ($\mu\varepsilon$)	ε_{xx} **compression** ($\mu\varepsilon$)	ε_{yy} **tension** ($\mu\varepsilon$)	ε_{yy} **compression** ($\mu\varepsilon$)
Spar	10043	6815	7875	8489
Upper Skin	10866	8874	8114	8822
Lower Skin	10743	6870	8155	8411

Table 8.2: Damaged Allowables for Composite Semi-Span.

Component	**# of Stacks**	ε_{xx} **TAI** ($\mu\varepsilon$)	ε_{xx} **CAI** ($\mu\varepsilon$)
Spars	2	NA	4439
	3	NA	4439
	4	NA	4887
	5	NA	5687
	6	NA	6342
	7	NA	6833
	8	NA	7144
	9	NA	7416
	10	NA	7751
	12	NA	8217
Upper Skin	2	NA	4132
	3	NA	4132
	4	NA	4132
	5	NA	4132
	6	NA	4158
	7	NA	4505
	8	NA	4734
	9	NA	5262
	10	NA	5731
	11*	NA	6000
	12	NA	6388
	13*	NA	6900
Lower Skin	AS4 Fiber	5963	NA
	IM7 Fiber	6626	NA

NA indicates not applicable, TAI is tension after impact and CAI is compression after impact
* indicates values were approximated by linear interpolation/extrapolation

Table 8.3: Rib Material Allowables for the Composite Semi-Span.

Condition	Major Principal Strain (με)	Minor Principal Strain (με)	Maximum Shear Strain (με)
Undamaged	9400	9300	1190
Damaged	5300	5300	6900

Table 8.4: Basic Laminate Stiffnesses for the Composite Semi-Span.

Component	E_x (ksi)	E_y (ksi)	G_{xy} (ksi)	ν_{xy}
Spar (Tension)	9210	5130	3150	.490
Spar (Compression)	8070	4700	2850	.479
Upper Skin (Tension)	10280	5090	2480	.403
Upper Skin (Compression)	9250	4670	2270	.397
Lower Skin (Tension)	12120	5150	2480	.403
Lower Skin (Compression)	10480	4720	2270	.397

Table 8.5: Basic Undamaged Laminate Allowable Strengths for the Composite Semi-Span.

Component	F_{TX} (ksi)	F_{CX} (ksi)	F_{TY} (ksi)	F_{CY} (ksi)
Spar	92.50	55.00	40.40	39.90
Upper Skin	111.70	82.08	41.30	41.20

Table 8.6: Factors of Safety and Margins of Safety for Upper Cover Failed Elements of the Upper Cover Sawcut Discrete Damaged Model Under 2.5G Up-Bending Load, LF=0.475 of DUL. (Column Allow is the strain allowable and column Calc is the calculated strain value, both in microstrain. Elements sorted By Increasing F.S.)

Element	Allow	Calc	F.S.	M.S.
7560	-8874	-18840	0.4710	-0.5290
7562	-8874	-18770	0.4728	-0.5272
7559	-8874	-18600	0.4771	-0.5229
7561	-8874	-18420	0.4818	-0.5182
27445	-8874	-12710	0.6982	-0.3018
27431	-8874	-12450	0.7128	-0.2872
27444	-8874	-12450	0.7128	-0.2872
27295	-8874	-12380	0.7168	-0.2832
27279	-8874	-12210	0.7268	-0.2732
27432	-8874	-12190	0.7280	-0.2720
27296	-8874	-12180	0.7286	-0.2714
27278	-8874	-12070	0.7352	-0.2648
27294	-8874	-9859	0.9001	-0.0999
27446	-8874	-9823	0.9034	-0.0966
27430	-8874	-9726	0.9124	-0.0876
27280	-8874	-9696	0.9152	-0.0848
27442	-8874	-8891	0.9981	-0.0019

Table 8.7: Factors of Safety and Margins of Safety for Lower Cover Failed Elements of the Lower Cover Sawcut Discrete Damaged Model Under 2.5G Up-Bending Load, LF=0.475 of DUL. (Column Allow is the strain allowable and column Calc is the calculated strain value, both in microstrain. Elements sorted By Increasing F.S.)

Element	Allow	Calc	F.S.	M.S.
7559	10743	18570	0.5785	-0.4215
7562	10743	18370	0.5848	-0.4152
7560	10743	18140	0.5922	-0.4078
7561	10743	18030	0.5958	-0.4042
27322	10743	12210	0.8799	-0.1201
27318	10743	12110	0.8871	-0.1129
27310	10743	12080	0.8893	-0.1107
27263	10743	11890	0.9035	-0.0965
27251	10743	11860	0.9058	-0.0942
27314	10743	11760	0.9135	-0.0865
27255	10743	11650	0.9221	-0.0779
27259	10743	11450	0.9383	-0.0617

Table 8.8: Factors of Safety and Margins of Safety for Lower Cover Failed Elements, Aft Edge of Cutout Between Ribs 7 and 8, Tapered-Height Model Under 2.5G Up-Bending Load, LF=1.0 of DUL. (Column Allow is the strain allowable and column Calc is the calculated strain value, both in microstrain. Elements sorted By Increasing F.S.)

Element	Allow	Calc	F.S.	M.S.
31359	5963	6822	0.8741	-0.1259
31358	5963	6816	0.8749	-0.1251
31360	5963	6795	0.8776	-0.1224
31340	5963	6766	0.8813	-0.1187
31400	5963	6762	0.8818	-0.1182
31341	5963	6761	0.8820	-0.1180
31342	5963	6747	0.8838	-0.1162
31387	5963	6718	0.8876	-0.1124
31388	5963	6669	0.8941	-0.1059
31399	5963	6655	0.8960	-0.1040
31338	5963	6634	0.8989	-0.1011
31337	5963	6633	0.8990	-0.1010
31339	5963	6621	0.9006	-0.0994
31412	5963	6590	0.9049	-0.0951
31357	5963	6589	0.9050	-0.0950
31385	5963	6584	0.9057	-0.0943
31356	5963	6551	0.9102	-0.0898
31386	5963	6541	0.9116	-0.0884
31355	5963	6511	0.9158	-0.0842
31413	5963	6504	0.9168	-0.0832
31414	5963	6477	0.9206	-0.0794
31449	5963	6462	0.9228	-0.0772
31398	5963	6458	0.9234	-0.0766
31415	5963	6396	0.9323	-0.0677

Element	Allow	Calc	F.S.	M.S.
31424	5963	6393	0.9327	-0.0673
31397	5963	6353	0.9386	-0.0614
31426	5963	6296	0.9471	-0.0529
31448	5963	6253	0.9536	-0.0464
31425	5963	6230	0.9571	-0.0429
31346	5963	6225	0.9579	-0.0421
31348	5963	6224	0.9581	-0.0419
31366	5963	6220	0.9587	-0.0413
31347	5963	6217	0.9591	-0.0409
31365	5963	6204	0.9612	-0.0388
31451	5963	6204	0.9612	-0.0388
31391	5963	6196	0.9624	-0.0376
31364	5963	6180	0.9649	-0.0351
31404	5963	6153	0.9691	-0.0309
31392	5963	6140	0.9712	-0.0288
31427	5963	6126	0.9734	-0.0266
31436	5963	6122	0.9740	-0.0260
31416	5963	6081	0.9806	-0.0194
31403	5963	6057	0.9845	-0.0155
31450	5963	6052	0.9853	-0.0147
31461	5963	6000	0.9938	-0.0062
31417	5963	5997	0.9943	-0.0057
31437	5963	5992	0.9952	-0.0048

8.4 Figures

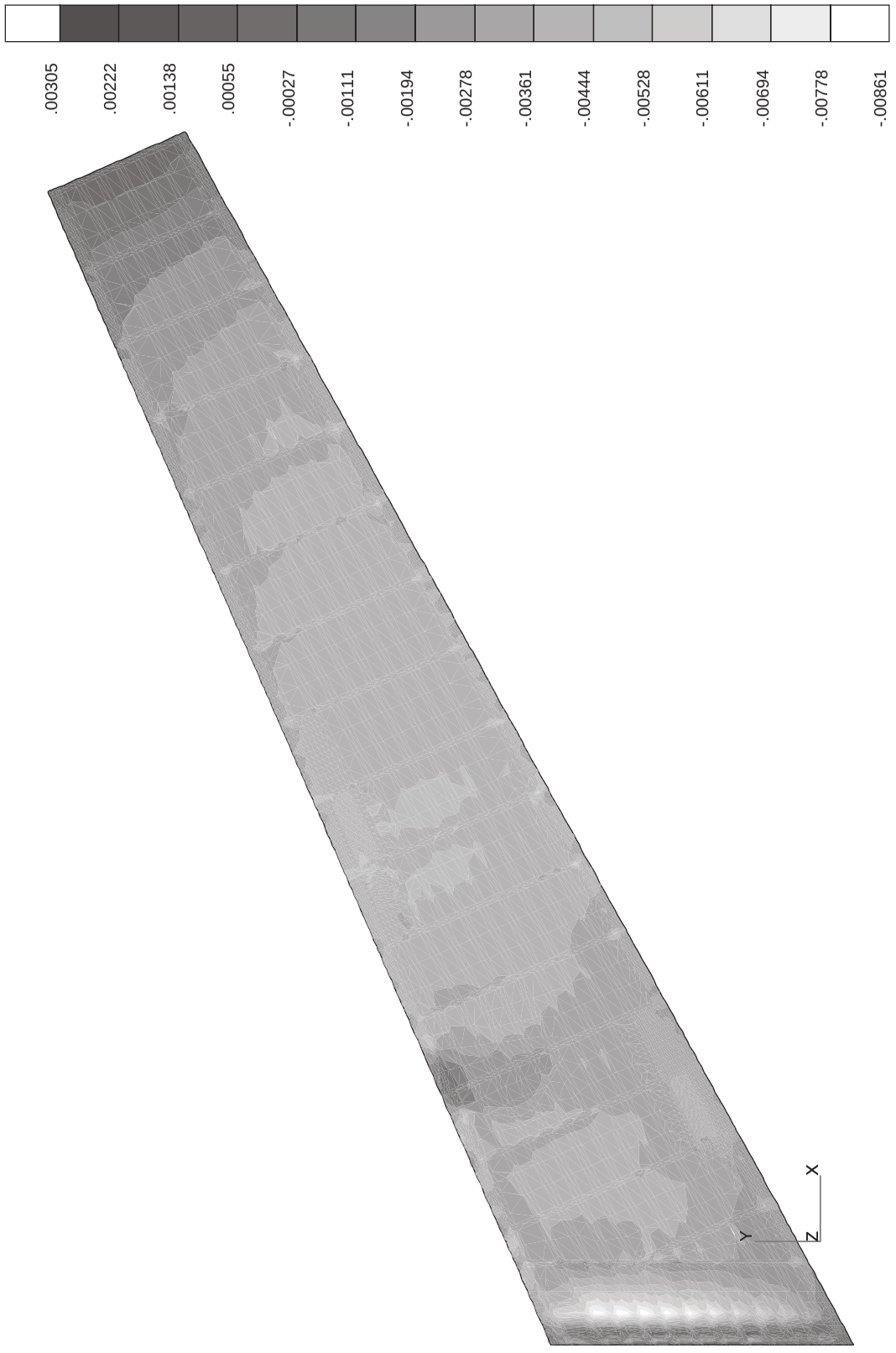

Figure 8.1: Upper Cover Top Surface Spanwise Strain for 2.5G Up-Bending, LF=1.0 of DUL.

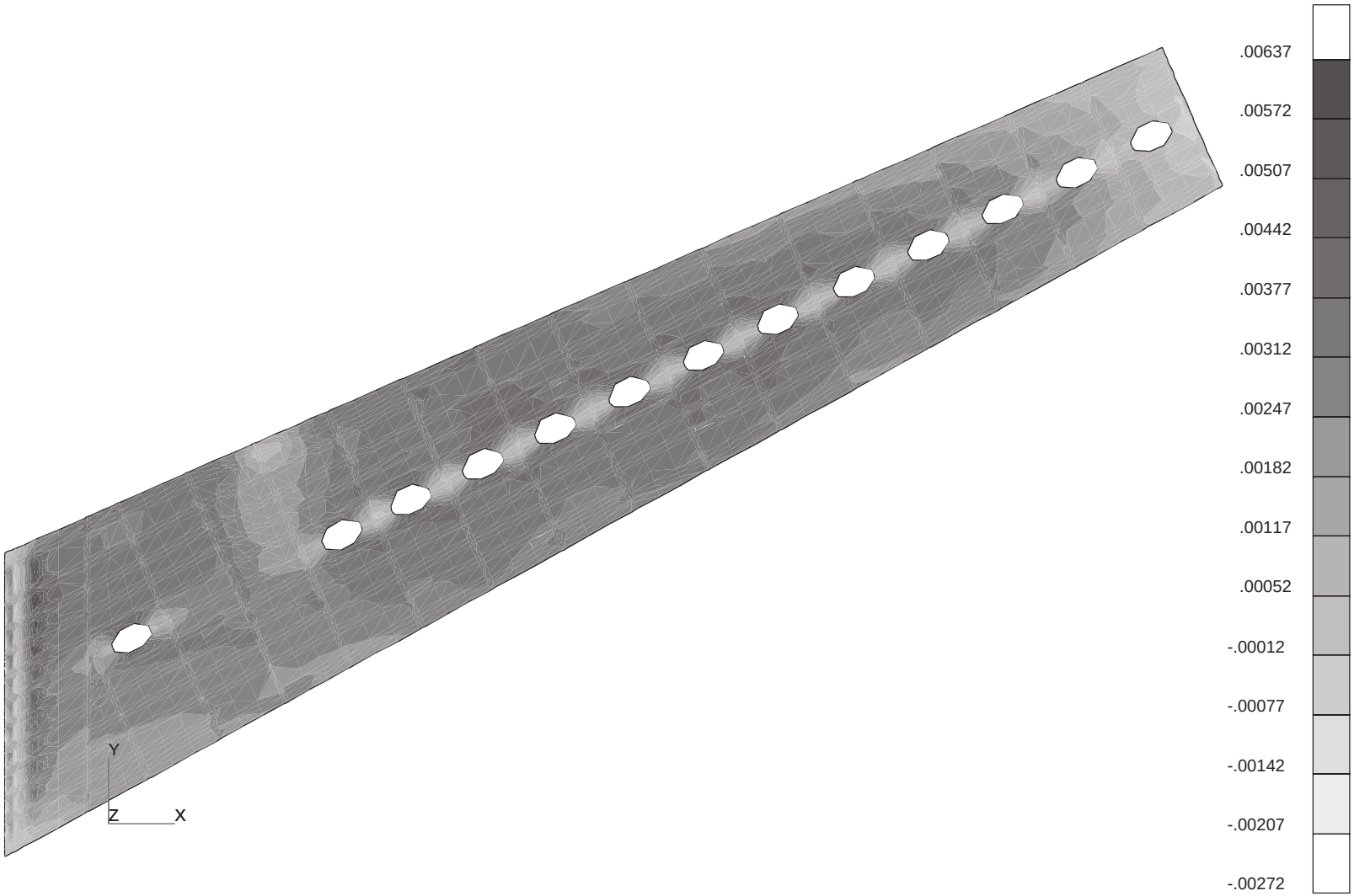

Figure 8.2: Lower Cover Top Surface Spanwise Strain for 2.5G Up-Bending, LF=1.0 of DUL.

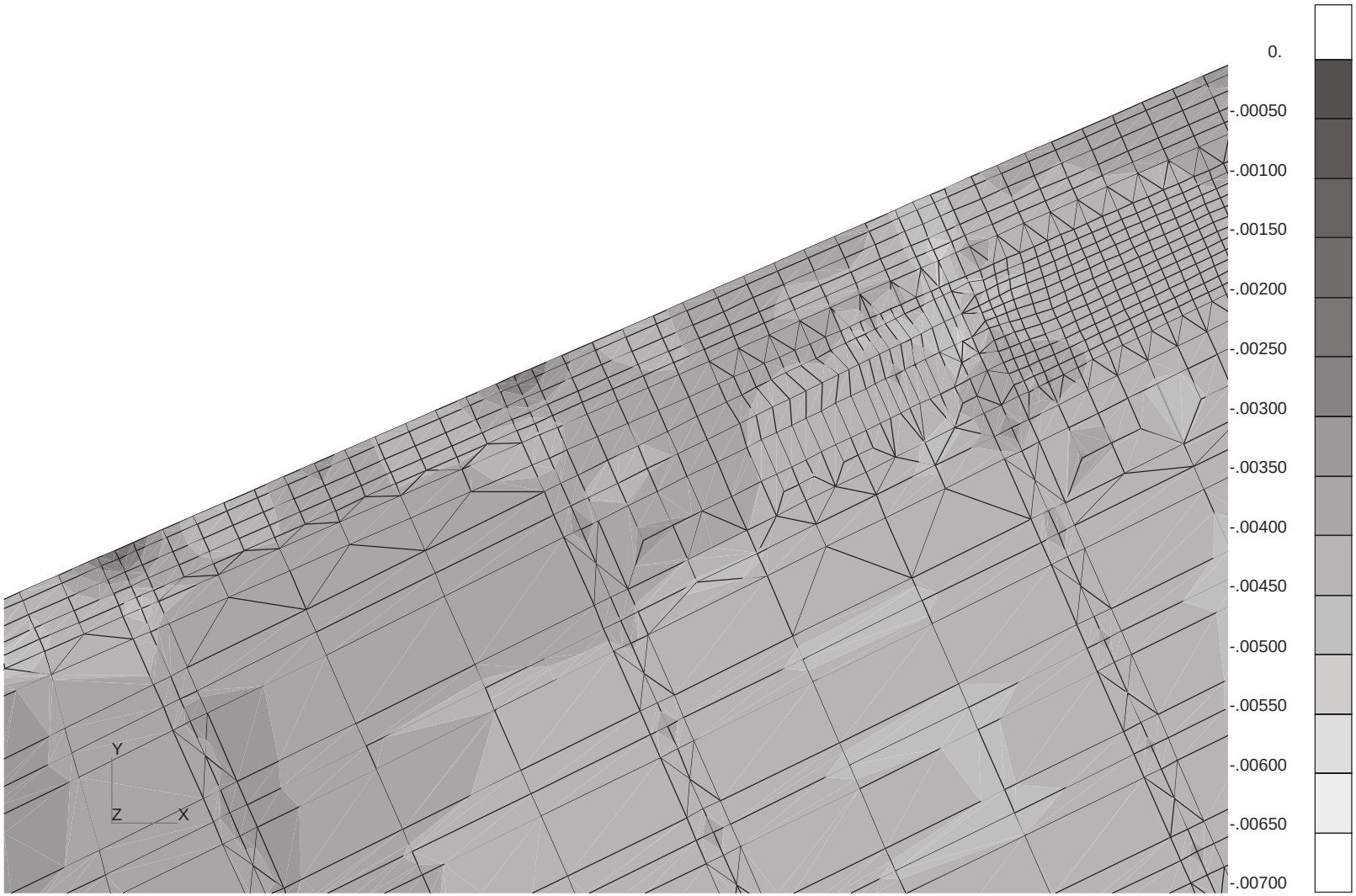

Figure 8.3: Upper Cover Top Surface Spanwise Strain Near the Stringer #10 Runout for 2.5G Up-Bending, LF=1.0 of DUL.

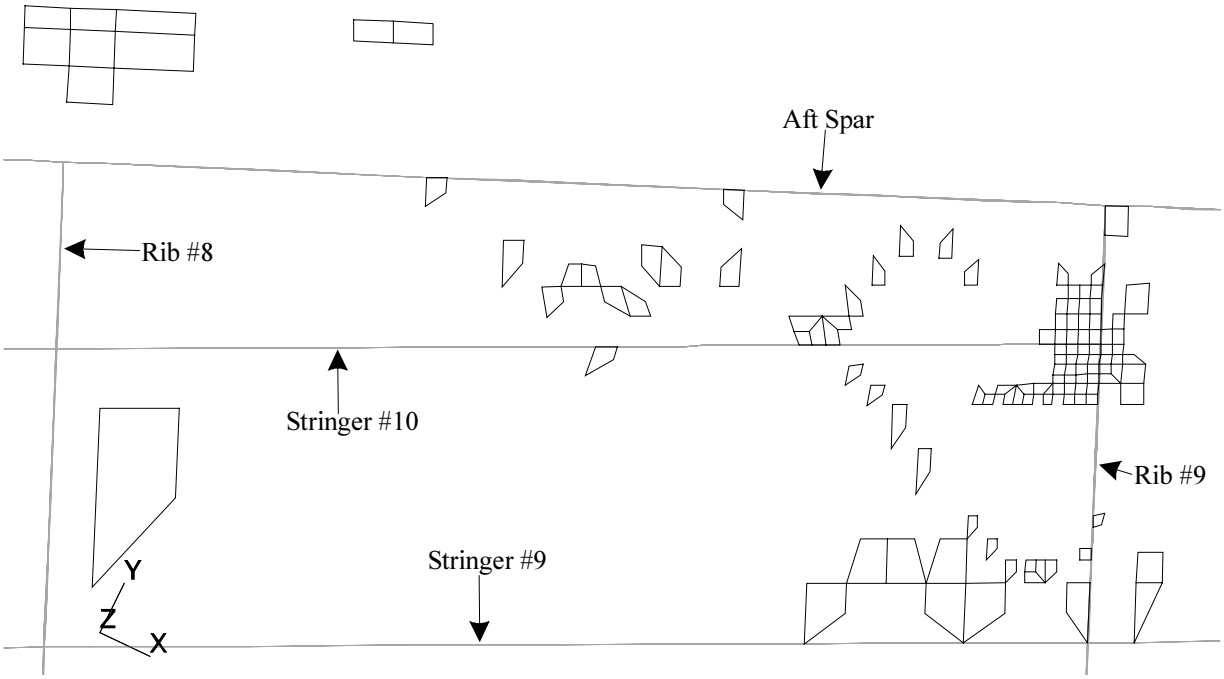

Figure 8.4: Upper Cover Elements In the Vicinity of the Stringer #10 Runout Exhibiting Greater Than 20% Bending.

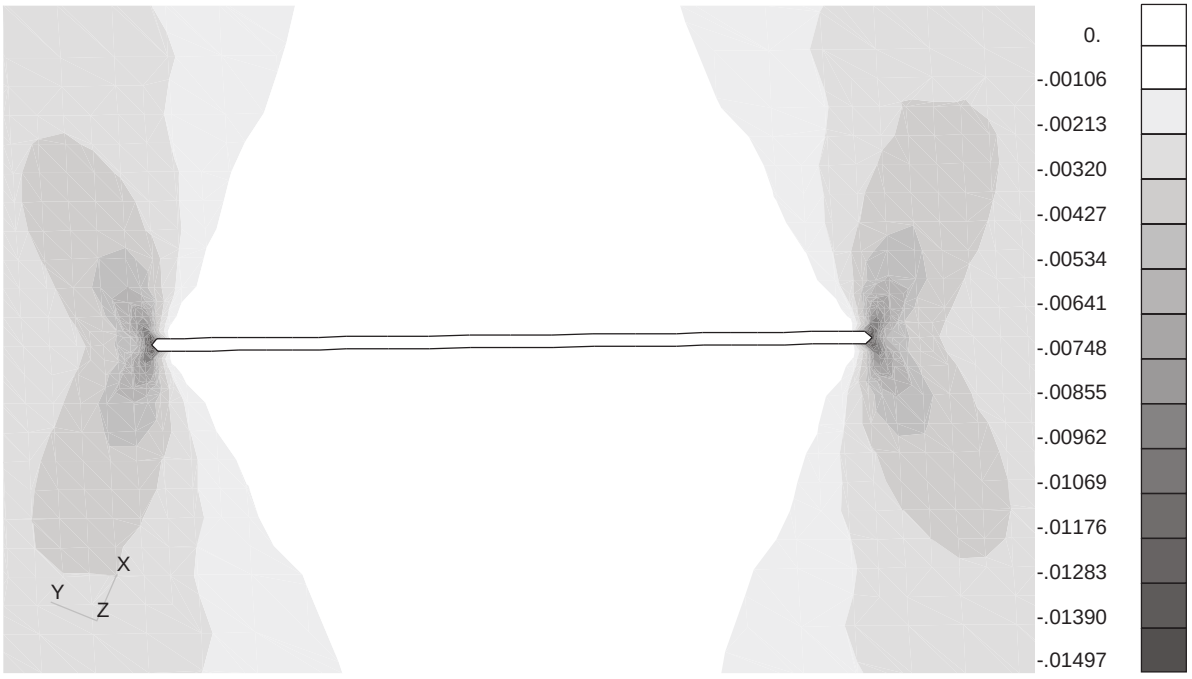

Figure 8.5: Upper Cover Top Surface Strains, ε_{xx}, Near Sawcut for the Upper Cover Sawcut Discrete Damage Model Under 2.5G Up-Bending Load, LF=0.475 of DUL.

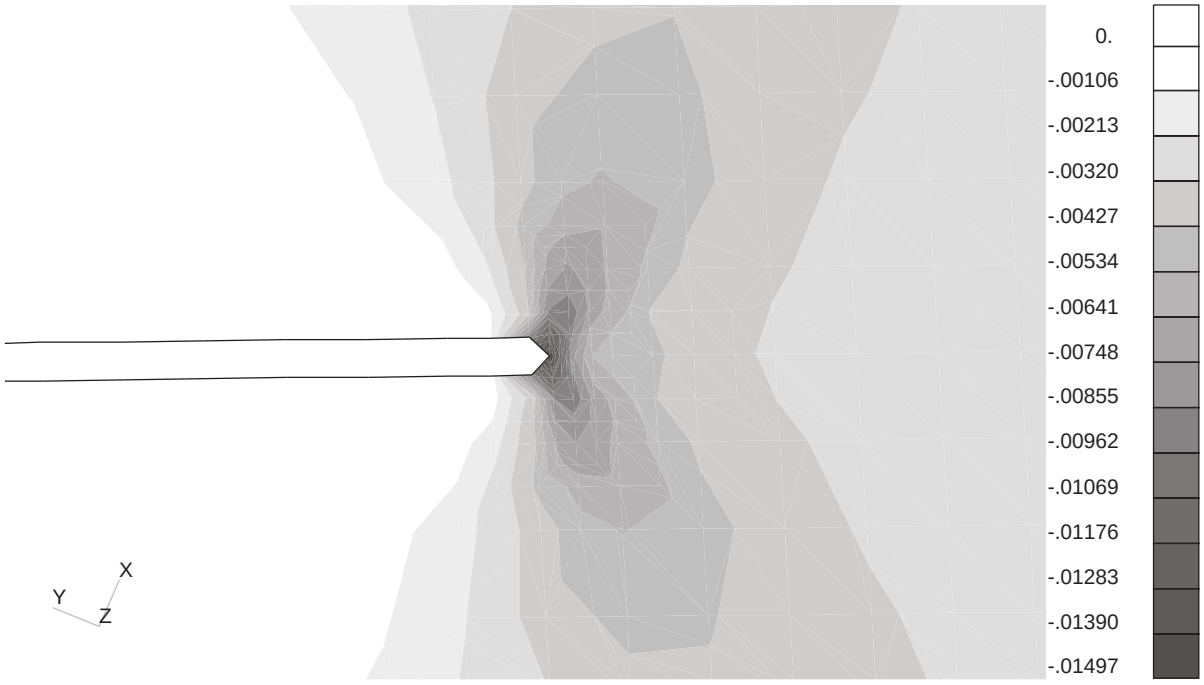

Figure 8.6: Close-Up of Upper Cover Top Surface Strains, ε_{xx}, Near Sawcut for the Upper Cover Sawcut Discrete Damage Model Under 2.5G Up-Bending Load, LF=0.475 of DUL.

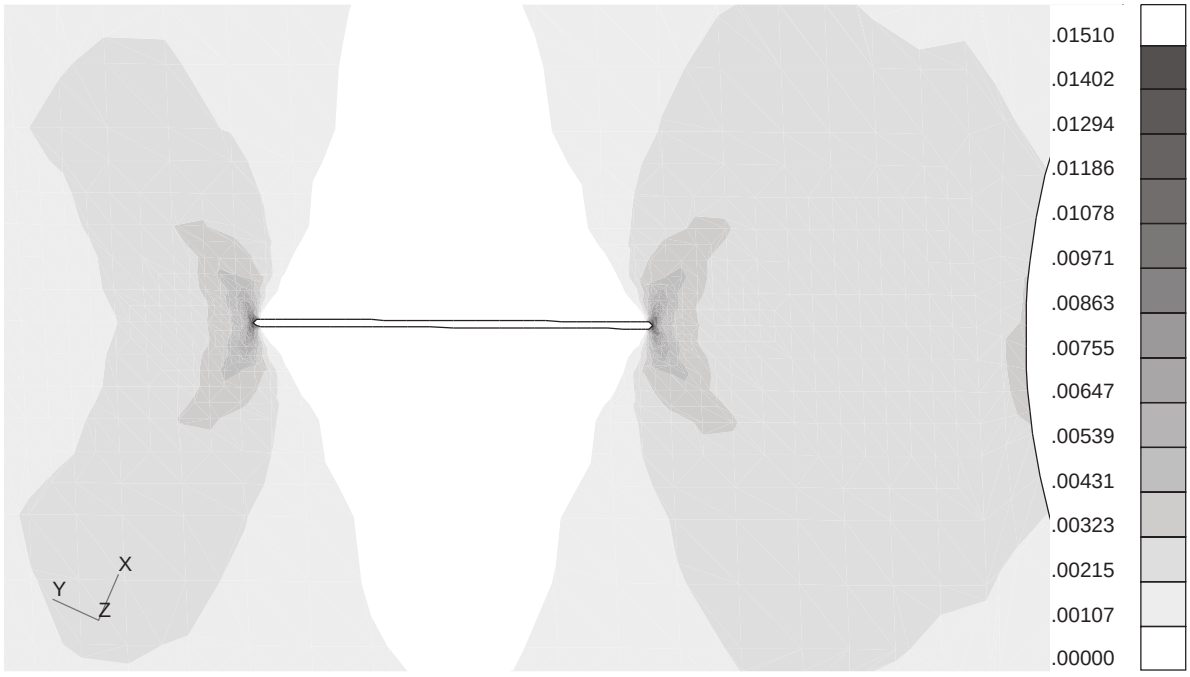

Figure 8.7: Lower Cover Strains Near Sawcut for the Lower Cover Sawcut Discrete Damage Model Under 2.5G Up-Bending Load, LF=0.475 of DUL.

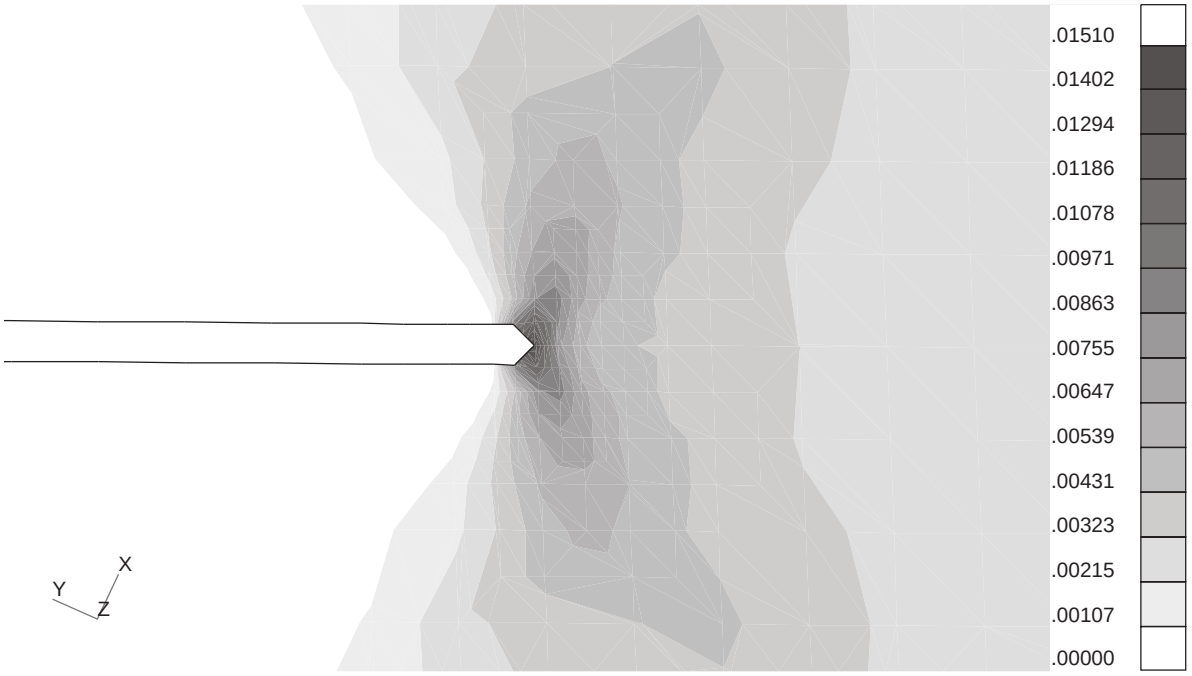

Figure 8.8: Close-Up of Lower Cover Strains Near Sawcut for the Lower Cover Sawcut Discrete Damage Model Under 2.5G Up-Bending Load, LF=0.475 of DUL.

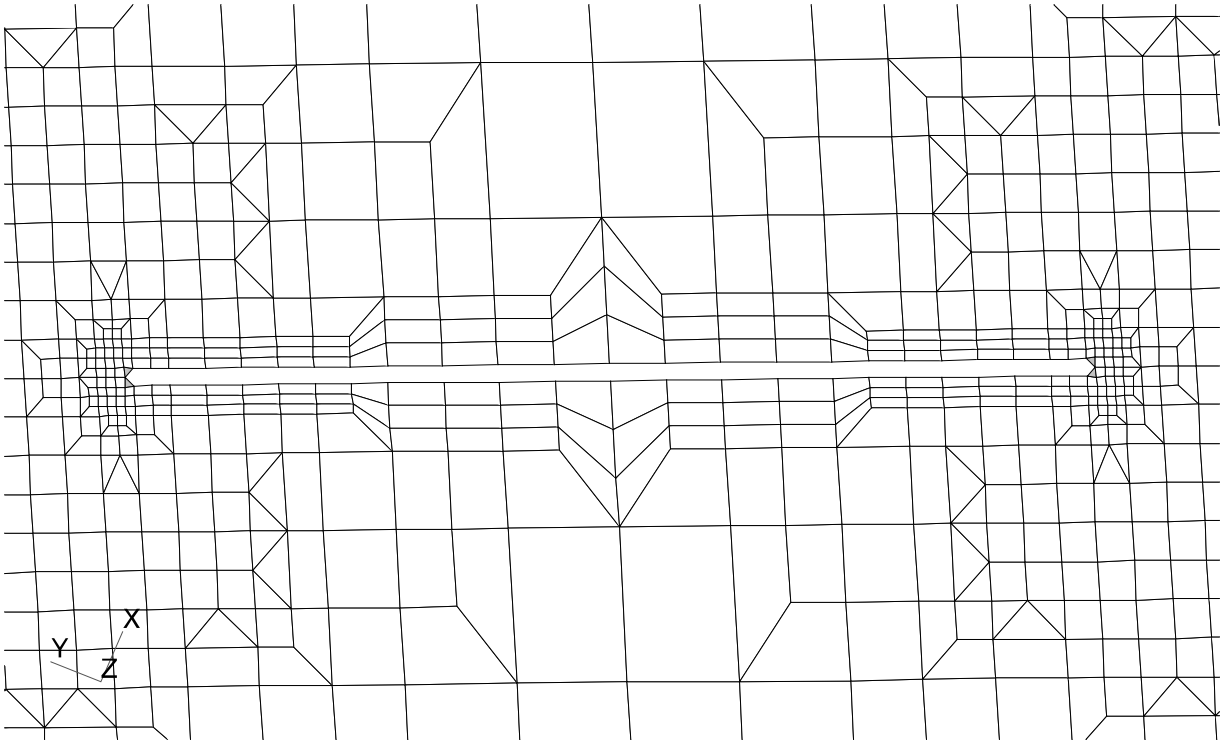

Figure 8.9: Upper Cover Failed Elements (Grey) for the Upper Cover Sawcut Discrete Damage Model Under 2.5G Up-Bending Load, LF=0.25 of DUL.

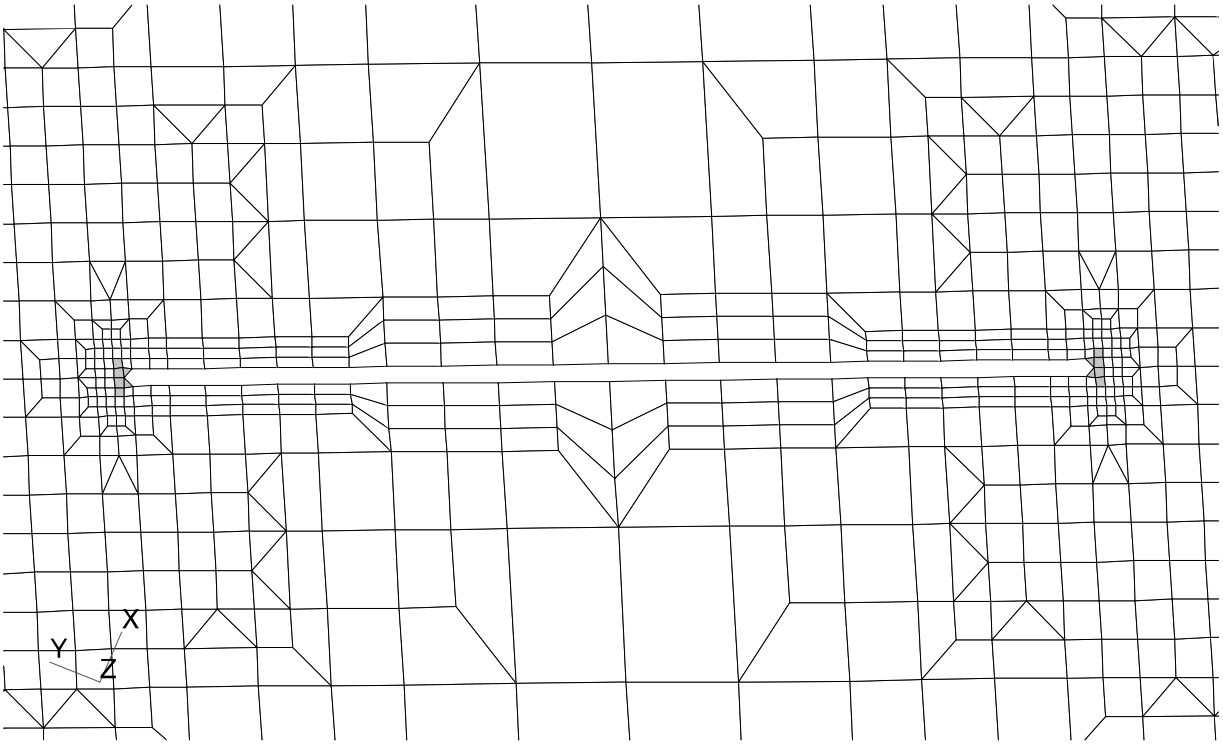

Figure 8.10: Upper Cover Failed Elements (Grey) for the Upper Cover Sawcut Discrete Damage Model Under 2.5G Up-Bending Load, LF=0.35 of DUL.

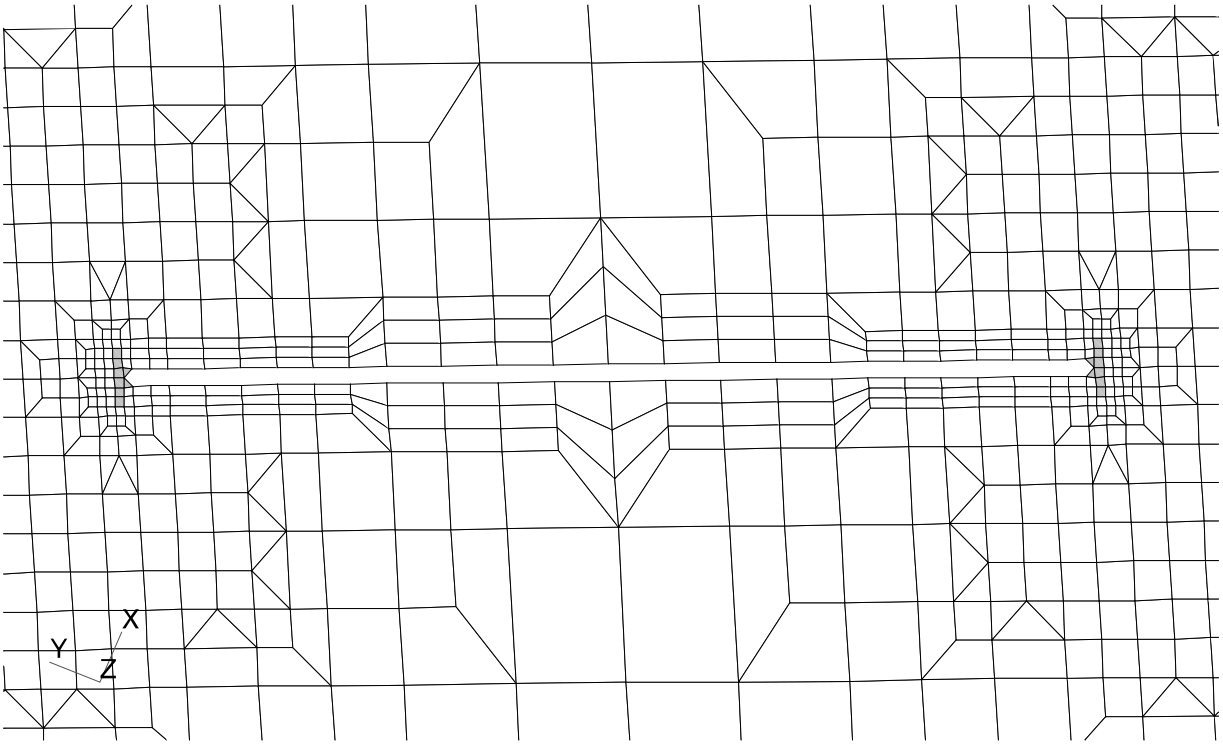

Figure 8.11: Upper Cover Failed Elements (Grey) for the Upper Cover Sawcut Discrete Damage Model Under 2.5G Up-Bending Load, LF=0.45 of DUL.

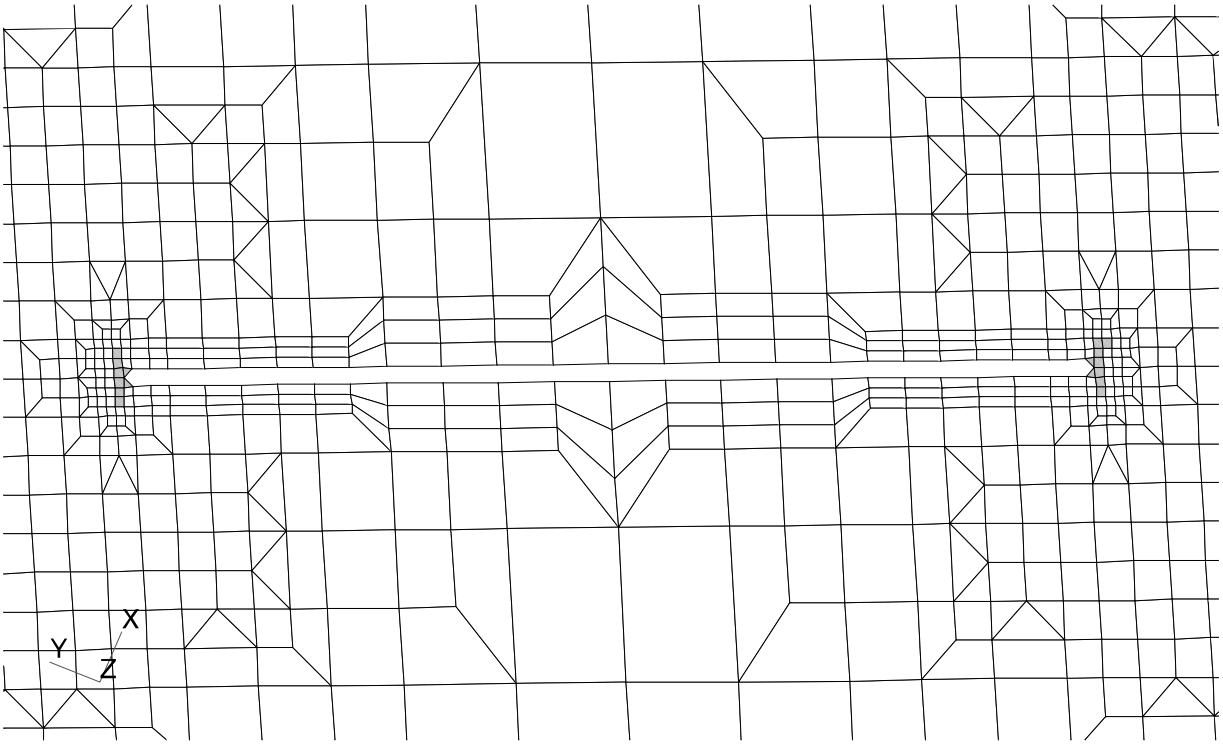

Figure 8.12: Upper Cover Failed Elements (Grey) for the Upper Cover Sawcut Discrete Damage Model Under 2.5G Up-Bending Load, LF=0.475 of DUL.

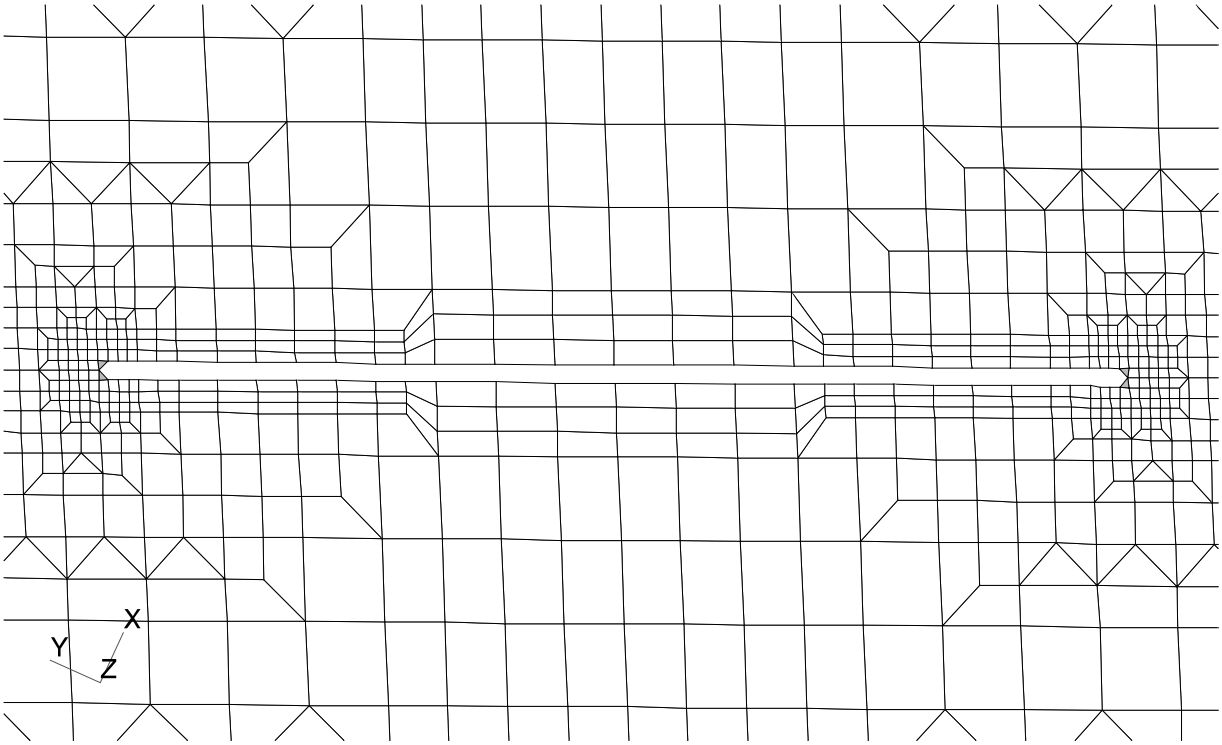

Figure 8.13: Lower Cover Failed Elements (Grey) for the Lower Cover Sawcut Discrete Damage Model Under 2.5G Up-Bending Load, LF=0.3 of DUL.

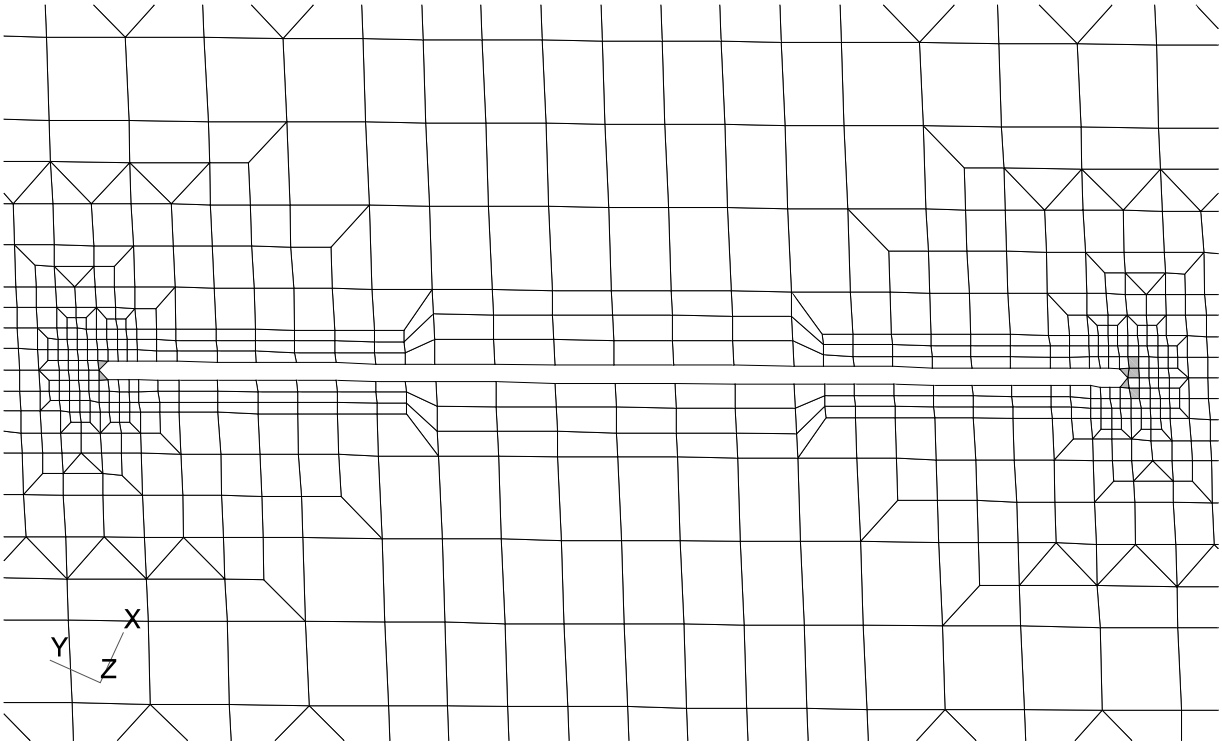

Figure 8.14: Lower Cover Failed Elements (Grey) for the Lower Cover Sawcut Discrete Damage Model Under 2.5G Up-Bending Load, LF=0.425 of DUL.

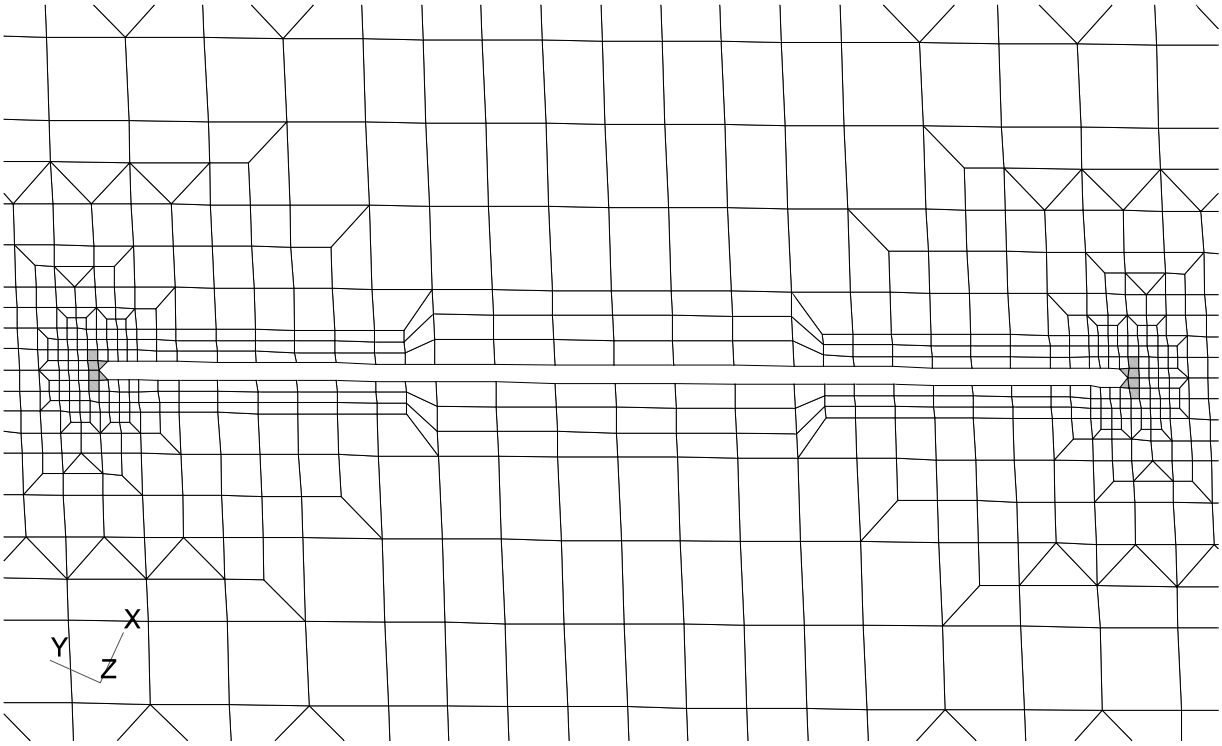

Figure 8.15: Lower Cover Failed Elements (Grey) for the Lower Cover Sawcut Discrete Damage Model Under 2.5G Up-Bending Load, LF=0.45 of DUL.

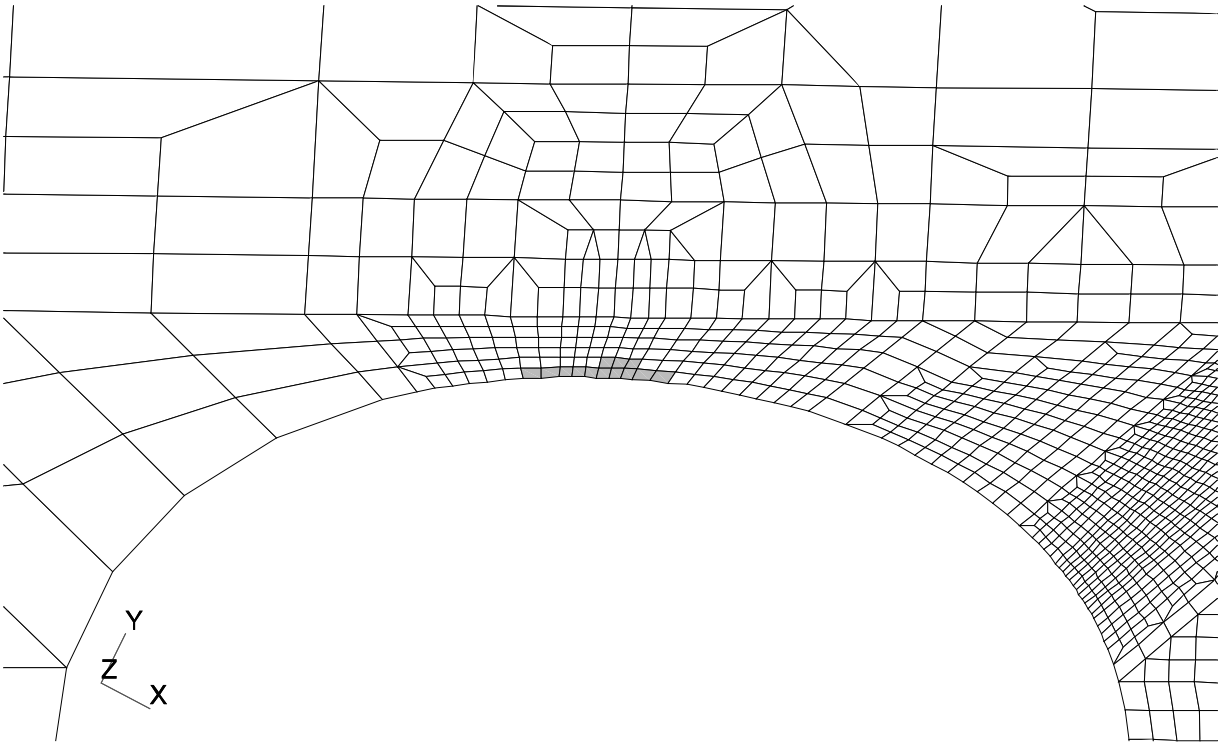

Figure 8.16: Lower Cover Failed Elements (grey) on Aft Edge of Hole Centered Between Ribs 7 and 8 for the Tapered Height Model Under 2.5G Up-Bending Load, LF=0.9 of DUL.

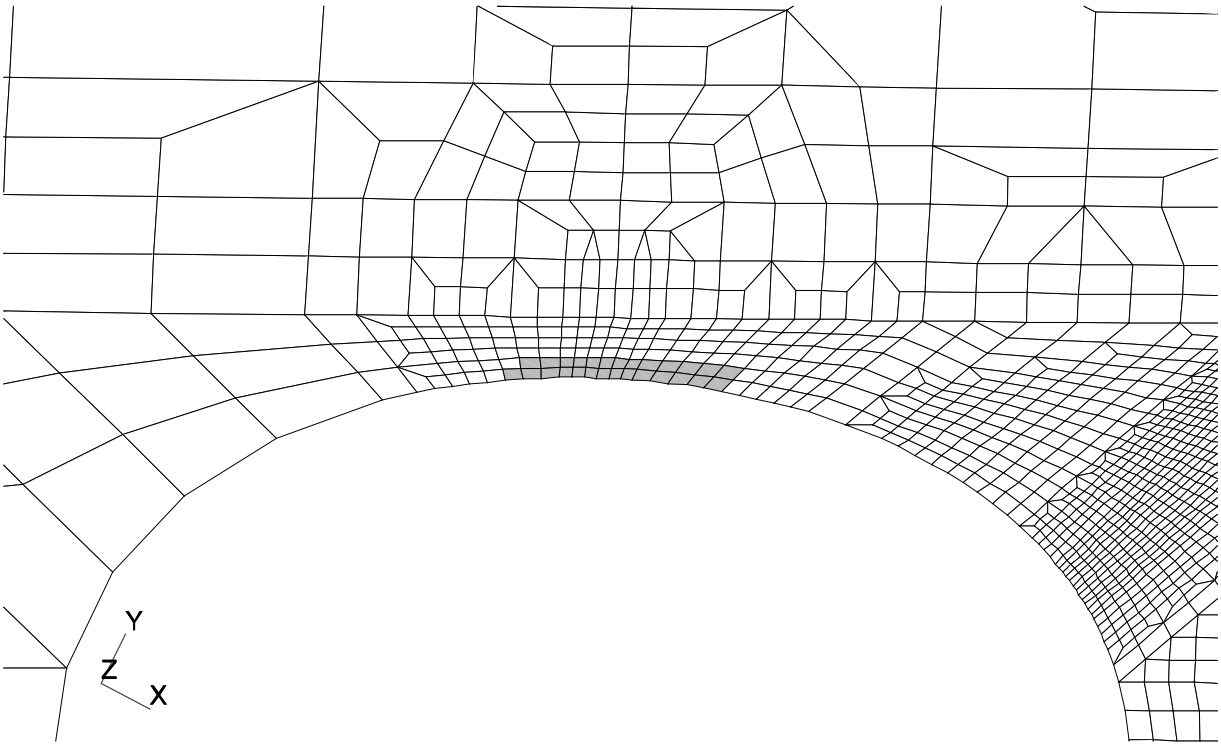

Figure 8.17: Lower Cover Failed Elements (grey) on Aft Edge of Hole Centered Between Ribs 7 and 8 for the Tapered Height Model Under 2.5G Up-Bending Load, LF=0.95 of DUL.

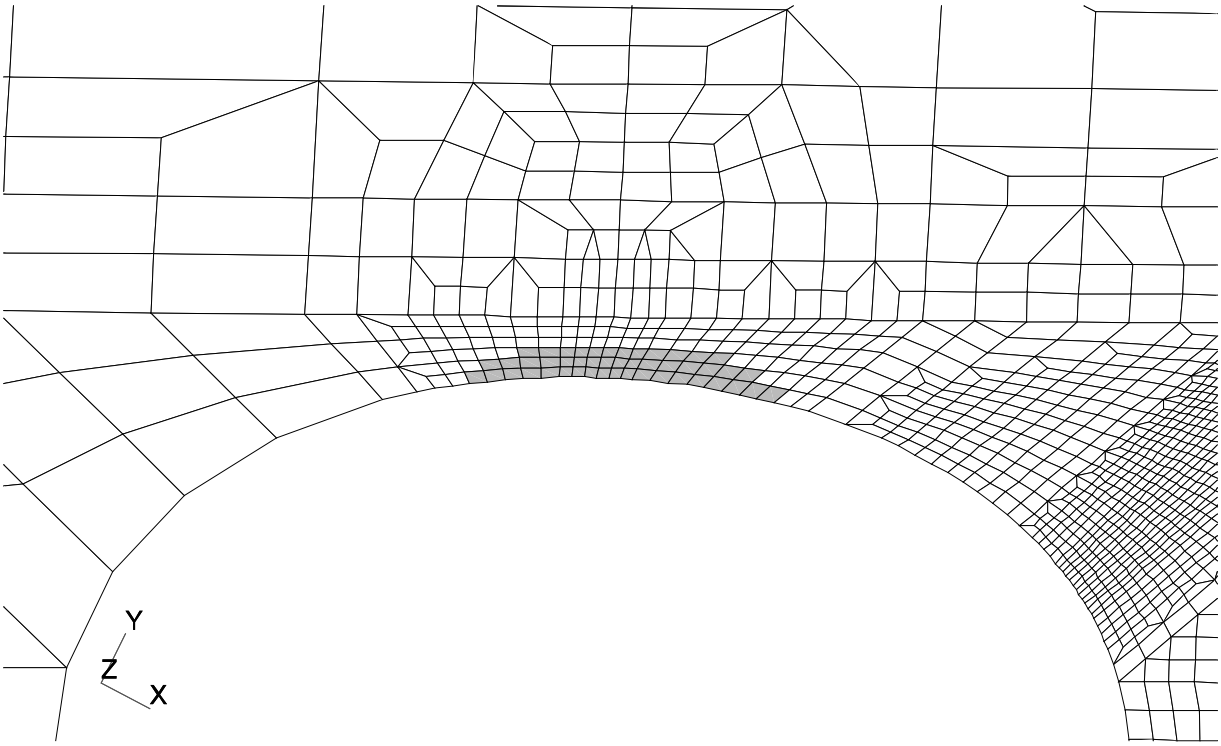

Figure 8.18: Lower Cover Failed Elements (grey) on Aft Edge of Hole Centered Between Ribs 7 and 8 for the Tapered Height Model Under 2.5G Up-Bending Load, LF=1.0 of DUL.

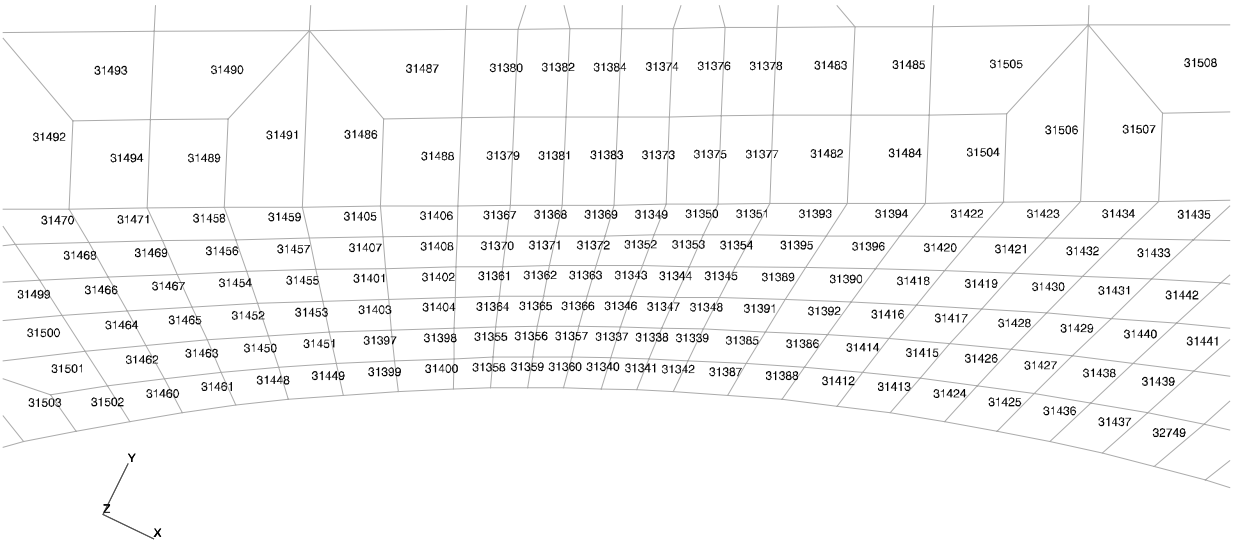

Figure 8.19: Lower Cover Element Numbers for Aft Edge of Hole Centered Between Ribs 7 and 8 for the Tapered Height Model.

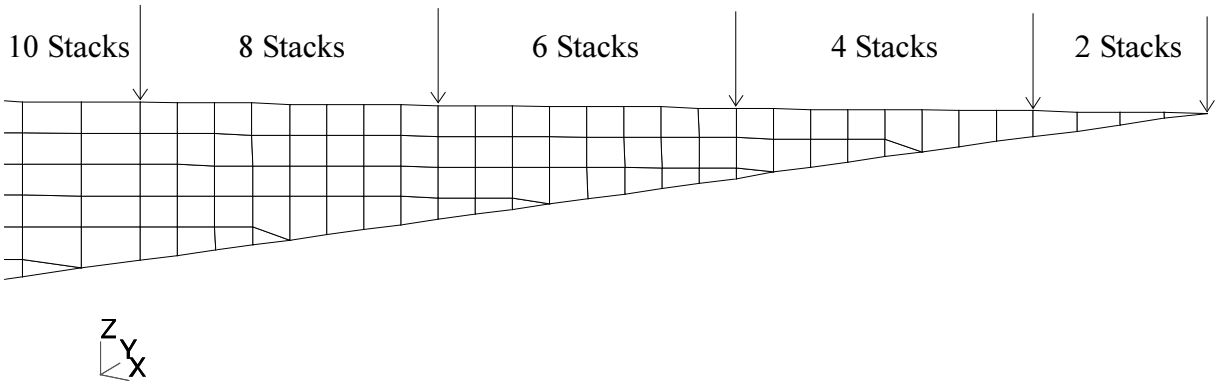

Figure 8.20: Stringer #10 Blade Stack Thickness Change Locations for the Tapered Height Mode.

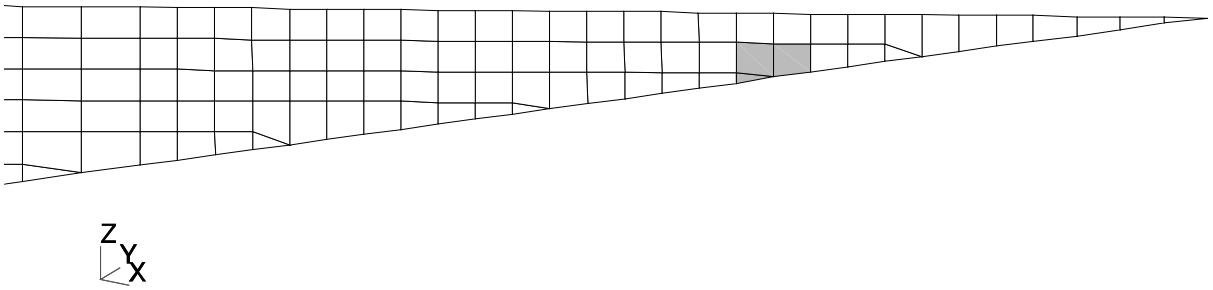

Figure 8.21: Failed Elements (grey) on Stringer #10 Blade Near the Runout for the Tapered Height Model Under 2.5G Up-Bending Load, LF=0.8 of DUL.

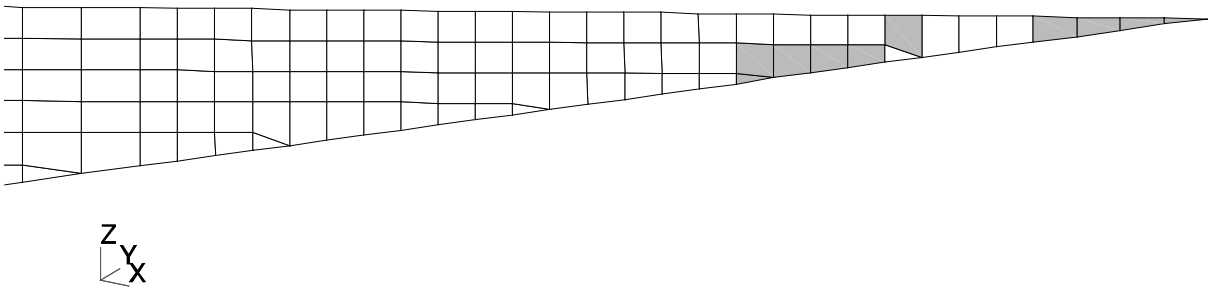

Figure 8.22: Failed Elements (grey) on Stringer #10 Blade Near the Runout for the Tapered Height Model Under 2.5G Up-Bending Load, LF=0.9 of DUL.

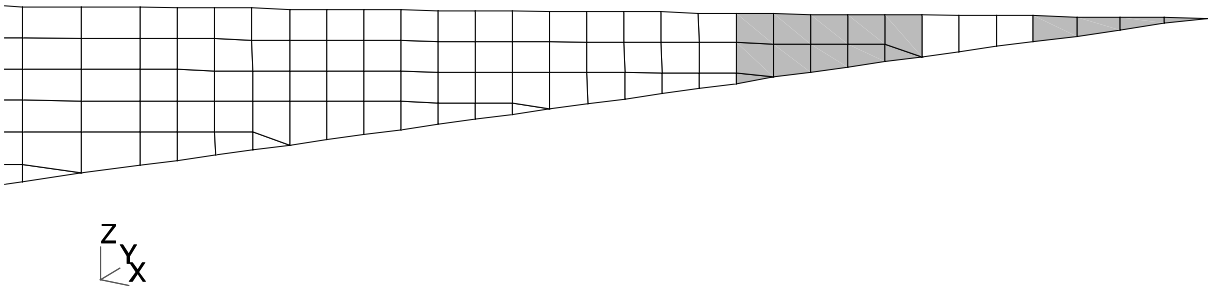

Figure 8.23: Failed Elements (grey) on Stringer #10 Blade Near the Runout for the Tapered Height Model Under 2.5G Up-Bending Load, LF=0.95 of DUL.

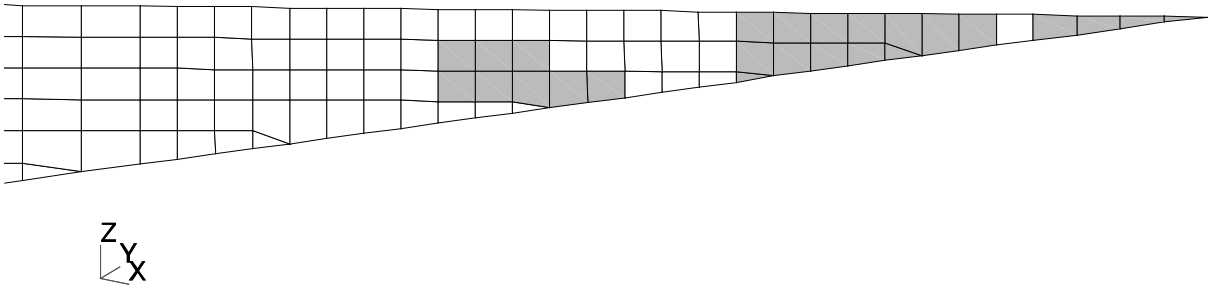

Figure 8.24: Failed Elements (grey) on Stringer #10 Blade Near the Runout for the Tapered Height Model Under 2.5G Up-Bending Load, LF=1.0 of DUL.

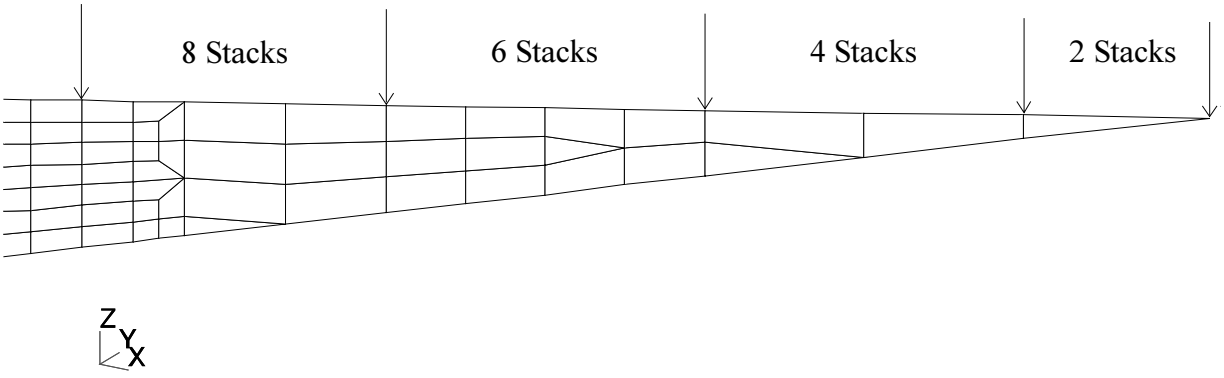

Figure 8.25: Stringer #2 Blade Stack Thickness Change Locations for the Tapered Height Mode.

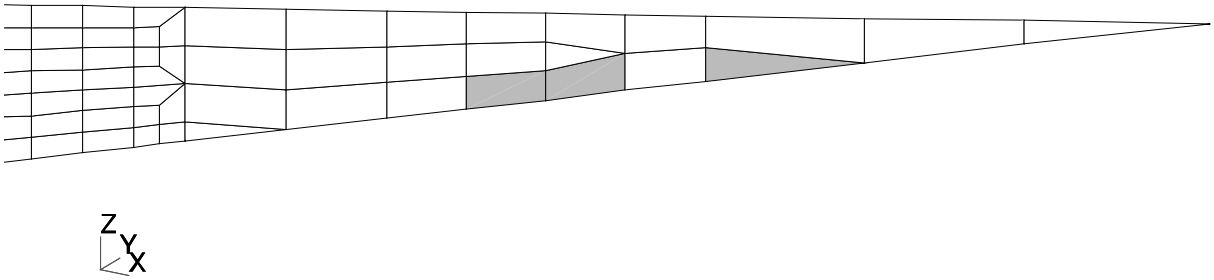

Figure 8.26: Failed Elements (grey) on Stringer #2 Blade Near the Runout for the Tapered Height Model Under 2.5G Up-Bending Load, LF=0.8 of DUL.

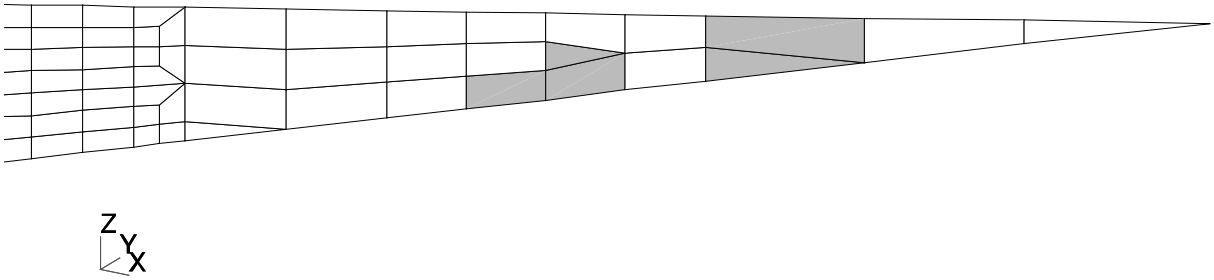

Figure 8.27: Failed Elements (grey) on Stringer #2 Blade Near the Runout for the Tapered Height Model Under 2.5G Up-Bending Load, LF=0.9 of DUL.

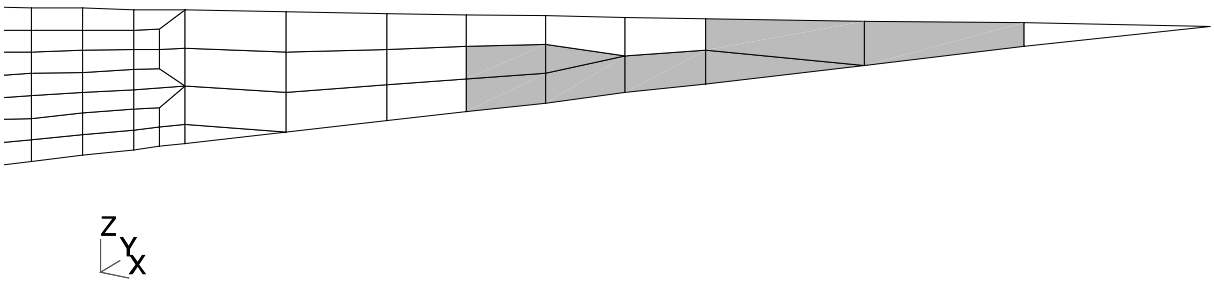

Figure 8.28: Failed Elements (grey) on Stringer #2 Blade Near the Runout for the Tapered Height Model Under 2.5G Up-Bending Load, LF=0.95 of DUL.

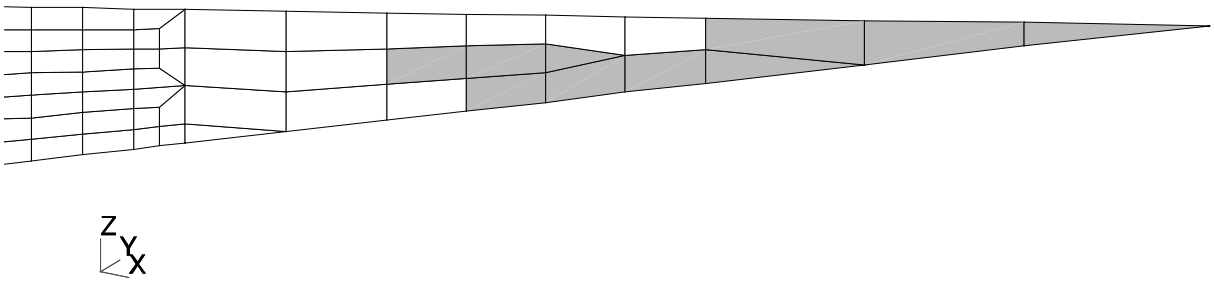

Figure 8.29: Failed Elements (grey) on Stringer #2 Blade Near the Runout for the Tapered Height Model Under 2.5G Up-Bending Load, LF=1.0 of DUL.

9. Semi-Span Strain Gage Prediction

The Government provided locations for the strain gages that will be included in the testing of the composite semi-span. At the request of the technical monitor, only those strain gages located on the upper and lower covers and their attached stringers, and indicated in Tables 9.1 and 9.2 were studied by AS&M. Strain gage predictions were made either by extracting element centroidal strain values from the STAGS output or by being calculated from the nodal displacements. For both of these methods, extrapolation of values was generally required. Due to the extremely large number of data points, the strain gage predictions were generated by a FORTRAN code that was written in order to automate and expedite the procedure. To ensure convergence of the strain gage predicted results, a convergence study was carried out using the undamaged detailed model as the starting point.

9.1 Convergence Study

The convergence study was initiated using the undamaged detailed model as the basis. Convergence was studied at a load factor of 1.1 DUL using the 2.5G up-bending load case results. Due to the lack of lower cover fidelity in the detailed model, gages 114 and 118 were omitted from the basis calculations. Areas with strain gages present were then refined and the strain gage values recalculated. When reasonable strain gage value convergence was observed for a particular convergence study step, further refinement was not carried out in the vicinity of that strain gage in subsequent steps. Reasonable convergence was defined as strain gage predicted value changes on the order of 2% or less between successively refined models. This process was carried out several times until the desired level of convergence was obtained. It is interesting to note that on several occasions, meshes which were "more refined" than the previous mesh demonstrated adverse convergence qualities. This behavior was linked to the presence of triangular elements, which were required for mesh transition, being to close to the strain gage location. Therefore, it is demonstrated that the introduction of triangular elements in a primarily quadrilateral mesh near the region of interest for strain predictions is contraindicated. Figure 9.1 shows the original mesh and Figure 9.2 shows the final mesh in the region of strain gages 10 and 11.

9.2 Results

9.2.2 Strain Gage Model

Results for all three load cases were obtained for the undamaged strain gage model. For the strain gage model with the upper cover sawcut discrete damage, only load case 2 was studied. No strain gage predictions were made for the semi-span with the lower cover sawcut discrete damage.

9.2.2.1 Undamaged

After selection of a mesh which provided satisfactory convergence behavior, strain gage predictions for the three load cases were made for the undamaged wing. Tables 9.4-9.6 provide the strain gage predicted values, in microstrain, at their associated load step values for the three load cases. Load step values for load cases 1 and 2 are given for actuator #2, while for load case 3 the load step values are given for actuator #7a. The load step value is equal to the load factor times the actuator DUL value at that particular nonlinear load step.

Plots of strain gage value as a function of load step value show that most strain gages demonstrated linear behavior for all three load cases. Although several gages exhibited nonlinear behavior for load case 3, these gages were located in regions of very low strain, and therefore of little interest. Plots of strain versus load for strain gages that exhibited interesting behavior are shown in Figures 9.3-9.17, and the associated strain gage numbers are tabulated in Table 9.7 for reference.

9.2.2.2 With Discrete Damage

9.2.2.2.1 Upper Cover Sawcut

The strain gage model with an upper cover sawcut was studied and the effect of the upper cover sawcut presence on the strain gage values determined. However, the strain gage locations studied were limited to those whose results are given in Table 9.8, i.e., only those strain gages whose response would expect to be affected by the introduction of the crack. Also, only load case 2 was investigated for this damaged model. Additionally, although the test for this damaged case will not progress to as high a load level as that for the undamaged semi-span, results are again presented up to 1.1DUL (recall that the test is only expected to progress to about 0.47 DUL). As seen by the response of strain gage 332, which is shown in Figure 9.18, even at these high load levels the response of the strain gages near the crack remains linear (gage 332 is 0.5 inches from the crack tip). Strain gages exhibiting nonlinear behavior for this case are the same as for the undamaged wing given in Table 9.7 with the exclusion of gages 254, 255, 319, and 323. Plots for the nonlinear strain gage response of the upper cover discrete damaged strain gage model under load case 2 loading are given in Figures 9.19-9.24.

Finally, some remarks about the discretization near the crack tip and its effect on the response of the strain gage predicted values is warranted. The mesh at the upper cover aft crack tip shown in Figure 9.25 was used in the strain gage predictions. Far field outer surface strains, ε_{xx}, which are found with this discretization are shown in Figure 9.26, with a close-up of the crack tip shown in Figure 9.27. A refinement of the mesh near the crack tip was carried out, providing the discretization shown in Figure 9.28. Far field outer surface strains, ε_{xx}, which are found with this highly refined discretization are shown in Figure 9.29, with a close-up of the crack tip shown in Figure 9.30. The contour scale for these two figures is the same as that in Figures 9.26 and 9.27, respectively, which has the maximum compressive strain predicted by the mesh in Figure 9.25 as the lower limit. Note, however, that the strains in the region of the strain gage, at a distance of approximately 2.5 times the crack width from the crack tip, are approximately the same. In fact, the predicted values for gages 331 and 332 are within an acceptable value of 2% for the two meshes. However, as seen in Figure 9.41, which uses the maximum compressive strain predicted by the discretization of Figure 9.28 as the lower contour limit, the crack tip strain has increased approximately two and a half times from the coarse mesh to the refined mesh (from 2989με to 7512με). Since it is the strain gage predicted value that is of importance, and not an accurate prediction of the crack tip strain, the coarse mesh provides sufficient results. Therefore, using one element edge length to span the region of high strain gradient, then introducing only a few more elements up to the strain gage location is a reasonable meshing practice for determining strain gage predictions. That is, the "pointed" crack tip of Figure 9.25 does not adversely affect the predicted strain gage results when compared to the "round" crack tip, provided that the strain gage is sufficiently "far" from the crack tip and a reasonable mesh is used. Lastly, the refined mesh in Figure 9.28 increases model size by approximately 7-8% over the model with the mesh shown in Figure 9.25, which is an unnecessary and undesired result.

9.3 Tables

Table 9.1: Lower Cover Strain Gage Numbers and Locations Investigated by AS&M for the Composite Semi-Span.

Gage #	Location	Orientation
10	stringer 4, mid. ribs 12-13, 0.15 in. from blade edge, aft surface	spanwise
11	stringer 4, mid. ribs 12-13, exterior skin surface	spanwise
35	mid. ribs 8-9, skin 1.4 in. fore from stringer 4, exterior surface	spanwise
36	mid. ribs 8-9, flange 1.4 in. fore from stringer 4, interior surface	spanwise
37	mid. ribs 8-9, skin 4. in. aft from stringer 3, exterior surface	spanwise
38	mid. ribs 8-9, skin 4. in. aft from stringer 3, interior surface	spanwise
39	mid. ribs 8-9, skin 4. in. fore from stringer 3, exterior surface	spanwise
40	mid. ribs 8-9, skin 4. in. fore from stringer 3, interior surface	spanwise
41	mid. ribs 8-9, skin 1.4 in. aft from stringer 2, exterior surface	spanwise
42	mid. ribs 8-9, flange 1.4 in. aft from stringer 2, interior surface	spanwise
82	skin between ribs 4-5, 2 in. from rib 4, stringer 10 fore flange edge, exterior surface	spanwise
83	skin between ribs 4-5, 2 in. from rib 4, 3.4 in. fore from stringer 10 blade, exterior surface	spanwise
84	skin between ribs 4-5, 2 in. from rib 4, 4.2 in. fore from stringer 10 blade, exterior surface	spanwise
85	skin between ribs 4-5, 2 in. from rib 4, stringer 10 fore flange edge, interior surface	spanwise
86	skin between ribs 4-5, 2 in. from rib 4, 3.4 in. fore from stringer 10 blade, interior surface	spanwise
87	skin between ribs 4-5, 2 in. from rib 4, 4.2 in. fore from stringer 10 blade, interior surface	spanwise
114	skin mid. ribs 7-8, aft hole edge, centered on thickness	parallel to edge
118	skin mid. ribs 7-8, aft hole, 6.71 in. outboard from center, center on thickness	parallel to edge

Table 9.2: Upper Cover Strain Gage Numbers and Locations Investigated by AS&M for the Composite Semi-Span.

Gage #	Location	Orientation
208	skin between ribs 13-14, 2 in. from rib 13, stringer 3 aft flange edge, exterior surface	spanwise
209	skin between ribs 13-14, 2 in. from rib 13, 3.4 in. aft from stringer 3 blade, exterior surface	spanwise
210	skin between ribs 13-14, 2 in. from rib 13, 4.2 in. aft from stringer 3 blade, exterior surface	spanwise
211	skin between ribs 13-14, 2 in. from rib 13, stringer 3 aft flange edge, interior surface	spanwise
212	skin between ribs 13-14, 2 in. from rib 13, 3.4 in. aft from stringer 3 blade, interior surface	spanwise
213	skin between ribs 13-14, 2 in. from rib 13, 4.2 in. aft from stringer 3 blade, interior surface	spanwise
224	stringer 6, mid. ribs 10-11, 0.15 in. from blade edge, fore surface	spanwise
225	stringer 6, mid. ribs 10-11, exterior skin surface	spanwise
231	stringer 6, mid. ribs 8-9, 0.15 in. from blade edge, fore surface	spanwise
232	stringer 6, mid. ribs 8-9, exterior skin surface	spanwise
237	stringer 4, mid. ribs 8-9, 0.15 in. from blade edge, fore surface	spanwise
238	stringer 4, mid. ribs 8-9, exterior skin surface	spanwise
251	skin between ribs 5-6, center on bay, 6.8 in. from rib 5, exterior surface	spanwise
252	skin between ribs 5-6, center on bay, 6.8 in. from rib 5, interior surface	spanwise
254	skin between ribs 4-5, center on bay, 6.8 in. from rib 4, exterior surface	spanwise
255	skin between ribs 4-5, center on bay, 6.8 in. from rib 4, interior surface	spanwise
300	stringer 8, mid. ribs 8-9, 0.15 in. from blade edge, fore surface	spanwise
301	stringer 8, mid. ribs 8-9, exterior skin surface	spanwise
304	aft spar, mid. ribs 8-9, exterior skin surface	spanwise
305	stringer 10 runout, 10.5 in. from rib 9, 1.0 in. from blade edge, fore surface	spanwise
306	stringer 10 runout, 4.5 in. from rib 9, 1.0 in. from blade edge, fore surface	spanwise
307	stringer 10 runout, 1.4 in. from rib 9, 2.0 in. fore from blade center, exterior skin surface	spanwise
308	stringer 10 runout, 1.4 in. from rib 9, 2.0 in. fore from blade center, interior skin surface	spanwise
309	stringer 10 runout, 1.4 in. from rib 9, 4.0 in. fore from blade center, exterior skin surface	spanwise
310	stringer 10 runout, 1.4 in. from rib 9, blade center, exterior skin surface	spanwise
311	stringer 10 runout, 4.5 in. from rib 9, blade center, exterior skin surface	spanwise
312	stringer 10 runout, 10.5 in. from rib 9, blade center, exterior skin surface	spanwise
317	skin between ribs 9-10, center on bay, 6.8 in. from rib 9, exterior surface	spanwise
318	skin between ribs 9-10, center on bay, 6.8 in. from rib 9, interior surface	spanwise
319	stringer 7, mid. ribs 10-11, 0.15 in. from blade edge, fore surface	spanwise
320	stringer 7, mid. ribs 10-11, exterior skin surface	spanwise
323	stringer 9, mid. ribs 10-11, 0.15 in. from blade edge, fore surface	spanwise
324	stringer 9, mid. ribs 10-11, exterior skin surface	spanwise
327	mid. ribs 10-11, 1.4 in. aft stringer 7, flange interior surface	spanwise
328	mid. ribs 10-11, 1.4 in. aft stringer 7, skin exterior surface	spanwise
329	mid. ribs 10-11, 4 in. fore stringer 8, skin exterior surface	spanwise
330	mid. ribs 10-11, 4 in. fore stringer 8, skin interior surface	spanwise
331	mid. ribs 10-11, 4 in. aft stringer 8, skin exterior surface	spanwise
332	mid. ribs 10-11, 4 in. aft stringer 8, skin interior surface	spanwise
333	mid. ribs 10-11, 1.4 in. fore stringer 9, flange interior surface	spanwise
334	mid. ribs 10-11, 1.4 in. fore stringer 9, skin exterior surface	spanwise

Table 9.3: Strain Gage Convergence Study with Error Calculations.

Strain	Strain				Percent Error		
Gage #	DM*	DGM*	DG2M*	DG3M*	DM*/DGM*	DGM*/DG2M*	DG2M*/DG3M*
10	2556	2657	2688	2693	3.806	1.152	0.185
11	3965	3480	3999	3997	-13.925	12.974	-0.046
35	3776	3909	3810	3823	3.395	-2.609	0.340
36	3423	3449	3401	3408	0.737	-1.390	0.210
37	3737	3865	3742	3754	3.295	-3.267	0.324
38	3573	3592	3574	3582	0.552	-0.518	0.227
39	3514	3605	3541	3549	2.517	-1.798	0.211
40	3387	3383	3396	3402	-0.108	0.383	0.171
41	3464	3534	3503	3507	1.976	-0.893	0.130
42	3197	3172	3152	3154	-0.767	-0.664	0.071
82	4156	3849	3828	3828	-7.965	-0.568	0.012
83	4121	3870	3918	3916	-6.490	1.234	-0.050
84	4105	3862	3942	3943	-6.303	2.043	0.019
85	3994	3854	3870	3870	-3.636	0.417	0.012
86	3959	3864	3920	3918	-2.452	1.419	-0.049
87	3943	3828	3894	3895	-3.018	1.704	0.020
114	6933	8034	8208	8432	13.705	2.119	2.660
118	4766	4269	4395	4352	-11.643	2.874	-0.982
208	-4441	-4126	-4171	-4171	-7.634	1.080	-0.007
209	-4423	-4134	-4226	-4226	-6.998	2.179	-0.003
210	-4414	-4182	-4268	-4272	-5.543	1.997	0.113
211	-4134	-4227	-4234	-4234	2.185	0.171	0.002
212	-4116	-4242	-4295	-4296	2.963	1.252	0.003
213	-4107	-4249	-4282	-4287	3.330	0.770	0.117
224	-2655	-2440	-2528	-2501	-8.787	3.452	-1.050
225	-4932	-4927	-4952	-4819	-0.108	0.505	-2.753
231	-2433	-2084	-2098	-2118	-16.767	0.676	0.981
232	-5171	-5298	-5303	-5302	2.386	0.107	-0.032
237	-2353	-2111	-2123	-2124	-11.498	0.557	0.093
238	-4957	-5038	-5045	-5044	1.601	0.147	-0.033
251	-3667	-3793	-3730	-3728	3.314	-1.691	-0.056
252	-3566	-3723	-3762	-3759	4.211	1.028	-0.072
254	-3642	-3707	-3780	-3779	1.752	1.928	-0.023
255	-3475	-3496	-3573	-3572	0.607	2.165	-0.037
300	-2472	-2286	-2311	-2306	-8.128	1.082	-0.197
301	-5174	-5198	-5197	-5198	0.463	-0.014	0.010
304	-4310	-4369	-4381	-4385	1.365	0.276	0.093
305	-2169	-2168	-2155	-2149	-0.056	-0.583	-0.320
306	-2277	-2264	-2237	-2237	-0.573	-1.195	-0.018
307	-5033	-5066	-5094	-5099	0.646	0.554	0.103
308	-4354	-4394	-4235	-4220	0.925	-3.756	-0.354
309	-5471	-5516	-5535	-4797	0.822	0.334	-15.369
310	-5301	-5345	-5290	-5660	0.827	-1.047	6.541
311	-4849	-4917	-4953	-4959	1.395	0.717	0.126
312	-4494	-4581	-4644	-4656	1.904	1.350	0.269
317	-4866	-4739	-4930	-4940	-2.685	3.874	0.208
318	-4365	-3664	-4394	-4379	-19.125	16.608	-0.339
319	-2790	-2497	-2478	-2436	-11.722	-0.771	-1.747
320	-4925	-4875	-4862	-4864	-1.035	-0.256	0.041
323	-1802	-2221	-2234	-2220	18.864	0.585	-0.635
324	-4961	-4674	-4627	-4635	-6.148	-1.028	0.182
327	-4092	-4163	-4068	-4068	1.711	-2.332	0.000
328	-4844	-4766	-4771	-4793	-1.648	0.117	0.459
329	-4733	-4699	-4721	-4743	-0.731	0.470	0.461
330	-4215	-4206	-4225	-4226	-0.213	0.450	0.017
331	-4612	-4610	-4626	-4637	-0.059	0.353	0.245
332	-4084	-4084	-4089	-4093	-0.016	0.133	0.096
333	-3870	-3875	-3846	-3841	0.129	-0.756	-0.116
334	-4664	-4653	-4616	-4620	-0.223	-0.813	0.084

* DM=Detailed Model, DGM=DM w/1st Gage Refinement, DG2M=DM w/2nd Gage Refinement, DG3M=DM w/3rd Gage Refinement

Table 9.4: Load Case 1, 1.0G Down-Bending, Predicted Strain Gage Values (microstrain, με) for the Undamaged Semi-Span.

Strain Gage #	Actuator #2 Load (kips)									
	-9	**-18**	**-27**	**-31.5**	**-36**	**-40.5**	**-42.75**	**-45**	**-47.25**	**-49.5**
10	-193	-384	-572	-665	-758	-850	-895	-941	-986	-1031
11	-308	-618	-928	-1083	-1239	-1395	-1472	-1550	-1629	-1707
35	-302	-606	-912	-1065	-1219	-1373	-1450	-1527	-1604	-1682
36	-263	-526	-789	-921	-1052	-1184	-1249	-1315	-1380	-1446
37	-296	-592	-890	-1039	-1189	-1339	-1414	-1489	-1564	-1639
38	-279	-559	-839	-979	-1119	-1260	-1330	-1400	-1470	-1540
39	-280	-561	-842	-983	-1125	-1266	-1337	-1408	-1478	-1549
40	-266	-533	-799	-933	-1066	-1199	-1266	-1333	-1399	-1466
41	-277	-556	-836	-976	-1116	-1257	-1327	-1398	-1468	-1539
42	-245	-489	-734	-856	-978	-1101	-1162	-1223	-1284	-1345
82	-323	-647	-972	-1135	-1298	-1461	-1542	-1624	-1706	-1787
83	-330	-661	-992	-1157	-1323	-1489	-1572	-1655	-1738	-1821
84	-332	-665	-999	-1166	-1332	-1499	-1583	-1667	-1750	-1834
85	-325	-650	-975	-1137	-1300	-1463	-1544	-1625	-1707	-1788
86	-327	-654	-981	-1145	-1308	-1471	-1553	-1635	-1716	-1798
87	-325	-649	-974	-1136	-1298	-1460	-1541	-1622	-1703	-1783
114	-691	-1384	-2081	-2430	-2779	-3130	-3305	-3481	-3656	-3832
118	-195	-391	-588	-686	-787	-884	-937	-987	-1036	-1087
208	339	680	1021	1192	1364	1536	1621	1707	1793	1878
209	336	673	1011	1181	1350	1520	1605	1689	1775	1860
210	337	674	1013	1183	1352	1522	1607	1693	1777	1862
211	324	648	971	1133	1295	1457	1537	1618	1698	1778
212	322	643	964	1124	1284	1444	1524	1603	1684	1763
213	319	638	956	1116	1274	1433	1512	1592	1670	1749
224	230	464	702	821	941	1063	1123	1184	1245	1306
225	358	714	1068	1245	1422	1598	1685	1773	1861	1948
231	241	487	737	865	993	1121	1186	1251	1317	1382
232	394	787	1176	1371	1566	1759	1856	1952	2048	2145
237	225	455	689	807	927	1046	1107	1167	1228	1288
238	372	741	1110	1294	1477	1659	1750	1842	1933	2024
251	299	598	896	1045	1194	1343	1418	1492	1566	1641
252	295	590	885	1032	1180	1327	1401	1475	1549	1622
254	318	636	954	1113	1272	1432	1511	1591	1670	1750
255	283	567	851	993	1135	1277	1348	1419	1490	1561
300	249	502	760	890	1021	1153	1220	1286	1353	1420
301	397	792	1185	1381	1576	1771	1869	1966	2063	2160
304	361	722	1083	1263	1443	1624	1714	1803	1894	1984
305	200	403	607	710	813	916	968	1020	1072	1124
306	207	415	625	730	836	941	994	1047	1100	1153
307	423	848	1274	1488	1701	1915	2022	2129	2236	2343
308	336	671	1006	1173	1340	1507	1590	1673	1757	1840
309	408	818	1230	1436	1643	1850	1954	2057	2161	2265
310	463	927	1392	1624	1856	2089	2205	2321	2438	2554
311	393	785	1177	1373	1568	1763	1860	1957	2054	2152
312	368	735	1101	1283	1465	1647	1737	1828	1919	2009
317	399	797	1194	1392	1590	1788	1887	1985	2084	2183
318	361	723	1087	1268	1450	1633	1724	1815	1906	1997
319	227	458	692	811	930	1050	1110	1170	1231	1292
320	362	722	1080	1259	1437	1616	1704	1793	1881	1970
323	206	416	629	738	847	957	1012	1068	1123	1179
324	353	705	1055	1230	1403	1577	1664	1751	1837	1923
327	320	641	962	1122	1283	1444	1524	1604	1684	1764
328	358	716	1071	1248	1425	1602	1689	1777	1865	1952
329	357	713	1067	1244	1420	1596	1684	1772	1859	1947
330	330	660	990	1155	1320	1484	1567	1649	1731	1813
331	354	706	1058	1233	1407	1582	1669	1756	1843	1930
332	323	647	971	1133	1294	1457	1537	1618	1699	1780
333	308	617	927	1082	1237	1392	1469	1547	1625	1702
334	352	702	1050	1224	1397	1570	1656	1742	1829	1915

Table 9.5: Load Case 2, 2.5G Up-Bending, Predicted Strain Gage Values (microstrain, με) for the Undamaged Semi-Span.

Strain Gage #	Actuator #2 Load (kips)									
	19.95	**39.9**	**59.85**	**69.825**	**79.8**	**89.775**	**94.7625**	**99.75**	**104.7375**	**109.725**
10	474	957	1448	1695	1945	2191	2320	2443	2562	2693
11	751	1493	2225	2586	2946	3301	3472	3649	3821	3997
35	719	1428	2126	2471	2814	3153	3322	3489	3657	3823
36	629	1255	1877	2187	2495	2801	2954	3106	3258	3408
37	701	1395	2081	2420	2757	3092	3259	3425	3590	3754
38	664	1323	1977	2302	2625	2946	3106	3265	3424	3582
39	661	1317	1965	2286	2605	2922	3079	3236	3393	3549
40	629	1255	1876	2185	2492	2797	2949	3101	3252	3402
41	657	1306	1947	2264	2579	2891	3046	3201	3354	3507
42	581	1160	1736	2022	2307	2592	2733	2874	3014	3154
82	707	1410	2108	2456	2801	3146	3317	3488	3658	3828
83	723	1443	2158	2513	2867	3219	3394	3569	3743	3916
84	729	1453	2174	2532	2888	3242	3418	3594	3769	3943
85	712	1421	2127	2478	2828	3177	3351	3524	3698	3870
86	719	1436	2151	2506	2861	3215	3391	3567	3743	3918
87	714	1427	2137	2491	2844	3195	3371	3545	3720	3895
114	1581	3142	4684	5446	6201	6952	7325	7696	8065	8432
118	830	1647	2444	2837	3223	3606	3797	3985	4168	4352
208	-800	-1586	-2357	-2731	-3102	-3464	-3648	-3822	-4001	-4171
209	-808	-1604	-2382	-2763	-3142	-3510	-3692	-3873	-4050	-4226
210	-816	-1620	-2405	-2792	-3171	-3546	-3727	-3911	-4093	-4272
211	-782	-1560	-2336	-2719	-3102	-3480	-3674	-3859	-4050	-4234
212	-786	-1571	-2354	-2745	-3137	-3524	-3717	-3912	-4103	-4296
213	-784	-1568	-2347	-2739	-3126	-3514	-3705	-3900	-4094	-4287
224	-544	-1059	-1537	-1762	-1972	-2169	-2259	-2344	-2428	-2501
225	-858	-1722	-2596	-3031	-3472	-3918	-4141	-4362	-4588	-4819
231	-533	-1022	-1454	-1643	-1809	-1948	-2006	-2054	-2093	-2118
232	-927	-1866	-2818	-3300	-3788	-4282	-4532	-4784	-5038	-5302
237	-509	-983	-1409	-1599	-1771	-1921	-1985	-2042	-2091	-2124
238	-884	-1777	-2683	-3141	-3607	-4075	-4311	-4553	-4796	-5044
251	-689	-1378	-2066	-2408	-2749	-3085	-3252	-3415	-3575	-3728
252	-678	-1355	-2030	-2368	-2707	-3048	-3221	-3396	-3575	-3759
254	-713	-1425	-2132	-2483	-2830	-3170	-3334	-3494	-3644	-3779
255	-635	-1269	-1901	-2219	-2539	-2864	-3031	-3202	-3381	-3572
300	-546	-1055	-1515	-1722	-1909	-2074	-2145	-2209	-2262	-2306
301	-914	-1838	-2773	-3245	-3724	-4207	-4448	-4695	-4944	-5198
304	-807	-1612	-2414	-2812	-3211	-3602	-3798	-3996	-4188	-4385
305	-442	-869	-1276	-1470	-1656	-1834	-1918	-1999	-2077	-2149
306	-457	-901	-1328	-1533	-1730	-1918	-2007	-2092	-2169	-2237
307	-967	-1921	-2858	-3319	-3774	-4223	-4445	-4665	-4884	-5102
308	-768	-1537	-2307	-2692	-3077	-3461	-3653	-3844	-4034	-4223
309	-928	-1837	-2721	-3151	-3573	-3985	-4187	-4386	-4581	-4773
310	-1050	-2093	-3126	-3639	-4147	-4656	-4906	-5156	-5409	-5660
311	-889	-1782	-2677	-3126	-3577	-4030	-4256	-4487	-4719	-4959
312	-828	-1661	-2502	-2924	-3350	-3780	-3996	-4212	-4433	-4656
317	-910	-1820	-2729	-3182	-3632	-4077	-4297	-4515	-4730	-4940
318	-816	-1623	-2419	-2813	-3204	-3594	-3789	-3984	-4180	-4379
319	-536	-1042	-1511	-1727	-1931	-2122	-2208	-2290	-2365	-2436
320	-864	-1737	-2623	-3056	-3510	-3960	-4176	-4411	-4634	-4864
323	-484	-940	-1362	-1556	-1745	-1919	-1996	-2078	-2145	-2220
324	-826	-1659	-2500	-2921	-3349	-3770	-3987	-4200	-4412	-4635
327	-761	-1515	-2260	-2630	-2995	-3355	-3533	-3713	-3891	-4068
328	-854	-1715	-2581	-3019	-3457	-3897	-4117	-4343	-4567	-4793
329	-850	-1705	-2565	-2998	-3432	-3864	-4081	-4302	-4523	-4743
330	-783	-1562	-2335	-2720	-3101	-3476	-3664	-3852	-4041	-4226
331	-831	-1669	-2506	-2932	-3354	-3783	-3994	-4210	-4422	-4637
332	-759	-1514	-2259	-2633	-3000	-3371	-3551	-3735	-3913	-4093
333	-721	-1436	-2140	-2488	-2835	-3174	-3342	-3513	-3680	-3841
334	-825	-1657	-2495	-2916	-3341	-3764	-3977	-4194	-4409	-4620

Table 9.6: Load Case 3, Braked Roll, Predicted Strain Gage Values (microstrain, με) for the Undamaged Semi-Span.

Strain Gage #	Actuator #7a Load (kips)									
	37.335	**74.67**	**112.005**	**130.6725**	**149.34**	**168.0075**	**177.34125**	**186.675**	**196.00875**	**205.3425**
10	-18	-35	-53	-62	-71	-80	-85	-89	-94	-98
11	-25	-50	-74	-87	-100	-112	-118	-125	-131	-137
35	-23	-46	-70	-83	-95	-108	-115	-121	-128	-135
36	-20	-40	-61	-71	-82	-94	-99	-105	-111	-117
37	-20	-40	-62	-72	-83	-95	-100	-106	-112	-118
38	-19	-38	-58	-68	-79	-89	-95	-100	-106	-111
39	-13	-26	-39	-46	-52	-59	-63	-66	-70	-73
40	-12	-24	-37	-43	-50	-57	-60	-63	-67	-70
41	-11	-22	-33	-39	-45	-51	-54	-57	-60	-63
42	-10	-20	-30	-35	-40	-46	-48	-51	-54	-57
82	255	509	761	886	1011	1135	1197	1259	1320	1381
83	235	468	699	813	927	1040	1096	1152	1207	1262
84	231	460	686	798	910	1020	1075	1129	1183	1237
85	238	474	708	824	940	1054	1110	1166	1222	1278
86	211	419	626	728	828	928	977	1026	1075	1123
87	205	409	609	709	807	904	952	1000	1047	1094
114	-105	-211	-320	-376	-432	-490	-518	-547	-576	-607
118	-27	-43	-43	-36	-24	-6	4	18	32	48
208	24	47	71	83	95	106	112	118	124	129
209	25	50	74	87	99	111	117	124	130	136
210	25	51	76	88	101	114	120	126	132	139
211	24	48	71	83	95	106	112	118	124	130
212	24	49	73	85	97	109	115	121	127	133
213	25	49	73	85	98	110	116	122	128	134
224	22	43	65	76	87	98	103	108	114	119
225	34	67	101	118	135	152	160	169	177	186
231	15	30	46	54	62	71	75	80	84	89
232	35	69	104	122	139	157	166	175	183	193
237	13	26	40	47	55	62	66	70	75	79
238	23	46	69	81	92	104	110	116	122	129
251	-29	-57	-82	-93	-104	-114	-119	-123	-127	-131
252	-26	-51	-74	-84	-94	-104	-108	-112	-116	-120
254	-23	-43	-60	-66	-71	-74	-76	-76	-77	-77
255	-21	-41	-58	-66	-73	-79	-82	-85	-88	-90
300	21	41	62	72	82	92	96	101	106	111
301	50	101	151	176	201	226	239	251	264	276
304	87	173	262	305	349	393	415	437	459	481
305	40	80	120	140	160	179	189	199	209	218
306	42	83	125	145	166	187	197	207	218	228
307	63	127	191	222	254	286	302	318	334	350
308	57	115	173	201	230	259	273	288	302	316
309	57	114	172	201	229	258	273	287	301	316
310	71	142	213	249	285	321	339	357	375	393
311	66	132	199	232	266	299	315	332	349	366
312	72	144	216	252	288	324	342	360	378	396
317	56	112	168	197	225	253	267	281	296	310
318	52	104	157	183	209	236	249	262	276	289
319	24	47	71	83	95	107	112	118	124	130
320	36	73	109	128	145	164	173	183	191	201
323	24	49	74	86	98	111	117	123	130	135
324	39	78	118	137	157	178	186	197	207	217
327	33	66	99	115	132	148	156	164	173	181
328	36	73	110	128	146	164	173	182	192	200
329	37	74	111	129	148	167	176	185	194	204
330	34	69	103	120	138	155	164	172	181	189
331	38	76	115	134	153	172	182	191	201	211
332	35	70	106	123	141	159	168	177	185	194
333	34	69	103	120	138	155	164	172	181	190
334	39	77	116	136	155	175	185	194	204	214

Table 9.7: Tabulation of Strain Gages Exhibiting Nonlinear Behavior for the Undamaged Composite Semi-Span.

Load Case	Gages
1.0G Down-Bending	None
2.5G Up-Bending	224, 231, 237, 254, 255, 300, 305, 306, 319, 323
Braked Roll	92, 251, 252, 254, 255

Table 9.8: Load Case 2, 2.5G Up-Bending, Predicted Strain Gage Values (microstrain, με) for the Damaged Semi-Span with Upper Cover Sawcut.

Strain	Actuator #2 Load (kips)									
Gage #	19.95	39.9	59.85	69.825	79.8	89.775	94.7625	99.75	104.7375	109.725
224	-553	-1072	-1549	-1768	-1969	-2157	-2240	-2320	-2395	-2464
225	-896	-1802	-2718	-3177	-3645	-4114	-4344	-4583	-4822	-5062
231	-531	-1018	-1447	-1634	-1799	-1938	-1994	-2041	-2080	-2106
232	-928	-1867	-2820	-3303	-3791	-4286	-4534	-4789	-5044	-5302
237	-513	-990	-1419	-1610	-1782	-1931	-1994	-2049	-2094	-2127
238	-889	-1788	-2698	-3160	-3628	-4099	-4339	-4581	-4832	-5080
300	-548	-1064	-1541	-1761	-1967	-2157	-2245	-2327	-2406	-2477
301	-903	-1814	-2733	-3197	-3663	-4133	-4365	-4602	-4844	-5082
304	-809	-1616	-2419	-2819	-3215	-3615	-3809	-4003	-4201	-4395
305	-418	-821	-1206	-1389	-1566	-1735	-1814	-1891	-1965	-2033
306	-457	-901	-1329	-1535	-1735	-1924	-2016	-2102	-2183	-2254
307	-994	-1975	-2939	-3413	-3879	-4340	-4566	-4791	-5014	-5237
308	-749	-1501	-2257	-2638	-3017	-3398	-3587	-3777	-3967	-4159
309	-931	-1842	-2729	-3161	-3584	-3995	-4199	-4396	-4591	-4781
310	-997	-1987	-2967	-3453	-3935	-4415	-4651	-4891	-5126	-5362
311	-894	-1790	-2688	-3139	-3591	-4043	-4272	-4501	-4731	-4967
312	-828	-1661	-2500	-2923	-3346	-3775	-3991	-4208	-4426	-4648
317	-913	-1827	-2742	-3198	-3652	-4103	-4326	-4547	-4767	-4987
318	-816	-1621	-2415	-2807	-3196	-3584	-3777	-3971	-4164	-4356
319	-724	-1439	-2146	-2496	-2845	-3193	-3372	-3549	-3724	-3903
320	-963	-1927	-2887	-3376	-3855	-4328	-4569	-4803	-5039	-5279
323	-652	-1290	-1914	-2219	-2523	-2826	-2977	-3128	-3280	-3439
324	-933	-1869	-2803	-3272	-3733	-4194	-4421	-4650	-4878	-5108
327	-1049	-2100	-3152	-3678	-4203	-4733	-4995	-5260	-5524	-5793
328	-963	-1920	-2869	-3339	-3803	-4267	-4493	-4721	-4946	-5172
329	-1503	-2987	-4442	-5154	-5853	-6537	-6871	-7198	-7523	-7840
330	-2201	-4412	-6632	-7744	-8859	-9979	-10540	-11099	-11666	-12233
331	-1492	-2965	-4409	-5120	-5811	-6489	-6825	-7151	-7471	-7787
332	-2149	-4306	-6471	-7560	-8644	-9733	-10283	-10830	-11378	-11932
333	-1030	-2063	-3098	-3609	-4130	-4648	-4906	-5163	-5424	-5685
334	-934	-1864	-2788	-3238	-3694	-4142	-4361	-4578	-4797	-5012

9.4 Figures

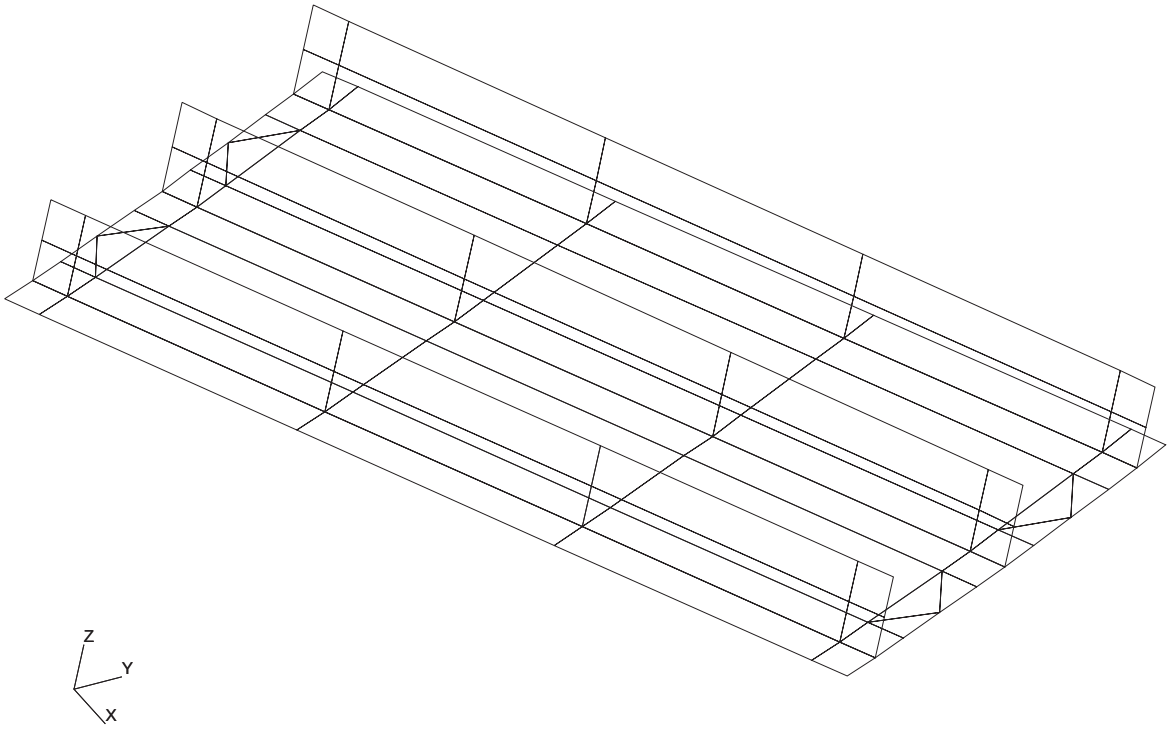

Figure 9.1: Original Mesh from the Detailed Model for the Region Containing Strain Gages #10 and #11.

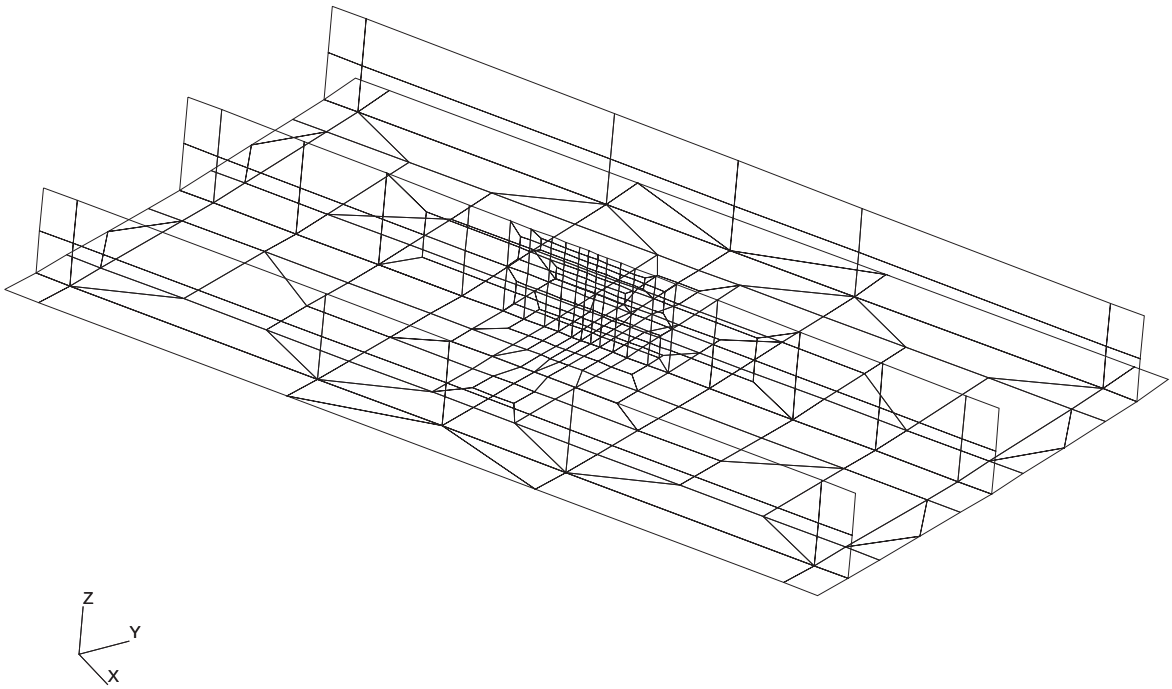

Figure 9.2: Converged Mesh from the Strain Gage Model for the Region Containing Strain Gages #10 and #11.

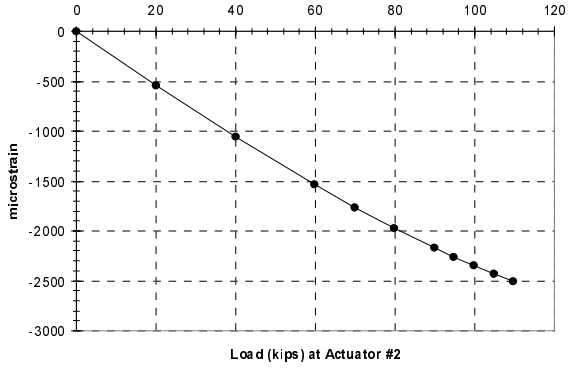

Figure 9.3: Strain Gage #224 Predicted Value as a Function of Actuator #2 Load, Load Case 2.

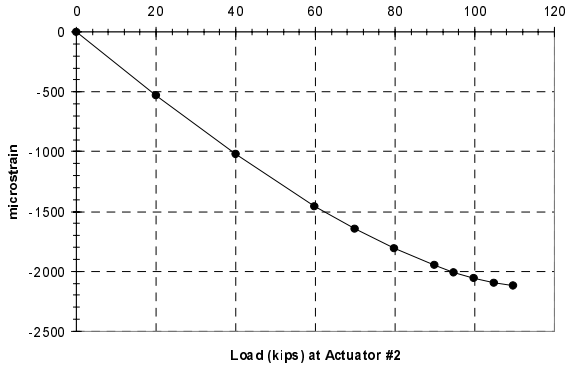

Figure 9.4: Strain Gage #231 Predicted Value as a Function of Actuator #2 Load, Load Case 2.

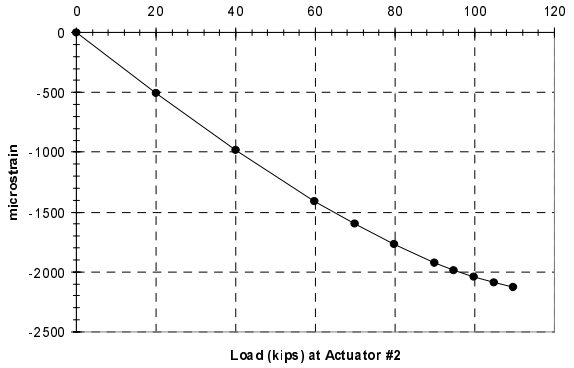

Figure 9.5: Strain Gage #237 Predicted Value as a Function of Actuator #2 Load, Load Case 2.

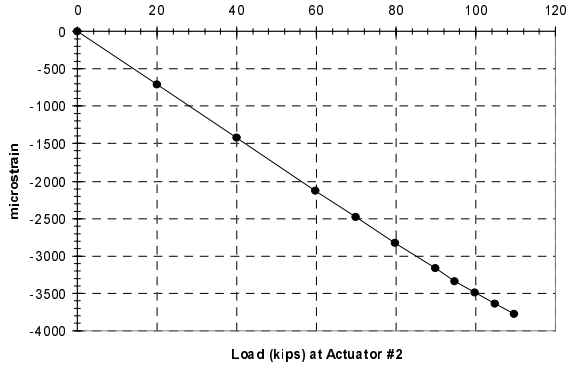

Figure 9.6: Strain Gage #254 Predicted Value as a Function of Actuator #2 Load, Load Case 2.

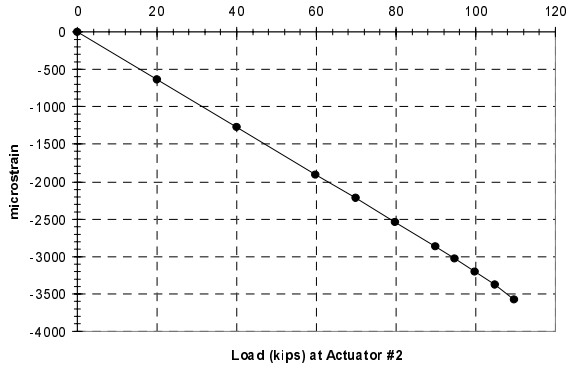

Figure 9.7: Strain Gage #255 Predicted Value as a Function of Actuator #2 Load, Load Case 2.

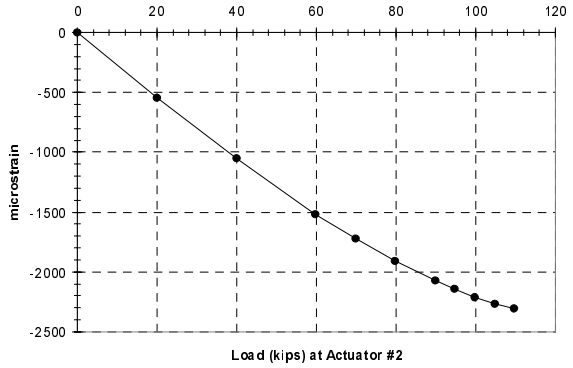

Figure 9.8: Strain Gage #300 Predicted Value as a Function of Actuator #2 Load, Load Case 2.

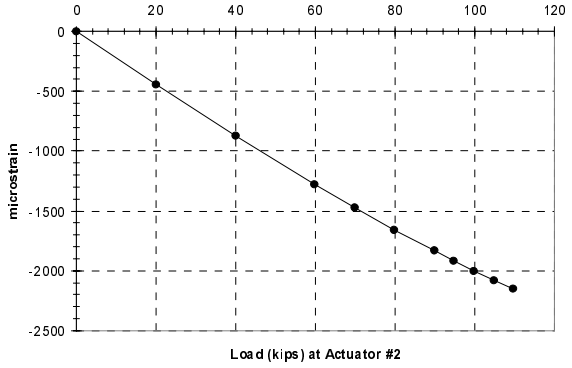

Figure 9.9: Strain Gage #305 Predicted Value as a Function of Actuator #2 Load, Load Case 2.

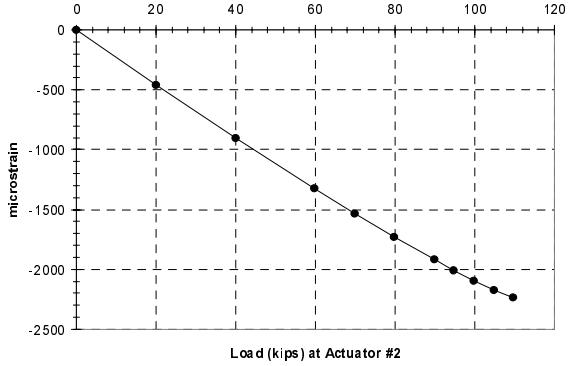

Figure 9.10: Strain Gage #306 Predicted Value as a Function of Actuator #2 Load, Load Case 2.

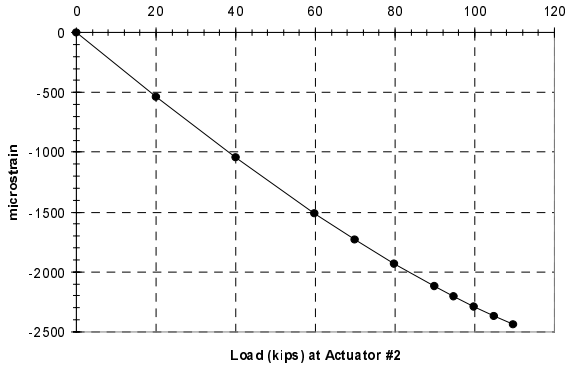

Figure 9.11: Strain Gage #319 Predicted Value as a Function of Actuator #2 Load, Load Case 2.

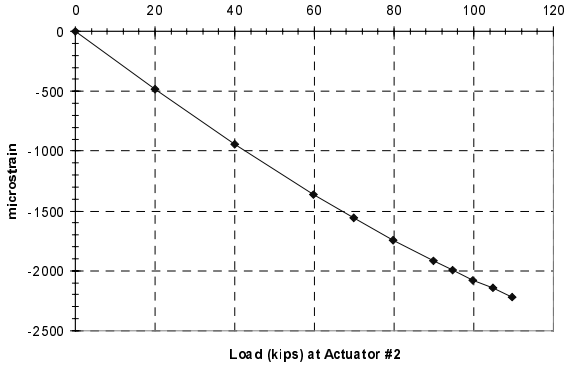

Figure 9.12: Strain Gage #323 Predicted Value as a Function of Actuator #2 Load, Load Case 2.

Figure 9.13: Strain Gage #118 Predicted Value as a Function of Actuator #7a Load, Load Case 3.

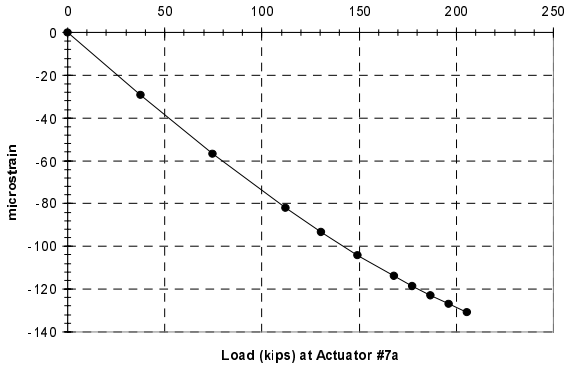

Figure 9.14: Strain Gage #251 Predicted Value as a Function of Actuator #7a Load, Load Case 3.

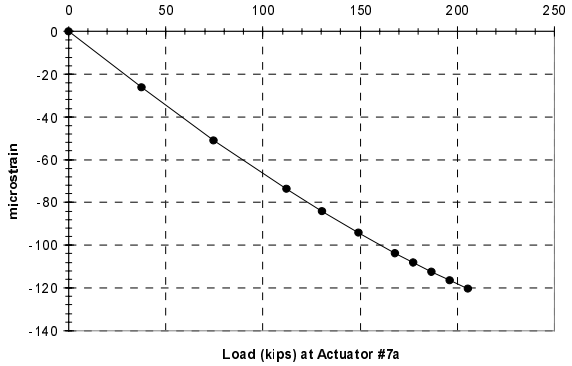

Figure 9.15: Strain Gage #252 Predicted Value as a Function of Actuator #7a Load, Load Case 3.

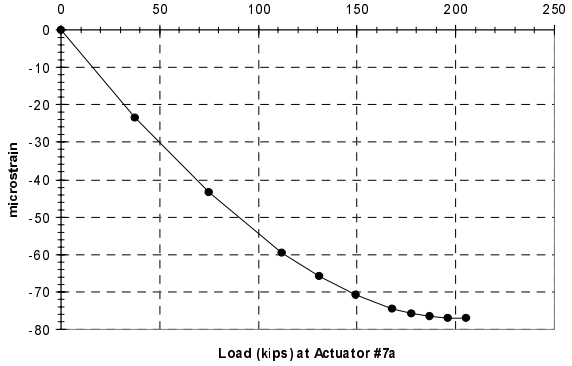

Figure 9.16: Strain Gage #254 Predicted Value as a Function of Actuator #7a Load, Load Case 3.

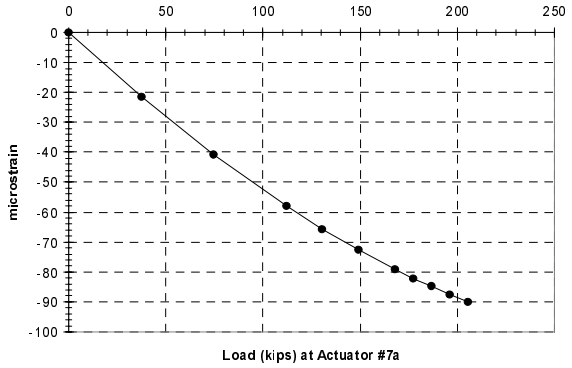

Figure 9.17: Strain Gage #255 Predicted Value as a Function of Actuator #7a Load, Load Case 3.

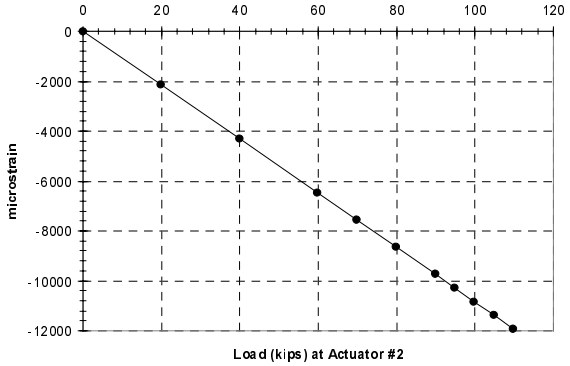

Figure 9.18: Strain Gage #332 Predicted Value as a Function of Actuator #2 Load, Upper Cover Sawcut, Load Case 2.

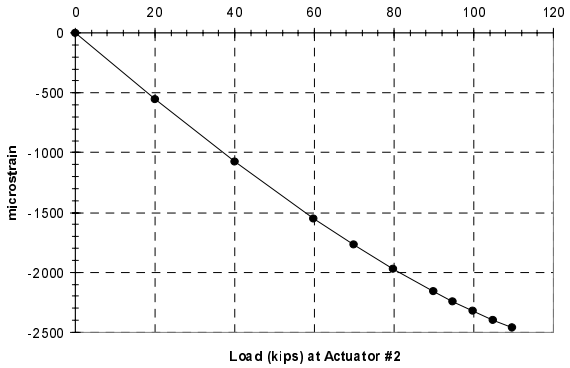

Figure 9.19: Strain Gage #224 Predicted Value as a Function of Actuator #2 Load, Upper Cover Sawcut, Load Case 2.

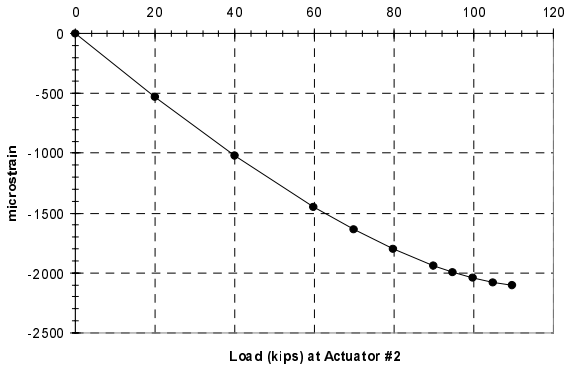

Figure 9.20: Strain Gage #231 Predicted Value as a Function of Actuator #2 Load, Upper Cover Sawcut, Load Case 2.

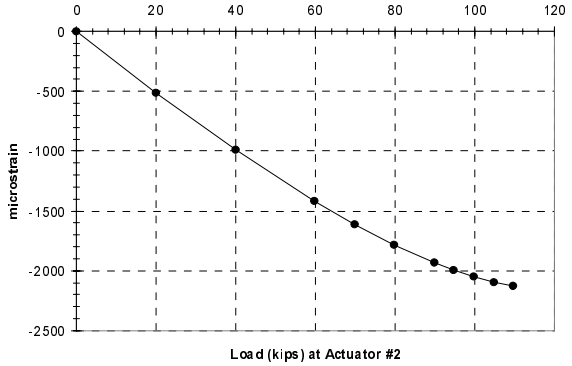

Figure 9.21: Strain Gage #237 Predicted Value as a Function of Actuator #2 Load, Upper Cover Sawcut, Load Case 2.

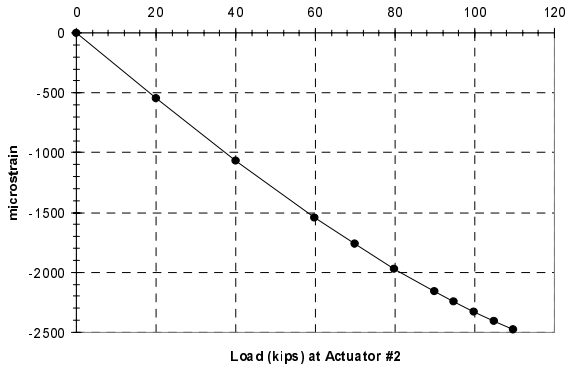

Figure 9.22: Strain Gage #300 Predicted Value as a Function of Actuator #2 Load, Upper Cover Sawcut, Load Case 2.

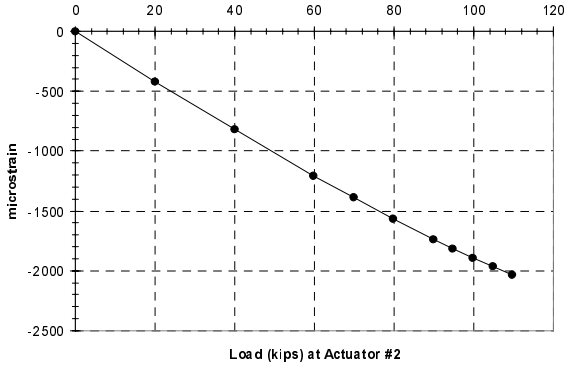

Figure 9.23: Strain Gage #305 Predicted Value as a Function of Actuator #2 Load, Upper Cover Sawcut, Load Case 2.

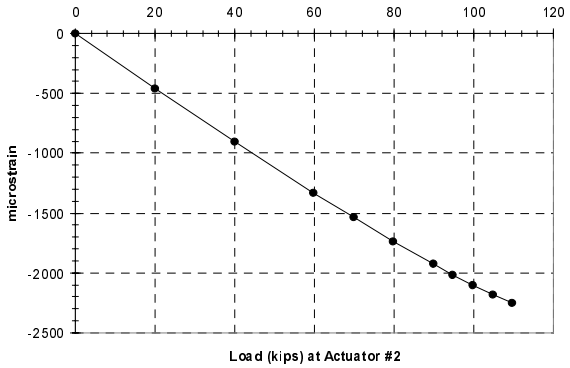

Figure 9.24: Strain Gage #306 Predicted Value as a Function of Actuator #2 Load, Upper Cover Sawcut, Load Case 2.

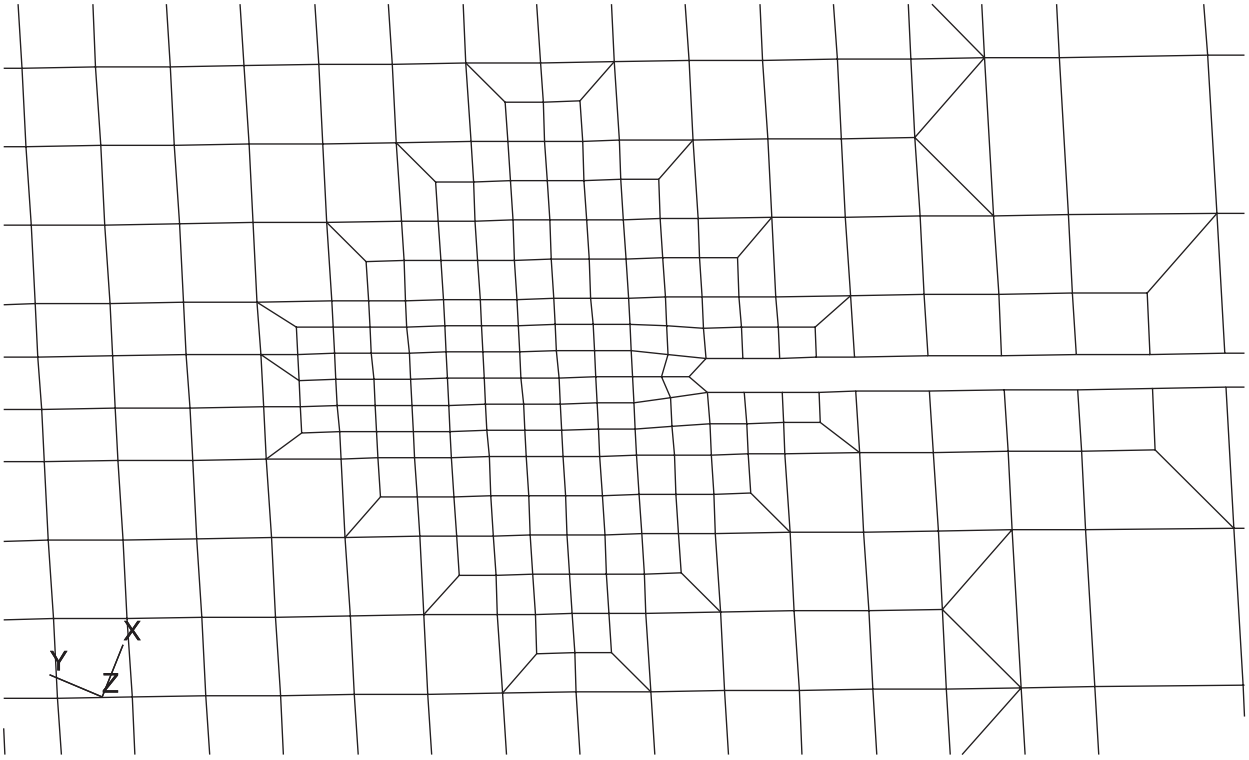

Figure 9.25: Plan View of the Finite Element Mesh at the Aft Portion of the Crack Tip for the Upper cover Sawcut Discrete Damage.

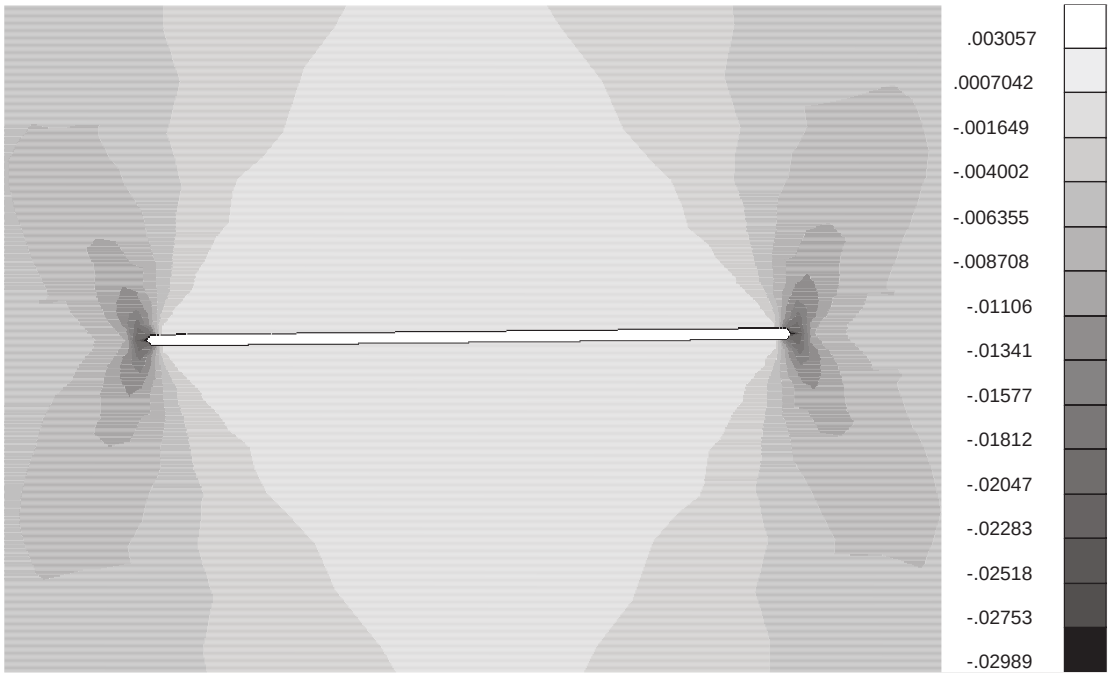

Figure 9.26: Aft Crack Tip Strain, ε_{xx}, for Upper Cover Sawcut Discrete Damage, Plan View, Load Case 2.

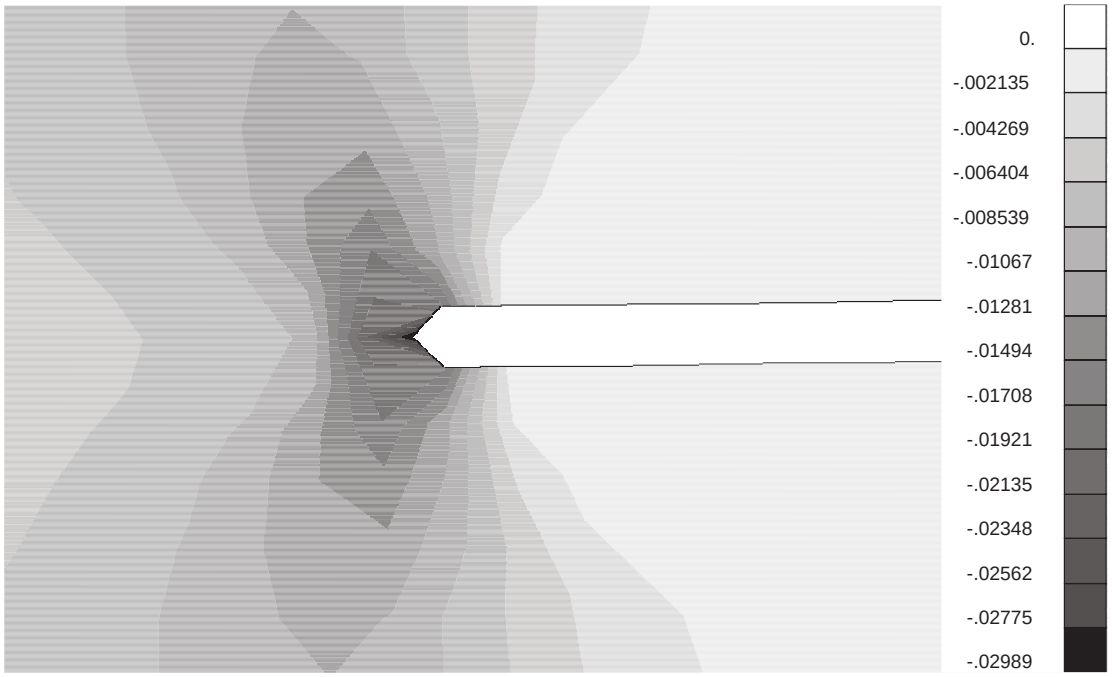

Figure 9.27: Close-Up of Aft Crack Tip Strain, ε_{xx}, for Upper Cover Sawcut Discrete Damage, Plan View, Load Case 2.

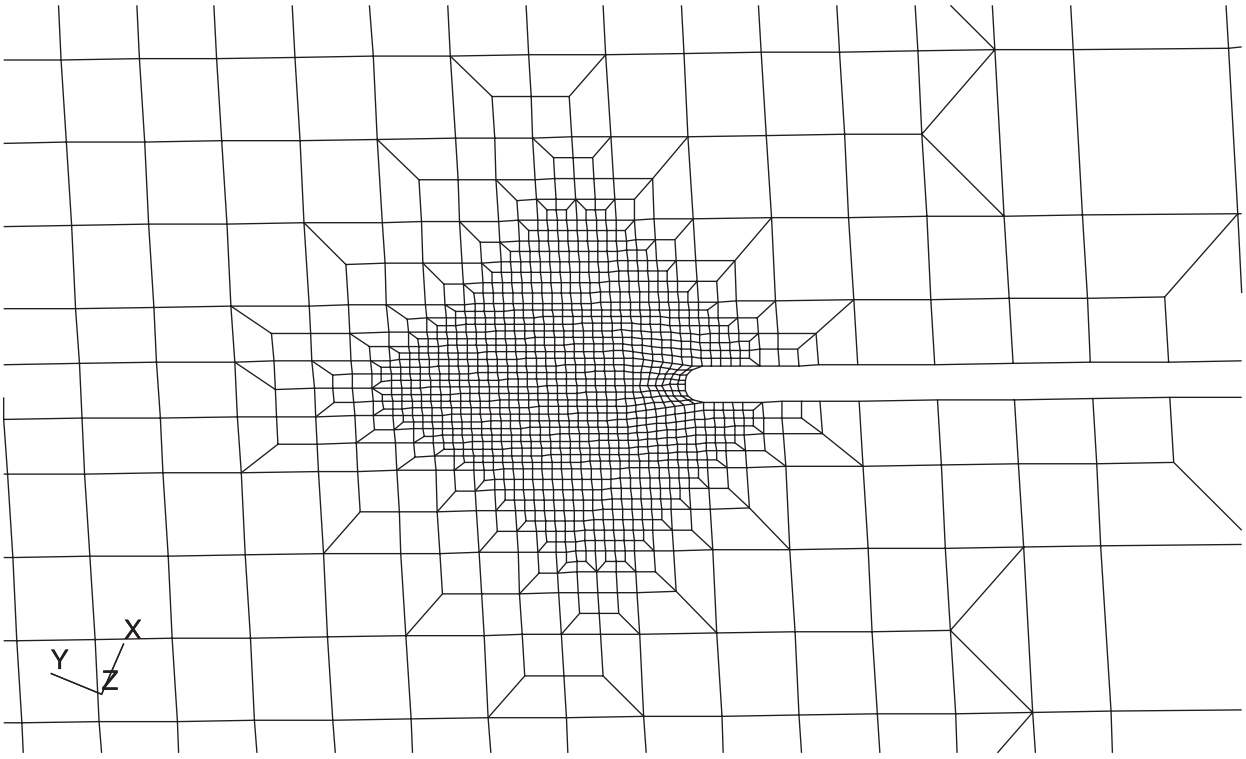

Figure 9.28: Plan View of the Refined Finite Element Mesh at the Aft Crack Tip for the Upper Cover Sawcut Discrete Damage.

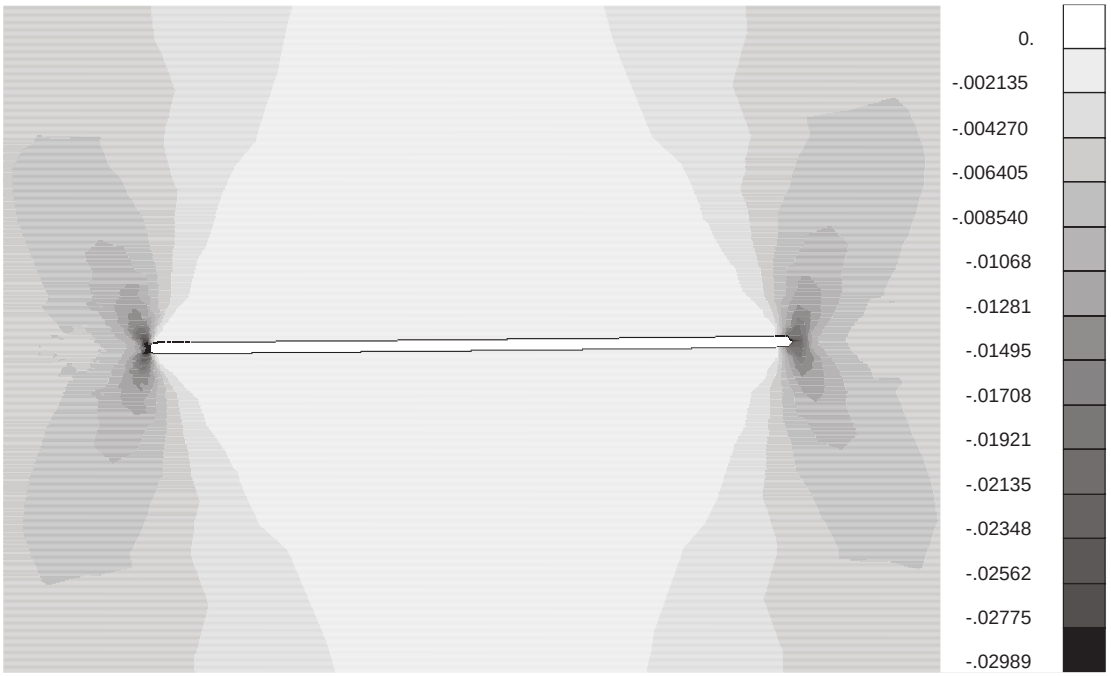

Figure 9.29: Refined Mesh Aft Crack Tip Strain, ε_{xx}, for Upper Cover Sawcut Discrete Damage, Plan View, Load Case 2.

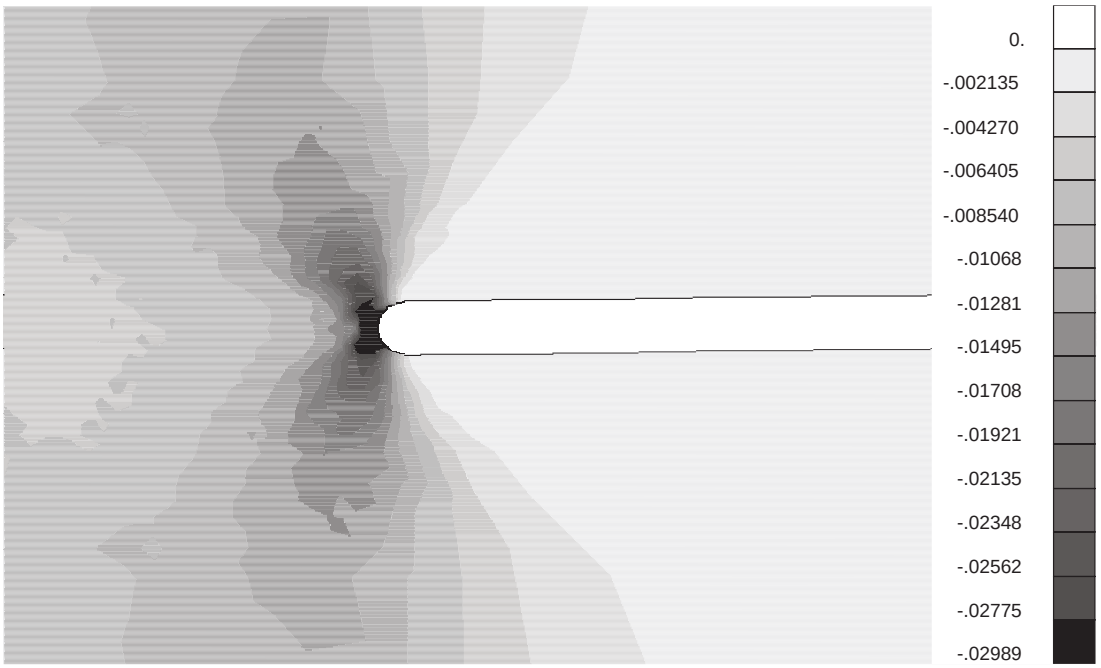

Figure 9.30: Close-Up of Refined Aft Crack Tip Strain, ε_{xx}, for Upper Cover Sawcut Discrete Damage, Plan View, Load Case 2.

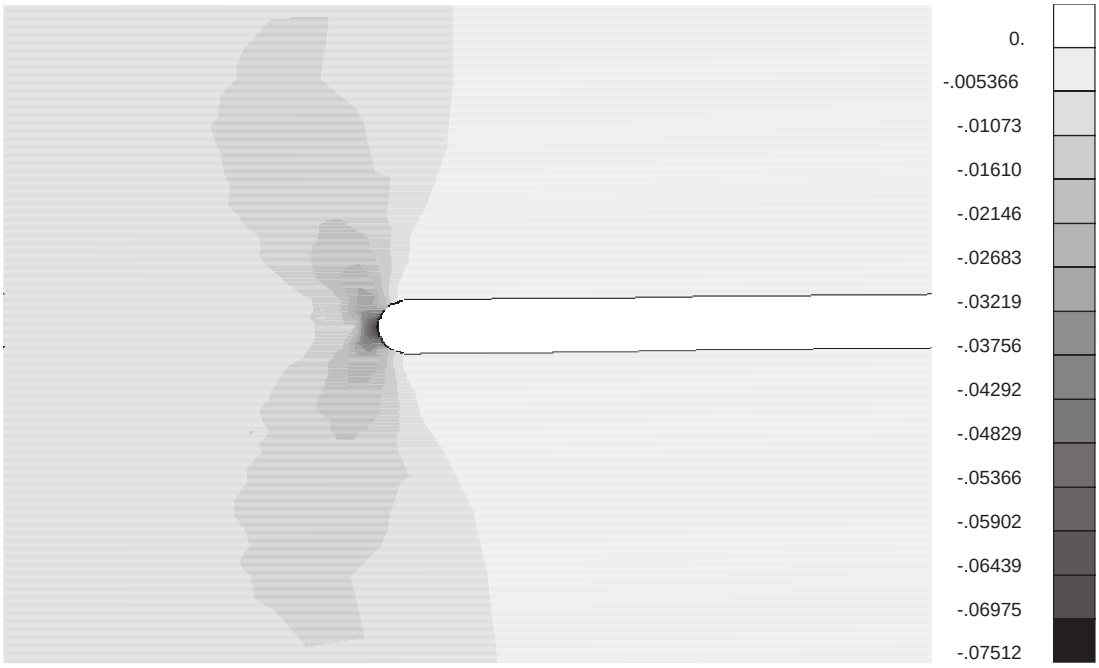

Figure 9.31: Close-Up of Refined Aft Crack Tip Strain, ε_{xx}, for Upper Cover Sawcut Discrete Damage, Plan View, Load Case 2, Adjusted Contour Scale Showing Maximum Value at the Crack Tip.

10. Semi-Span Deflection Prediction

Deflection results for the three load cases were required at various location on the composite semi-span test article. Displacements at the actuator ends attached to the semi-span and at the intersection points of rib 2 and the lower cover with the fore and aft spars were found (10 locations per load case). A convergence study was carried out and the results reported only for the undamaged detailed model.

10.1 Convergence Study

A convergence study was carried out using the detailed model and the strain gage convergence study models. Comparison of the detailed model displacement results with the first strain gage convergence study model refinement indicated that, as expected, the refinement for the strain gages has no effect on the predicted displacements at the desired ten locations. Tables 10.1-10.8 show the error comparison between these two models for the global displacement components under the 2.5G up-bending load condition at the eight actuator locations. It is seen that with the exception of the x-displacement errors for actuator 7b shown in Table 10.7, none of these values exceeds 1%. The larger errors found for the actuator #7b x-displacement, especially at smaller load factors, is easily explained by noticing that the actual x-displacement value is extremely small (see Table 10.25). However, for higher load factors the errors in the x-displacement quantity are still within a few percent between the two models, so the displacement results found using the original finite element mesh for the detailed model are taken as being converged and are presented herein.

10.2 Results

Displacement result values for the load factors given in Table 2.2 are presented in terms of actuator loads. For the 1.0G down-bending and the 2.5G up-bending load cases, load values are provided for actuator #2, and for the braked roll load case, load values are provided for actuator #7a. Lastly, since introduction of small, localized damage is not expected to affect the overall displacement response of the composite semi-span, results are only presented for the undamaged detailed model.

10.2.1 Detailed Model

10.2.2.1 Undamaged

Displacement results at the desired ten locations are provided in Tables 10.9-10.18 for 1.0G down-bending, Tables 10.19-10.28 for 2.5G up-bending and Tables 10.29-10.38 for braked roll. Individual displacement component plots are shown in Figures 10.1-10.3 for the actuator #2 load node under the 2.5G up-bending loading, and Figure 10.4 shows a plot for the total displacement distance at the same node. The x-component seen in Figure 10.1 indicates mild nonlinearity at this location, whereas the y-displacement component seen in Figure 10.2 indicates that the response is highly nonlinear. However, the largest displacement component at this location is the z-displacement as seen in Figure 10.3, which exhibits nearly linear behavior. As a result, the total displacement distance shown in Figure 10.4 exhibits nearly linear response since it is dominated by the z-displacement component. Similar results are seen at the other locations for all three load cases, where any apparent nonlinear displacement component response is dominated by a nearly linear displacement component response in the total response. Thus, nodal displacement plots are provided in Figures 10.5-10.14 for 1.0G down-bending, Figures 10.15-10.24 for 2.5G up-bending and Figures 10.25-10.34 for braked roll. These compiled results are provided so that it can be determined if the actuators will exceed their maximum stroke during the testing. Lastly, overall deformation plots are provided in Figures 10.35-10.37 for the three load cases.

10.3 Tables

Table 10.1: Actuator #1 Load Node Component Displacement Errors Between Detailed Model and First Strain Gage Refinement Model, Load Case 2.

Act. #2 Load (kips)	X-Disp. Error (%)	Y-Disp. Error (%)	Z-Disp. Error (%)
19.9500	-0.31259	-0.49041	-0.20403
39.9000	-0.33343	-0.49234	-0.20392
59.8500	-0.34866	-0.49293	-0.20356
69.8250	-0.35481	-0.49204	-0.20338
79.8000	-0.36026	-0.48916	-0.20326
89.7750	-0.36524	-0.48045	-0.20346
94.7625	-0.36762	-0.47020	-0.20382
99.7500	-0.37000	-0.45244	-0.20448
104.7375	-0.37253	-0.42815	-0.20542
109.7250	-0.37531	-0.40288	-0.20647

Table 10.2: Actuator #2 Load Node Component Displacement Errors Between Detailed Model and First Strain Gage Refinement Model, Load Case 2.

Act. #2 Load (kips)	X-Disp. Error (%)	Y-Disp. Error (%)	Z-Disp. Error (%)
19.9500	-0.33282	-0.50257	-0.20233
39.9000	-0.34707	-0.50708	-0.20208
59.8500	-0.35789	-0.51103	-0.20158
69.8250	-0.36232	-0.51217	-0.20133
79.8000	-0.36627	-0.51139	-0.20116
89.7750	-0.36978	-0.50413	-0.20130
94.7625	-0.37134	-0.49356	-0.20161
99.7500	-0.37282	-0.47376	-0.20223
104.7375	-0.37435	-0.44556	-0.20312
109.7250	-0.37625	-0.41540	-0.20412

Table 10.3: Actuator #3 Load Node Component Displacement Errors Between Detailed Model and First Strain Gage Refinement Model, Load Case 2.

Act. #7a Load (kips)	X-Disp. Error (%)	Y-Disp. Error (%)	Z-Disp. Error (%)
19.9500	-0.28691	-0.31842	-0.16049
39.9000	-0.29802	-0.31217	-0.16056
59.8500	-0.30732	-0.30427	-0.16049
69.8250	-0.31142	-0.29937	-0.16057
79.8000	-0.31517	-0.29325	-0.16073
89.7750	-0.31842	-0.28411	-0.16127
94.7625	-0.31972	-0.27667	-0.16176
99.7500	-0.32066	-0.26579	-0.16267
104.7375	-0.32151	-0.25227	-0.16389
109.7250	-0.32295	-0.23889	-0.16522

Table 10.4: Actuator #4 Load Node Component Displacement Errors Between Detailed Model and First Strain Gage Refinement Model, Load Case 2.

Act. #2 Load (kips)	X-Disp. Error (%)	Y-Disp. Error (%)	Z-Disp. Error (%)
19.9500	-0.24210	-0.41382	-0.15146
39.9000	-0.26065	-0.41407	-0.15188
59.8500	-0.27573	-0.41313	-0.15222
69.8250	-0.28231	-0.41192	-0.15238
79.8000	-0.28858	-0.40968	-0.15282
89.7750	-0.29445	-0.40474	-0.15352
94.7625	-0.29757	-0.39959	-0.15421
99.7500	-0.30078	-0.39149	-0.15524
104.7375	-0.30436	-0.38100	-0.15662
109.7250	-0.30815	-0.37070	-0.15818

Table 10.5: Actuator #5 Load Node Component Displacement Errors Between Detailed Model and First Strain Gage Refinement Model, Load Case 2.

Act. #2 Load (kips)	X-Disp. Error (%)	Y-Disp. Error (%)	Z-Disp. Error (%)
19.9500	-0.28495	-0.49261	0.05681
39.9000	-0.27479	-0.50145	0.05712
59.8500	-0.26472	-0.51038	0.05746
69.8250	-0.25964	-0.51492	0.05761
79.8000	-0.25439	-0.51951	0.05780
89.7750	-0.24872	-0.52422	0.05797
94.7625	-0.24543	-0.52659	0.05803
99.7500	-0.24161	-0.52901	0.05809
104.7375	-0.23740	-0.53120	0.05809
109.7250	-0.23323	-0.53280	0.05800

Table 10.6: Actuator #6 Load Node Component Displacement Errors Between Detailed Model and First Strain Gage Refinement Model, Load Case 2.

Act. #7a Load (kips)	X-Disp. Error (%)	Y-Disp. Error (%)	Z-Disp. Error (%)
19.9500	-0.03694	-0.44088	0.12315
39.9000	-0.03164	-0.44652	0.12386
59.8500	-0.02685	-0.45164	0.12470
69.8250	-0.02467	-0.45396	0.12527
79.8000	-0.02254	-0.45617	0.12581
89.7750	-0.02043	-0.45820	0.12655
94.7625	-0.01926	-0.45914	0.12708
99.7500	-0.01787	-0.45999	0.12779
104.7375	-0.01614	-0.46075	0.12872
109.7250	-0.01406	-0.46139	0.12980

Table 10.7: Actuator #7b Load Node Component Displacement Errors Between Detailed Model and First Strain Gage Refinement Model, Load Case 2.

Act. #2 Load (kips)	X-Disp. Error (%)	Y-Disp. Error (%)	Z-Disp. Error (%)
19.9500	-7.48687	0.16902	0.17076
39.9000	-5.08259	0.16183	0.17071
59.8500	-3.77358	0.15410	0.17041
69.8250	-3.31353	0.14997	0.17023
79.8000	-2.93308	0.14552	0.16998
89.7750	-2.61076	0.14065	0.16965
94.7625	-2.46639	0.13808	0.16947
99.7500	-2.33114	0.13533	0.16937
104.7375	-2.20382	0.13243	0.16923
109.7250	-2.08348	0.12934	0.16909

Table 10.8: Actuator #8 Load Node Component Displacement Errors Between Detailed Model and First Strain Gage Refinement Model, Load Case 2.

Act. #2 Load (kips)	X-Disp. Error (%)	Y-Disp. Error (%)	Z-Disp. Error (%)
19.9500	-0.27580	-0.12868	0.10101
39.9000	-0.23888	-0.13357	0.10243
59.8500	-0.20603	-0.13841	0.10375
69.8250	-0.19061	-0.14081	0.10444
79.8000	-0.17547	-0.14315	0.10503
89.7750	-0.16022	-0.14552	0.10562
94.7625	-0.15236	-0.14664	0.10585
99.7500	-0.14419	-0.14770	0.10609
104.7375	-0.13566	-0.14869	0.10632
109.7250	-0.12679	-0.14958	0.10655

Table 10.9: Actuator #1 Load Node Displacement Values, Load Case 1.

Act. #2 Load (kips)	X-Disp. (in.)	Y-Disp. (in.)	Z-Disp. (in.)
0.0000	0.0000	0.0000	0.0000
-9.0000	0.2785	-0.1724	-3.5061
-18.0000	0.5229	-0.3618	-7.0155
-27.0000	0.7333	-0.5682	-10.5270
-31.5000	0.8256	-0.6777	-12.2832
-36.0000	0.9094	-0.7914	-14.0396
-40.5000	0.9846	-0.9093	-15.7959
-42.7500	1.0190	-0.9698	-16.6741
-45.0000	1.0513	-1.0313	-17.5522
-47.2500	1.0814	-1.0938	-18.4303
-49.5000	1.1094	-1.1574	-19.3083

Table 10.10: Actuator #2 Load Node Displacement Values, Load Case 1.

Act. #2 Load (kips)	X-Disp. (in.)	Y-Disp. (in.)	Z-Disp. (in.)
0.0000	0.0000	0.0000	0.0000
-9.0000	0.2217	-0.1980	-3.5461
-18.0000	0.4080	-0.4135	-7.0952
-27.0000	0.5587	-0.6464	-10.6459
-31.5000	0.6207	-0.7693	-12.4216
-36.0000	0.6738	-0.8966	-14.1973
-40.5000	0.7180	-1.0281	-15.9728
-42.7500	0.7367	-1.0955	-16.8605
-45.0000	0.7532	-1.1639	-17.7481
-47.2500	0.7676	-1.2334	-18.6356
-49.5000	0.7796	-1.3039	-19.5231

Table 10.11: Actuator #3 Load Node Displacement Values, Load Case 1.

Act. #2 Load (kips)	X-Disp. (in.)	Y-Disp. (in.)	Z-Disp. (in.)
0.0000	0.0000	0.0000	0.0000
-9.0000	0.1444	-0.1078	-1.5369
-18.0000	0.2787	-0.2205	-3.0754
-27.0000	0.4027	-0.3383	-4.6154
-31.5000	0.4609	-0.3990	-5.3859
-36.0000	0.5166	-0.4609	-6.1568
-40.5000	0.5697	-0.5241	-6.9279
-42.7500	0.5953	-0.5561	-7.3136
-45.0000	0.6202	-0.5884	-7.6994
-47.2500	0.6445	-0.6211	-8.0852
-49.5000	0.6681	-0.6540	-8.4712

Table 10.12: Actuator #4 Load Node Displacement Values, Load Case 1.

Act. #2 Load (kips)	X-Disp. (in.)	Y-Disp. (in.)	Z-Disp. (in.)
0.0000	0.0000	0.0000	0.0000
-9.0000	0.0976	-0.1337	-1.4789
-18.0000	0.1857	-0.2719	-2.9594
-27.0000	0.2644	-0.4147	-4.4415
-31.5000	0.3001	-0.4878	-5.1830
-36.0000	0.3335	-0.5620	-5.9249
-40.5000	0.3645	-0.6373	-6.6672
-42.7500	0.3791	-0.6754	-7.0385
-45.0000	0.3931	-0.7137	-7.4098
-47.2500	0.4065	-0.7523	-7.7813
-49.5000	0.4193	-0.7912	-8.1528

Table 10.13: Actuator #5 Load Node Displacement Values, Load Case 1.

Act. #2 Load (kips)	X-Disp. (in.)	Y-Disp. (in.)	Z-Disp. (in.)
0.0000	0.0000	0.0000	0.0000
-9.0000	0.0526	-0.0506	-0.5103
-18.0000	0.1034	-0.1020	-1.0210
-27.0000	0.1522	-0.1541	-1.5323
-31.5000	0.1760	-0.1804	-1.7882
-36.0000	0.1992	-0.2069	-2.0443
-40.5000	0.2220	-0.2336	-2.3006
-42.7500	0.2333	-0.2470	-2.4288
-45.0000	0.2444	-0.2604	-2.5571
-47.2500	0.2553	-0.2739	-2.6855
-49.5000	0.2662	-0.2874	-2.8139

Table 10.14: Actuator #6 Load Node Displacement Values, Load Case 1.

Act. #2 Load (kips)	X-Disp. (in.)	Y-Disp. (in.)	Z-Disp. (in.)
0.0000	0.0000	0.0000	0.0000
-9.0000	0.0283	-0.0438	-0.2987
-18.0000	0.0559	-0.0879	-0.5982
-27.0000	0.0827	-0.1323	-0.8987
-31.5000	0.0958	-0.1545	-1.0493
-36.0000	0.1088	-0.1768	-1.2003
-40.5000	0.1215	-0.1992	-1.3515
-42.7500	0.1278	-0.2104	-1.4272
-45.0000	0.1340	-0.2217	-1.5030
-47.2500	0.1402	-0.2329	-1.5789
-49.5000	0.1464	-0.2441	-1.6549

Table 10.15: Actuator #7b Load Node Displacement Values, Load Case 1.

Act. #2 Load (kips)	X-Disp. (in.)	Y-Disp. (in.)	Z-Disp. (in.)
0.0000	0.0000	0.0000	0.0000
-9.0000	0.0014	-0.0242	-0.1679
-18.0000	0.0023	-0.0485	-0.3359
-27.0000	0.0025	-0.0728	-0.5041
-31.5000	0.0025	-0.0851	-0.5883
-36.0000	0.0022	-0.0973	-0.6727
-40.5000	0.0018	-0.1096	-0.7571
-42.7500	0.0016	-0.1158	-0.7993
-45.0000	0.0013	-0.1219	-0.8416
-47.2500	0.0010	-0.1281	-0.8839
-49.5000	0.0006	-0.1343	-0.9262

Table 10.16: Actuator #8 Load Node Displacement Values, Load Case 1.

Act. #2 Load (kips)	X-Disp. (in.)	Y-Disp. (in.)	Z-Disp. (in.)
0.0000	0.0000	0.0000	0.0000
-9.0000	0.0046	-0.0261	-0.1504
-18.0000	0.0088	-0.0522	-0.3013
-27.0000	0.0127	-0.0784	-0.4529
-31.5000	0.0145	-0.0916	-0.5289
-36.0000	0.0162	-0.1047	-0.6050
-40.5000	0.0178	-0.1179	-0.6814
-42.7500	0.0185	-0.1245	-0.7197
-45.0000	0.0193	-0.1311	-0.7580
-47.2500	0.0200	-0.1377	-0.7964
-49.5000	0.0207	-0.1443	-0.8349

Table 10.17: Rib 2/Lower Cover/Aft Spar Junction Node Displacement Values, Load Case 1.

Act. #2 Load (kips)	X-Disp. (in.)	Y-Disp. (in.)	Z-Disp. (in.)
0.0000	0.0000	0.0000	0.0000
-9.0000	-0.0155	-0.0071	-0.0299
-18.0000	-0.0313	-0.0142	-0.0598
-27.0000	-0.0473	-0.0214	-0.0897
-31.5000	-0.0555	-0.0250	-0.1046
-36.0000	-0.0637	-0.0286	-0.1196
-40.5000	-0.0720	-0.0323	-0.1347
-42.7500	-0.0762	-0.0341	-0.1422
-45.0000	-0.0804	-0.0360	-0.1497
-47.2500	-0.0846	-0.0378	-0.1572
-49.5000	-0.0889	-0.0396	-0.1648

Table 10.18: Rib 2/Lower Cover/Fore Spar Junction Node Displacement Values, Load Case 1.

Act. #2 Load (kips)	X-Disp. (in.)	Y-Disp. (in.)	Z-Disp. (in.)
0.0000	0.0000	0.0000	0.0000
-9.0000	-0.0067	-0.0041	-0.0009
-18.0000	-0.0134	-0.0083	-0.0018
-27.0000	-0.0203	-0.0125	-0.0029
-31.5000	-0.0237	-0.0146	-0.0034
-36.0000	-0.0272	-0.0167	-0.0040
-40.5000	-0.0307	-0.0188	-0.0046
-42.7500	-0.0325	-0.0199	-0.0049
-45.0000	-0.0343	-0.0210	-0.0052
-47.2500	-0.0360	-0.0220	-0.0055
-49.5000	-0.0378	-0.0231	-0.0059

Table 10.19: Actuator #1 Load Node Displacement Values, Load Case 2.

Act. #2 Load (kips)	X-Disp. (in.)	Y-Disp. (in.)	Z-Disp. (in.)
0.0000	0.0000	0.0000	0.0000
19.9500	-0.6383	0.3566	8.3668
39.9000	-1.4837	0.6307	16.6925
59.8500	-2.5323	0.8231	24.9606
69.8250	-3.1315	0.8892	29.0690
79.8000	-3.7801	0.9357	33.1591
89.7750	-4.4776	0.9632	37.2306
94.7625	-4.8447	0.9700	39.2596
99.7500	-5.2240	0.9722	41.2846
104.7375	-5.6157	0.9699	43.3058
109.7250	-6.0198	0.9633	45.3241

Table 10.20: Actuator #2 Load Node Displacement Values, Load Case 2.

Act. #2 Load (kips)	X-Disp. (in.)	Y-Disp. (in.)	Z-Disp. (in.)
0.0000	0.0000	0.0000	0.0000
19.9500	-0.7572	0.3056	8.1761
39.9000	-1.7112	0.5318	16.3102
59.8500	-2.8584	0.6796	24.3873
69.8250	-3.5033	0.7245	28.4008
79.8000	-4.1950	0.7507	32.3964
89.7750	-4.9335	0.7586	36.3741
94.7625	-5.3202	0.7558	38.3565
99.7500	-5.7186	0.7487	40.3349
104.7375	-6.1288	0.7372	42.3099
109.7250	-6.5509	0.7215	44.2821

Table 10.21: Actuator #3 Load Node Displacement Values, Load Case 2.

Act. #2 Load (kips)	X-Disp. (in.)	Y-Disp. (in.)	Z-Disp. (in.)
0.0000	0.0000	0.0000	0.0000
19.9500	-0.3355	0.2024	3.3492
39.9000	-0.7213	0.3842	6.6872
59.8500	-1.1571	0.5456	10.0128
69.8250	-1.3939	0.6189	11.6710
79.8000	-1.6436	0.6874	13.3267
89.7750	-1.9063	0.7515	14.9808
94.7625	-2.0428	0.7819	15.8077
99.7500	-2.1827	0.8113	16.6347
104.7375	-2.3262	0.8397	17.4624
109.7250	-2.4735	0.8672	18.2912

Table 10.22: Actuator #4 Load Node Displacement Values, Load Case 2.

Act. #2 Load (kips)	X-Disp. (in.)	Y-Disp. (in.)	Z-Disp. (in.)
0.0000	0.0000	0.0000	0.0000
19.9500	-0.2429	0.2556	3.4557
39.9000	-0.5399	0.4892	6.8987
59.8500	-0.8908	0.7011	10.3271
69.8250	-1.0864	0.7991	12.0358
79.8000	-1.2957	0.8922	13.7414
89.7750	-1.5187	0.9804	15.4447
94.7625	-1.6356	1.0228	16.2959
99.7500	-1.7561	1.0642	17.1472
104.7375	-1.8803	1.1045	17.9990
109.7250	-2.0084	1.1438	18.8517

Table 10.23: Actuator #5 Load Node Displacement Values, Load Case 2.

Act. #2 Load (kips)	X-Disp. (in.)	Y-Disp. (in.)	Z-Disp. (in.)
0.0000	0.0000	0.0000	0.0000
19.9500	-0.1135	0.0990	1.0930
39.9000	-0.2361	0.1951	2.1850
59.8500	-0.3684	0.2886	3.2771
69.8250	-0.4384	0.3344	3.8239
79.8000	-0.5113	0.3798	4.3718
89.7750	-0.5874	0.4248	4.9215
94.7625	-0.6267	0.4473	5.1973
99.7500	-0.6670	0.4697	5.4740
104.7375	-0.7083	0.4922	5.7517
109.7250	-0.7507	0.5147	6.0307

Table 10.24: Actuator #6 Load Node Displacement Values, Load Case 1.

Act. #2 Load (kips)	X-Disp. (in.)	Y-Disp. (in.)	Z-Disp. (in.)
0.0000	0.0000	0.0000	0.0000
19.9500	-0.0646	0.0934	0.6735
39.9000	-0.1334	0.1858	1.3443
59.8500	-0.2067	0.2772	2.0137
69.8250	-0.2453	0.3228	2.3486
79.8000	-0.2853	0.3683	2.6841
89.7750	-0.3269	0.4140	3.0210
94.7625	-0.3484	0.4369	3.1902
99.7500	-0.3704	0.4600	3.3601
104.7375	-0.3929	0.4831	3.5309
109.7250	-0.4161	0.5065	3.7027

Table 10.25: Actuator #7b Load Node Displacement Values, Load Case 2.

Act. #2 Load (kips)	X-Disp. (in.)	Y-Disp. (in.)	Z-Disp. (in.)
0.0000	0.0000	0.0000	0.0000
19.9500	-0.0032	0.0503	0.3641
39.9000	-0.0094	0.1002	0.7286
59.8500	-0.0189	0.1500	1.0944
69.8250	-0.0251	0.1748	1.2783
79.8000	-0.0324	0.1998	1.4631
89.7750	-0.0409	0.2248	1.6493
94.7625	-0.0457	0.2374	1.7431
99.7500	-0.0509	0.2501	1.8374
104.7375	-0.0566	0.2628	1.9323
109.7250	-0.0627	0.2756	2.0279

Table 10.26: Actuator #8 Load Node Displacement Values, Load Case 2.

Act. #2 Load (kips)	X-Disp. (in.)	Y-Disp. (in.)	Z-Disp. (in.)
0.0000	0.0000	0.0000	0.0000
19.9500	-0.0100	0.0568	0.3288
39.9000	-0.0220	0.1133	0.6564
59.8500	-0.0364	0.1697	0.9838
69.8250	-0.0446	0.1980	1.1480
79.8000	-0.0536	0.2264	1.3129
89.7750	-0.0635	0.2550	1.4789
94.7625	-0.0688	0.2694	1.5626
99.7500	-0.0744	0.2840	1.6467
104.7375	-0.0804	0.2986	1.7315
109.7250	-0.0867	0.3134	1.8170

Table 10.27: Rib 2/Lower Cover/Aft Spar Junction Node Displacement Values, Load Case 2.

Act. #2 Load (kips)	X-Disp. (in.)	Y-Disp. (in.)	Z-Disp. (in.)
0.0000	0.0000	0.0000	0.0000
19.9500	0.0339	0.0146	0.0638
39.9000	0.0665	0.0291	0.1280
59.8500	0.0979	0.0436	0.1927
69.8250	0.1131	0.0508	0.2255
79.8000	0.1280	0.0581	0.2586
89.7750	0.1424	0.0655	0.2920
94.7625	0.1494	0.0692	0.3089
99.7500	0.1564	0.0729	0.3260
104.7375	0.1632	0.0767	0.3432
109.7250	0.1698	0.0805	0.3606

Table 10.28: Rib 2/Lower Cover/Fore Spar Junction Node Displacement Values, Load Case 1.

Act. #2 Load (kips)	X-Disp. (in.)	Y-Disp. (in.)	Z-Disp. (in.)
0.0000	0.0000	0.0000	0.0000
19.9500	0.0145	0.0087	0.0015
39.9000	0.0287	0.0173	0.0027
59.8500	0.0425	0.0257	0.0039
69.8250	0.0493	0.0298	0.0044
79.8000	0.0560	0.0340	0.0050
89.7750	0.0626	0.0380	0.0057
94.7625	0.0658	0.0400	0.0060
99.7500	0.0691	0.0421	0.0064
104.7375	0.0723	0.0441	0.0068
109.7250	0.0755	0.0461	0.0073

Table 10.29: Actuator #1 Load Node Displacement Values, Load Case 3.

Act. #7a Load (kips)	X-Disp. (in.)	Y-Disp. (in.)	Z-Disp. (in.)
0.0000	0.0000	0.0000	0.0000
37.3350	-0.1253	0.1793	0.2144
74.6700	-0.2496	0.3572	0.4191
112.0050	-0.3726	0.5331	0.6121
130.6725	-0.4333	0.6202	0.7034
149.3400	-0.4935	0.7066	0.7908
168.0075	-0.5531	0.7921	0.8737
177.3413	-0.5826	0.8346	0.9132
186.6750	-0.6119	0.8768	0.9515
196.0088	-0.6409	0.9187	0.9882
205.3425	-0.6698	0.9604	1.0235

Table 10.30: Actuator #2 Load Node Displacement Values, Load Case 3.

Act. #7a Load (kips)	X-Disp. (in.)	Y-Disp. (in.)	Z-Disp. (in.)
0.0000	0.0000	0.0000	0.0000
37.3350	-0.0973	0.2011	-0.0148
74.6700	-0.1943	0.4018	-0.0400
112.0050	-0.2905	0.6016	-0.0778
130.6725	-0.3382	0.7011	-0.1022
149.3400	-0.3855	0.8000	-0.1309
168.0075	-0.4324	0.8985	-0.1644
177.3413	-0.4557	0.9474	-0.1831
186.6750	-0.4788	0.9962	-0.2033
196.0088	-0.5018	1.0448	-0.2250
205.3425	-0.5246	1.0932	-0.2483

Table 10.31: Actuator #3 Load Node Displacement Values, Load Case 3.

Act. #7a Load (kips)	X-Disp. (in.)	Y-Disp. (in.)	Z-Disp. (in.)
0.0000	0.0000	0.0000	0.0000
37.3350	-0.1013	0.1169	0.2857
74.6700	-0.2017	0.2318	0.5653
112.0050	-0.3007	0.3444	0.8376
130.6725	-0.3496	0.3998	0.9705
149.3400	-0.3980	0.4545	1.1009
168.0075	-0.4459	0.5084	1.2285
177.3413	-0.4696	0.5350	1.2911
186.6750	-0.4932	0.5614	1.3529
196.0088	-0.5165	0.5876	1.4137
205.3425	-0.5397	0.6136	1.4736

Table 10.32: Actuator #4 Load Node Displacement Values, Load Case 3.

Act. #7a Load (kips)	X-Disp. (in.)	Y-Disp. (in.)	Z-Disp. (in.)
0.0000	0.0000	0.0000	0.0000
37.3350	-0.0598	0.1365	-0.0102
74.6700	-0.1193	0.2725	-0.0277
112.0050	-0.1782	0.4075	-0.0537
130.6725	-0.2074	0.4746	-0.0705
149.3400	-0.2363	0.5413	-0.0902
168.0075	-0.2649	0.6076	-0.1131
177.3413	-0.2791	0.6405	-0.1259
186.6750	-0.2932	0.6733	-0.1397
196.0088	-0.3072	0.7060	-0.1545
205.3425	-0.3211	0.7385	-0.1704

Table 10.33: Actuator #5 Load Node Displacement Values, Load Case 3.

Act. #7a Load (kips)	X-Disp. (in.)	Y-Disp. (in.)	Z-Disp. (in.)
0.0000	0.0000	0.0000	0.0000
37.3350	-0.0840	0.0844	0.2912
74.6700	-0.1673	0.1669	0.5793
112.0050	-0.2498	0.2473	0.8636
130.6725	-0.2906	0.2867	1.0040
149.3400	-0.3312	0.3255	1.1431
168.0075	-0.3714	0.3637	1.2807
177.3413	-0.3913	0.3825	1.3489
186.6750	-0.4112	0.4012	1.4167
196.0088	-0.4309	0.4197	1.4839
205.3425	-0.4505	0.4380	1.5507

Table 10.34: Actuator #6 Load Node Displacement Values, Load Case 1.

Act. #7a Load (kips)	X-Disp. (in.)	Y-Disp. (in.)	Z-Disp. (in.)
0.0000	0.0000	0.0000	0.0000
37.3350	-0.0063	0.0662	-0.1309
74.6700	-0.0127	0.1325	-0.2658
112.0050	-0.0191	0.1986	-0.4054
130.6725	-0.0223	0.2316	-0.4772
149.3400	-0.0255	0.2645	-0.5505
168.0075	-0.0287	0.2972	-0.6255
177.3413	-0.0303	0.3135	-0.6637
186.6750	-0.0318	0.3298	-0.7024
196.0088	-0.0334	0.3460	-0.7416
205.3425	-0.0349	0.3622	-0.7814

Table 10.35: Actuator #7a Load Node Displacement Values, Load Case 3.

Act. #7a Load (kips)	X-Disp. (in.)	Y-Disp. (in.)	Z-Disp. (in.)
0.0000	0.0000	0.0000	0.0000
37.3350	-0.7409	1.0898	1.3426
74.6700	-1.5603	2.1704	2.7169
112.0050	-2.4761	3.2406	4.1267
130.6725	-2.9774	3.7713	4.8465
149.3400	-3.5124	4.2989	5.5774
168.0075	-4.0856	4.8230	6.3206
177.3413	-4.3881	5.0837	6.6972
186.6750	-4.7022	5.3434	7.0775
196.0088	-5.0286	5.6021	7.4617
205.3425	-5.3683	5.8598	7.8501

Table 10.36: Actuator #8 Load Node Displacement Values, Load Case 3.

Act. #7a Load (kips)	X-Disp. (in.)	Y-Disp. (in.)	Z-Disp. (in.)
0.0000	0.0000	0.0000	0.0000
37.3350	-0.0074	0.0530	-0.0953
74.6700	-0.0150	0.1059	-0.1928
112.0050	-0.0230	0.1589	-0.2927
130.6725	-0.0271	0.1853	-0.3438
149.3400	-0.0313	0.2116	-0.3957
168.0075	-0.0356	0.2379	-0.4484
177.3413	-0.0378	0.2510	-0.4751
186.6750	-0.0400	0.2640	-0.5021
196.0088	-0.0422	0.2771	-0.5293
205.3425	-0.0445	0.2901	-0.5569

Table 10.37: Rib 2/Lower Cover/Aft Spar Junction Node Displacement Values, Load Case 2.

Act. #7a Load (kips)	X-Disp. (in.)	Y-Disp. (in.)	Z-Disp. (in.)
0.0000	0.0000	0.0000	0.0000
37.3350	-0.0163	0.0395	0.0648
74.6700	-0.0328	0.0788	0.1298
112.0050	-0.0496	0.1180	0.1950
130.6725	-0.0581	0.1375	0.2276
149.3400	-0.0667	0.1570	0.2603
168.0075	-0.0754	0.1765	0.2930
177.3413	-0.0798	0.1862	0.3094
186.6750	-0.0842	0.1959	0.3258
196.0088	-0.0886	0.2056	0.3422
205.3425	-0.0931	0.2152	0.3586

Table 10.38: Rib 2/Lower Cover/Fore Spar Junction Node Displacement Values, Load Case 1.

Act. #7a Load (kips)	X-Disp. (in.)	Y-Disp. (in.)	Z-Disp. (in.)
0.0000	0.0000	0.0000	0.0000
37.3350	0.0016	0.0089	-0.0264
74.6700	0.0031	0.0178	-0.0528
112.0050	0.0043	0.0266	-0.0793
130.6725	0.0049	0.0310	-0.0925
149.3400	0.0054	0.0354	-0.1057
168.0075	0.0058	0.0398	-0.1189
177.3413	0.0060	0.0420	-0.1255
186.6750	0.0061	0.0441	-0.1321
196.0088	0.0063	0.0463	-0.1387
205.3425	0.0064	0.0485	-0.1454

10.4 Figures

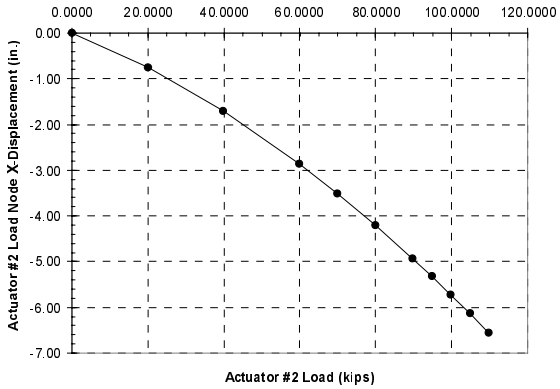

Figure 10.1: Actuator #2 Load Node X-Displacement as a Function of Actuator #2 Load, Load Case 2.

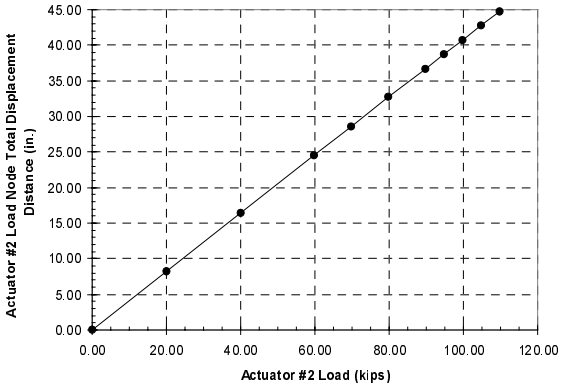

Figure 10.4: Actuator #2 Load Node Total Displacement Distance as a Function of Actuator #2 Load, Load Case 2.

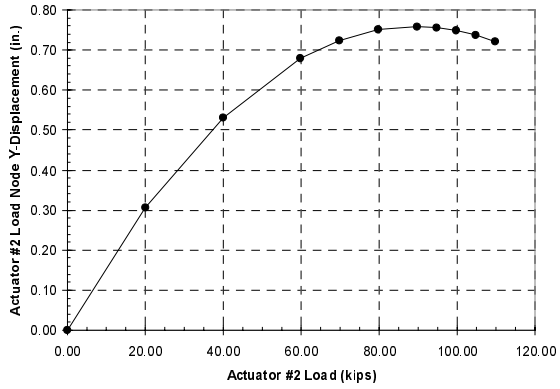

Figure 10.2: Actuator #2 Load Node Y-Displacement as a Function of Actuator #2 Load, Load Case 2.

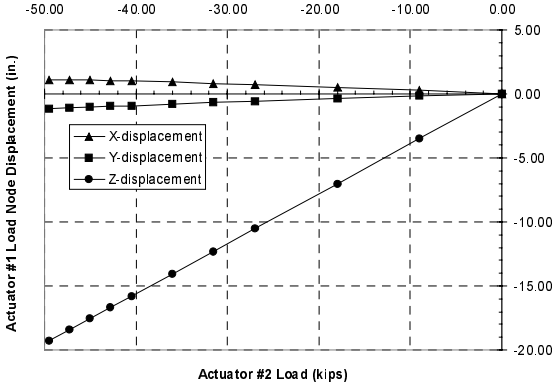

Figure 10.5: Actuator #1 Load Node Component Displacements as a Function of Actuator #2 Load, Load Case 1.

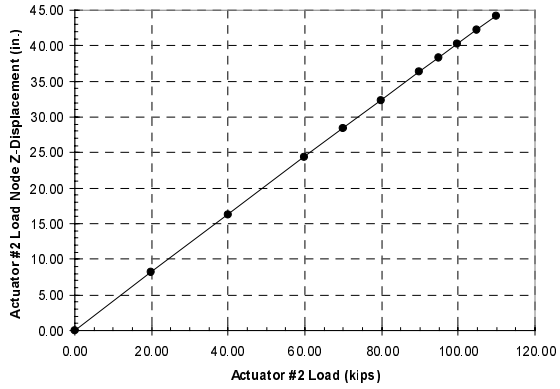

Figure 10.3: Actuator #2 Load Node Z-Displacement as a Function of Actuator #2 Load, Load Case 2.

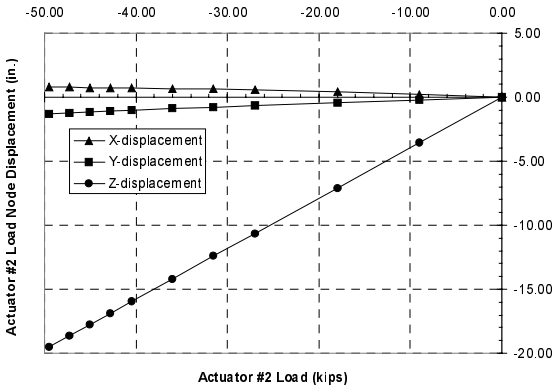

Figure 10.6: Actuator #2 Load Node Component Displacements as a Function of Actuator #2 Load, Load Case 1.

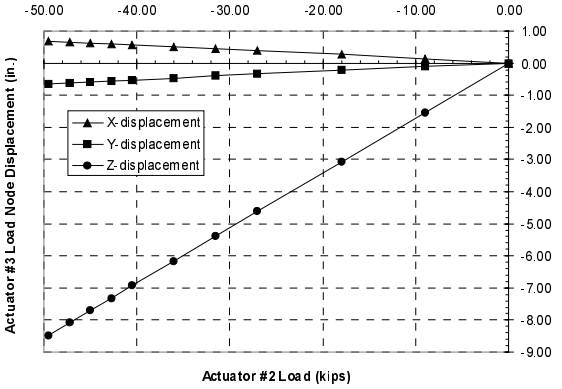

Figure 10.7: Actuator #3 Load Node Component Displacements as a Function of Actuator #2 Load, Load Case 1.

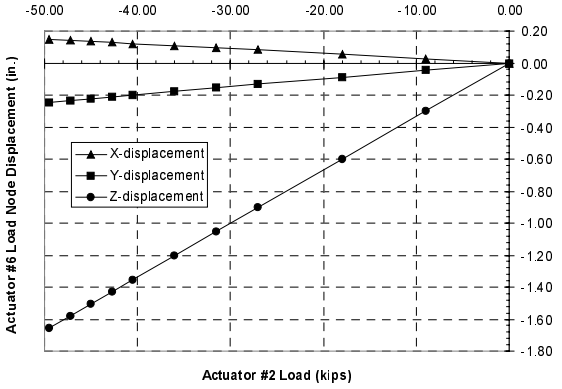

Figure 10.10: Actuator #6 Load Node Component Displacements as a Function of Actuator #2 Load, Load Case 1.

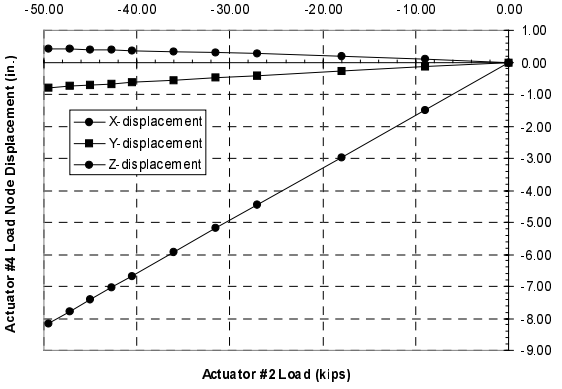

Figure 10.8: Actuator #4 Load Node Component Displacements as a Function of Actuator #2 Load, Load Case 1.

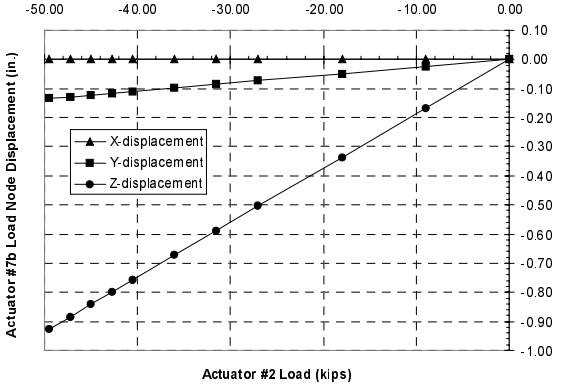

Figure 10.11: Actuator #7b Load Node Component Displacements as a Function of Actuator #2 Load, Load Case 1.

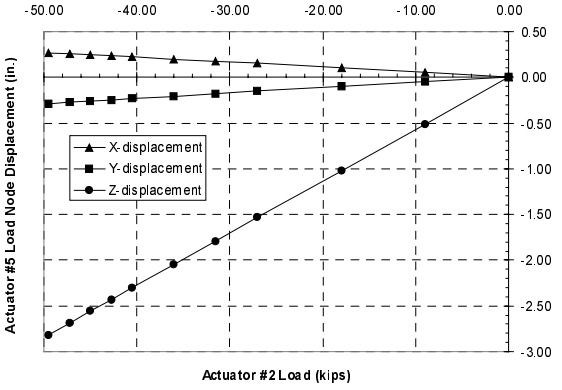

Figure 10.9: Actuator #5 Load Node Component Displacements as a Function of Actuator #2 Load, Load Case 1.

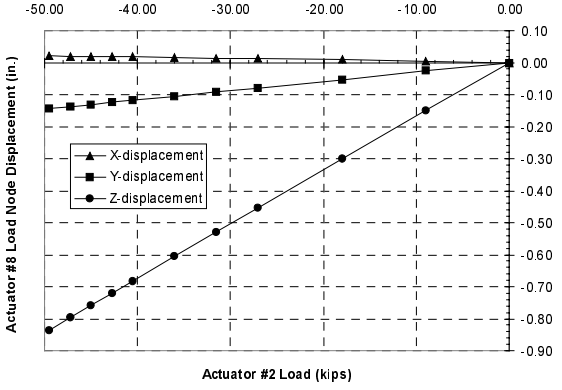

Figure 10.12: Actuator #8 Load Node Component Displacements as a Function of Actuator #2 Load, Load Case 1.

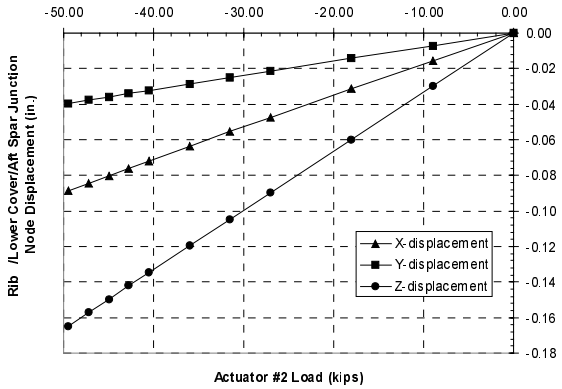

Figure 10.13: Rib 2/Lower Cover/Aft Spar Junction Node Component Displacements as a Function of Actuator #2 Load, Load Case 1.

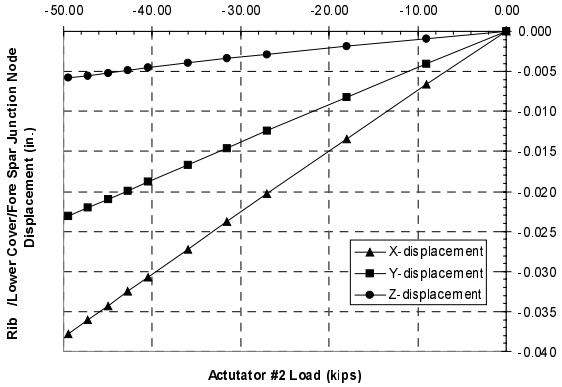

Figure 10.14: Rib 2/Lower Cover/Fore Spar Junction Node Component Displacements as a Function of Actuator #2 Load, Load Case 1.

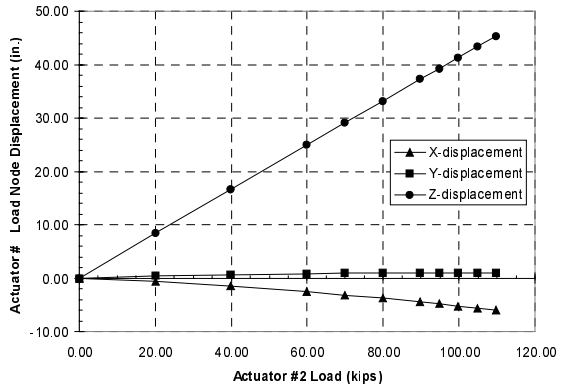

Figure 10.15: Actuator #1 Load Node Component Displacements as a Function of Actuator #2 Load, Load Case 2.

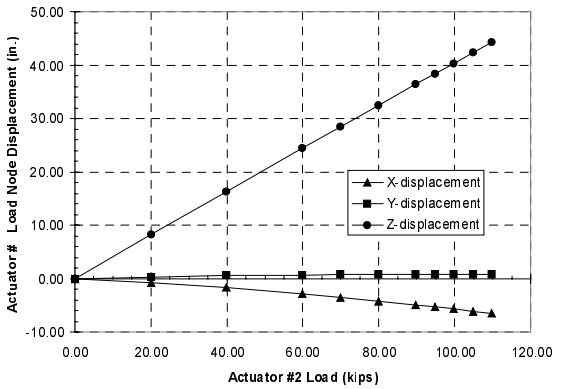

Figure 10.16: Actuator #2 Load Node Component Displacements as a Function of Actuator #2 Load, Load Case 2.

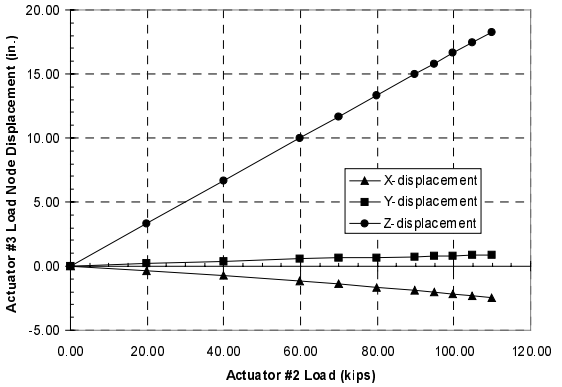

Figure 10.17: Actuator #3 Load Node Component Displacements as a Function of Actuator #2 Load, Load Case 2.

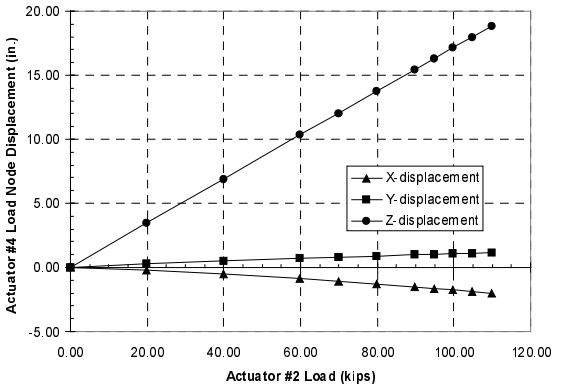

Figure 10.18: Actuator #4 Load Node Component Displacements as a Function of Actuator #2 Load, Load Case 2.

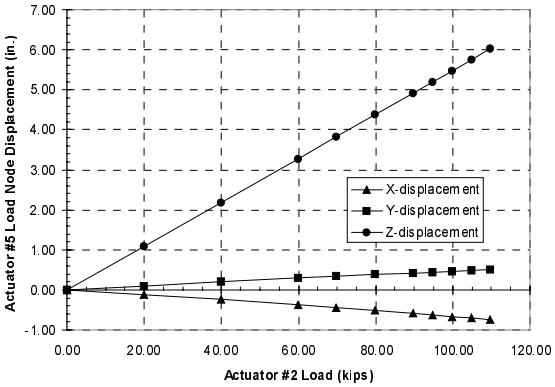

Figure 10.19: Actuator #5 Load Node Component Displacements as a Function of Actuator #2 Load, Load Case 2.

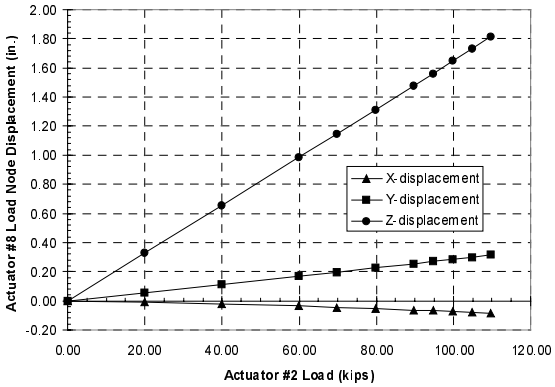

Figure 10.22: Actuator #8 Load Node Component Displacements as a Function of Actuator #2 Load, Load Case 2.

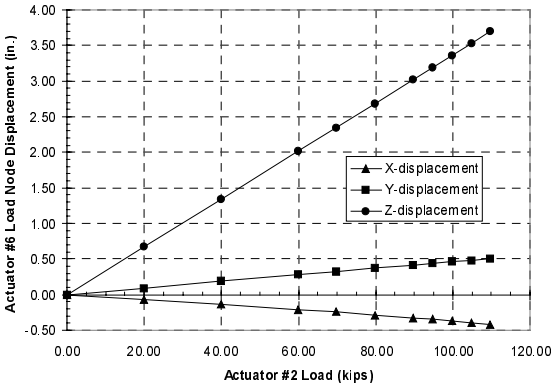

Figure 10.20: Actuator #6 Load Node Component Displacements as a Function of Actuator #2 Load, Load Case 2.

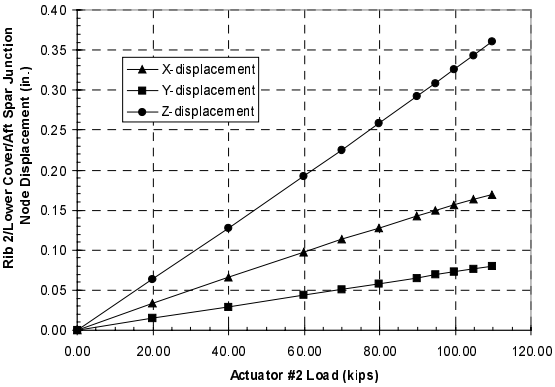

Figure 10.23: Rib 2/Lower Cover/Aft Spar Junction Node Component Displacements as a Function of Actuator #2 Load, Load Case 2.

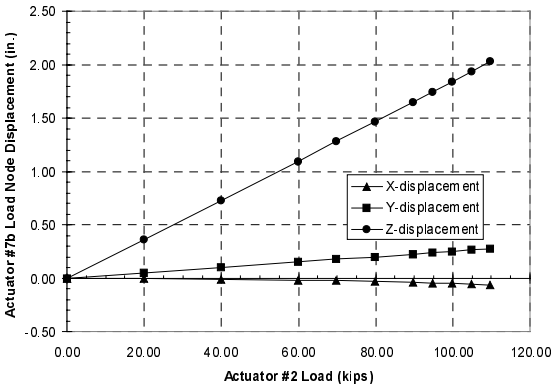

Figure 10.21: Actuator #7b Load Node Component Displacements as a Function of Actuator #2 Load, Load Case 2.

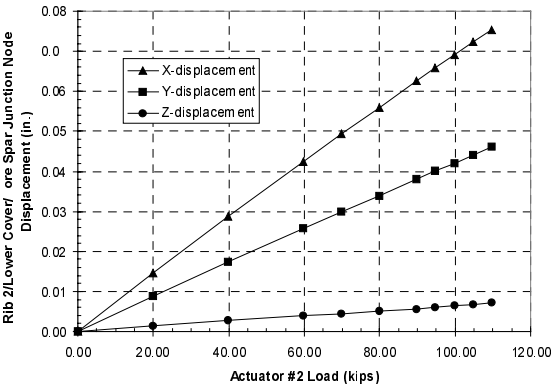

Figure 10.24: Rib 2/Lower Cover/Fore Spar Junction Node Component Displacements as a Function of Actuator #2 Load, Load Case 2.

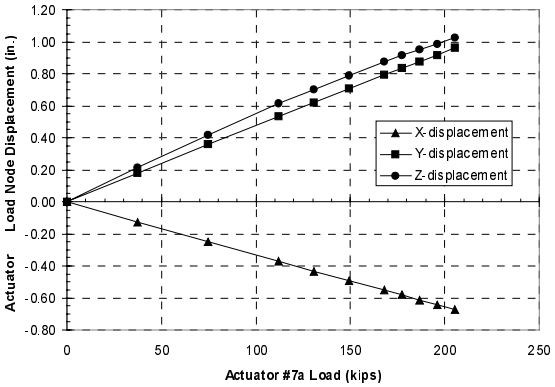

Figure 10.25: Actuator #1 Load Node Component Displacements as a Function of Actuator #7a Load, Load Case 3.

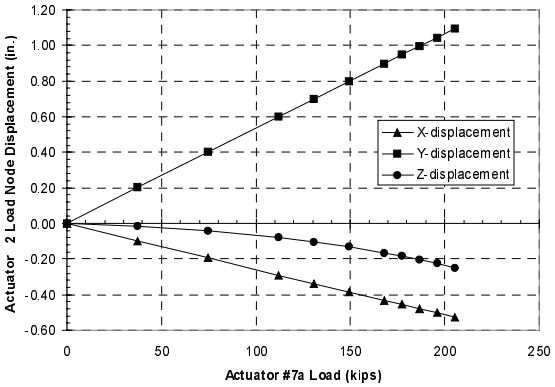

Figure 10.26: Actuator #2 Load Node Component Displacements as a Function of Actuator #7a Load, Load Case 3.

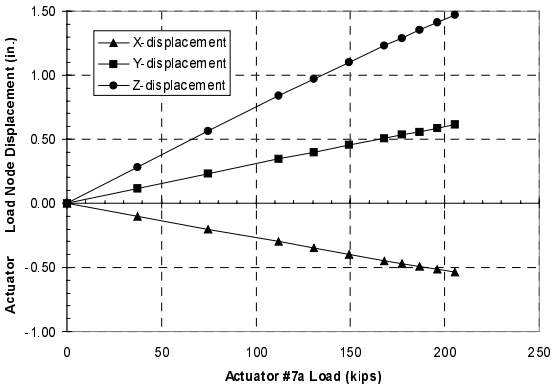

Figure 10.27: Actuator #3 Load Node Component Displacements as a Function of Actuator #7a Load, Load Case 3.

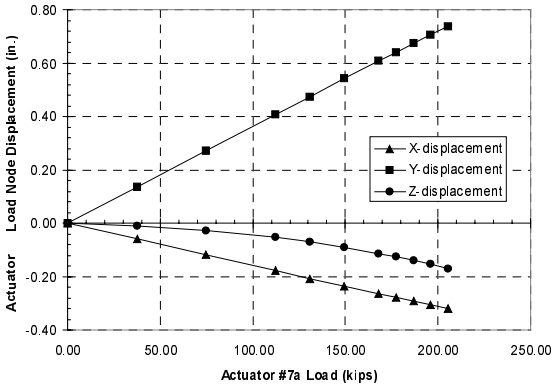

Figure 10.28: Actuator #4 Load Node Component Displacements as a Function of Actuator #7a Load, Load Case 3.

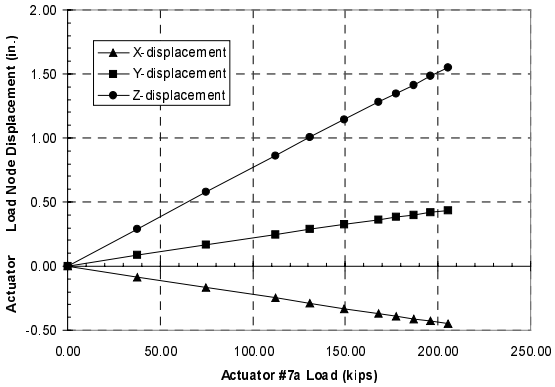

Figure 10.29: Actuator #5 Load Node Component Displacements as a Function of Actuator #7a Load, Load Case 3.

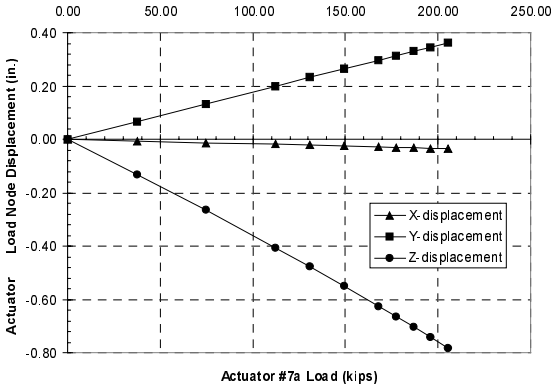

Figure 10.30: Actuator #6 Load Node Component Displacements as a Function of Actuator #7a Load, Load Case 3.

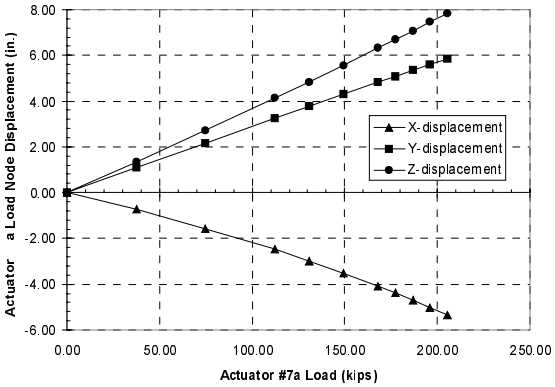

Figure 10.31: Actuator #7a Load Node Component Displacements as a Function of Actuator #7a Load, Load Case 3.

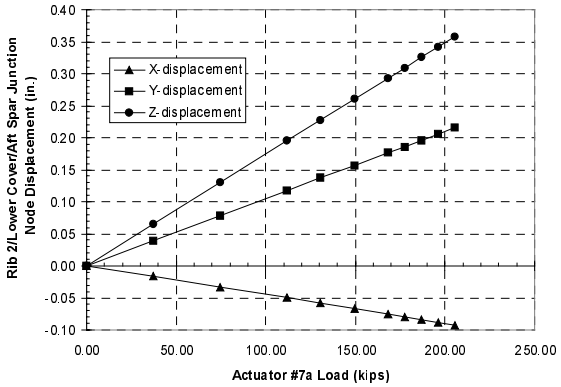

Figure 10.33: Rib 2/Lower Cover/Aft Spar Junction Node Component Displacements as a Function of Actuator #7a Load, Load Case 3.

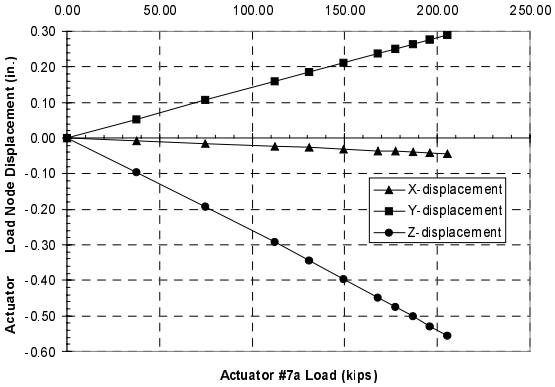

Figure 10.32: Actuator #8 Load Node Component Displacements as a Function of Actuator #7a Load, Load Case 3.

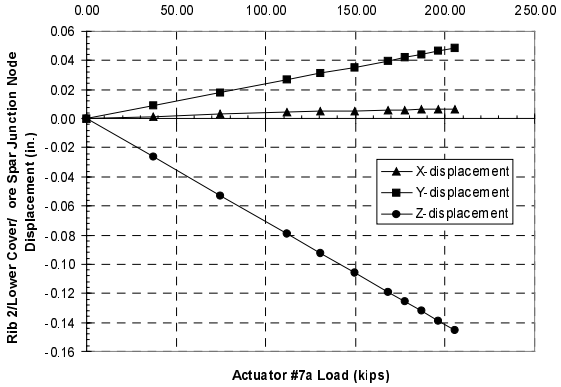

Figure 10.34: Rib 2/Lower Cover/Fore Spar Junction Node Component Displacements as a Function of Actuator #7a Load, Load Case 3.

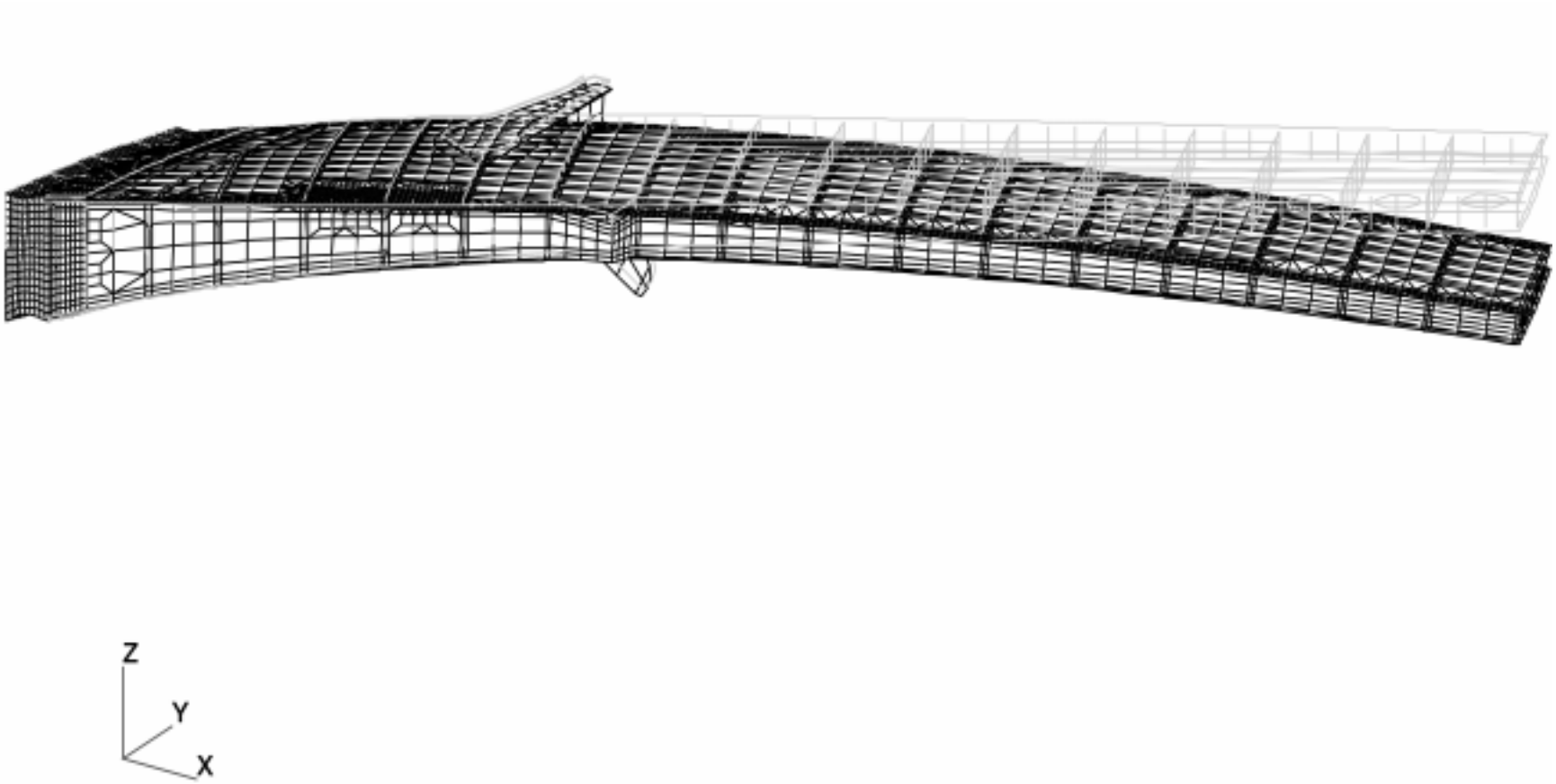

Figure 10.35: Detailed Model Overall Deformation Plot for the Composite Semi-Span Under 1.0G Down Bending. Undeformed Shape Shown as Skeleton in Grey, Deformations Multiplied by a Factor of 2.

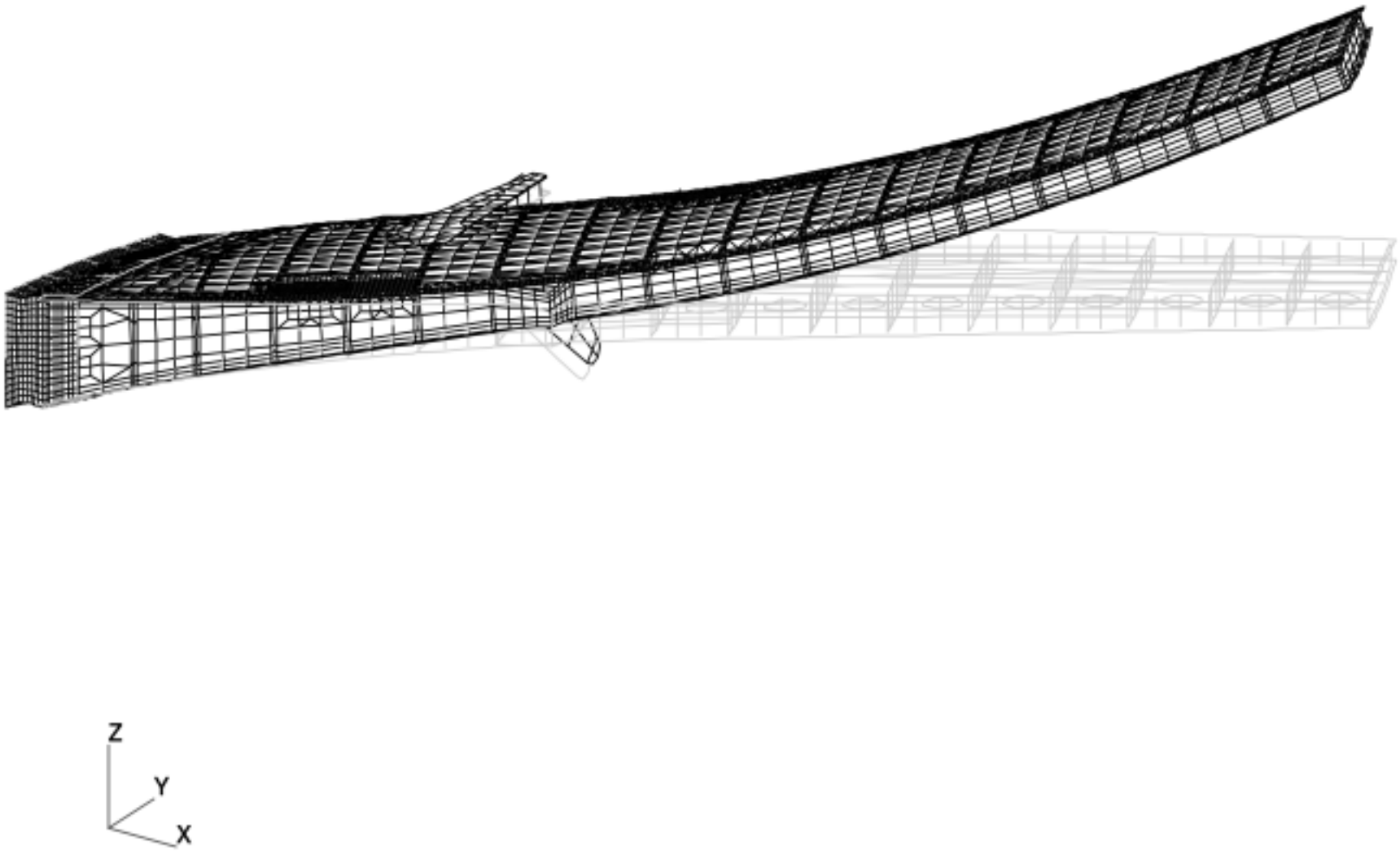

Figure 10.36: Detailed Model Overall Deformation Plot for the Composite Semi-Span Under 2.5G Up Bending. Undeformed Shape Shown as Skeleton in Grey, Deformations Multiplied by a Factor of 2.

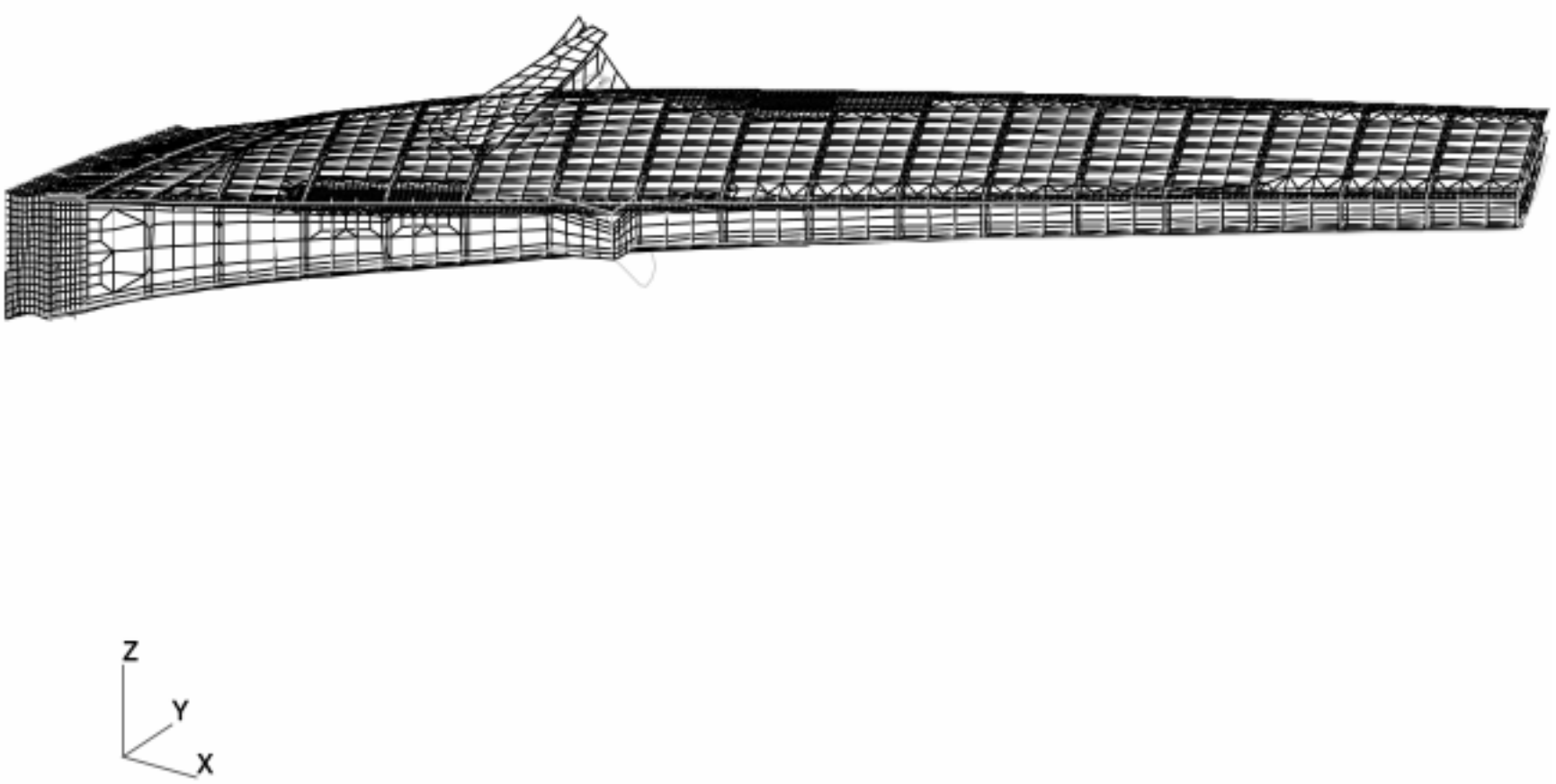

Figure 10.37: Detailed Model Overall Deformation Plot for the Composite Semi-Span Under Braked Roll. Undeformed Shape Shown as Skeleton in Grey, Deformations Multiplied by a Factor of 3.

11. Loadarm Region Analysis with Follower Load

11.1 Follower Load Implementation

The load applied by actuator #7a for the braked roll case was made to be a follower load, with all other applied loads remaining as fixed loads in the z-direction. In previous analyses, this actuator #7a load was applied to a node attached to the loadarm plate. However, simply applying this load as a follower load does not have the required effect. This is because the conventional follower load will rotate with the node to which it is applied, whereas what is required is a load that remains oriented along the axis of the load actuator cell. Therefore, as mentioned in Section 3.3.6, a beam was added to the model to act as the load actuator cell. The applied load is therefore attached to the end node of this actuator beam, where it then becomes a conventional follower load with respect to the actuator beam.

The base of the actuator beam is fixed to the ground by setting all three translations equal to zero (see Figures 2.1, 3.15, 3.16 and 3.18 for actuator location). However, since setting only these three degrees of freedom does not restrain rigid body rotation about the beam axis, the rotation about the y-axis was also set to zero. This added boundary condition does not over constrain the system, it simply eliminates the rigid body rotation about the beam axis. The remaining rigid body rotations are eliminated when translational compatibility between the force end of the actuator beam and the loadarm plate is enforced. Translational compatibility between the actuator beam load node and the loadarm attachment node satisfies the requirement that the two nodes have the same location in space, but they are free to rotate independent of each other. It is this capability of independent rotation of the actuator beam and loadarm plate that ensures that the follower load is oriented properly. However, the connection of these two nodes turned out to be problematic.

The initial connection method for the actuator load beam and the loadarm plate was via the STAGS G2 record [1]. G2 records are used to enforce partial compatibility between displacements at particular nodes. Using this single record appeared to be the best method to use, but this turned out not to be the case. Examination of the final orientation for the follower force indicated that this method appears to orient the follower force based upon the average rotation of the connected nodes. This, naturally, is not the correct orientation for the follower force. Therefore, and alternative method which used the G3 and G4 records was implemented. These records define Lagrange constraints, permitting the user to effectively enforce the compatibility of the required degrees of freedom (translations in this case). Using this method of connection resulted in a follower force that was oriented along the axis of the actuator beam, which was the desired result. Unfortunately, this method has several difficulties that must be addressed. First, the constraint equations increase the number of degrees of freedom in the model (1 degree of freedom for each constraint). Second, constraints with large numbers of term can have a detrimental effect on the bandwidth of the system, causing the solution time to increase dramatically. Third, numerical difficulties can arise unless the constraint is scaled so that the stiffness terms introduced by the constraint equation are of the same order of magnitude as the other stiffness matrix terms. Lastly, one negative root will appear for each constraint equation. For the semi-span test article analysis, none of these problems were of great importance since only three equations containing two terms each were introduced (one for each tranlational degree of freedom at the coincident nodes).

11.2 Results

Results were obtained under the follower load braked roll load case for two different cases. The first case was the semi-span with no constraint on the loadarm plate. During this analysis case, the loadarm plate is able to deform freely. The second analysis case has a constraint added so that the loadarm plate

is forced to have a small x-deflection near the actuator #7a attachment point. This constraint is necessary since the x-deflection for the actuator load node in the unconstrained case is sufficiently large as to possibly exceed the range of motion allowed by the swivel at the load actuator cell base. Discussion of the two analyses and their results follows.

11.2.1 Loadarm Model

11.2.1.1 Unconstrained Loadarm Plate

The loadarm model was first studied with no constraints applied to the loadarm plate. This is the same as for all previous analyses where the only boundary conditions are those applied to the root mount plates at the wall nodes. Therefore, the loadarm plate is able to deform freely according to the applied loading. Because of this, the loadarm plate exhibits bending and torsion that result from the actuator load being eccentrically applied with respect to the loadarm I-beam web. Figures 11.1 and 11.2 clearly show the bending and twisting response of the loadarm plate. Figure 11.1 shows the undeformed and deformed loadarm plate at DUL for a view looking down the negative z-axis, while Figure 11.2 shows the same for a view looking down the negative y-axis. The out-of-plane deformation of the loadarm plate is emphasized further in Figure 11.3 that shows a contour plot of x-deflection. Larger x-deflections seen at the actuator load end of the loadarm plate demonstrate the bending response, while the contour lines not being perpendicular to the edges indicates the twisting response. Lastly, Figure 11.4 shows the overall deflection pattern for the composite semi-span test article under braked roll with a follower load. Note that this primarily produces a torsional deformation of the semi-span as was seen with the constant direction load, but the loadarm plate suffers from additional out-of-plane deformations not seen under the constant direction load scenario.

Deflection results for three node locations have also been compiled and are presented in Tables 11.1-11.3. Figure 11.5 shows the locations of the three nodes with respect to the loadarm plate. Table 11.1 gives the deflections of node 131 of the loadarm plate, which is tied through the Lagrange constraints to the actuator beam end node. Table 11.2 gives the deflections of a node approximately 3 inches interior to the loadarm from the actuator attachment fixture, shown as node 71 in the figure. Table 11.3 gives the deflection of the uppermost leading edge node of the loadarm plate, node 6684 in the figure. Load factor/deflection plots corresponding to Tables 11.1-11.3 are shown in Figures 11.6-11.8.

Finally, the NASTRAN file of the loadarm, flat.bdf, that was provided by NASA was modified and the NASTRAN run was completed for comparison to the STAGS results. Modification of the NASTRAN input file flat.bdf was necessary since the analysis did not obtain converged nonlinear results with the input file as provided. Therefore, the plasticity effects were eliminated and the loading was reduced to DLL from DUL since testing will only be to DLL for the braked roll condition. A plot comparing deflection results of the current STAGS loadarm model with the deflection results from NASTRAN model is shown in Figure 11.9. It is seen that the x-deflections predicted by the two models are nearly identical. However, the y- and z-direction deflections are significantly larger for the NASTRAN model (approximately 20% and 14% for y- and z-deflections at DLL, respectively). This can possibly be explained by the lack of fidelity in the NASTRAN model where stringers are still primarily modeled as offset beams connected to the skins by multipoint constraints. Additionally, the regions of the stringer that are modeled as shells are not correctly attached to the portions of the stringer modeled as beams. This effectively creates discontinuous stringers, resulting in a more flexible model. Therefore, the results from the model developed by AS&M are deemed to be more accurate since the finite element model is a more accurate representation of the structure.

11.2.1.2 Constrained Loadarm Plate

The swivel joint at the base of load actuator cell #7a will allow approximately 3 inches of x-direction travel at the actuator tip. As seen by the results of Section 11.2.1.1, this limit value is exceeded at DUL. Even though loading will be stopped at DLL, enough concern is raised by the x-direction deflection of the loadarm plate that a means of reducing this x-deflection was proposed by NASA. The method consists of adding of a load actuator cell attached to the wall on one end and attached to the loadarm plate at the other end. The application location for this load actuator is approximately node 71, which is indicated in Figure 11.5. This added actuator will then constrain the attachment node to have an x-deflection equal to that of a node near the aft spar that has small x-deflection, namely node 6684 of Figure 11.5. Computationally, this is enforced by adding a fourth Lagrange constraint that ties the x-deflection of node 78 to the x-deflection of node 6684. The constraint forces can be recovered from the results, providing the forces necessary in the actuator to accomplish the loadarm deflection constraint.

Figure 11.10 shows a view along the negative z-axis of the loadarm plate mesh deflection under braked roll with a follower load and the additonal x-displacement constraint. Figure 11.11 is the same as Figure 11.0 but with the view along the negative y-axis. A contour plot of the loadarm plate x-deflection is shown in Figure 11.12 under the same conditions. From this figure, it is clear that the loadarm plate still suffers from out-of-plane bending, with the central portion of the loadarm plate having the maximum x-displacement. Also, these figures clearly show that the x-deflection has been controlled successfully by the application of a load actuator cell attached between the wall and the loadarm plate.

Deflections for the three nodes shown in Figure 11.5 are given in Tables 11.4-11.6, and the associated forces at nodes 131 and 71 for the same load factors are given in Tables 11.7 and 11.8, respectively. Having both deflections and forces at these nodes provides NASA with the opportunity to program the test control program for either displacement control or load control.

11.3 Tables

Table 11.1: Deflection Components (in.) for Node 131 Under Braked Roll with a Follower Load at Actuator #7a.

LF	X-Displacement	Y-Displacement	Z-Displacement
0.2	-0.3704	0.5943	0.8480
0.3	-0.5858	0.8901	1.2750
0.4	-0.8264	1.1851	1.7043
0.4667	-1.0031	1.3815	1.9922
0.5	-1.0968	1.4793	2.1364
0.6	-1.4027	1.7727	2.5716
0.6667 (DLL)	-1.6305	1.9678	2.8639
0.7	-1.7525	2.0651	3.0106
0.8	-2.1562	2.3565	3.4545
0.9	-2.6276	2.6467	3.9045
0.95	-2.8961	2.7913	4.1325
1 (DUL)	-3.1899	2.9354	4.3630

Table 11.2: Deflection Components (in.) for Node 71 Under Braked Roll with a Follower Load at Actuator #7a.

LF	X-Displacement	Y-Displacement	Z-Displacement
0.2	-0.3543	0.5160	0.9169
0.3	-0.5592	0.7724	1.3782
0.4	-0.7873	1.0277	1.8418
0.4667	-0.9542	1.1974	2.1524
0.5	-1.0425	1.2820	2.3080
0.6	-1.3299	1.5351	2.7772
0.6667 (DLL)	-1.5431	1.7033	3.0921
0.7	-1.6570	1.7871	3.2501
0.8	-2.0328	2.0379	3.7276
0.9	-2.4693	2.2873	4.2109
0.95	-2.7171	2.4113	4.4555
1 (DUL)	-2.9875	2.5349	4.7024

Table 11.3: Deflection Components (in.) for Node 6684 Under Braked Roll with a Follower Load at Actuator #7a.

LF	X-Displacement	Y-Displacement	Z-Displacement
0.2	-0.0697	0.0820	0.2693
0.3	-0.1052	0.1227	0.4041
0.4	-0.1411	0.1632	0.5392
0.4667	-0.1654	0.1901	0.6294
0.5	-0.1777	0.2035	0.6744
0.6	-0.2150	0.2436	0.8100
0.6667 (DLL)	-0.2403	0.2703	0.9005
0.7	-0.2531	0.2837	0.9458
0.8	-0.2922	0.3236	1.0820
0.9	-0.3327	0.3635	1.2187
0.95	-0.3535	0.3835	1.2873
1 (DUL)	-0.3749	0.4035	1.3561

Table 11.4: Deflection Components (in.) for Node 131 Under Braked Roll with a Follower Load at Actuator #7a and the X-Deflection Constraint on the Loadarm Plate.

LF	X-Displacement	Y-Displacement	Z-Displacement
0.2	-0.0728	0.5877	0.8387
0.3	-0.1087	0.8798	1.2597
0.4	-0.1443	1.1706	1.6818
0.4667	-0.1679	1.3640	1.9639
0.5	-0.1796	1.4603	2.1049
0.6	-0.2146	1.7488	2.5292
0.6667 (DLL)	-0.2377	1.9405	2.8129
1 (DUL)	-0.3512	2.8910	4.2384

Table 11.5: Deflection Components (in.) for Node 71 Under Braked Roll with a Follower Load at Actuator #7a and the X-Deflection Constraint on the Loadarm Plate.

LF	X-Displacement	Y-Displacement	Z-Displacement
0.2	-0.0658	0.5104	0.9069
0.3	-0.0988	0.7635	1.3617
0.4	-0.1318	1.0153	1.8175
0.4667	-0.1538	1.1824	2.1221
0.5	-0.1648	1.2657	2.2743
0.6	-0.1979	1.5147	2.7321
0.6667 (DLL)	-0.2200	1.6801	3.0380
1 (DUL)	-0.3310	2.4976	4.5740

Table 11.6: Deflection Components (in.) for Node 6684 Under Braked Roll with a Follower Load at Actuator #7a and the X-Deflection Constraint on the Loadarm Plate.

LF	X-Displacement	Y-Displacement	Z-Displacement
0.2	-0.0658	0.0816	0.2680
0.3	-0.0988	0.1219	0.4021
0.4	-0.1318	0.1619	0.5361
0.4667	-0.1538	0.1885	0.6256
0.5	-0.1648	0.2017	0.6703
0.6	-0.1979	0.2411	0.8044
0.6667 (DLL)	-0.2200	0.2673	0.8940
1 (DUL)	-0.3310	0.3962	1.3421

Table 11.7: Applied Force Components for Node 131 Under Braked Roll with a Follower Load at Actuator #7a and the X-Deflection Constraint on the Loadarm Plate.

LF	X-Force	Y-Force	Z-Force
0.2	-0.0267	22.0440	30.1320
0.3	-0.0593	33.0600	45.2020
0.4	-0.1046	44.0720	60.2760
0.4667	-0.1415	51.4140	70.3330
0.5	-0.1619	55.0780	75.3540
0.6	-0.2309	66.0790	90.4360
0.6667 (DLL)	-0.2834	73.4120	100.5000
1 (DUL)	-0.6178	110.0100	150.8100

Table 11.8: Constraint Force Components (kips) for Node 71 Under Braked Roll with a Follower Load at Actuator #7a and the X-Deflection Constraint on the Loadarm Plate.

LF	X-Force	Y-Force	Z-Force
0.2	1.5963	0.0000	0.0000
0.3	2.4250	0.0000	0.0000
0.4	3.2731	0.0000	0.0000
0.4667	3.8487	0.0000	0.0000
0.5	4.1390	0.0000	0.0000
0.6	5.0216	0.0000	0.0000
0.6667 (DLL)	5.6192	0.0000	0.0000
1 (DUL)	8.6979	0.0000	0.0000

11.4 Figures

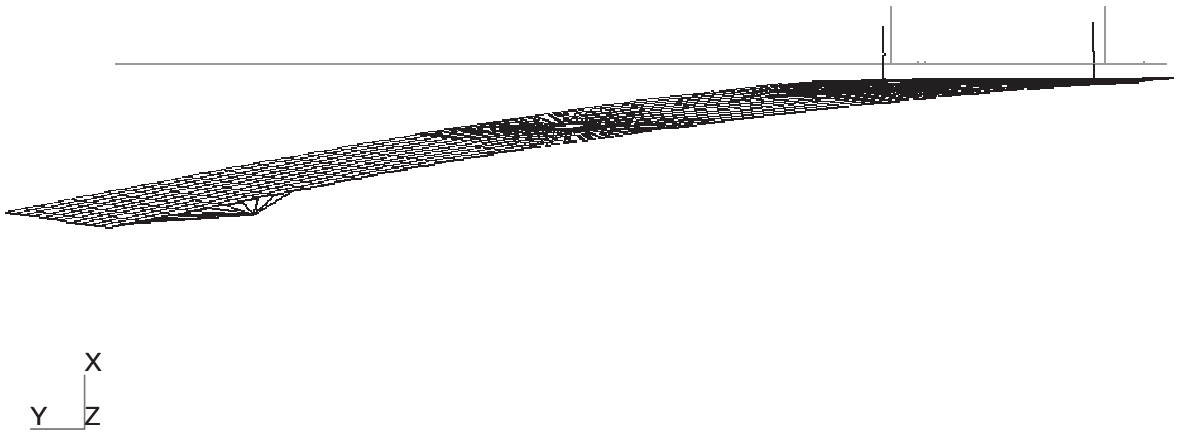

Figure 11.1: Deformed (black) and Undeformed (grey) loadarm plate at DUL for Braked Roll with the Actuator #7a Follower Load, View Along Negative Z-Axis.

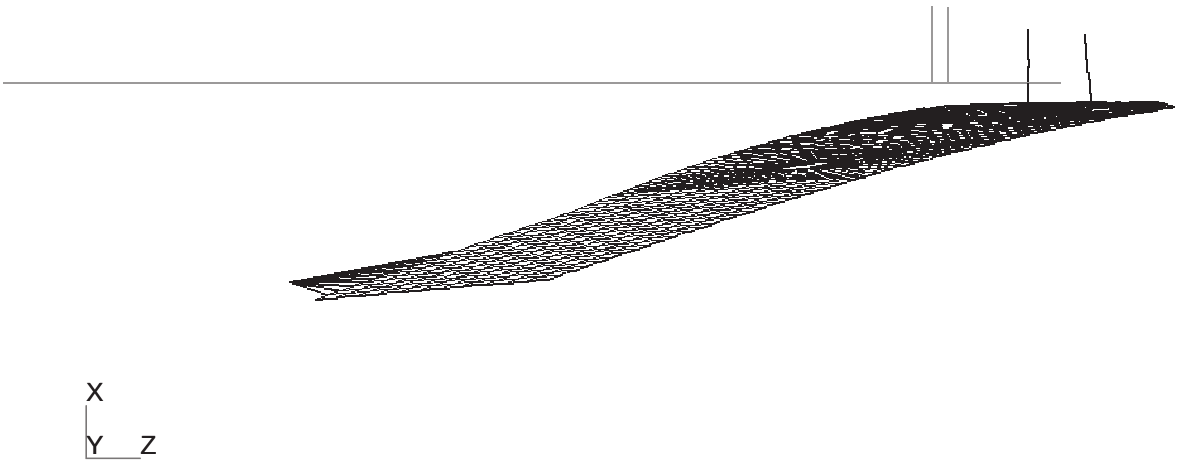

Figure 11.2: Deformed (black) and Undeformed (grey) Loadarm Plate Finite Element Mesh at DUL for Braked Roll with the Actuator #7a Follower Load, View Along Negative Y-Axis.

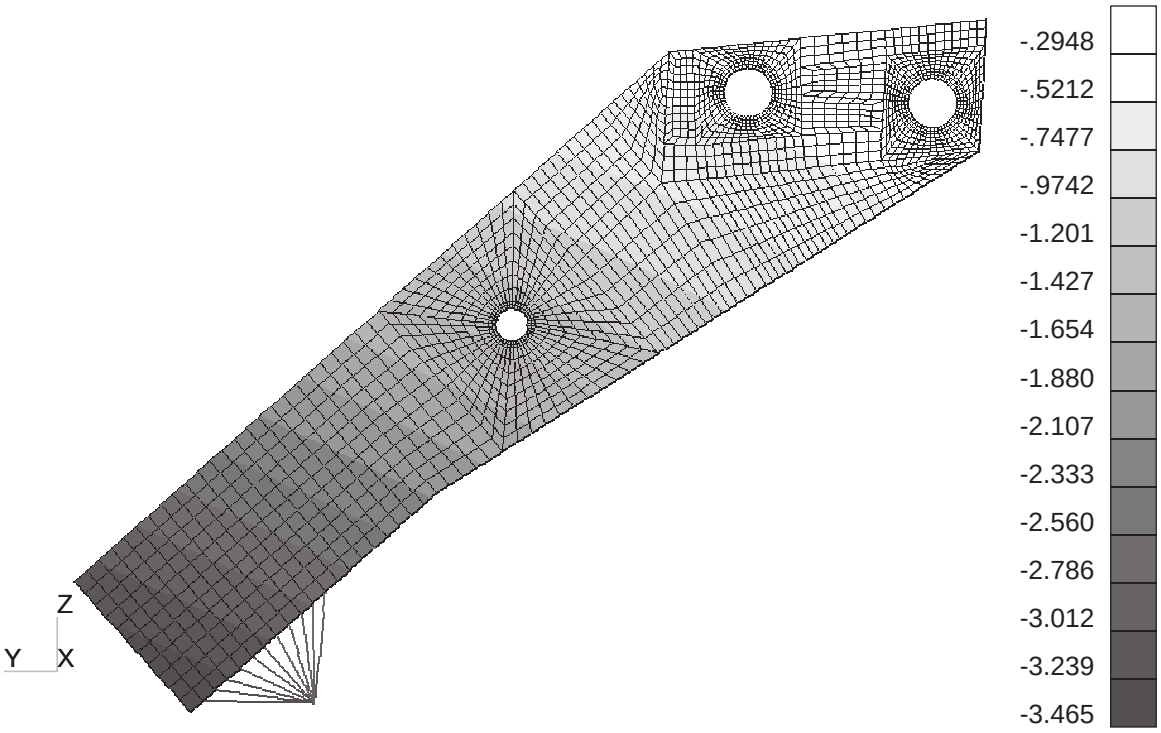

Figure 11.3: X-Deflection Contour Plot of the Loadarm Plate at DUL for Braked Roll with the Actuator #7a Follower Load.

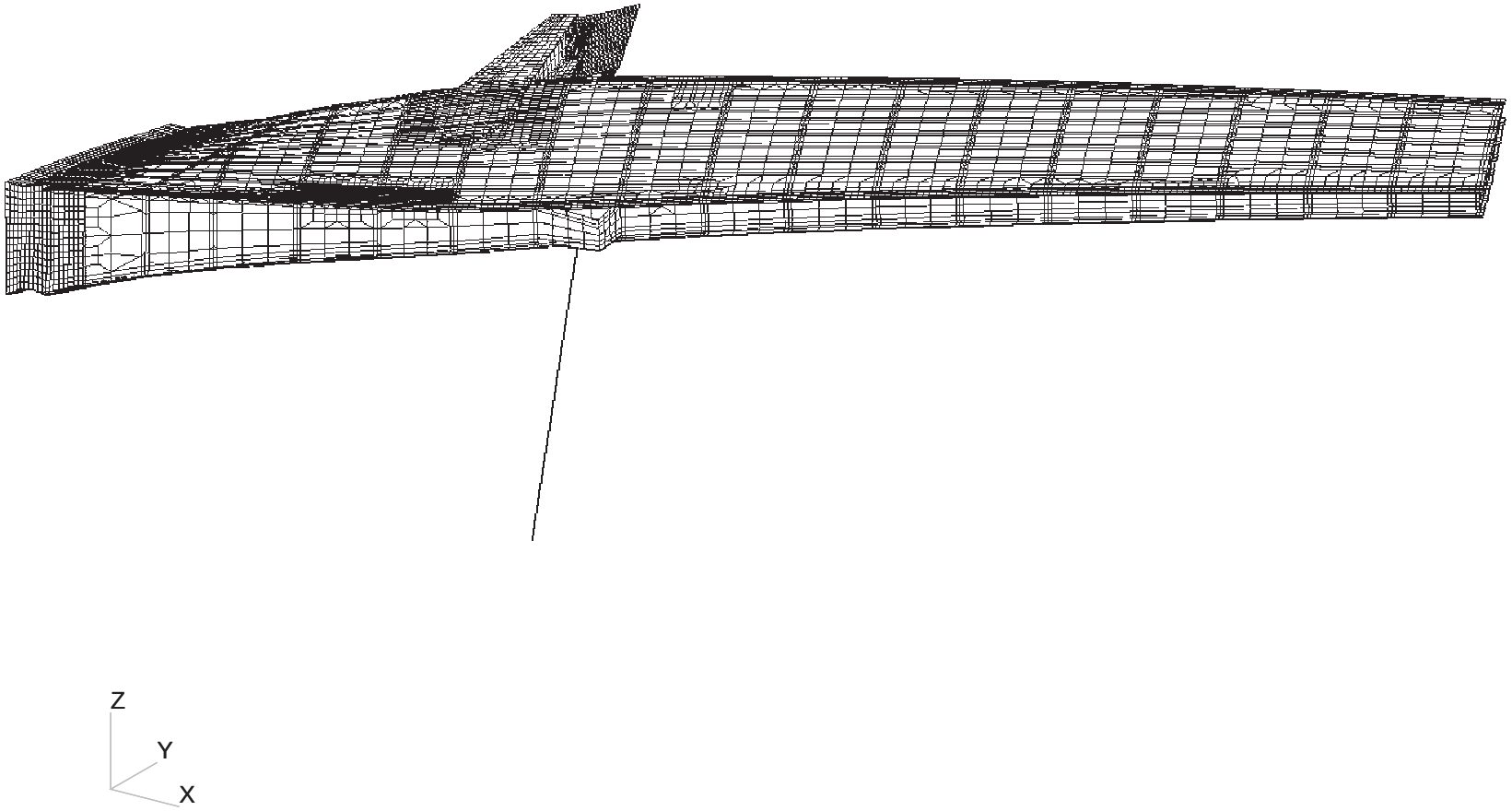

Figure 11.4: Deflection Pattern for the Loadarm Model at DUL (deflections multiplied by a factor of 10 for clarity).

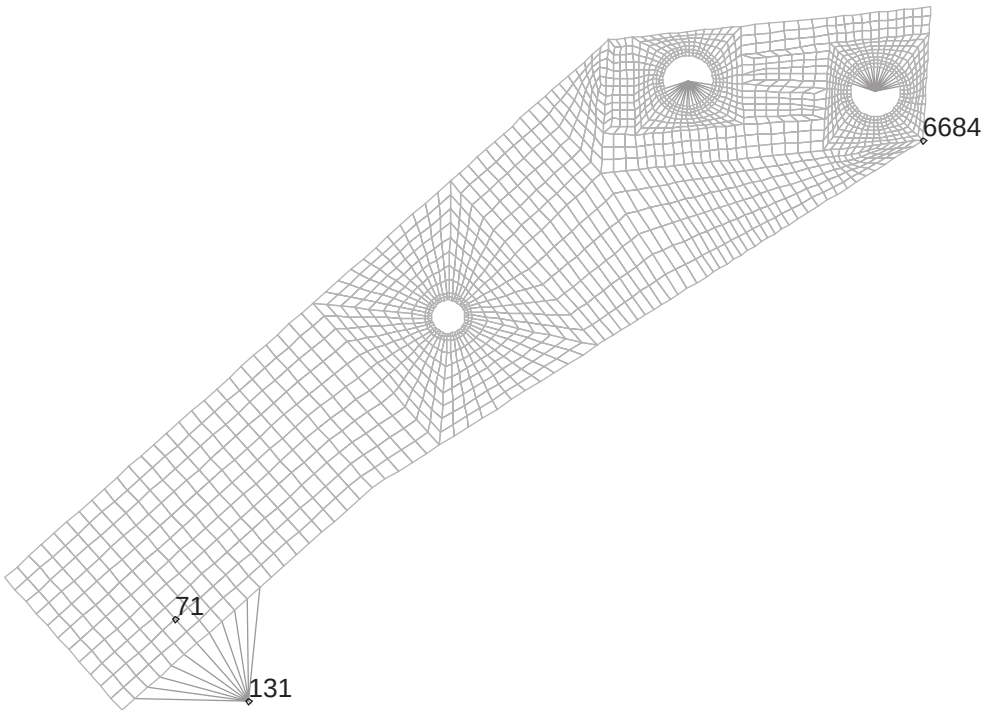

Figure 11.5: Nodal Locations Used for Deflection Reporting of the Loadarm Plate.

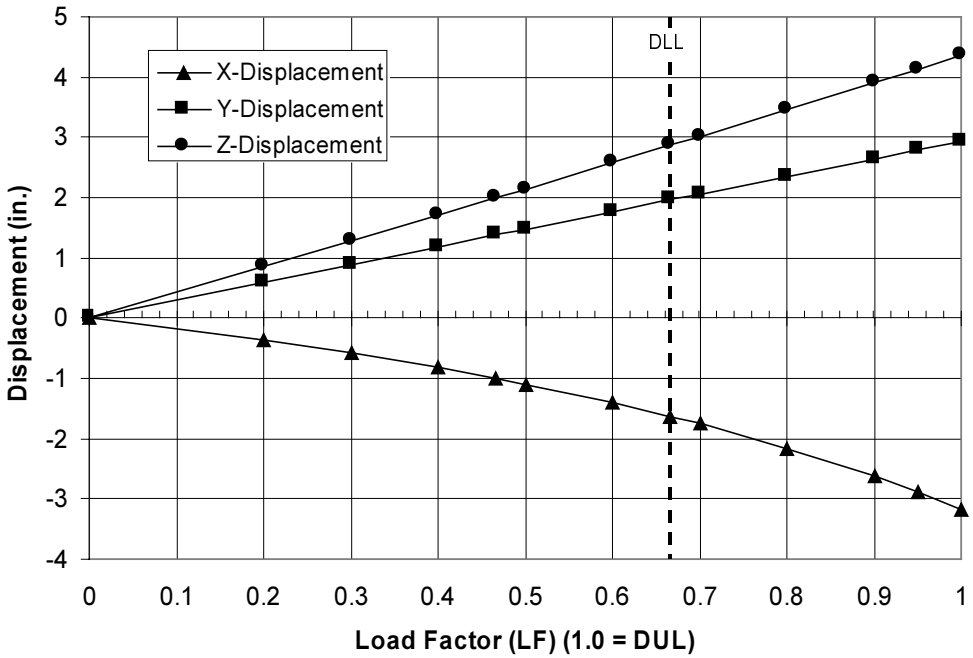

Figure 11.6: Load Factor/Deflection Plot for Node 131 Displacement Components.

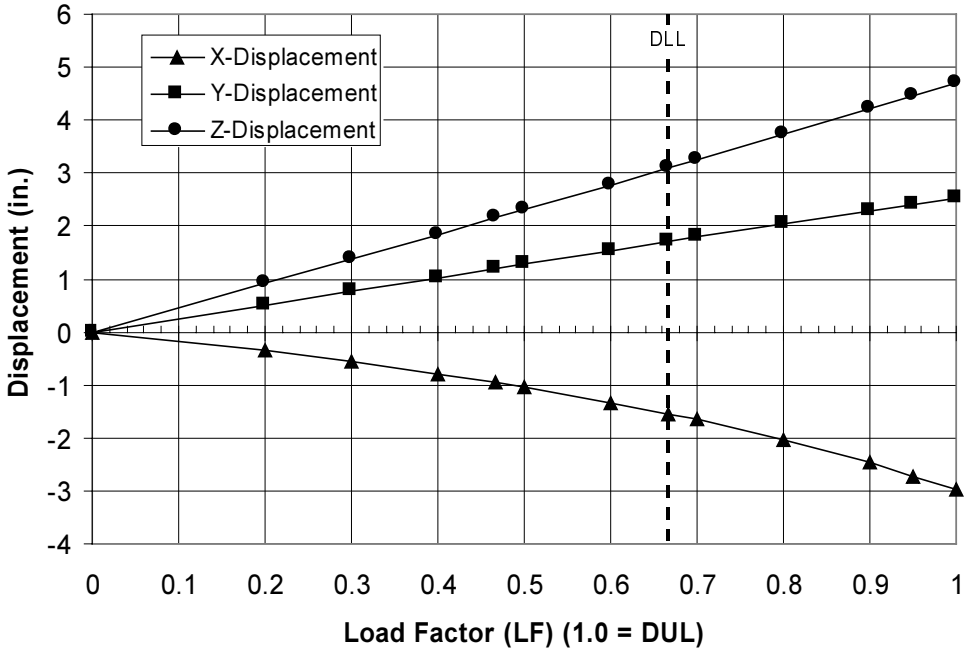

Figure 11.7: Load Factor/Deflection Plot for Node 71 Displacement Components.

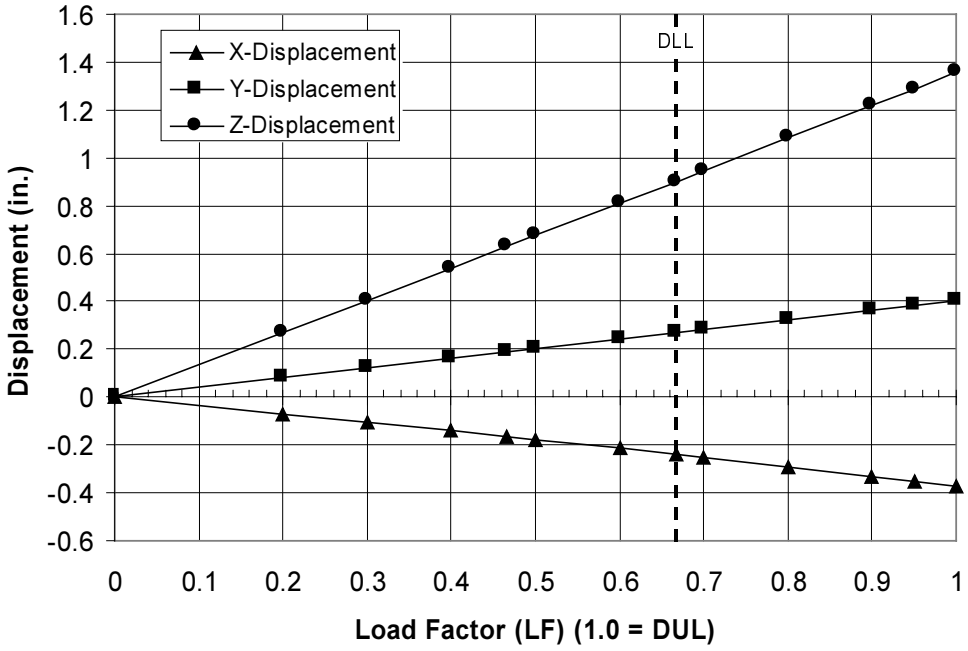

Figure 11.8: Load Factor/Deflection Plot for Node 6684 Displacement Components.

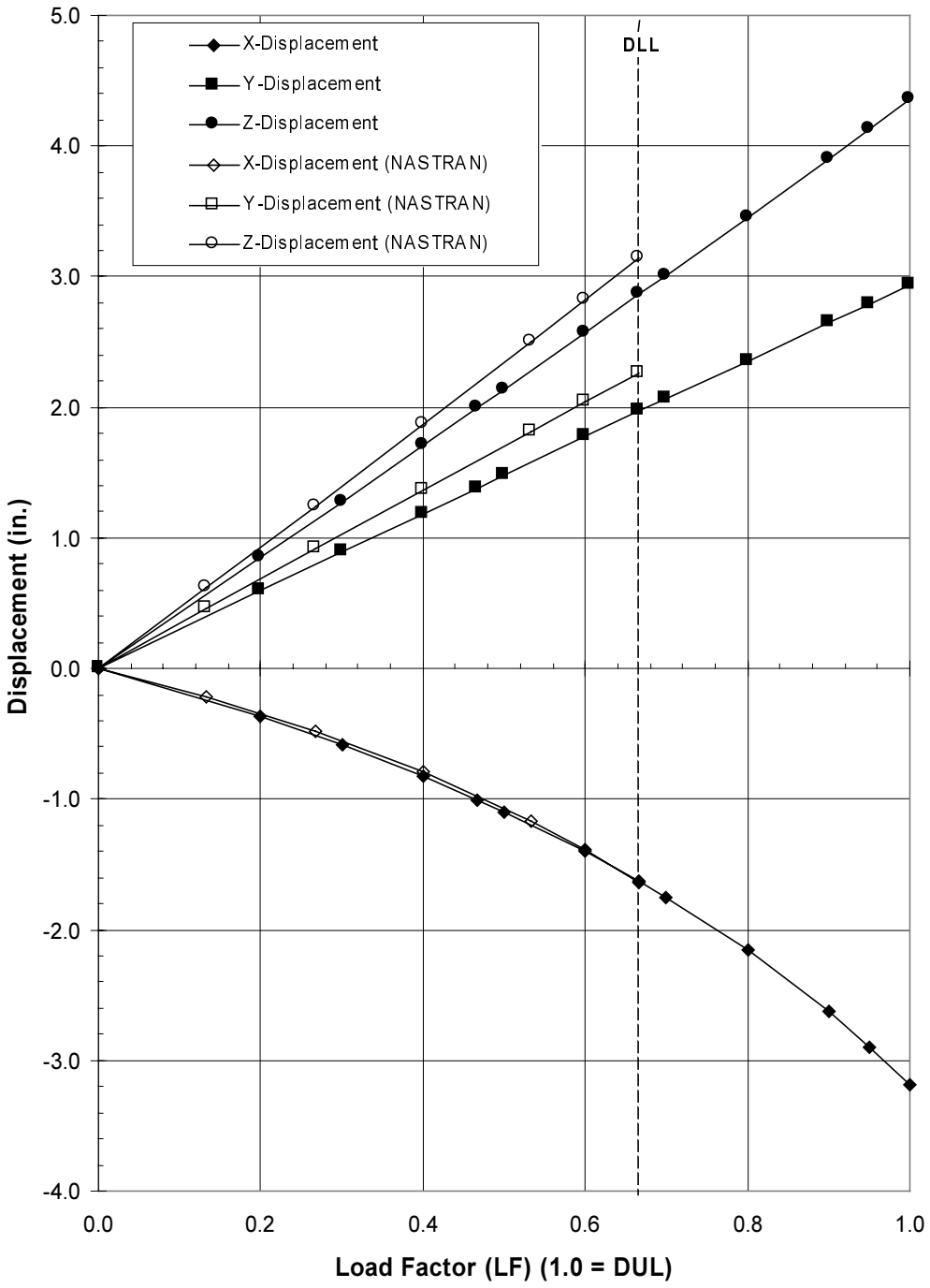

Figure 11.9: Comparison of Node 131 Displacement Components Between the Loadarm Model STAGS Finite Element Analysis and the NASTRAN Finite Element Analysis.

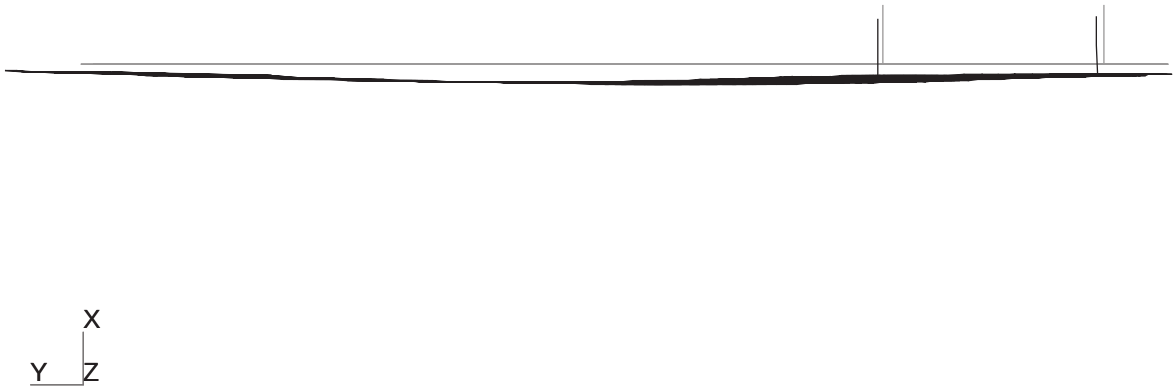

Figure 11.10: Deformed (black) and Undeformed (grey) loadarm plate at DLL for Braked Roll with the Actuator #7a Follower Load and X-Constrained Deflection, View Along Negative Z-Axis.

Figure 11.11: Deformed (black) and Undeformed (grey) loadarm plate at DLL for Braked Roll with the Actuator #7a Follower Load and X-Constrained Deflection, View Along Negative Y-Axis.

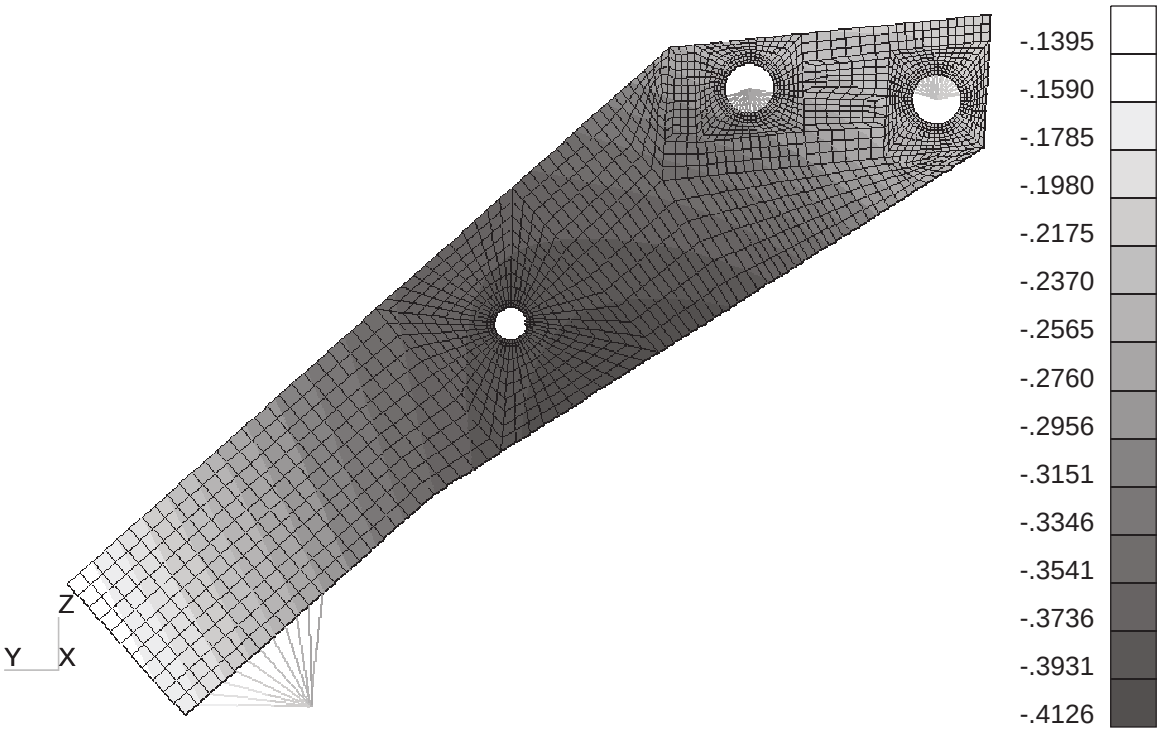

Figure 11.12: X-Deflection Contour Plot of the Loadarm Plate at DLL for Braked Roll with the Actuator #7a Follower Load and X-Constrained Deflection.

12. Conclusions

Numerous analyses have been conducted in order to predict the response of a composite semi-span test article. These analyses cover undamaged and damaged scenarios for three loading conditions; 1.0G down bending, 2.5G up bending and braked roll. The models with and without discrete damage were studied for linear and nonlinear response, with stress and strain, factors of safety, buckling, deflection and strain gage responses presented in the form of tables and plots. Several performance issues have been identified and they are as follows:

1. Comparison of linear and nonlinear results for both static response and buckling response indicates that geometric nonlinearity is only important in localized regions of the semi-span test article.

2. Since scenarios for the semi-span with discrete damage are loaded to 70% of DLL, and not up to DUL as with the undamaged scenarios, only response in the immediate vicinity of the discrete damage is of interest (e.g., high strains at the sawcut tips).

3. Possible local failure problems in the root mount plates caused by the presence of the double sweep angles. The semi-span contractor assures that the failure is small and that plasticity effects will prevent structural failure.

4. Buckling of the upper cover skin panel located between stringer #2, the forward spar, and ribs 4 and 5. This problem was corrected by adding an additional skin stack to the region.

5. Buckling of the upper cover overhangs. This problem was corrected by reducing the overhang length from 4.25 inches to 4.0 inches.

6. The presence of failed elements on the aft edge of the lower cover cutout between ribs 7 and 8 in the tapered-height model for 2.5G up bending, indicating this region should not be impacted. Failed elements in the upper cover stringers #2 and 10 for the same model and loading are ignored since these regions shall not be impacted and comparison to undamaged allowbles indicates no failure.

7. Excessive x-deflection of the loadarm plate when the follower load was considered for the braked roll loading condition. This problem was corrected by enforcing a maximum x-deflection by means of an additional load actuator.

8. Numerous other data was also presented in this report for comparison to the test results and for test planning.

Additional issues reported include the use of triangular elements and trapezoidal shaped quadrilateral elements in the STAGS finite element code, and the manner in which to implement the follower load. Both the triangular and trapezoidal shaped quadrilateral elements behaved poorly. This may be due to the presence of shell offsets that are present in the model. As a result, these elements were avoided in areas of interest. Lastly, several methods exist in STAGS for implementing the follower load needed to study the composite semi-span. However, even though these methods should yield identical results, it was found that only by using the G4 records to attach the coincident nodes on the loadarm plate and the actuator beam could the correct follower load action be achieved.

13. References

1. Rankin, Charles C.; Brogan, Frank A.; Loden, William A.; and Cabiness, Harold D.: *STAGS User Manual, Version 3.0*. Lockheed Martin Missiles & Space Co., Inc., March 1999.

REPORT DOCUMENTATION PAGE

Form Approved
OMB No. 0704-0188

1. AGENCY USE ONLY (Leave blank)	2. REPORT DATE	3. REPORT TYPE AND DATES COVERED
	August 2000	Contractor Report

4. TITLE AND SUBTITLE
Finite Element Analysis of a Composite Semi-Span Test Article With and Without Discrete Damage

5. FUNDING NUMBERS
C NAS1-96014

WU 522-83-11-01

6. AUTHOR(S)
Andrew E. Lovejoy

7. PERFORMING ORGANIZATION NAME(S) AND ADDRESS(ES)
Analytical Services and Materials, Inc.
Hampton, VA 23666

8. PERFORMING ORGANIZATION REPORT NUMBER

9. SPONSORING/MONITORING AGENCY NAME(S) AND ADDRESS(ES)
National Aeronautics and Space Administration
Langley Research Center
Hampton, VA 23681-2199

10. SPONSORING/MONITORING AGENCY REPORT NUMBER
NASA/CR-2000-210308

11. SUPPLEMENTARY NOTES
Langley Technical Monitor: Dawn C. Jegley

12a. DISTRIBUTION/AVAILABILITY STATEMENT
Unclassified-Unlimited
Subject Category 39 Distribution: Nonstandard
Availability: NASA CASI (301) 621-0390

12b. DISTRIBUTION CODE

13. ABSTRACT (Maximum 200 words)
AS&M, Inc. performed finite element analysis, with and without discrete damage, of a composite semi-span test article that represents the Boeing 220-passenger transport aircraft composite semi-span test article. A NASTRAN bulk data file and drawings of the test mount fixtures and semi-span components were utilized to generate the baseline finite element model. In this model, the stringer blades are represented by shell elements, and the stringer flanges are combined with the skin. Numerous modeling modifications and discrete source damage scenarios were applied to the test article model throughout the course of the study. This report details the analysis method and results obtained from the composite semi-span study. Analyses were carried out for three load cases: Braked Roll, 1.0G Down-Bending and 2.5G Up-Bending. These analyses included linear and nonlinear static response, as well as linear and nonlinear buckling response. Results are presented in the form of stress and strain plots, factors of safety for failed elements, buckling loads and modes, deflection prediction tables and plots, and strain gage prediction tables and plots. The collected results are presented within this report for comparison to test results.

14. SUBJECT TERMS
Composite; Stitching; Finite Element; Wing; Damage Tolerance

15. NUMBER OF PAGES
153

16. PRICE CODE
A08

17. SECURITY CLASSIFICATION OF REPORT	18. SECURITY CLASSIFICATION OF THIS PAGE	19. SECURITY CLASSIFICATION OF ABSTRACT	20. LIMITATION OF ABSTRACT
Unclassified	Unclassified	Unclassified	UL